

# **Characterization of Catalytically Active Solid-Liquid Interfaces by Scanning Electrochemical Microscopy (SECM)**

(Charakterisierung von katalytisch aktiven fest-flüssig-Grenzflächen unter  
Nutzung des elektrochemischen Rastermikroskops (SECM))

Von der Fakultät für Mathematik und Naturwissenschaften  
der Carl von Ossietzky Universität Oldenburg  
zur Erlangung des Grades und Titels einer

Doktorin der Naturwissenschaften (Dr. rer. nat.)

angenommene **Dissertation**

von Frau Chem. Ing.

**Carolina Nunes Kirchner**

geboren am 01.04.1979

in São Paulo, Brasilien

Oldenburg, November 2008

This work was carried out from September 2003 to July 2008 at the Carl von Ossietzky University of Oldenburg, Faculty of Mathematics and Science, Center of Interface Science (CIS), Department of Pure and Applied Chemistry and Institute of Chemistry and Biology of the Marine Environment under the guidance of Prof. Dr. Gunther Wittstock.

Part of this work has been published and is cited as [A#]. The list of own cited work is given after the Bibliography.

Gutachter: Prof. Dr. Gunther Wittstock  
Zweitgutachterin: Prof. Dr. Katharina Al-Shamery  
Tag der Disputation: 14. November 2008

# Acknowledgements

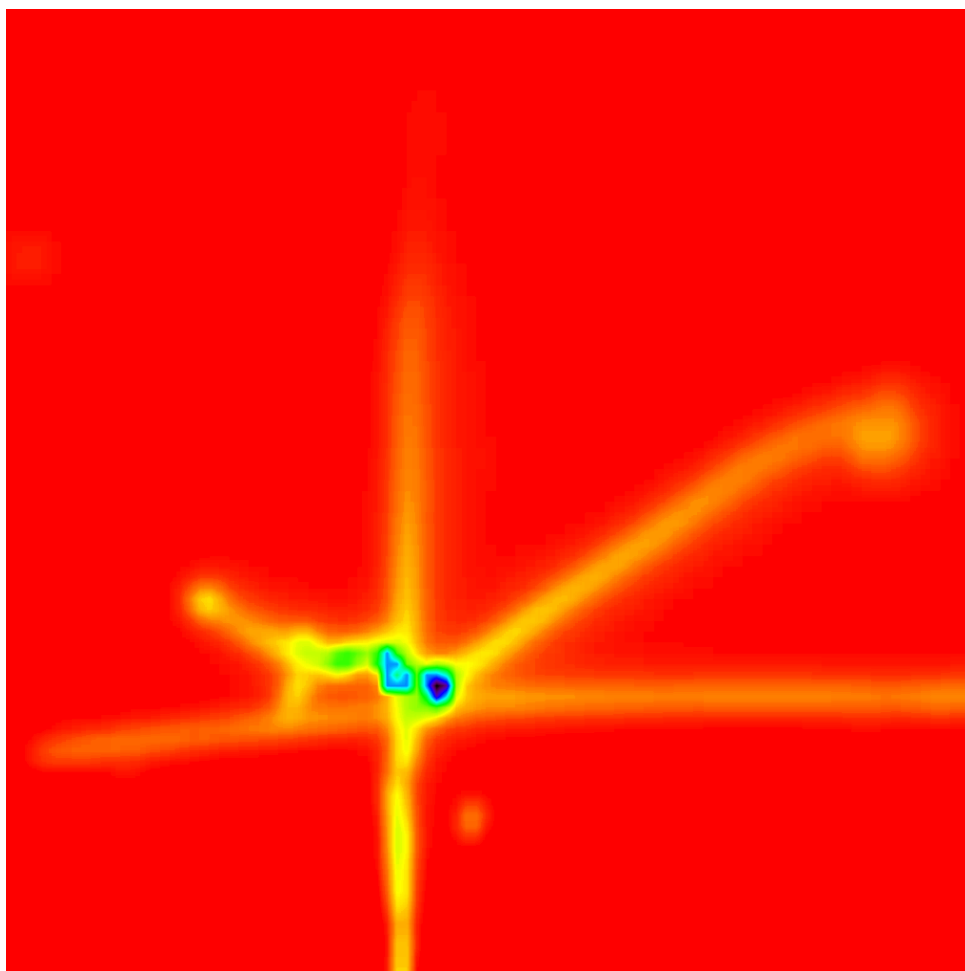
First and foremost, I would like to thank my advisor Prof. Dr. Gunther Wittstock. Without his guidance, great ideas and support, this dissertation would not have been possible. I am indebted to him not only for what he has taught me technically, but also for believing in me, it motivated me to complete this thesis. I am especially grateful for his patience and advice when progress was difficult.

I would like to thank all my former and current colleagues in our group, specially Malte Burchardt, Dr. Yan Shen and Dr. Jatin Sinha for their active cooperation. I would like to thank Markus Träuble for providing me the simulations and for his patience. I would also acknowledge my former colleague Dr. Chuan Zhao for introducing me to the SECM. I am very grateful to Sascha Pust for invaluable help through several discussions and of course, his "computer help" and for correcting the manuscript. I would like to express my deepest thanks to Prof. Dr. Sabine Szunerits from LEPMI for the exciting cooperation and enthusiasm for the results. I would like to thank Dr. Karl Heinz Hallmeier from University of Leipzig for the XPS measurement. My deepest thanks are also to Mr. Folkert Roelfs and Mr. Harry Happatz from the University of Oldenburg who helped me with SECM construction. Especially, I would like to acknowledge Carl von Ossietzky Universität Oldenburg for financial support.

I would like to thank Elke and Dora Schwetje who helped me a lot at the beginning of my stay in Germany (without you I would not be here). I would thank my parents in law Eckart Kirchner and Maria Apke for the immense help and for always being there. I cannot forget to thank all my friends from Oldenburg that made my life more colorful throughout these years, specially Anne, Jörn, Anna and Tolga. I would like to express my sincere gratitude to Thais and Carlos for their constant support and friendship.

I would like to thank all of my family and friends in São Paulo, without their emotional support it would be impossible to have the peace of mind to work away from home. I would like to express my gratitude especially to my sisters Nathalia and Gabriela, to my brother-in-law Caio, and my dear nephew Arthur. I would like to thank my parents, João and Iara, who have provided love and support to me for my life and school career. They have been my strongest supporting foundation and my biggest fans through everything. I am forever indebted to them for all they have done for me and for making me who I am. Last but not least, I would like to thank Thomas who makes me laugh everyday, for his continuous support, patience, friendship, and love.





*Aos meus pais Iara e João,  
e ao meu marido Thomas*



## Abstract

The development and optimization of biosensor components with respect to sensitivity, biospecificity, response time, reliability and costs has been the object of research for many years. Scanning electrochemical microscopy (SECM) has been used in this context to analyze the functional properties of sensor components, mainly in a qualitative or comparative way. This thesis deals with the quantitative characterization of such materials and active layers using SECM. The results were compared to theoretical models and corroborated with other electrochemical techniques.

The SECM feedback mode has been used to analyze new electrode materials and insulating cover materials. Titanium nitride thin film electrodes have been analyzed regarding their suitability as electrode material that offers access to nanostructured transducers. It was shown that enhanced surface area, cover layers from contaminations or surface oxidation have a large influence on the charging currents and the electron transfer rate. Silicon dioxide (SiO<sub>x</sub>) layers were investigated as insulating coatings. The insulation properties of gas-phase-deposited SiO<sub>x</sub> varied with film thickness. The electrochemical characterization of SiO<sub>x</sub> layers showed only electrochemical activity for 6.5 nm thickness due to presence of pinholes, while thicker layers showed a very good insulating characteristic.

Many electrochemical biosensors, but also biofuel cells show a very complicated interplay of intrinsic chemical kinetics of the materials and various mass-transport limitation. These relations were investigated using model systems agglomerates of paramagnetic microbeads that were coated with the enzyme  $\beta$ -galactosidase. By variation of the ratio between modified and unmodified beads, the size of the bead agglomerates and the solution composition, the internal and external diffusion of reagents and products was varied independently and product fluxes were measured by the generation-collection mode of SECM. The fluxes could be compared to the results of digital simulations. The analysis of the external diffusion demonstrated that there was enough substrate to diffuse within the agglomerate. The apparent Michaelis-Menten constant extracted from the SECM measurements has been compared with a digital simulation and showed that the model used to analyze the SECM is a good approximation for quantification of spot systems. Relating this flux to the number of enzyme-modified beads in the agglomerate gave quantitative results on the shielding of mass transport by bare beads in agreement with numerical models.

SECM in the generator-collector configuration has been used to determine the surface concentration of accessible oligonucleotides (ODN) bound to microelectrochemically deposited polypyrrole. The ODN strands were hybridized with an enzyme-labeled ODN strand. The measurements were calibrated using bead-immobilized enzymes. Feedback effects as possible interference were investigated and showed to become insignificant at distances larger than 3 microelectrode radii. A SECM image of the ODN pattern has been recorded, providing the amount of ODN that were available for hybridization in such systems.





# Zusammenfassung

Die Entwicklung von Biosensorkomponenten in Bezug auf Sensitivität, Biospezifität, Antwortverhalten, Zuverlässigkeit und Kosten ist seit vielen Jahren Gegenstand der Forschung. Die elektrochemische Rastermikroskopie (SECM) wurde in diesem Zusammenhang genutzt, um die funktionellen Eigenschaften von Sensorkomponenten hauptsächlich in qualitativer oder vergleichender Hinsicht zu untersuchen. Diese Arbeit beschäftigt sich mit der quantitativen Charakterisierung solcher Materialien und aktiver Schichten mit der SECM. Die Resultate werden mit theoretischen Modellen verglichen und durch Ergebnisse anderer elektrochemischer Messverfahren gestützt.

Der SECM-Feedback-Modus wurde eingesetzt, um neue Elektrodenmaterialien und isolierende Deckschichten zu untersuchen. Titanitrid-Dünnschichtenelektroden wurden auf ihre mögliche Eignung als Elektrodenmaterial untersucht, das einen Zugang zu nanostrukturierten Transducern ermöglicht. Es wurde nachgewiesen, dass eine vergrößerte Oberfläche und Deckschichten aus Kontaminationen oder Oberflächenoxidation einen großen Einfluss auf die Ladeströme und die Elektronentransfargeschwindigkeit haben. Siliziumdioxid ( $\text{SiO}_x$ )-Schichten wurden als isolierende Beschichtungen untersucht. Die isolierenden Eigenschaften von gasphasenabgeschiedenem  $\text{SiO}_x$  variierte mit der Schichtdicke. Die elektrochemische Charakterisierung der  $\text{SiO}_x$ -Schichten zeigte elektrochemische Aktivitäten nur für Schichten von 6.5 nm Dicke, die auf die Gegenwart von kleinen Kanälen (pinholes) zurückzuführen ist. Dickere Schichten zeigte gute isolierende Eigenschaften unter elektrochemischen Bedingungen.

Viele elektrochemische Biosensoren, aber auch Biobrennstoffzellen zeigen ein sehr kompliziertes Zusammenspiel der intrinsischen chemischen Kinetik der Materialien und verschiedenen Massentransportlimitierungen. Diese Beziehungen wurden mit einem Modellsystem untersucht, das aus Agglomeraten paramagnetischer Mikropartikel bestand. Die Partikel waren mit dem Enzym  $\beta$ -Galactosidase beschichtet. Durch Variation des Verhältnisses zwischen modifizierten und nicht modifizierten Partikeln, der Größe der Agglomerate und der Lösungszusammensetzung konnte die interne und externe Diffusion der Reaktanten unabhängig variiert und der Produktfluss im SECM-Generator-Kollektor-Modus gemessen werden. Die Flüsse konnte mit den Ergebnissen digitaler Simulationen verglichen werden. Die Analyse der externen Diffusion zeigte, dass genügend Substrat vorhanden war, um in das Agglomerat hinein zu diffundieren. Die scheinbare Michaelis-Menten-Konstante, die aus den SECM-Messungen extrahiert werden konnte, wurde mit dem Ergebnis digitaler Simulationen verglichen und zeigte, dass das verwendete Modell zur Analyse der SECM-Messungen eine gute Näherung für die Quantifizierung in punktförmigen Systemen darstellt. Normierung der Flüsse auf die in einem Agglomerat enthaltenen enzymmodifizierten Partikel lieferte quantitative Ergebnisse über die Abschirmung des Massentransports durch unmodifizierte Partikel in Übereinstimmung mit numerischen Modellen.

Die SECM in der Generator-Kollektor-Konfiguration wurde zur Bestimmung der Grenzflächenkonzentration von zugänglichen Oligonucleotiden (ODN) verwendet, die an mikroelektrochemisch abgeschiedenes Polypyrrol gebunden waren. Die ODN-Stränge wurden mit enzymmarkierten ODN-Strängen hybridisiert. Die Messungen wurden mit Partikel-gebundenen Enzymen kalibriert. Es konnte gezeigt werden, dass der Feedback-Effekt als mögliche Störung keinen signifikanten Einfluss ausübt, wenn der Arbeitsabstand größer als drei Mikroelektrodenradien ist. Eine SECM-Abbildung eines ODN-Musters wurde aufgezeichnet und zeigte die Menge an ODN, die für eine Hybridisierung in dem System zugänglich war.



# Table of Contents

<b>1</b>	<b>Introduction</b> .....	<b>1</b>
<b>2</b>	<b>Principles of scanning electrochemical microscopy</b> .....	<b>7</b>
2.1	<i>Ultramicroelectrodes</i> .....	8
2.2	<i>Feedback mode</i> .....	11
2.3	<i>Generation/Collection mode</i> .....	19
2.4	<i>Direct mode</i> .....	22
<b>3</b>	<b>Scanning Electrochemical Microscopy Instrumentation</b> .....	<b>25</b>
3.1	<i>Overview</i> .....	26
3.2	<i>Realized SECM setups</i> .....	28
3.3	<i>Positioning System</i> .....	33
3.3.1	Stepper Motor .....	33
3.3.2	Piezoelectric actuator .....	36
3.3.3	Piezoelectric motors .....	37
3.3.4	Translation stages .....	39
3.4	<i>ADC and DAC converter</i> .....	39
3.5	<i>Software</i> .....	41
3.6	<i>Constant distance mode</i> .....	42
3.7	<i>Overview and future developments</i> .....	43
<b>4</b>	<b>Material characterization by SECM approach curves</b> .....	<b>45</b>
4.1	<i>Evaluation of thin film TiN electrodes for electroanalytical applications</i> .....	45
4.1.1	Introduction .....	45
4.1.2	Structural characterization .....	47
4.1.3	Electrical and basic electrochemical characteristics .....	50
4.1.4	SECM investigation of electron transfer kinetics .....	54
4.1.5	Conclusions .....	63
4.2	<i>Electrochemical investigation of the influence of thin SiO<sub>x</sub> films deposited on gold on charge transfer characteristics</i> .....	65
4.2.1	Introduction .....	65
4.2.2	Deposition of SiO <sub>x</sub> thin films on gold .....	67
4.2.3	Characterization of the gold/SiO <sub>x</sub> films .....	68
4.2.4	SECM investigation of SiO <sub>x</sub> .....	70

---

4.2.5	Electrochemical impedance analysis .....	73
4.2.6	Conclusions .....	75
<b>5</b>	<b>Study of diffusion and reaction in microbead agglomerates .....</b>	<b>77</b>
5.1	<i>Introduction</i> .....	77
5.1.1	Use of magnetic microbeads as bioreceptor support .....	79
5.1.2	Design of the experiment.....	82
5.2	<i>Kinetics of immobilized enzymes</i> .....	84
5.2.1	Effects of substrate diffusion on the kinetics of immobilized enzyme in porous support .....	88
5.3	<i>Digital simulation of external diffusion</i> .....	99
5.4	<i>Optimization of SECM imaging conditions</i> .....	100
5.4.1	Hindered diffusion .....	100
5.4.2	Experimental determination and simulation of the Michaelis-Menten curve .....	103
5.4.3	Study of the bead spot height .....	106
5.5	<i>Investigation of the shielding inside the bead spot</i> .....	109
5.5.1	Experimental data .....	109
5.5.2	Calculation of PAP fluxes .....	112
5.5.3	Analysis of the internal diffusion .....	117
5.5.4	Diffusion Model 1: uniform layer of beads .....	118
5.5.5	Diffusion Model 2, Case 1: big half-sphere with $h = r_S$ (exp).....	120
5.5.6	Diffusion Model 2, Case 2: small half-sphere with $r_S = h$ (exp) .....	122
5.5.7	Diffusion Model 2, Case 3: medium half-sphere, with $N_{tot}$ from experiment .....	124
5.5.8	Comparison of the fluxes for the three models.....	125
5.6	<i>Conclusions</i> .....	127
<b>6</b>	<b>Polymerization of polypyrrole and detection of hybridization events.....</b>	<b>131</b>
6.1	<i>Introduction</i> .....	131
6.2	<i>Localized immobilization of oligonucleotides onto thin gold films and hybridization</i> .....	133
6.3	<i>Determination of the accessible ODN concentration using the GC mode of SECM</i> .....	138
6.4	<i>Conclusion</i> .....	147

---

<b>7</b>	<b>General Concluding Remarks and Outlook .....</b>	<b>149</b>
<b>8</b>	<b>Appendix .....</b>	<b>155</b>
8.1	<i>Procedures</i> .....	155
8.1.1	Preparation of the TiN layers .....	155
8.1.2	Preparation of the gold/SiO <sub>2</sub> composite slides.....	155
8.1.3	Gold evaporation on glass .....	156
8.1.4	Modification of magnetic microbeads .....	156
8.1.5	Preparation of modified beads solution in different concentrations .....	157
8.1.6	Formation of microbeads microspot array .....	158
8.1.7	Experimental set up for Michaelis-Menten study .....	158
8.1.8	Preparation of modified beads suspensions for analysis of $K_M'$ and $v_{max}$ of modified bead free in solution.....	159
8.1.9	Experiment setup for investigation of the shielding effect inside the bead spot .....	161
8.1.10	Local deposition of polypyrrole-ODN spots.....	162
8.1.11	Hybridization and construction of biological assembly for the determination of the DNA density grafted.....	162
8.2	<i>Material and chemicals</i> .....	163
8.3	<i>Standard solutions</i> .....	165
8.4	<i>Equipments</i> .....	165
8.5	<i>Abbreviations and symbols</i> .....	168
8.5.1	Abbreviations .....	168
8.5.2	Symbols.....	170
<b>9</b>	<b>Bibliography .....</b>	<b>175</b>
	<b>List of own publications .....</b>	<b>191</b>
	<b>Curriculum vitae .....</b>	<b>194</b>



# 1 Introduction

The incomparable ability of biological organisms to recognize trace amounts of biochemicals in complex systems stimulated scientists to develop systems containing bioreceptors from biological organisms as recognition element for a given substance.<sup>[1]</sup> The first biosensor<sup>[2]</sup> originated from the modification of the oxygen electrode invented by Clark et al.<sup>[3, 4]</sup> by applying an enzyme-containing membrane (glucose oxidase, GOx) onto the oxygen electrode in 1962. Since then many concepts, definitions and prototypes of biosensor have been developed with different sensing technologies and devices. An explosive amount of research related to biosensor has been appeared in the last three decades.<sup>[1, 5, 6]</sup>

The International Union of Pure and Applied Chemistry (IUPAC) defines a biosensor as "a device that uses specific biochemical reactions mediated by isolated enzymes, immunosystems, tissues, organelles or whole cells to detect chemical compounds usually by electrical, thermal or optical signals".<sup>[10]</sup> Alternatively a biosensor is defined as consisting of a biological recognition element in direct contact with a transducer and a detection element.<sup>[11]</sup> The selective biological event (e.g. enzymatic reaction) gives a rise to a signal that must be picked up by a transducer.

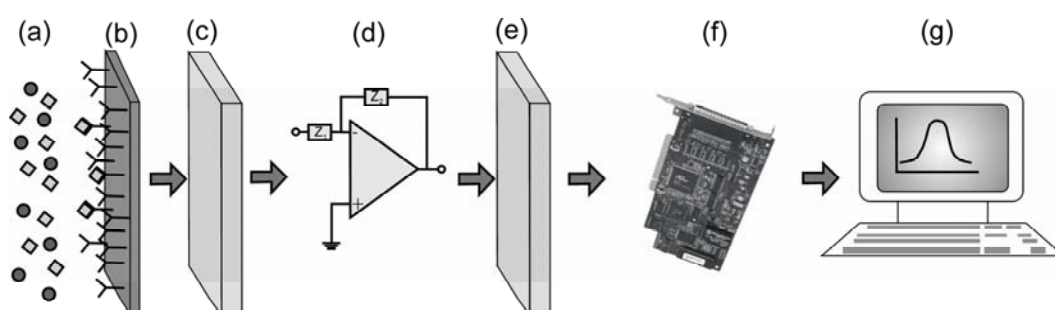


**Figure 1.1.** Basic elements of a biosensor: (a) sample containing an analyte (squares) and other compounds (circles), (b) the bioreceptor/biological recognition element binds specifically to the analyte and a specific biological event take place (e.g. an enzyme converts a substrate to product), which is monitored in the (c) transducer which converts the signal to an electronic signal that is then (d) amplified, (e) detected, (f) processed, and (g) displayed.

The transducer is a key element in the biosensor because it is responsible for conversion and transduction of the binding event into a detectable electrical, optical or other physical signal. The signal is then amplified by a detector circuit and displayed on an output device (Fig. 1.1).

According to Scheller et al.<sup>[12]</sup> biosensors can be classified as bioaffinity sensors or biocatalytic sensors. Bioaffinity sensors detect one binding event per biorecognition element (e.g. for an antibody-antigen binding) whereas biocatalytic sensors cause a continuous conversion of the analyte by an immobilized enzyme (e.g. glucose sensor). Further classification can be performed according to the biorecognition elements, the type of transducer (Table 1.1),<sup>[1]</sup> the analyte (e.g. glucose, urea, glutamate) and the origin of the sample (whole blood, serum, cell culture medium, food sample, environmental samples).<sup>[5]</sup>

**Table 1.1:** Biosensor classification.

Biorecognition element	Transducer type
Antibody	Optical
Enzyme	Electrochemical
DNA	Mass-based
Cell	Thermal
Biomimetic	

Biosensors incorporated with enzymes are the most used and studied type due to their specific binding capability and its biocatalytic activity,<sup>[5]</sup> and the electrochemical detection is the most common among other detection principles. The advantages in using electrochemical biosensors over other types of biosensors are several:<sup>[5]</sup> simple setup, low cost, easy miniaturization, excellent detection limits and its ability to be used in turbid solution.

The aims of biosensor research are the optimization of existing biosensor designs and concepts, and development of new detection principles, materials and biosensing designs in order to improve sensitivity and biospecificity. The development of electrochemical biosensors requires a highly interdisciplinary approach, requiring input from chemistry, physics and biochemistry. The biosensor design depends upon the principle of operation of the transducer, analyte, and working environment.<sup>[6]</sup> The performance of the electrochemical biosensor for a given problem is greatly influenced by the material used. More specifically functional materials must be selected for the following parts:<sup>[6]</sup>

- materials for the electrode and supporting substrate (transducer);
- materials for immobilization of biological recognition elements;
- materials for the fabrication of the outer membrane;
- biological elements, such as enzymes, antibodies, antigens, oligonucleotides, mediators and cofactors.



Apart from glucose monitoring for diabetes patients (market is approximately  $5.95 \times 10^9$  USD a year),<sup>[7]</sup> most biosensors have been restricted to academic studies rather than practical applications,<sup>[8]</sup> contradicting the early positive predictions.<sup>[9]</sup> While it appears conceptually straight forward to combine the high selectivity of the biological recognition element with the high sensitivity of electrochemical techniques, a bioreceptor directly immobilized on the electrode surface may inhibit electron transfer reactions thereby degrading the high sensitivity of electrochemical sensors. In other cases an electronic communication between enzymes and electrodes occurs only for specific relative orientations of the enzyme towards the electrode that are difficult to achieve. One approach to overcome this problem is the use of a reversible or quasi-reversible redox couple as an electron mediator carrying electrons between the biomolecule and the electrode. Nevertheless, the possibility of realizing this setup depends on the characteristic of each element of the biosensor and on the interaction between them. An alternative concept is the development of so-called biochips in which the support surface of the biomolecules is separated from the transducer surface. This allows individual replacement of either the transducer or the biorecognition elements. It opens up more possibilities for multiplexing and parallel analysis and makes possible the use of costly but long living transducers together with disposable and affordable biomolecules on a disposable chip. Since these miniaturized systems require optimization that is in several aspects similar to biosensor research they are treated here together.

Scanning electrochemical microscopy (SECM), which is the most important method used in this work, has been shown to be a prominent technique to characterize and optimize biosensor components. Since Wang et al.<sup>[13]</sup> used SECM to probe the bioactivity of tissue-containing carbon surfaces the potential of this techniques to gain local information on biosensor components, the SECM has been used for a wide range of materials.<sup>[A4]</sup> SECM offers unique possibilities to prepare and investigate advanced sensing concepts.<sup>[A4, A10]</sup> An amperometric ultramicroelectrode (UME) can be used as a positionable chemical sensor. It detects faradaic currents originated from specific chemical species, obtains qualitative and quantitative information on localized redox catalysts, detects species in very small volumes trapped between the UME and the sample, and induces chemical reactions in limited spaces, and can be used as a tool for fabrication and characterization of biological materials.<sup>[14-23]</sup>

One of the promising potentials of SECM for biosensor research is the possibility to investigate immobilized enzymes independent of the communication to the electrode onto

which they are immobilized. SECM can be used to probe the enzymatic activity from the solution side of an immobilized enzyme film with an UME that is free of any cover layer. Microstructured biosensor surfaces have been investigated and fabricated by SECM.<sup>[13][A4]</sup> It can also be used to locally modify surfaces by different defined electrochemical mechanisms.<sup>[24-26]</sup> The combination of the imaging capabilities for specific enzymatic reactions and the possibility to modify the surfaces in a buffer solution make SECM an ideal tool to explore the potential of such micropatterned surfaces for sensing applications. SECM can also be used as a read-out tool for proteins and DNA chips.<sup>[27, 28][A6]</sup>

The main scope of this thesis is the use of SECM to characterize materials and active layers occurring in biosensors. Compared to the status of the literature at the beginning of the thesis, the SECM analysis was not restricted to qualitative or comparative investigations but measurements are optimized to yield quantitative results that can be related to theoretical diffusion-reaction models at the solid-liquid interface. The theory of the methods will be outlined in Chapter 2. The difficulty of quantitative analysis of biosensor materials stems from the complexity and local heterogeneity of many materials and layers. In order to deal with such materials, the application of complementary techniques represents a sensible approach which becomes more and more evident also for SECM.<sup>[A4]</sup> Within this work some instrumental designs were developed that allow to combine SECM with other techniques. This required a reconsideration or adaptation of the hardware (positioning system, potentiostat) used for SECM. A summary of the design principles is outlined in Chapter 3. These instruments have been used within this thesis but were also crucial for other related work.<sup>[29-32]</sup>

One of the main limitation for miniaturization of biosensors is that the components used in sensors (carbon-based electrodes, gold, etc) are difficult to handle in established processes of the semiconductor industry. Therefore the search continues for alternative materials that can be processed according to the protocols of the semiconductor industry and provide sufficient performance when immersed in liquid electrolytes and under potentiostatic control. As an example Chapter 4 contains investigations of TiN as electrode material<sup>[A7, A3]</sup> that can be nanostructured and of vapor-deposited thin films of SiO<sub>x</sub><sup>[A1]</sup> that might be used as insulating barrier layers.

Chapter 5 contains an investigation of the conversion produced by agglomerates of enzyme-modified beads. A known procedure was used to form mound-shaped agglomerates of these beads. The mutual influence of enzyme loading, mass transport in solution and within

the agglomerate was investigated by a combination of quantitative SECM experiments and theoretical simulation. It could be shown that the arrangement of such beads has important consequences for analytical signals in procedures that use such microbeads as dispersed, yet heterogeneous sensing platform such sandwich immunoassay<sup>[33, 34]</sup> and integrated microfluidic biochemical detection system.<sup>[35]</sup>

A widely used class of materials for immobilization of biological elements is substituted, electronically conducting polypyrrole due to its adherence to metallic and carbon supporting electrodes and their compatibility with biological elements. SECM has been used to study polypyrrole deposition,<sup>[26, 36-38][A9]</sup> ion transport and electron transfer at polypyrrole films,<sup>[39]</sup> immobilization of glucose oxidase via direct electrochemical microspotting of polypyrrole-biotin film<sup>[16]</sup> and DNA hybridization.<sup>[20, 27, 28, 40-42]</sup> This work adds new facets to these studies by providing a way for quantification of hybridization events after oligonucleotide immobilization into the polypyrrole matrix (Chapter 6).<sup>[A6]</sup> This was possible by combining localized deposition of oligonucleotide-functionalized polypyrrole with quantitative measurements of a captured enzyme label with a calibration of such measurements using enzyme-modified beads. In Chapter 7 the results of this thesis are summarized. The Appendix contains the experimental procedures, used materials and instruments, and a list of abbreviations and symbols.



## 2 Principles of scanning electrochemical microscopy

Scanning probe microscopy (SPM) is a family of techniques that record a distance dependent interaction between a scanning probe and a sample.<sup>[43]</sup> The most applied SPM are scanning force microscopy (SFM), also known as atomic force microscopy (AFM),<sup>[44-46]</sup> scanning tunneling microscopy (STM),<sup>[47-50]</sup> scanning electron microscopy (SEM),<sup>[51-54]</sup> scanning near-field optical microscopy (SNOM),<sup>[55, 56]</sup> and scanning electrochemical microscopy (SECM).<sup>[57-63]</sup> The acronym is used for both, the method (scanning electrochemical microscopy) and the instrument (scanning electrochemical microscope)

Generally an SPM images local physical properties of the sample such as topography, morphology, geometry, density of states, stiffness, adhesion, etc. The SECM allows to map the topography of sample as well as to record spatially resolved variations in the (electro)chemical reactivities, induce local electrochemical modifications, measure local solute concentration and investigate heterogeneous and homogeneous kinetics. In SECM, faradaic currents are measured at an ultramicroelectrode (UME). The UME is a specific probe with an active electrode smaller than the diffusion length in the critical time of the experiment. It can be applied to a large variety of interfaces<sup>[64]</sup> including solid-liquid,<sup>[65-67]</sup> liquid-liquid,<sup>[68-72]</sup> and liquid-gas<sup>[73-75]</sup> interfaces. It has often been used to analyze components of chemical and biochemical sensors as outlined in a recent review.<sup>[A4]</sup> The sample can be conductive, semiconductive or insulating. In contrast to other SPM, larger scan areas are feasible in SECM (100 nm to 1000  $\mu\text{m}$ ) by the probe and thus and diffusion layer near the surface can be measured.<sup>[76]</sup>

SECM emerged from experiments performed with UME and electrochemical scanning tunneling microscopes (ECSTM). In 1986 Engstrom et al.<sup>[77]</sup> used an amperometric UME to measure concentration profiles close to a macroscopic sample electrode. At the same period Bard et al.<sup>[78]</sup> reported large currents at large sample-tip distances in an ECSTM. Although these were considered the first SECM experiments, the use of SECM technique was just possible after Kwak and Bard<sup>[76, 79]</sup> developed the feedback concept, describing the diffusion-limited faradaic current measured at an UME as a function of the distance  $d$  above a macroscopic planar sample immersed in an electrolyte solution. Theory regarding SECM has been developed since the SECM invention for several operation modes and probe geometries and can be found in several reviews.<sup>[76, 79-93]</sup>

Recently Wittstock et al.<sup>[60]</sup> published a review where several applications are discussed. In this thesis the most important contributions were done using SECM and therefore the principle will be outlined here. The most important working modes are feedback mode (Section 2.2), generation-collection mode (Section 2.3), and direct mode (Section 2.4).<sup>[A4]</sup> The chemically selective UME is the local probe in SECM. For quantitative work, the response of such UME is compared to the response in the solution bulk. Therefore the respective theory is detailed here.

## 2.1 Ultramicroelectrodes

The SECM probe<sup>1</sup> is normally an amperometric disk-shaped UME that is embedded in an insulating sheath, typically made from glass. The insulating sheath of the UME is beveled in order allow the tip to approach close to the sample and to improve resolution. Conventionally, the UMEs are made from Pt, Au and carbon fibers but electrodes such as boron-doped diamond (BDD)<sup>[94]</sup> and Pt-Ir<sup>[95]</sup> have been successfully used as amperometric UME. Potentiometric electrodes<sup>[96, 97]</sup> have also been used, but not for this work.

The term UME is used for amperometric electrodes with at least one of the characteristic dimension (e.g. radius) smaller than the diffusion length of the diluted reactant through the duration of the experiments ( $\sqrt{2Dt}$ ), where  $D$  is the diffusion coefficient and  $t$  is the time scale of the experiment).<sup>[98-101]</sup> For amperometric experiments, the condition is typically met by electrodes with one dimension less than 25  $\mu\text{m}$ . Typical UME diameters are 10 or 25  $\mu\text{m}$ , although many effort has been put to produce smaller electrodes in the nm range.<sup>[102-104]</sup> There are theoretical treatment for disk,<sup>[76]</sup> conical,<sup>[82]</sup> hemispherical,<sup>[86]</sup> spherical,<sup>[105]</sup> and ring geometries<sup>[84]</sup> of UMEs. While these UME shapes are suitable for SECM experiments, all experiments in this thesis were done with Pt disk-shaped 25  $\mu\text{m}$  diameter UME unless stated otherwise. The UME dimensions such as current  $i_T$ , electrode potential  $E_T$  and radius  $r_T$  are indexed with "T" (refers to tip) and accordingly, these dimensions are indexed with "S" for the sample (refers to sample, substrate, specimen). The geometry of a disk-shaped UME can be characterized by two important radii: The radius  $r_T$  of the active electrode area and the radius  $r_{\text{glass}}$  of the insulating glass sheath (Fig. (2.1)). The ratio  $RG = r_{\text{glass}} / r_T$  is an important measure that influences the theoretical approaches.

---

<sup>1</sup> UME = electrode = active electrode area  
Probe = physical body (insulation) + active electrode area

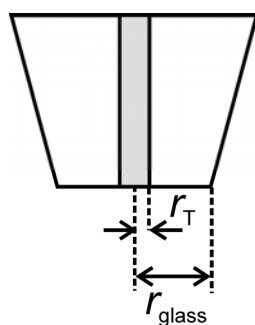


**Figure 2.1.** Important parameters of UME.

Among other techniques, the UME can be characterized by recording cyclic voltamograms (CV), scanning confocal laser microscopy (SCLM) images and approach curves to an inert, insulating sample<sup>[106]</sup> (Fig. (2.2)):

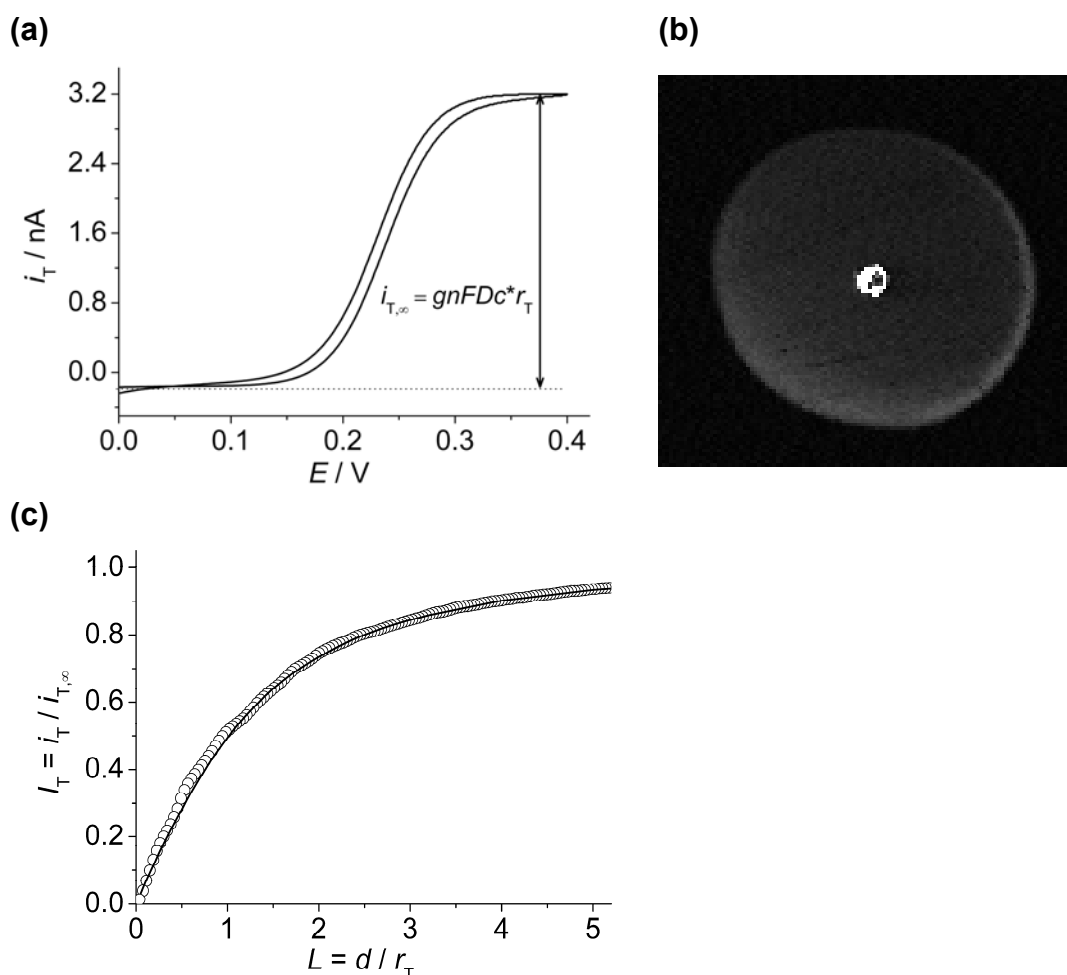


**Figure 2.2.** Techniques used for characterization of an UME: (a) CV of the UME resulted in a  $r_T \cong 12.96 \mu\text{m}$  according to Eq. (2.2) (redox mediator: 1 mM Ferrocenemethanol (Fc) in 0.1 M KCl), (b) SCLM image of the same UME gave  $r_T = 12.26 \mu\text{m}$  and  $RG = 9.96$  (reflection image showing the reflection intensity), (c) SECM approach curve to an inert insulating surface using the same UME. The curve fit to the theory<sup>[88]</sup> for an UME with  $RG = 10.2$  led to  $r_T = 13.23$ .

The use of UME enhances the mass transport and reduces the IR drop and double-layer charging effects.<sup>[A7]</sup> The enhanced mass transport causes a hemispherical diffusion layer, in contrast to macroelectrodes where planar diffusion occurs. The hemispherical diffusion assures large current densities in quiescent solution what makes convective effects like stirring in the solution negligible. This allows the treatment of UME currents recorded at the scanning probe ( $1 - 15 \mu\text{m s}^{-1}$ ) by theory derived for a resting electrode.<sup>[60]</sup> The UME current reaches steady state within short time ( $\sim r_T^2 / D$ ).

When the UME is poised at  $E_T$ , a potential sufficiently large to cause the diffusion-controlled oxidation of R, the conversion of the oxidizable compound occurs according to Eq. (2.1):<sup>1</sup>



The steady-state diffusion-controlled UME current can be obtained as the plateau current from a CV with small scan rates (Fig. (2.2a)) measured at a quasi-infinite distance  $d$  from the sample in the bulk solution ( $d > 20 r_T$ ). This current is named infinity current ( $i_{T,\infty}$ ) and is described by Eq. (2.2):

$$i_{T,\infty} = gnFDc^* r_T \quad (2.2)$$

in which  $n$  is the number of transferred electrons per molecule,  $F$  the Faraday constant,  $D$  the diffusion coefficient,  $c^*$  the bulk concentration of the mediator,  $r_T$  the radius of the disk-shaped active electrode area and  $g$  is the geometry-dependent factor that assumes different values according to  $RG$  value (Table (2.1)).<sup>[60, 107]</sup> The value  $g = 4$  is a good approximation if  $RG \geq 10$ :<sup>[A4]</sup>

**Table 2.1:** Geometry-dependent factor  $g$  values with respect to  $RG$  values.<sup>[60, 107]</sup>

	<b>RG</b>			
	$\infty^*$	<b>10</b>	<b>2</b>	<b>1.2</b>
<b>g</b>	4	4.07	4.44	4.95

\* infinitely large insulator.<sup>[108]</sup>

<sup>1</sup> Of course, analogous experiments may be carried out if the oxidized form O is provided. Reaction directions are reversed in this case.



## 2.2 Feedback mode

The working solution for SECM feedback<sup>1</sup> experiments contains one redox form of a (quasi-reversible) redox couple. For discussion of the working principle it is assumed that the reduced form R is added at a concentration  $c^*$ . This compound serves as electron mediator and is added typically in millimolar concentrations to an excess of an electrolyte that can be considered as inert at the given conditions. The mathematical models with empirical constants developed for SECM do not consider migration and convection, hence these types of mass transfer must be eliminated to decrease the solution resistance and to ensure that the transport of R to the UME occurs predominantly by diffusion.

The UME acts as working electrode (WE) in the electrochemical cell, and an auxiliary electrode (AE) completes the cell. As the AE is placed far from the UME, its reaction products do not reach the UME during the experiment, hence it does not disturb the measurement. The UME potential is monitored against a stable reference electrode (RE). The sample can be connected as a WE2, but in many cases in this work the samples were not connected.

Two basic experiments can be distinguished in the feedback mode: scanning the UME at a constant distance  $d$  provides an image that reflects the distribution of heterogeneous reaction rates of the sample (reaction rate imaging). Translating the UME vertically towards the sample allows a more detailed kinetic investigation of the reaction  $O + ne^- \rightarrow R$  at a specific location. The translation of the UME from the bulk solution towards sample is called approach curve.

The SECM approach curves record  $i_T$  as a function of the UME-sample separation  $d$ . For a unified description, the UME current is normalized to  $i_{T,\infty}$  ( $I_T = i_T/i_{T,\infty}$ ) and the UME-sample separation is normalized to  $r_T$  ( $L = d/r_T$ ). The normalized curves are independent of  $c^*$ ,  $D$  and  $r_T$ . There are two limiting cases for a quasi-infinitely large sample:

- when the UME approaches an inert and insulating surface (Fig. (2.3), (2)),
- when the UME approaches a conducting surface at which UME-generated species O are regenerated to R at a diffusion-controlled rate (Fig. (2.3), (3)).

---

<sup>1</sup> The feedback term is used to indicate that the measured UME current is influenced by the rate at which the mediator is regenerated at the sample and must not be confused with the current-independent feedback system used to control the motor position.

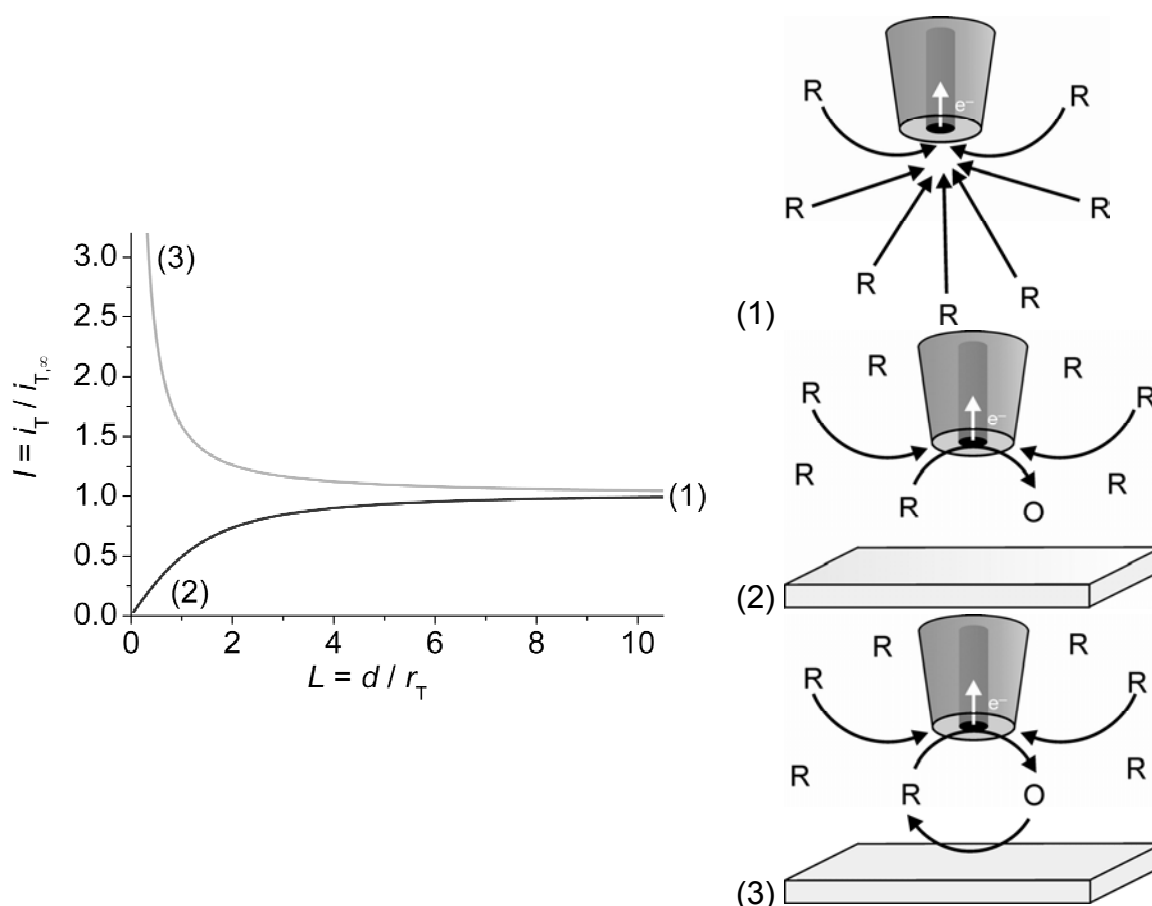


**Figure 2.3.** Principle of feedback mode. (1) Steady-state diffusion-limited current in the bulk solution, (2) normalized approach curve for hindered diffusion when the UME approaches an inert and insulating surface (negative feedback), (3) normalized approach curve for mediator regeneration by a heterogeneous reaction at the sample surface (positive feedback).

If the UME approaches an insulating, inert surface, e.g. glass, the diffusional flux of R toward the active area of the UME is hindered by the sample surface and the insulating sheath of the UME (curve 2, Fig. (2.3)). Thus, the resulting mass-transfer resistance will increase and the faradaic current  $i_T$  falls below  $i_{T,\infty}$  as the interelectrode space narrows (decreasing  $d$ ). The diffusional flux of R towards the UME is also hindered as the  $RG$  increases. This kind of UME response is called "negative feedback"<sup>[109]</sup> and represents the lower limit of an approach curve (curve 2, Fig. (2.3)). However, if the UME approaches a surface where the UME-generated species O are recycled to the mediator R by (electro)chemical conversion of O at the sample, the sample represents an additional source of R for the reaction at the UME. Hence as  $d$  decreases the mass transport between UME and sample become faster and  $i_T$  exceeds  $i_{T,\infty}$ . The term "positive feedback" was coined for the communication between UME and sample by a diffusing redox mediator.<sup>[76]</sup> The regeneration process of the mediator might be:

- an electrochemical reaction (if the sample is an electrode itself),<sup>[76]</sup>
- an oxidation of the sample surface (if the sample is an insulator or semiconductor),<sup>[110]</sup>
- the consumption of O as an electron acceptor in a reaction catalyzed by enzymes or other catalysts immobilized at the sample surface.<sup>[111]</sup>

If the rate of regeneration of R at the sample is diffusion-controlled, the UME current reaches a maximum value and gives the upper limit of the approach curve (curve 3, Fig. (2.3)).

Approach curves provide important information about the reaction kinetics at the sample and are dependent upon the nature of the sample, the UME-sample distance  $d$  and  $RG$  value of UME. A significant dependence on the  $RG$  value is observed in approaches to inert and insulating samples, since the insulating sheath of the UME blocks the diffusion of the mediator to the active area of the UME. The larger the  $RG$  value, the smaller  $I_T$  is at a given  $L$  (Fig. (2.4)). Approaches to samples answering with a positive feedback are less influenced by the  $RG$  value.

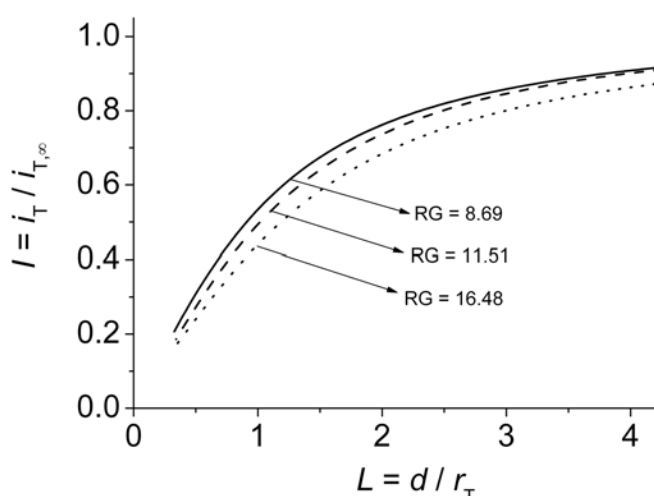


**Figure 2.4.** Approach curves to glass with Pt disk-shaped UMEs ( $r_T \cong 12.5 \mu\text{m}$ ) and  $RG = 8.69$  (solid line),  $RG = 11.51$  (dashed line), and  $RG = 16.48$  (dotted line). Solution: 1mM Fc in 0.1 M KCl.

Quantitative description of approach curves can be obtained by solving the diffusion equations for various heterogeneous and homogeneous processes and different tip and substrate geometries.<sup>[59, 62, 85, 88, 109, 112, 113]</sup> As disk-shaped UME are the most frequently used electrodes in SECM and were exclusively used in this work, discussions are limited to this shape. The simulation results for various values of  $d$  can be described by analytical approximations for both limiting cases.<sup>[79, 88]</sup> An analytical approximation for an inert, insulating sample is described by Eq. (2.3):

$$I_T^{\text{ins}}(L) = \frac{i_T}{i_{T,\infty}} = \frac{1}{k_1 + \frac{k_2}{L} + k_3 \exp\left(\frac{k_4}{L}\right)} \quad (2.3)$$

The contribution for the normalized current for an insulator  $I_T^{\text{ins}}$  may be taken from Ref. [88] for  $RG = 10.2$  and provides the analytical functions with  $k_1 = 0.40472$ ,  $k_2 = 1.60185$ ,  $k_3 = 0.58819$  and  $k_4 = -2.37294$ .

Often a slightly different normalization is used where  $I_T^{\text{insr}} = i_T / 4nFDc^*r_T$  is calculated (current at UME in infinitely large insulating sheath). The conversion between  $I_T^{\text{ins}}$  and  $I_T^{\text{insr}}$  is carried out by a factor  $i_{T,\infty} / 4nFDc^*r_T$  taken from Refs. [107] and [114] (Eq. (2.4)):

$$I_T^{\text{insr}}(L) = \frac{i_T}{i_{T,\infty}(RG) \cdot \frac{4nFDc^*r_T}{i_{T,\infty}(RG)}} = \frac{i_T}{4nFDc^*r_T} \cdot 1.019 = I_T^{\text{ins}}(L) \cdot 1.019 \quad (2.4)$$

The analytical approximations for hindered diffusion provide a way to determine  $r_T$  and  $d_{\text{offset}}$  from experimental approach curves. For this purpose one can use an irreversible reaction at the UME (often  $O_2$  reduction). The recorded approach curve is independent of the nature of the sample. By fitting an experimental approach curve value towards an inert, insulating substrate to Eq. (2.4),  $r_T$  and  $d_{\text{offset}}$  can be obtained as adjustable parameters. [A3, A4] The accurate knowledge of the distance between the UME and the sample is essential for any quantitative SECM measurement.

Equation (2.5) describes the upper limit of the UME current, when the UME approaches to a conducting surface and the reaction at the UME and sample are diffusion-controlled:

$$I_T^{\text{cond}}(L) = \frac{i_T}{i_{T,\infty}} = k_1 + \frac{k_2}{L} + k_3 \exp\left(\frac{k_4}{L}\right) \quad (2.5)$$

The contribution  $I_T^{\text{cond}}$  taken from Ref. [88] for  $RG = 10.2$  gives  $k_1 = 0.72627$ ,  $k_2 = 0.76651$ ,  $k_3 = 0.26015$ ,  $k_4 = -1.4132$  and the correction for normalizations to  $4nFDc^*r_T$  leads to Eq. (2.6):

$$I_T^{\text{condr}}(L) = \frac{i_T}{i_{T,\infty}(RG) \cdot \frac{4nFDc^*r_T}{i_{T,\infty}(RG)}} = \frac{i_T}{i_{T,\infty}} \cdot 1.019 = I_T^{\text{cond}}(L) \cdot 1.019 \quad (2.6)$$

The recycling of the mediator at the conducting sample can be caused by a connection to a potentiostat, however in some cases it is not possible or not necessary. If the sample is much larger than the UME or is connected to a larger conducting region in contact with the mediator solution, the thermodynamically defined open circuit potential (OCP) allows the

electrochemical conversion of the UME-generated O to R. The SECM setup for the feedback experiment resembles a concentration cell where the electrode potential is controlled by the mediator concentration in the solution (Fig. (2.5)):

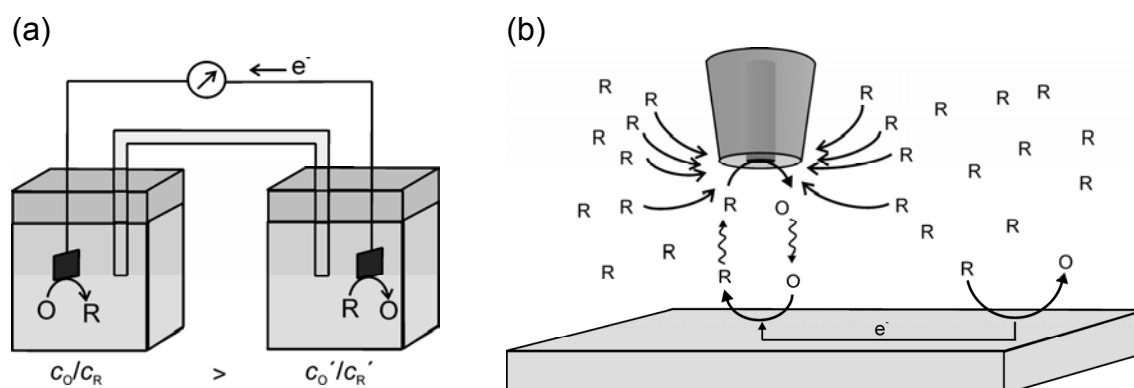


**Figure 2.5.** a) Conventional electrochemical concentration cell, b) SECM positive feedback at open circuit potential (formation of a concentration cell in FB experiments).

The electrode potential of the electronically conductive macroscopic sample immersed in the mediated solution is determined by the activity ratio of the oxidized and reduced mediator forms and can be calculated from the known formal potential  $E^{\circ'}$  of the mediator according to the Nernst equation (Eq. (2.7)):

$$E_s = E^{\circ'} + \frac{R \cdot T}{n \cdot F} \cdot \ln\left(\frac{c_O}{c_R}\right) \quad (2.7)$$

where  $R$  the gas constant,  $T$  the temperature,  $c_O$  and  $c_R$  are the concentrations of the oxidized and reduced form of the redox mediator respectively. If the bulk solution contains basically only R as illustrated in Fig. (2.5b) and the UME is located in the close proximity of the sample, the electrochemical conversion at the UME causes an enhanced concentration of O underneath the UME. This builds up a concentration cell leading to reduction of O to R underneath the UME (Fig. (2.5a)). An equal amount of R is oxidized to O at the sample far away from the UME (Fig. (2.5b)). The negative value of the OCP is responsible for the reduction of O underneath the UME under nearly diffusion-controlled conditions. Instead of diffusion of O into the bulk solution electrons are transported in the conducting sample.

The curves described above represent the limiting cases in which the sample is either an insulating, inert sample (no mediator regeneration) or the sample is a conductor (diffusion-controlled regeneration of the mediator at the sample). However, if the electrochemical mediator regeneration at the sample is not diffusion-controlled, but limited by the heterogeneous electron transfer rate at the sample, a unique approach curve can be found for each rate constant of the substrate that lies between these limiting cases.<sup>[90]</sup> Such curves

are described by analytical approximations for finite kinetics and diffusion-limited current at the UME. An analytical approximation often used for the UME current is given by Eq. (2.8) and is valid under three conditions: (i) the distance range is  $0.1 < L < 1.6$ , (ii)  $RG \approx 10$  and (iii) the reaction at the sample is of first order with respect to the mediator:<sup>[72]</sup>

$$I_T'(L) = \frac{i_T}{4nFDc * r_T} = I_T'^{\text{ins}}(L) + I_S^{\text{kin}}(L) \cdot \left( 1 - \frac{I_T'^{\text{ins}}(L)}{I_T^{\text{cond}}(L)} \right) \quad (2.8)$$

where  $I_T'(L)$  is the normalized UME current for finite substrate kinetics,  $I_T'^{\text{ins}}(L)$  is the normalized UME current for insulating sample,  $I_T^{\text{cond}}(L)$  is the normalized UME current for diffusion-controlled regeneration of a redox mediator, and  $I_S^{\text{kin}}(L)$  is the kinetically controlled normalized substrate current. The normalized substrate current  $I_S^{\text{kin}} = i_S / 4nFDc * r_T$  is the current equivalent at the sample  $i_S$ . It can be estimated for  $RG = 10$  and  $0.1 < L < 1.6$  by the analytical approximation (Eq. (2.9)):<sup>[72]</sup>

$$I_S^{\text{kin}}(L, k_{\text{eff}}) = \frac{0.78377}{L \cdot \left( 1 + \frac{1}{\kappa \cdot L} \right)} + \frac{0.68 + 0.3315 \exp\left(\frac{-1.0672}{L}\right)}{1 + \left( \frac{\frac{11}{\kappa \cdot L} + 7.3}{110 - 40 \cdot L} \right)} \quad (2.9)$$

where  $\kappa$  is the normalized first-order rate constant. The calculated current  $I_T'(L)$  (normalized to  $4nFDc * r_T$ ) can be compared to the normalized experimental current  $I_T(L)$  (normalized by the experimental  $i_{T,\infty}$ ):

$$I_T(L) = \frac{i_T(L)}{i_{T,\infty}(RG)} = I_T'(L) \cdot \frac{4nFDc * r_T}{i_{T,\infty}(RG)} = \left[ I_T'^{\text{ins}}(L) + I_S^{\text{kin}}(L) \cdot \left( 1 - \frac{I_T'^{\text{ins}}(L)}{I_T^{\text{cond}}(L)} \right) \right] \cdot 1.019 \quad (2.10)$$

This equation has been used for Section 4.1, 5, and 6. Recently, a new analytical approximation was developed for SECM feedback approach curves with a microdisk UME.<sup>[115]</sup> This new expression proposed by Cornut and Lefrou<sup>[115]</sup> is an analytical function with  $L$ ,  $\kappa$  and  $RG$  as variables, and therefore can be used for  $RG \leq 20$ ,  $L \geq 0.1$ , for any given  $\kappa$ . The approach curve fits done in Chapter 4 for  $\text{SiO}_x$  (Section 4.2) used this theory.

$$I_T(L, \kappa, RG) = I_T^{\text{cond}}\left(L + \frac{1}{\kappa}, RG\right) + \frac{I_T^{\text{ins}}(L, RG) - 1}{(1 + 2.47RG^{0.31}L\kappa)(1 + L'\kappa^{-\sigma})} \quad (2.11)$$

with

$$I_T^{\text{cond}}\left(L + \frac{1}{\kappa}, RG\right) = \alpha(RG) + \frac{1}{2\beta(RG)\xi\left(L + \frac{1}{\kappa}\right)} + \left(1 - \alpha(RG) - \frac{1}{2\beta(RG)}\right)\xi\left(L + \frac{1}{\kappa}\right) \quad (2.12)$$

$$I_T^{\text{ins}}(L, RG) = \frac{\frac{2.08}{RG^{0.358}}\left(L - \frac{0.145}{RG}\right) + 1.585}{\frac{2.08}{RG^{0.358}}(L + 0.0023RG) + 1.57 + \frac{\ln RG}{L} + \frac{2}{\pi RG} \ln\left(1 + \frac{\pi RG}{2L}\right)} \quad (2.13)$$

$$\alpha(RG) = \ln 2 + \ln 2 \left(1 - \frac{2}{\pi} \arccos\left(\frac{1}{RG}\right)\right) - \ln 2 \left(1 - \left(\frac{2}{\pi} \arccos\left(\frac{1}{RG}\right)\right)^2\right) \quad (2.14)$$

$$\beta(RG) = 1 + 0.639 \left(1 - \frac{2}{\pi} \arccos\left(\frac{1}{RG}\right)\right) - 0.186 \left(1 - \left(\frac{2}{\pi} \arccos\left(\frac{1}{RG}\right)\right)^2\right) \quad (2.15)$$

$$\xi\left(L + \frac{1}{\kappa}\right) = \frac{2}{\pi} \arctan\left(L + \frac{1}{\kappa}\right) \quad (2.16)$$

$$\gamma = 0.006RG + 0.113 \quad (2.17)$$

$$\sigma = 0.0236RG + 0.91 \quad (2.18)$$

The magnitude of the feedback is sensitive to the rate of mediator regeneration at the sample, hence the approach curve provides information about the kinetics at the sample. By variation of the value  $\kappa$  in Eq. (2.9) and  $i_{T,\infty}$  (in the normalized UME current  $I_T = i_T / i_{T,\infty}$ ), the calculated values for  $I_T(L)$  from Eq. (2.10) may be brought into agreement with the experimental curve. It is also valid for Eq. (2.11), where the  $\kappa$  value and  $i_{T,\infty}$  can be varied until it fits to the experimental curve. From  $\kappa$ , an effective heterogeneous first order rate constant  $k_{\text{eff}}$  can be derived from Eq. (2.19).<sup>[A7, A8]</sup>

$$k_{\text{eff}} = \kappa \cdot \frac{D}{r_T} \quad (2.19)$$

The rate of ET at the sample can be controlled by applying different external potentials. When R is oxidized at the UME and O reduced at the sample, the more negative the overpotential ( $E_S - E^\circ$ ) the faster is the regeneration of O to R at the sample. Each overpotential leads to a different approach curve and hence different  $k_{\text{eff}}$ . When  $k_{\text{eff}}$  is known for every substrate potential, a first order heterogeneous standard rate constant  $k^\circ$  at the sample may be calculated from the Butler-Volmer equation (Eq. (2.20)) for sufficiently high overvoltages,<sup>[116]</sup> where  $\alpha$  is the transfer coefficient:

$$\ln k_{\text{eff}} = \ln k^{\circ} - \alpha \cdot \frac{n \cdot F}{R \cdot T} (E_s - E^{\circ'}) \quad (2.20)$$

Fig. (2.6) shows two examples of FB imaging:

- (a) reaction rate imaging: a gold sample was stamped with hexadecanethiol, which "blocks" the recycling of the mediator. The carbon chains do not allow the ET between the solution and sample, and therefore the current is decreased when the UME passes over the functionalized area. One can distinguish from this image the sites covered by the hexadecanethiol (lower current values) and bare gold (higher current values).
- (b) topography imaging: a plastic sample patterned with a grid was imaged in FB mode, but as the mediator is not recycled at the sample, one can only see the sites where the mediator could reach the UME more easily and the sites where the diffusion of the mediator towards the UME was blocked by the sample topography.

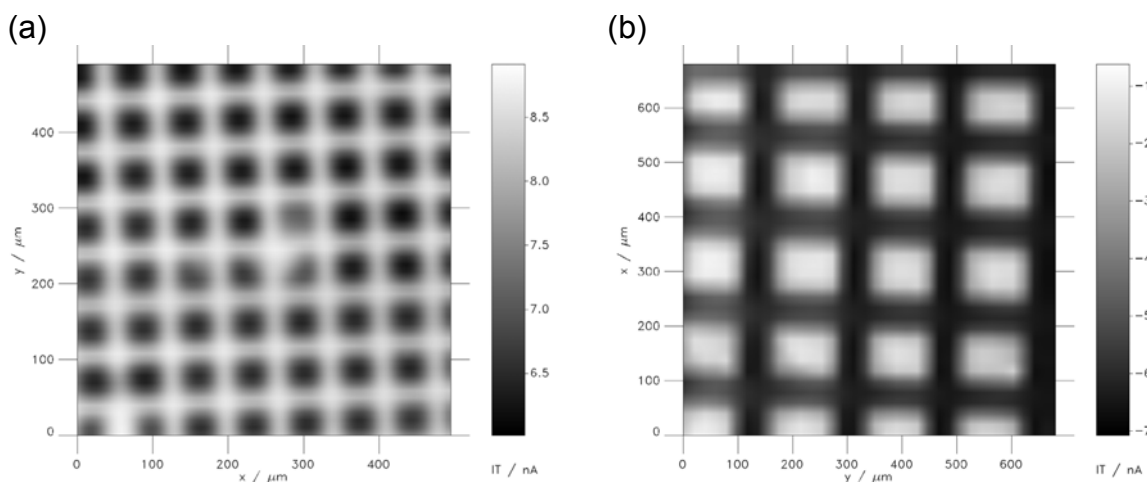


**Figure 2.6.** FB images of reactivity and topography. (a) SECM image of stamped hexadecanethiol (micro-contact printing) on a gold sample. The mediator solution was 2 mM Fc in 0.1 M  $\text{Na}_2\text{SO}_4$ ,  $r_T = 12.5 \mu\text{m}$  and  $d = 5 \mu\text{m}$ . An oxidation current is measured for Fc, leading to positive currents. (b) SECM image of a grid patterned on plastic. The mediator solution was 2 mM  $\text{Ru}(\text{NH}_3)_6\text{Cl}_3$  in 0.1 M KCl,  $r_T = 12.5 \mu\text{m}$  and  $d = 10 \mu\text{m}$ . A reduction current is measured for  $\text{Ru}(\text{NH}_3)_6\text{Cl}_3$ , and therefore the current is negative.

In this thesis (Chapter 4) the FB mode was used to extract kinetic information from the sample by translating the UME towards the sample (approach curves). In all experimental chapters the negative feedback curve (either approach to glass or approach using the oxygen reduction current) was done in order to position the UME at a certain  $d$ .



## 2.3 Generation/Collection mode

In contrast to feedback mode the generation-collection mode (GC) works in a solution that initially does not contain a substance that can be electrochemically oxidized or reduced at the UME at  $E_T$ . The GC mode can be used to monitor heterogeneous processes such as corrosion<sup>[65, 117, 118]</sup> and enzymatic reactions,<sup>[19, 119-123]</sup> investigate mass transport across skin samples<sup>[124-130]</sup> and dentine.<sup>[131-134]</sup> There are two types of GC mode: tip-generation/sample-collection (TG/SC) and sample-generation/tip-collection (SG/TC). In TG/SC the UME is held at a potential  $E_T$  where an electrochemical reaction occurs and the sample is at a certain potential capable to "collect" the UME reaction product (Fig. (2.7a)).<sup>[135-138]</sup> A constant current is passed through the UME (galvanostatic operation). An image is constructed by plotting the sample current versus the UME position. Generally, in TG/SC the sample is much larger than the UME and the collection efficiency can be estimated by  $i_s/i_T$  and is close to 100%. This mode has been used to image oxygen-reducing enzymes (laccase and bilirubin oxidase).<sup>[139]</sup> The other type of GC mode, SG/TC, can be performed with either amperometric<sup>[15, 65, 120, 140-142]</sup> (Fig. (2.7b)) or potentiometric<sup>[96, 143-146]</sup> microelectrodes (Fig. (2.7c)).

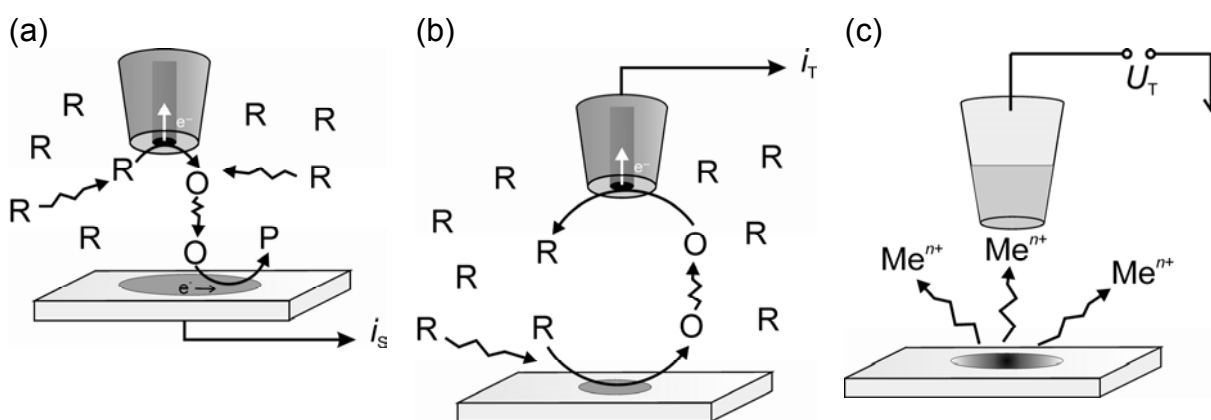


**Figure 2.7.** Principle of generation-collection mode. (a) TG/SC mode, (b) SG/TC mode with an amperometric UME, and (c) SG/TC mode with a potentiometric microelectrode (e. g. ion-selective electrodes).

In SG/TC operation, the sample surface generates a redox-active species that is probed by the UME when this is placed close to the active sample region. When the UME translates above the region where the redox-active species are generated, it measures a faradaic current that is related to the concentration profile formed around the sample surface. Thus, the UME maps the local concentration of redox-active species generated at the sample. As initially no redox active substances are added to the system, background currents approximate to zero.

The SG/TC mode was used in this thesis (Chapter 5 and 6) to probe the diffusion layer of immobilized enzymes and used the UME as an amperometric sensor, hence further discussion are limited to this.

At first the SG/TC mode with an amperometric UME seems to be a straight-forward experiment. However, this kind of experiments has some drawbacks:

- only if the active regions are well separated microstructures, there will be a steady-state concentration profile. Above macroscopic active regions of samples, the local concentrations depend on the time that has passed after the onset of the reaction at the sample,
- the diffusion layer of the specimen is disturbed by the presence of the UME (stirring, blocking of reactant diffusion to the sample, overlap of the diffusion layers of the UME and the sample in case of amperometric UME),
- in the GC mode there might be a current enhancement due to recycling if the reaction at the microelectrode is a reversible reaction and  $d \leq 3 r_T$ .<sup>[A6]</sup>

The lateral resolution of GC mode is inferior compared to FB mode, but it offers much higher sensitivity than FB mode (no background current).<sup>[147]</sup> In order to minimize the disturbance of the diffusion layer by the UME and feedback effects, one can use UME with smaller  $r_T$  and  $RG$ . Finding an optimal working distance to record SG/TC images when the enzyme is immobilized on a conducting support is also important for quantitative treatments and is shown in Chapter 6.<sup>[A6]</sup> The GC mode is used when FB experiments are either not possible or not sensitive enough.

Quantification of GC mode is only possible if the active sample regions are well separated microscopic regions that form steady-state concentration profiles. The signal over the active sample region can be described by a model developed for diffusion to an isolated disk-shaped pore.<sup>[93, 124, 148]</sup> This model is based on Fick's laws of diffusion and relates the UME current to the local flux of molecules generated by the active region of the sample. It assumes that the UME does not interact with the system being measured and acts as a passive probe. The current  $i_T$  depends on the radius of the active region of the sample  $r_S$ ,  $r_T$ , the concentration of the detected species  $[P]_S$  at the surface of the sample, and the dilution factor  $\theta$  describing the diffusion from the active sample region source into solution (Eq. (2.21)):

$$i_T = gnFD r_T [P]_S \theta \quad (2.21)$$

The dimensionless  $\theta$  factor describes the concentration decrease of the released redox-active species as a function of the lateral distance  $\Delta x$  from the center of the active

sample region ( $\Delta x = x - x_0$ , where  $x_0$  is the  $x$ -coordinate of the spot center), and the vertical distance  $d$  from the active center region of the sample and  $r_s$  (Eq. (2.22)):

$$\theta = \frac{2}{\pi} \arctan \frac{\sqrt{2}r_s}{\left( \sqrt{(\Delta x^2 + d^2 - r_s^2)} + \sqrt{(\Delta x^2 + d^2 - r_s^2)^2 + 4d^2r_s^2} \right)} \quad (2.22)$$

A detection limit described by Horrocks and Wittstock<sup>[147]</sup> is shown in Eq. (2.23) and represents an estimation of the minimum catalytic rate  $k_{cat}$  of the immobilized enzyme that still can be detected and quantified by the UME. The high sensitivity of GC experiments to kinetics (due to neglected background contribution) is directly proportional to the detection limit for the species observed at the UME:

$$k_{cat}\Gamma_{enz} \geq D[P]'/r_s \quad (2.23)$$

where  $\Gamma_{enz}$  is the surface concentration and  $[P]'$  is the detection limit for the species observed at the UME. A low turnover rate limits the detection even if  $\Gamma_{enz}$  is high. An example of detection limit is the immobilized  $\beta$ -glucosidase. This enzyme was immobilized according to a known procedure<sup>[A2]</sup> onto magnetic microbeads. Although all the binding sites of the streptavidin-coated magnetic microbeads were saturated with biotin-labeled  $\beta$ -glucosidase and an excess of an artificial substrate ( $p$ -aminophenyl  $\beta$ - $D$ -glucopyranoside) was given to the immobilized enzyme, low  $i_T$  were recorded in the SECM activity image reflecting low catalytic rates of glucosidase. Moreover an attempt to image  $\beta$ -glucosidase activity present in sediments of the north sea, showed that the low turnover number limited the reaction rate and thus could not be imaged by the SECM.

A fit of the experimental horizontal line scan  $i_T = f(x, d = \text{const})$  to Eqs. (2.21) and (2.22) provides the unknown parameters  $r_s$  and  $[P]_s$ . Thus the total flux  $\Omega$  from the active region can be calculated by Eq. (2.24)<sup>[108]</sup> denoting the rate of mass transport:

$$\Omega = 4 \cdot D \cdot r_s \cdot [P]_s \quad (2.24)$$

By assuming a uniform flux over the whole active sample region and a circular area  $A = \pi r_s^2$ , a generation rate  $J$  can be determined according to Eq. (2.25):<sup>[120]</sup>

$$J = \frac{\Omega}{\pi \cdot r_s^2} \quad (2.25)$$

This treatment will be used in Chapters 5 and 6 in order to detect the flux of the product of the enzymatic reaction coming from the immobilized enzyme.

## 2.4 Direct mode

The direct mode has mainly been used for surface modification, e.g. deposition or etching of metals and semiconductors.<sup>[26, 36-38, 149, 150][A6]</sup> In direct mode, the sample acts as working electrode (WE) and the UME as auxiliary electrode (AE). They are connected by an ionic conductor, e. g. an ion-conducting polymer. The UME is held close to the sample surface forming a thin layer cell and a voltage is applied between them to cause faradaic reactions at the sample surface and at the UME, hence current lines are formed between them. The experiment is different from feedback experiments because different electrode reactions take place in the UME and the sample, and the reactants are not diffusing between them.

The potentiostatic pulse method has been widely used for the deposition of conducting polymers onto electrodes because it can prevent the problems encountered in the constant-potential deposition.<sup>[38]</sup> The application of a constant potential leads to formation of a diffusion-controlled and thus steady-state concentration profile. The monomer concentration is then effectively zero at the electrode surface. Consequently, the diffusion-controlled current will determine the amount of monomeric radical cations formed. As the diffusion coefficient of the monomer and its radical cation are assumed to be equal, the radical cations formed will partially diffuse toward the solution bulk, not being available for further reactions. The pulse technique allows formation of high concentrations of radical cations, and consequently increases the radical-radical coupling and subsequent chain propagation up to the solubility limit leading to polymer formation.

Fig. (2.8) shows a sketch of a typical polymer deposition by direct mode. A potential pulse is applied to the electrode from a value at which no monomer oxidation occurs to a value above the oxidation potential of the monomer. The current response is the superimposed double layer charging current and the faradaic current due to oxidation of the monomer and the formed oligomer. Radical cations are formed from the oxidation of the monomers, that will couple with other radical cations forming oligomers, which in turn are also oxidized due to their decreased oxidation potential. Further coupling reactions cause a chain propagation until the polycationic polymer reaches its solubility limit, and is deposited onto the electrode surface. The UME acts as AE and the reaction taking place is neglected, however it is supposed that water electrolysis occurs.

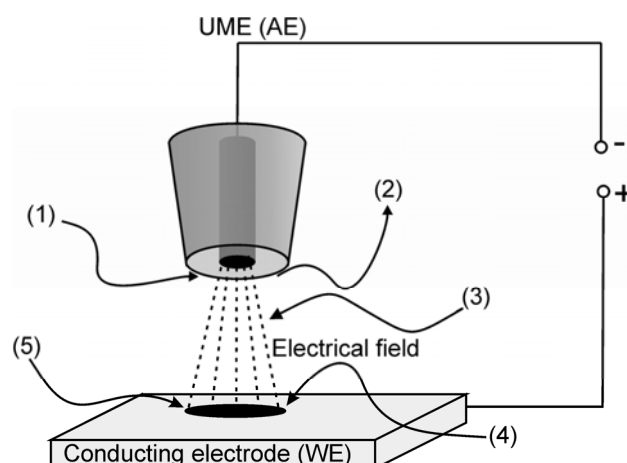


**Figure 2.8.** Sketch of the localized polymer deposition on an electrode surface. (1) Monomer diffusion into the electrical field. (2) Monomeric radical cations and soluble oligomers diffusion to the bulk of the solution. (3) Homogeneous oligomers growth. (4) Oxidation of monomers and oligomers. (5) Deposition of insoluble oligomers.

The resolution in the direct mode for deposition and etching depends on the UME size, UME current, scan rate, time that the voltage is applied, and penetration depth (in case of tip penetration into an ion-conducting polymer). As the current flow is limited to the gap between UME and sample, the modification or deposition is restricted to the sample region underneath the UME. This mode was used in Chapter 6 in order to deposit pyrrole on a gold sample.<sup>[A6]</sup>



### 3 Scanning Electrochemical Microscopy Instrumentation

SECM experiments involve the measurement of a current that passes through an UME when it is held or moved in a solution in the vicinity of a sample. For an accurate and well-resolved experiment the use of a good positioning system as well as sensitive potentiostat and fast analog-to-digital/digital-to-analog (AD/DA) board are crucial. However, the SECM involves many more parameters that are also important for a good experiment such as a suitable UME, the choice of a suitable mediator, enzyme and substrate concentration as well as a suitable supporting electrolyte, the working atmosphere (e.g.: O<sub>2</sub>, N<sub>2</sub>, air, etc.), isolation from vibration, reference electrode (RE) (according to the used medium), connection of the second working electrode, etc. All these parameters must be carefully chosen before the SECM measurement. Only if conditions are precisely controlled, one may expect a quantitative agreement with SECM theory, which was aimed for this work.

In the early stage of SECM, the microscope setup was normally home-built, which required a profound knowledge of the apparatus and programming in order to run the SECM experiments. After the SECM became commercially available the number of publications using this technique increased exponentially (Fig. (3.1)).<sup>[59]</sup> Despite this fact, home-built instruments still dominate in the leading SECM laboratories in the world because the measurement modes can be adapted to new experiments and hardware. This chapter introduces the components of the SECM apparatus, compares the features that are crucial for particular experiments and shows the variable setup developed in Wittstock's group which was used for the research presented in this thesis. This development was a group effort. My contribution consisted in conceptual work, the selection of hardware, the integration of different hardware including design of interfaces between components and testing of hardware and software interaction. While the work of this thesis contribute to the overall software concept, most of the coding work was performed by Prof. Dr. Gunther Wittstock and Dr. Oleg Sklyar.

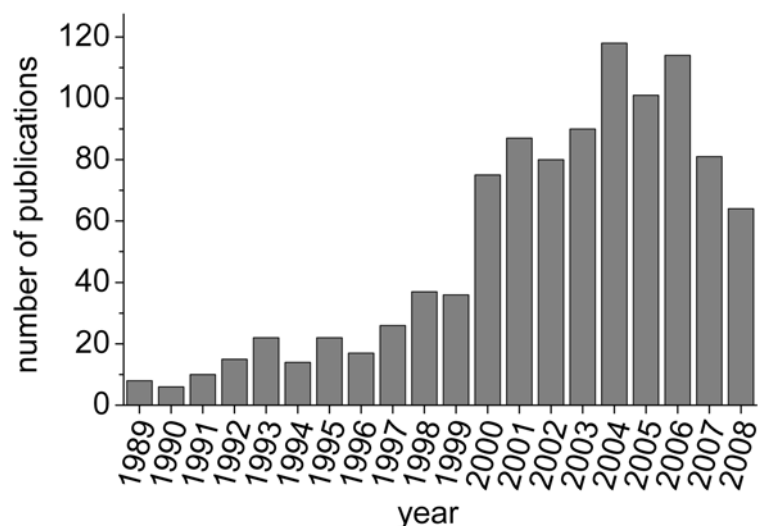


**Figure 3.1.** Number of SECM publications containing "scanning electrochemical microscopy" as entered until July 2008. Source: Sci Finder®.

### 3.1 Overview

The basic components of a SECM are shown in Fig. (3.2). The UME is moved by a positioning system normal to the sample surface ( $z$  coordinate) or horizontally above the sample ( $x$  and  $y$  coordinates). A constant potential is applied to the UME and the resulting current is measured by a (bi)potentiostat.

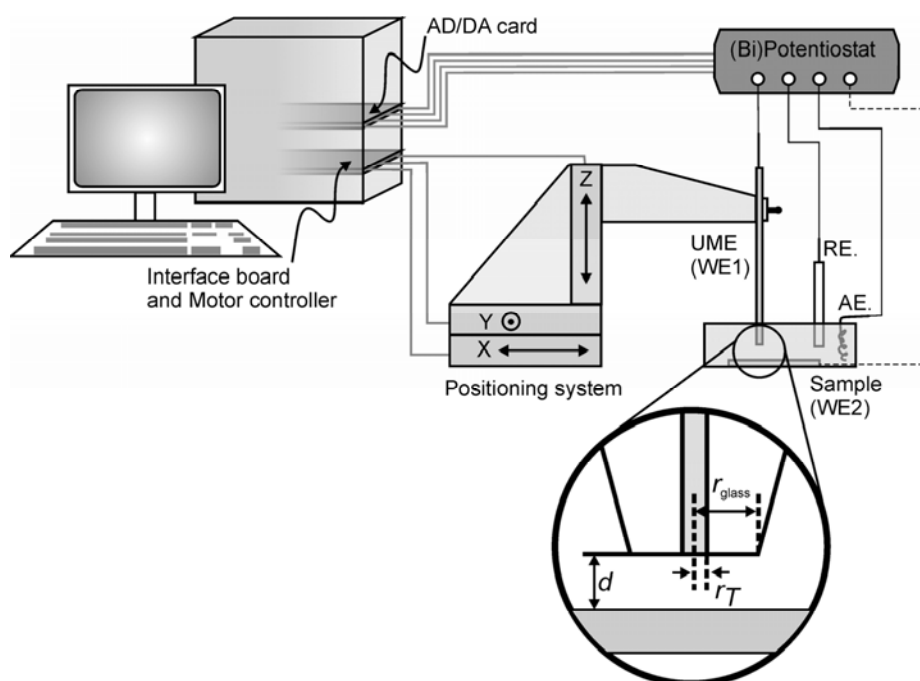


**Figure 3.2.** Basic setup of an SECM. Important components: disk shaped UME, sample, mono- or bipotentiostat, reference and auxiliary electrodes, positioning system, control computer.



In the sketch one can see that the UME is held by a probe holder connected to a high-resolution positioning system that consists of positioning elements, motor controllers and translation stages. The positioning system allows an accurate and reproducible movement in three directions,  $x$ ,  $y$ , and  $z$  with a certain translation rate (Section 3.3). Depending on the size of the UME, resolution required for the experiment and required travel range, the UME can be moved by stepper motors, piezoelectric elements, or piezoelectric motors.

The positioning is controlled by a motor controller that can provide "closed loop" and "open loop" positioning. In conventional set-ups, the UME is held by a probe mounting that is coupled with the positioning stage. However some positioners can move independently and therefore can be mounted in different arrangements. Generally the positioning elements are coupled with a translation stage in order to constrain motion into one direction. The most used positioning systems in SECM setups are stepper motors and piezoelectric actuators. Micrometers screws can also be used as positioners to record approach curves and perform substrate modifications, although the precision is much lower than in motorized systems.

Generally, the sample is fixed horizontally in an electrochemical cell that is mounted on a stable sample support. A tilt adjustment of the sample is important when the offset must be minimized. Tilt also disturbs imaging being sometimes the reason for artifacts in images and limited scan range. However it is not always possible to have a tilt adjustment table as in the case of placing the electrochemical cell on a microscope table.

A digital-to-analog converter (DAC) is frequently used to convert the digital signal coming from a computer in order to feed the motor controller or potentiostat with an analog signal (Section 3.4). A microscope can be used as a "help" for positioning the UME close to the area to be analyzed.

Conventionally, the UME is connected to a potentiostat as an amperometric microelectrode. The electrochemical cell is completed by a RE and an AE. A bipotentiostat can be used if the sample (or UME) is biased as second working electrode (WE2) with respect to the RE. The data acquisition is performed firstly by the potentiostat to amplify the UME signal. The analog output of the potentiostat is connected to an analog-to-digital converter (ADC), where the analog signal is converted to a digital signal. Some potentiostats do not require to be connected to an ADC and convert the analog signal internally by their own ADC. Finally the digital signal can be stored on a computer where data processing and plotting can be performed. A computer software is required in order to control the positioning system and potentiostat, and acquire, visualize, and analyze the data (Section 3.5).

Vibration isolation is not always necessary for SECM experiments using  $\mu\text{m}$ -sized UME. However vibration increases noise and decreases lateral and vertical resolution and can be minimized by placing the SECM away from vibration sources (pumps, air vents, big devices), minimizing the setup size and maximizing the rigidity, and placing the SECM on a vibration-isolation table. Thick granite plates can be used as SECM table isolated from the table structures by rubber pads (assembly used for all SECM setups). Further vibration isolation may be required depending on working mode or resolution to be achieved. A Faraday cage shields the SECM from external static electrical fields and electromagnetic radiations. For best performance, the cage should be directly connected to an earth ground. A Faraday cage is used in all SECM system, except when working on the SCLM.

The SECM concept realized in this group is that all users can control the different SECM systems although the setups are different. Each SECM setup was designed for different purposes and is introduced in the next Section.

## **3.2 Realized SECM setups**

Four different SECM systems were built up in our group under my assistance. They have different features and were built for different purposes. The main difference between the SECM systems are the positioning systems that have different working principles and therefore different performances. The potentiostats can be used in all SECM systems, being transferred from one system to another according to the needs of the experiment. The AD/DA cards were the same for all systems. All systems were controlled by the same SECM program, and were mounted on a table placed in a Faraday cage. Table (3.1) contains a comparison between the positioning systems of the SECM.

**Table 3.1:** Comparison between the SECM positioning systems.

	<b>System 1 (PI)</b>	<b>System 2 (Märzhäuser)</b>	<b>System 3 (Mechonics)</b>	<b>System 4 (OWIS)</b>
<b>motor type</b>	piezo actuator	2-phases hybrid stepper motor	piezo motor	2-phases permanent magnet stepper motor
<b>travel range</b>	500 $\mu\text{m}$	10cm in x, y; 5 cm in z	18 mm	25 mm
<b>closed loop</b>	yes, in x, y, z	yes, in x, y; no in z	yes, in x, y, z	no
<b>resolution</b>	<1 nm	15 nm	50 nm	0.274 $\mu\text{m}$
<b>repeatability</b>	open loop: 0.5 nm closed loop: 1.4 nm	<1 $\mu\text{m}$		$\pm 3 \mu\text{m}$
<b>accuracy</b>	0.01 %	open loop: $\pm 3 \mu\text{m}$ closed loop: $\pm 1.5 \mu\text{m}$		

A high-resolution SECM system for biological samples (System 1) was designed to be assembled either over an inverted microscope or SCLM for positioning of the UME relative to the sample. The "biological" SECM uses a piezoelectric PI HERA nanopositioning system P-625.2CD for  $x$ , and  $y$  axis and P-625.1CD for  $z$  axis with 500  $\mu\text{m}$  travel range, each axis implemented with a closed-loop capacitiv position sensor. The respective displacement sensor module with an integrated position servo-controller for closed-loop and a low voltage amplifier are used to move the piezo positioning system. Fig. (3.3) shows the positioning assembly over the inverted microscope and fixed over the SCLM column, over an adapter built by the mechanical workshop of the university. In both cases the sample is mounted separately from the positioning system, the inverted microscope assembly has a manual sample positioning that moves the sample in  $x$  and  $y$  axis with a micrometer screw and has a travel range of 25 mm, the SCLM has a motorized table that permits  $x$ ,  $y$  and  $z$  motion with  $\mu\text{m}$  resolution. The  $z$  axis is mounted on a micrometer translation stage which makes a fast but rough approach possible.

Although this system has a very high resolution, it has the disadvantage that the travel range is only 500  $\mu\text{m}$ . This plays a decisive role when the user has to define which system will be used to scan larger areas or analyze different sites of the sample.

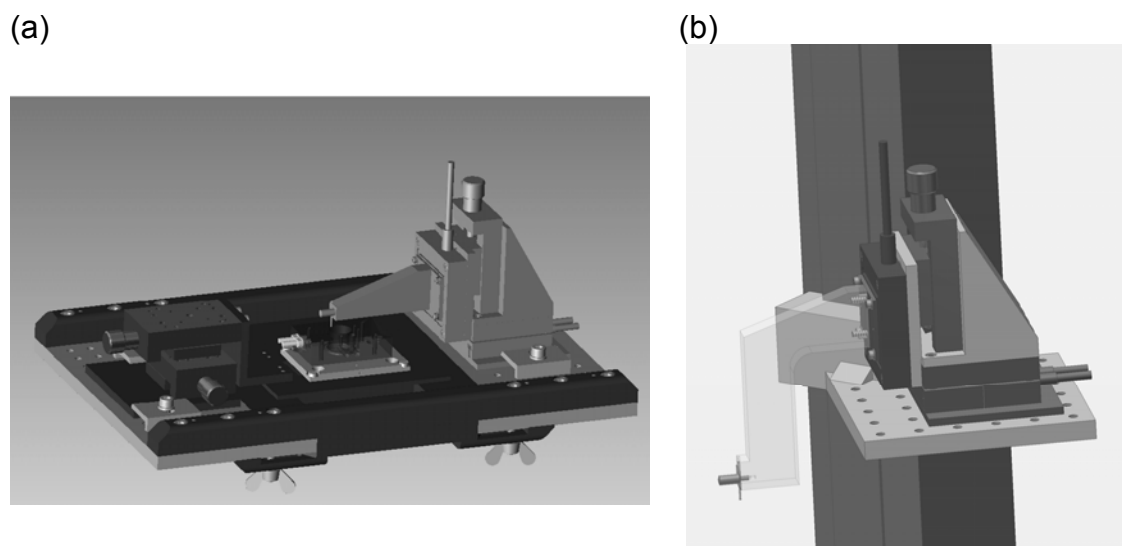


**Figure 3.3.** Assembly of biological SECM. The piezo positioning system can be assembled (a) over an inverted microscope or (b) over a SCLM.

A SECM with long travel ranges and high resolution was built for measurements of large samples (System 2) using a 2-phases hybrid stepper motor Märzhäuser positioning system. The  $x$  and  $y$  axis operate in closed-loop and the  $z$  axis in open-loop. An extra piezoelectric actuator (PI P-622.1CD) can be attached between the  $z$  axis of the Märzhäuser positioning system and the UME holder, providing a  $z$  approach with higher resolution. During the SECM experiment one can define which motor should move. Moreover, the  $z$  axis can be manually moved through a manual translation stage, facilitating the positioning of the UME close to the sample. A heavy movable table with tilt adjustment is used to place the sample under the UME holder. This system is preferred in our laboratory due to its long travel range and large assembly which allows easy access with further instrumental equipment.

System 3 was designed for experiments that need to be done under controlled atmosphere. The piezo motor positioning system (Mechonics) with 18 mm travel range was built in a chamber where  $O_2$  can be purged out and  $N_2$  can be inserted (or vice versa) (Fig. (3.4)). The  $x$ ,  $y$ , and  $z$  axis operate in closed loop, have a resolution of 50 nm and a large translation range. As in System 1 and 2, the sample is mounted separately from the positioning system. The potentiostat cables are connected to the chamber by BNC connectors, assuring that the atmosphere inside the chamber is controlled even if the cables must be exchanged. The small assembly of this positioning system makes it flexible and easy to move to other setups, thus one can also mount this positioning system on the SCLM (as in System 1), changing only the UME holder.

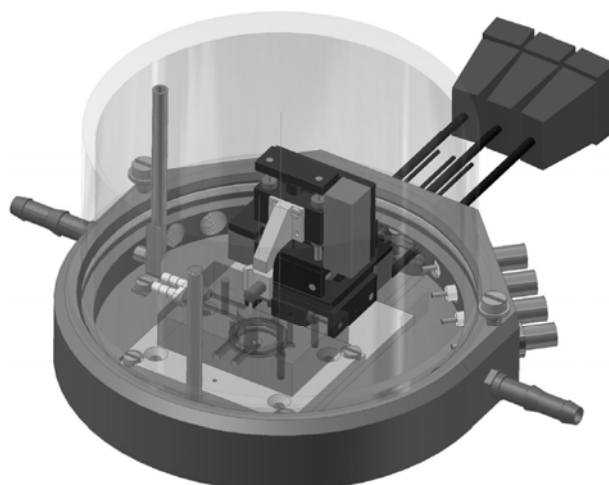


**Figure 3.4.** Assembly of controlled atmosphere SECM.

A simple 2-phases permanent magnet stepper motor OWIS positioning system with long travel range (25 mm) was designed for instruction propose (System 4). The stepper motor was mounted with a translation stage with crossed roller bearing guides. The UME holder is mounted with the  $x$  and  $y$  axis and moves separately from the  $z$  axis where a tilt table is assembled and the sample is placed. A piezo actuator (PI P-625.1CD) was coupled with the  $x$  and  $y$  stages and the UME holder was then mounted on it. This assembly makes accurate and reproducible  $z$  positioning (approach curves) possible.

The motors are properly controlled by the company-specified controller to assure the optimum motor function. The SECM program sends the commands to the motor controller through a common DLL and the interface between computer and motor can be through DAC converter (System 1), RS-232 host serial port (System 2), USB cable (System 3), and PCI-PC control card (System 4). All systems, except System 3, are equipped with an ADC board containing 16 single-ended or 8 differential analog inputs, 16 bit A/D resolution analog input, 200 kHz throughput, 2 D/A channels with 16 bit resolution. DAC boards containing 8 and 4 channels of 16 bit resolution were added to System 1 and 2 respectively.

As the SECM program allows the easy compilation of external hardware, the system worked with different potentiostats. Our laboratory has several potentiostats and bipotentiostats specified for different experiments. There are analog and digital (bi)potentiostats. The potentiostats are: CHI 7001B bipotentiostat (digital), Schramm potentiostat and bipotentiostat (analog), Ivium bipotentiostat (digital), npi potentiostat

(analog) and PalmSens bipotentiostat (digital). Like SECM positioning system, the potentiostats have different features.

CHI 7001B is computerized digital bipotentiostat that has a potential control range of  $\pm 10$  V and current range of  $\pm 250$  mA being able to measure current down to picoamperes (low end current gain of  $1 \text{ pA V}^{-1}$ ). The potential of this bipotentiostat cannot be controlled by the SECM program, but signal response can be read through an analog monitor signal connected to an AD channel. This instrument provides several electrochemical techniques that can be done using the instrument software. The monopotentiostat  $\mu$ -P3 (M. Schramm) is a very stable analog potentiostat with low end current gain of  $1 \text{ pA V}^{-1}$  being used for several years in our group. The bipotentiostat Schramm has similar features to the Schramm monopotentiostat. Ivium bipotentiostat is a digital device that can be operated through SECM program over an USB connection. It has automatic current range selection and automatic variable noise filter and measures currents in pA range. npi VA-10X potentiostat is a sensitive analog current amplifier that is intended for voltammetric measurements with carbon fiber microelectrodes in biological systems, where the total current does not exceed 100 nA, hence can only be used in SECM low current measurements. It can be controlled by the SECM program through DA channel and the response signal is read through an AD channel. PalmSens is a portable bipotentiostat controlled by SECM through serial port. It has a current range of  $\pm 10$  mA and current resolution of 1 pA on the lowest current range. The most frequent used potentiostat in my research were CHI 7001B and  $\mu$ -P3 Schramm potentiostat due to their high stability.

The theoretical limit of sensitivity in any measurement is determined by the noise generated by the resistances present in the circuit of the potentiostat.<sup>[151]</sup> Low currents are highly disturbed by noise, that must be minimized. The use of a Faraday cage is efficient against stray electromagnetic fields when properly closed and grounded, increasing the signal-to-noise ratio (SNR), however it does not exclude totally the noise interference. Hence other concern must be considered such as keeping all charged objects (including people) and conductors away from the potentiostat area, avoid movement and vibration near, when measuring currents  $< 1$  nA, shield the device under test by a Faraday cage and connect the enclosure electrically to the ground.<sup>[151]</sup>

The reproducibility of SECM systems can be tested by recording an image ( $i_T$  versus  $x$  and  $y$ ) of a sample and repeating the same image right after completion of the first image. The dimensions of both images can be compared and thus the reproducibility can be verified. Feedback images of hexadecanethiol stamped on gold were performed using System 1 to test

its reproducibility (Fig. (3.5)). One can observe that the images start and finish exactly at the same position, however, the second image (upper one) showed a slightly smaller  $i_T$ , probably due to adsorption or inhibition processes at the UME, or decomposition of the mediator in the solution caused by the long imaging time.

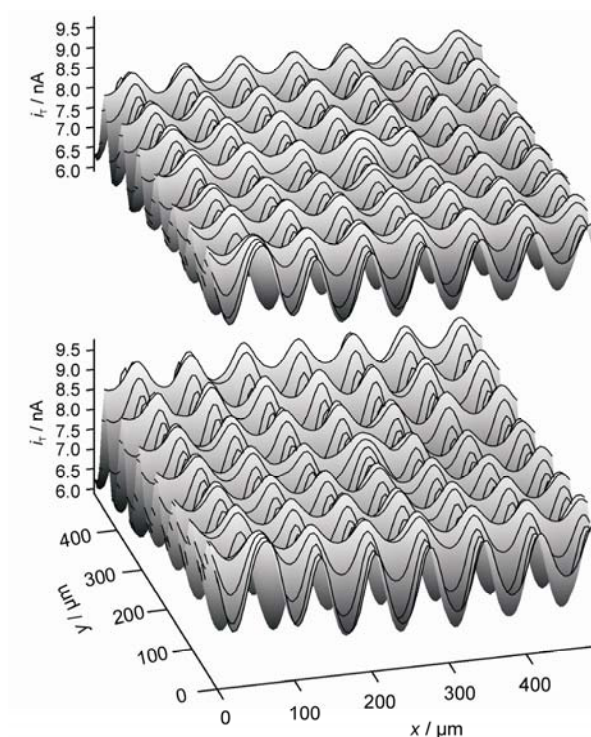


**Figure 3.5.** SECM feedback image of hexadecanethiol stamped on gold. The upper image was recorded after the lower image was completed, at the same place at the sample. Mediator: 2 mM Fc in 0.1 M Na<sub>2</sub>SO<sub>4</sub>.  $E_T = 0.4$  V,  $r_T = 12.5$   $\mu\text{m}$ ,  $v = 10$   $\mu\text{m s}^{-1}$ ,  $d = 10$   $\mu\text{m}$ .

Some features and working principles of the SECM components are introduced in the next Sections, giving an overview of some important parameters that must be considered when assembling a SECM. Some concepts described above are going to be discussed and thus clarified.

### 3.3 Positioning System

#### 3.3.1 Stepper Motor

A typical stepper motor system is composed of a pulse generator, also known as a controller or indexer, a motor driver and the stepper motor itself. A stepper motor<sup>[152-157]</sup> is a

synchronous electric motor which converts electrical pulses into mechanical movements moving a rotor in small angular steps or fractions of steps. It is basically composed of two parts: the stator and the rotor. The number of steps executed controls the degree of the motor shaft rotation. The motor shaft rotation, rate and length are proportional to the sequence, frequency and number of applied pulses, respectively. Stepper motors provide accurate positioning and repeatability, especially in low acceleration or static load applications. It has non-accumulative errors from step to step, is very reliable since there are no contact brushes in the motor, no feedback components are needed (motor response to digital input pulses provides open-loop control) making the motor simpler and less expensive. Although these advantages make the stepper motors very attractive for SECM positioning, it has some disadvantages that are disturbing for accurate SECM experiments such as resonance effect, relatively long settling times, current consumption regardless of load condition (motor heating and electromagnetic interference with UME current), and susceptibility to undetected position loss (open loop control). The performance of a stepper motor is strongly dependent upon the driver. The controller provides step and direction outputs to the driver. Other functions as acceleration, deceleration, steps per second and distance are also controlled by the controller.

Its basic operation consists of energizing<sup>1</sup> the stator winding in a certain sequence that a rotating magnetic field is created, thus the shaft will rotate following the rotating magnetic field. If the stator winding is energized, the shaft is magnetically attracted to the winding, when the next winding is energized and the first is turned off, the shaft rotates slightly to align with the next one, this process is called a "step". There are three main types of stepper motors: variable reluctance (VR), permanent magnet (PM) and hybrid. Their basic working principles are illustrated in Fig. (3.6).

The SECM System 2 uses a 2-phases, hybrid stepper motor (Fig. (3.6c)) with closed loop operation in  $x$  and  $y$  axis and SECM System 4 a 2-phases permanent magnet (Fig. (3.6b)) stepper motor.

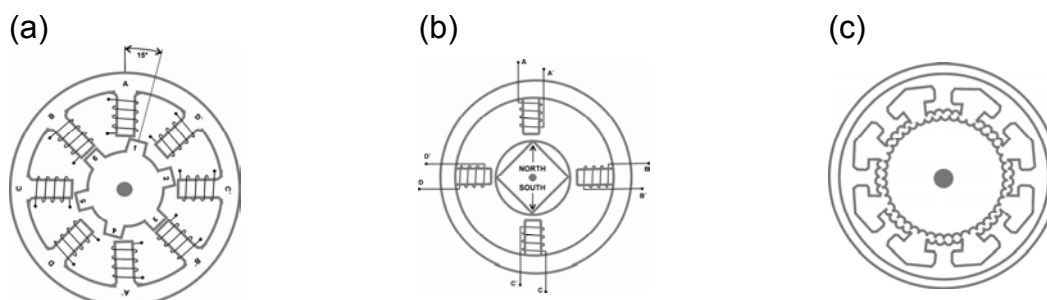


**Figure 3.6.** Working principle of a (a) variable reluctance, (b) permanent magnet and (c) hybrid stepper motor.

<sup>1</sup> To send current through a phase or phases of a stepper motor.



**Variable Reluctance Motor:** The VR consists of a multi-toothed rotor and a wound stator. In Fig. (3.6a) the stator has four pole sets (A, B, C, D), set 15 degrees apart. When the stator winding B is energized with DC current, the poles become magnetized and the rotor tooth is thus attracted to the energized stator pole being aligned to pole B. When pole C is energized, the rotor will rotate 15 degrees in order to align with pole C. This process can continue in clockwise direction (energizing D), or in counterclockwise direction, reversing the procedure (D to B). VR motors are generally noisy no matter what drive waveform is used, furthermore microstepping is not applicable to VR motors, thus being not appropriate for SECM.

**Permanent Magnet Motor:** Also known as "canstack" motor, has a permanent magnet rotor, as the name implies. The rotor does not have teeth as in VR motor, instead the rotor is radially magnetized with alternating north and south poles situated in a straight line parallel to the rotor shaft. Fig. (3.6b) shows a simple, 90 degree PM motor with four phases (A, B, C, D). As a current is passed through the winding of each phase in sequence, the rotor rotates by adjusting to the changing magnetic fields.

The PM motors generally bear step sizes from 30 to 3.6 degrees, however the rotor can be cut in finely spaced teeth making possible step sizes of 1.8 degrees and even smaller. PM motors can be microstepped with an appropriate control system, allowing smooth, jerk-free movement from one step to another. This type of motor is used in System 4, but it has only two phases, what makes the translation to be rough and noisy. However, the price of this positioning system was much lower in comparison to other systems and the resolution of the positioning is good enough for instructive experiment (e.g. practical training at the university).

**Hybrid Motor:** Hybrid motors combine the best features of VR and PM motors, therefore hybrid. It consists of multi-toothed stator poles like in VR motors and toothed permanent magnet rotor as in PM motors (Fig. (3.6c)). Hybrid rotors are axially magnetized, one end polarized as north and the other as polarized south. The microsteps are produced by proportioning the current in the two windings according to sine and cosine functions. The "teeth" align in various configurations during rotation. Typical step angles for hybrid stepper motors range from  $3.6^\circ$  to  $0.9^\circ$  (100 – 400 steps per revolution).

This kind of motor exhibits high static and dynamic torque and runs at very high step rates. As in PM, the hybrid motor can be microstepped depending on the driver. This type of motor is used in System 2. It moves very smoothly, can make very large steps with high speed, as well as very fine steps with small speed. The resolution of this motor is excellent

and after almost 5 years of intensive use it did not show any problem. The only disadvantage of this motor is the high cost.

### 3.3.2 Piezoelectric actuator

Piezoelectric actuators<sup>1</sup> convert electrical energy directly to mechanical energy reacting in a matter of milliseconds.<sup>[158, 159]</sup> Although the piezoelectric effect is small in naturally occurring crystals, materials science has developed ceramic materials with piezoelectric behavior. Piezoelectric material consists of a polycrystalline ferroelectric ceramic material such as barium titanate and lead (plumbum) zirconate titanate (PZT). The most common form of piezoelectric ceramics is based on PZT.

The piezoelectric actuator displacement principle is based on an expansion due to an applied electric potential to the ceramic material. The expansion is a function of the applied electric field strength, the length of the actuator, the forces applied to the actuator, and the properties of the piezoelectric material. High voltages are normally used to cause the piezo displacement, what limits the travel range. Typical travel ranges of piezo actuators are between tens to hundreds of nm, although longer travel ranges can be achieved by mechanical amplification techniques or stacking of piezos. As the displacement of a piezoelectric actuator is based on ionic shift and orientation of the PZT unit cells, the resolution is limited by the precision of the driving stage. The displacement produced is smooth and continuous because the expansion is a process at the atomic level, and therefore there is no friction or stiction, so that piezoelectric actuators exhibit no wear and tear. Because piezoelectric actuators do not produce magnetic fields and are not affected by them, they work well for applications in which magnetic fields cannot be tolerated. Nevertheless, the displacement of a PZT device may not be ideal, producing some hysteresis, drift (unwanted change of displacement over time), and thermal variations. In order to avoid these problems, a feedback system can be used.

System 1 has a very compact piezo positioning with a relative large travel range (500  $\mu\text{m}$ , closed-loop operation) in each axis, providing nanometer resolution. The piezo positioning systems that are attached to System 2 and System 4 have a travel range of 250  $\mu\text{m}$  and 500  $\mu\text{m}$  in closed-loop operation respectively. As in System 1, these positioners are compact, being easy to integrate to (or remove from) the system, and provide nanometer

---

<sup>1</sup> Actuators are devices that produce force or motion (displacement).

resolution. All piezo positioning stages from our group have a capacitive feedback sensor integrated in order to assure an optimum resolution.

### 3.3.3 Piezoelectric motors

The piezoelectric motor is a type of electric motor that makes use of changes in shape of a piezoelectric material to produce a linear or rotary motion when an electric field is applied. Piezo actuators and piezo motors differ because the actuators use the material deformation to displace the load while the motors are generally coupled with mechanical parts isolating the piezo material from the load. Although piezo actuators can be made up of stacks or plates in order to increase the travel range (displacement is directly proportional to the height of the piezo stack), limitations of stack size must be considered, what limits the displacement (larger stacks tend to have high capacitance and more side-to-side movement and thus are harder to control). As piezo motors translate small piezoelectric resonant vibrations into a larger, continuous mechanical motion, it has theoretically unlimited travel range.<sup>[160]</sup> The displacement of the piezo ceramic in the desired direction is transferred to the rotor or slider over an intermittent frictional coupling. The construction of piezo motors is very simple in comparison to conventional stepper motors, allowing to have miniaturized positing device, with no hold position power consumption and heating. There are two different groups of piezo linear motors: ultrasonic motors, also referred to as resonant motors, and step/walk motors (non-resonant, quasistatic motors).

The quasistatic piezo motors operate on either a clamping principle or the inertial principle. In the clamping principle, the piezo motors usually consist of several individual piezo actuators and generate motion through succession of coordinated clamp/unclamp and expand/contract cycles. Each extension cycle provides only a few microns of movement, but running at hundreds of Hertz, achieves continuous motion in the mm/second range. The Inchworm<sup>TM</sup> actuator is an example of a non-resonant piezo motor and that was used in most early SECM intruments. However, many disadvantages have made these motors not to be preferred as coarse positioning in SECM. The clamp-unclamp events procedure leads to a rough movement of the shaft causing an artefact in the probe signal (when it is mounted to the motor) which is especially noticeable at current-distance curves.<sup>[161]</sup> High costs due to proprietary supplier, specialized controller and constant calibration necessity are also relevant problems when one has to select a motor.

In the inertial principle, the piezo motors use the inertia and the difference between the static and dynamic friction coefficient in order to generate motion. When the piezo ceramic is expanded or contracted in the motion direction slowly, the slider follows this movement without slippage. The next step, the piezo is rapidly expanded or contracted in the opposite direction, so the slider does not follow its inertia although the piezo slips back over it. The quasistatic piezo motors operate well below the resonant frequency of their piezo ceramic actuator and have higher resolutions and forces than ultrasonic piezo motors.<sup>[162]</sup>

A fundamental construction of ultrasonic motors consists of a high frequency power supply, a vibrator and a slider. The vibrator is composed of a piezoelectric driving component and an elastic vibratory part, and the slider is composed of an elastic moving part and a friction coat.<sup>[163]</sup> The basic working principle of these motors is based on the conversion of a high frequency electrical signal applied to the piezo actuator into oscillation at one of its resonant frequencies in the ultrasonic range<sup>1</sup>. The oscillation cycle causes a smooth frictional contact with the mechanics executing a step of a few nanometers to obtain unlimited motion of the slider. The oscillations of the actuator result from excitation of different vibration modes (acoustic waves). Conventional displacement sensors may be used to measure motor travel and position such as a laser-based interferometer that measures motor position over time.

Ultrasonic motors allow fast and continuous motion, but as in these motors motion is transferred through friction, they have limited repeatability and cannot provide the unlimited resolution of linear piezo actuators. Furthermore, they require high power electronics and cannot support large loads. Quasistatic motors can provide higher resolution and holding forces. However, the maximum speed is lower than few  $\text{mm s}^{-1}$  in most cases. General advantages of the piezo motors are that it does not have motor heating and no power consumption when static as in conventional stepper motors, it has long lifetime (position is held with zero operating voltage), and has a much larger travel range than in piezo actuators.<sup>[164]</sup>

System 3 uses the piezo-driven stepper motor (quasistatic motor) that is very compact and flexible, has a very large travel range (18 mm) and makes smooth movements with resolution of about 50 nm and maximum velocity up to  $2 \text{ mm s}^{-1}$ . However, some problems with this positioner have already appeared, such as clamping of the motor after it has reached the end of the stage.

---

<sup>1</sup> Frequency greater than approximately 20 kHz.

### 3.3.4 Translation stages

Translation stages are the moving parts of the positioning system that allows mechanical movement and are generally coupled with a motor or with a micrometer screw. They also constrain the positioner (motor) motion to a single axis and provide a structure where the UME or sample can be mounted. Accuracy, load capacity and low friction are fundamental requirements for translation stages.<sup>[165]</sup> As the translation stages are generally mounted together with the positioner, an error contribution to the motion must be considered. The major types of errors in a horizontal translation stage are straightness, backlash and flatness. Roll, pitch or yaw are generally caused by assembly run out errors and are angular motions around  $x$ ,  $y$ , and  $z$  axis. There are several translation stage designs such as crossed-roller bearing stages, ball bearing stages, dovetail slides and flexures.

As the translation stages are mounted together with the positioners, one cannot define which translator is the preferable for certain system. Nevertheless, the motor manufacturer generally provides the most suitable translation stage for their motor, ensuring the best motor performance. The System 4 was the only one that we could choose the translation stage because the motor is sold separately from the translation stage (crossed-roller guides).

## 3.4 ADC and DAC converter

SECM data acquisition and command output are usually done through ADC and DAC converters. They are used to convert an analog input signal (typically voltage) to a digital number in the case of ADC and the reverse operation is done by DAC (digital numbers to analog signal). Nevertheless, analog signals generally arise from the output of a potentiostat and from the output of a piezoelectric actuator controller being digitalized by an ADC. Some minimum requirement must be fulfilled in order to allow good performance during voltammetric experiments and to improve SECM data by allowing averaging.<sup>[166]</sup>

An ADC board with 16 bit resolution is recommended for SECM because it covers the entire input dynamic range<sup>1</sup> and a minimum sampling rate of 100 kHz assure highly sensitive measurements. The number of input channels available in an ADC board determines the number of devices that can be connected to an ADC, this number of channels varies from 4 up to 64. Our ADC boards fulfill all requirements, having 16 bit resolution, 16 single-ended or 8 differential analog inputs and 200 kHz throughput containing 2 D/A channels with 16 bit

---

<sup>1</sup> Large dynamic range allows a "zoom" into the data to extract small signals from a large baseline.

resolution. Our DAC boards contain 8 and 4 channels of 16 bit resolution (System 1 and 2 respectively).

The ADC signal-to-noise ratio (SNR) must be maximized and distortion due to clock skew and aliasing must be minimized. Aliasing can be avoided by a low pass filter on the input to the ADC and sampling twice the filter cut-off frequency or higher<sup>1</sup>. SNR and digital resolution can be maximized by averaging the sample input signal in order to retain the effective sampling rate. In order to optimize the SNR and aliasing of our SECM systems, an analog potentiostat was connected to the ADC and the voltages from the output of the ADC were recorded as AD values using the oscilloscope experiment implemented in the SECM program. The oscilloscope data were recorded using different frequency filters (available in the potentiostat). The in-house software Microscopic Image Rapid Analysis (MIRA) written by Prof. Dr. G. Wittstock was used to process and analyze the data leading to best effective sampling signal average. The best average number was always used in SECM experiments and the data recorded were used in this thesis without further modifications.

ADC input channels can be single-ended or differential, depending on the connection done to input the signal into the data acquisition board. With single-ended inputs each signal source is connected to the data acquisition interface through one cable (wire) and the difference between the signal and the ground or earth is measured. As the ground has different values depending on its level and location, the measured difference can drive large currents and thus, measurement errors. In single-ended inputs, signal and noise can not be distinguished, moreover the wires may pick up electrical activity from the environment adding noise to measured signal. The ground and noise problems can be solved by differential inputs.

In differential inputs, each signal source is connected to two signal wires where one is connected to a + input and the other wire is connected to a - input. The voltage difference between the inputs and the interface ground is then monitored by a high-impedance amplifier and the difference between the + and - amplifier output leads to a "pure" signal. Differential inputs make the differences in ground negligible and reduce noise. A disadvantage of differential inputs is that special cable connections have to be constructed and only half of the channels are available for device connection, compared to single-ended inputs. Single ended input can be used if the system has short cables, close signal sources and signals higher than 100 mV.<sup>[167]</sup>

---

<sup>1</sup> Nyquist criterion states that an input signal can be recovered if its sampling frequency is greater than twice the signal bandwidth.

An interface with BNC connectors can be used to connect the analog devices to the ADC board, that is normally installed into a computer. DAC boards are also connected to the analog device through the BNC interface in order to send commands (motor movement, voltage, etc.). Initially single-ended input was used in our SECMs, the cables were short and could be connected directly, however special cables were constructed to make connections as differential inputs for an experiment that required measurement of currents in pA range. Since then we use differential inputs for SECM, although after comparison no difference to single-ended mode is detected in most experiments.

### 3.5 Software

The new SECM control software is based on the architecture that separates the main application block (experiment control; data acquisition and visualization) to the hardware access. The main control application is virtually independent on particular hardware (although provides tools for the hardware setup), hardware access is realized in form of dynamic link libraries (DLL) featuring common interface, DLLs can be instantly exchanged in order to adapt the control program to particular experimental hardware, i.e. potentiostats, AD/DA-board, positioning systems, etc.

Experiments are realized in a uniform way, so that new experiments can be added and easily fit into the existing concept. The block diagram (Fig. (3.7)) shows how the components are separated in the SECM software. All SECM data in this thesis were analyzed and visualized using the software MIRA.

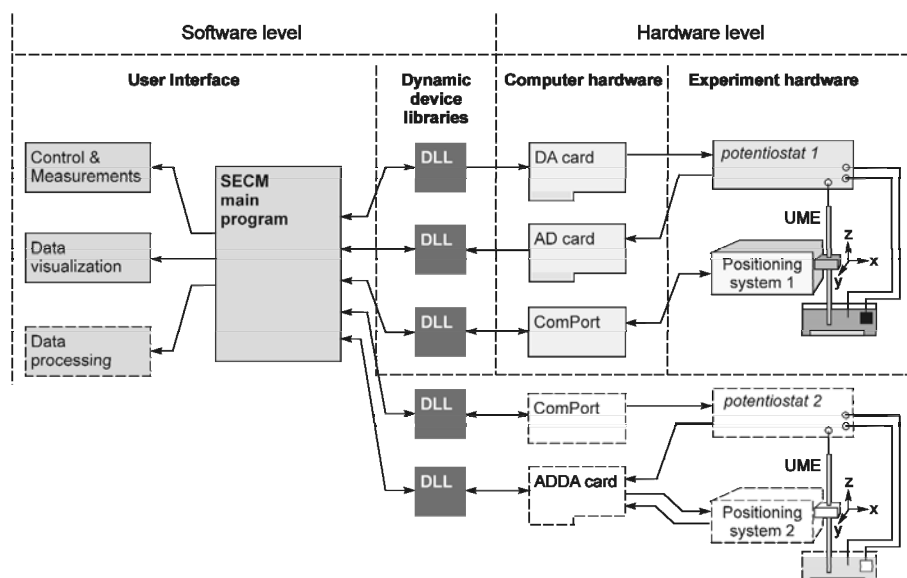


**Figure 3.7.** Block diagram of the SECM software.

### 3.6 Constant distance mode

Conventional SECM imaging and  $x$  and  $y$  line scan experiments measures the amperometric or potentiometric UME current when it translates across the sample surface at a constant height. In order to increase imaging resolution, smaller UME electrodes (nm range) must be used and the UME must be placed at a suitable working distance. The UME-to-sample separation has to be of the order of the diameter of active electrode of UME to ensure high resolution imaging (feedback mode) and good collection efficiency (GC mode).<sup>[142, 168, 169]</sup> Performing SECM imaging in constant-height mode has some drawbacks. In samples with variations in conductivity and topography, variations in UME response cannot be assigned to differences in topography or local reactivity. Another problem is that the sample tilt and protruding features can cause undesirable UME crashes or imaging artifacts.

In order to overcome these problems a shear force distance control system may be used. Using shear forces the UME-sample distance is measured and this information is used to keep the distance constant. Thus sample topography and reactivity can be measured at the same time. Shear force systems rely on measurement of the changes in resonance frequency, amplitude or phase shift of a nanometer-sized UME. There are two variations of shear force systems to keep a constant UME-to-sample distance. A quartz tuning fork may be attached to the UME by one leg and the resonance frequency is determined by a quartz resonator.<sup>[170-174]</sup> The variation is the use of a piezoelectric plate mechanically attached to the UME used to excite the UME with a frequency tuned to its mechanical properties.<sup>[175]</sup> The changes in resonance frequency, amplitude or phase shift can be recorded either by projection of a diffraction pattern onto a split photodiode<sup>[175]</sup> or by attaching a second piezoelectric plate to the UME.<sup>[102, 103, 168, 176-178]</sup> The latter type is used in our laboratory.<sup>[A8]</sup> Fig. (3.8) shows how the piezo ceramics are attached to the UME.



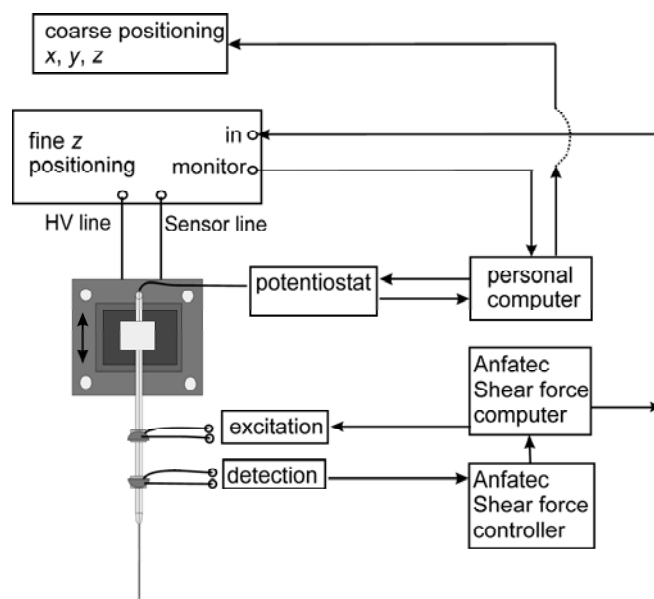


**Figure 3.8.** Shear force system.

The upper plate is used to excite the SECM probe causing it to vibrate, and the other detects the shear forces between the UME and sample, hence variations in amplitude of the UME oscillation. The detection piezoelectric plate is connected to a lock-in amplifier that amplifies the distance-dependent signal. A closed loop feedback system controller reacts to changes in amplitude by moving a piezo actuator (where the UME is attached by an UME holder) in vertical direction keeping the resonance frequency constant.

Although a successful constant height reaction rate image of the passive layer formed on  $\alpha$  and  $\beta$  phases of a titanium alloy was done in our group,<sup>[A8]</sup> this mode of positioning is still not commonly used in our lab. There are many difficulties to be overcome such as finding the right resonance frequency (there are many noise frequencies disturbing the measured signal), fabrication of nm-sized UME (well defined disk shaped UME are very demanding to fabricate, an estimate is that out of 10, 2 are suitable for a SECM shear force measurement) and breaking the UME during the assembly and experiment. The experiments shown in this thesis used the conventional positioning rather than shear-force positioning.

### 3.7 Overview and future developments

Recently, many groups have put effort in the development of hybrid SECM techniques. The hybrid SECM can be a combination of two different techniques such as AFM,<sup>[179-181]</sup> electrochemiluminescent detection,<sup>[182]</sup> ECSTM,<sup>[183]</sup> and electrochemical quartz crystal microbalance measurements<sup>[184]</sup> with new probe designs.<sup>[185]</sup> The combination enables the

application of SECM to several different samples that were not possible to analyze before with the conventional SECM, furthermore this leads to increased resolution and different data acquisition at the same time.<sup>[185]</sup> The combination of techniques is not limited to the assembly of SECM to other technique, it can be a combination of several techniques including implementation of SECM modes of operation such as combination of SECM line scans and imaging with CV and chronoamperometric measurements.

As the SECM setups of our group are very flexible, the combination of our SECMs with other techniques such as optical microscope and SCLM is already realized and leads to very good results.<sup>[186]</sup> However the combination of SECM imaging with techniques like CV and chronoamperometry is being developed and shows to be a very promising combination in order to locally induct reactions and construct 4D images of surface activity with optimal electrochemical contrast.<sup>[187]</sup>

## **4 Material characterization by SECM approach curves**

This chapter shows the electrochemical characterization of titanium nitride (TiN)<sup>[A7]</sup> and silicon dioxide (SiO<sub>2</sub>)<sup>[A1]</sup> surfaces by SECM approach curves. These materials are possible candidates to be used as transducers in sensors. Other techniques were used for further analysis and to corroborate the results obtained by the SECM.

### **4.1 Evaluation of thin film TiN electrodes for electroanalytical applications**

#### **4.1.1 Introduction**

Titanium nitride films exhibit an exceptional combination of chemical, physical, mechanical, and electrical properties, such as a high degree of hardness, chemical stability, high thermal conductivity, an immunity to wear and corrosion, chemical inertness, biocompatibility, and resistance to atomic diffusion within its matrix.<sup>[188-191]</sup> Thin films of TiN can be deposited by a number of physical and chemical vapor deposition methods including evaporation, ion plating and sputtering.<sup>[189, 192-194]</sup> The growth of TiN was studied<sup>[195]</sup> and showed that it forms a sodium chloride lattice already at very small sizes of TiN clusters. The properties of thin films, like preferred orientation of lattice plane and electrical resistance, grown by physical and chemical vapor deposition methods are highly dependent on total gas pressure, partial pressures of reactive gases, deposition rate, temperature and sample material,<sup>[196-202]</sup> which makes it suitable for a wide range of applications if the material properties are tuned right. Consequently, patterned TiN is a candidate material for microelectrode arrays.<sup>[189]</sup> Several studies about structural, mechanical and electrical properties of TiN thin films have been completed in the last years.<sup>[188-194, 196-207]</sup> They also include studies about the oxidation kinetics of TiN.<sup>[208-210]</sup> Titanium nitride has been used as the sensitive material in all solid-state potentiometric pH electrodes.<sup>[211]</sup> The electrochemical inactivation of adherently growing bacteria on TiN electrodes in seawater was demonstrated using a potentiostatic treatment that takes advantage of inertness of TiN.<sup>[212]</sup> On the other

hand TiN is considered as a biocompatible material<sup>[189, 205, 206]</sup> and has been used for electrically contacting adherent cells and tissue.<sup>[213]</sup>

One particular attractive feature of TiN thin film electrodes are the highly developed protocols that allow to produce well-adherent micro or nanostructured electrodes. Detection schemes that rely on redox-cycling at interdigitated electrode arrays (IDAs) show an increasing sensitivity with decreasing band size and electrode-electrode distances.<sup>[214, 215]</sup> Remarkable effects can be expected if electrode and gap sizes are pushed well below 1  $\mu\text{m}$ . However, up to now there is no well-developed technology for the mass production of nanometer-sized IDAs with noble metal electrodes. Developing such a technology is not an easy task because of the inertness of the noble metals typically employed for analytical electrodes. Wet etching steps are problematic because they would likely destroy the etch mask. Dry etching procedures are problematic because there are no suitable gaseous etching products, e.g.  $\text{AuX}_n$ , that are able to transport away the etched noble metal. Few reports describe reactive ion etching of gold (a dry process),<sup>[216-218]</sup> but the described structures are larger than 500 nm. Ref. <sup>[219]</sup> describes Au structures with sub-100 nm resolution obtained by negative nanoimprint lithography. However, a wet etching step with its limitations was used during the preparation. Lift-off techniques require thick mask layers in order to remove them after deposition contradicting the requirement for small distances. Ion milling as another alternative would distribute the material over the whole surrounding area and is not well suited for mass production. On the other side there is a well-developed and established TiN deposition and structuring technology for the mass production by the microelectronic industry.<sup>[220]</sup> This technology can be scaled down to nanostructures and it would be possible to produce nanosized IDAs even in mass production. For electroanalytical purposes some groups demonstrated the galvanic deposition of Pt on top of TiN structures in order to improve the electroanalytical characteristics of TiN electrodes<sup>[221]</sup> or to use TiN as catalytically inactive back contact for combinatorial libraries of Pt-Ru electrocatalysts for fuel cell anodes.<sup>[204]</sup>

In this chapter the properties of thin film TiN electrodes for electroanalytical application are evaluated. Double layer charging current densities and the heterogeneous electron transfer kinetics were investigated using SECM. The data are correlated to structural characterization by scanning force microscopy (SFM) and x-ray photoelectron spectroscopy (XPS). The reported data here are for TiN electrodes stored for 5 years in air (native samples). One sample set was cleaned by 5 minutes treatment with ultraviolet (UV) light that causes the generation of ozone (UV/ozone-treated samples). The emission of UV light causes molecular excitation, promoting an effective removal of organic contamination.<sup>[222]</sup>

### 4.1.2 Structural characterization

**Scanning Force Microscopy (SFM):** Topography and roughness were examined for the different layers by scanning force microscopy. Fig. ((4.1) a, b and c) shows a representative SFM image of the 300, 100 and 20 nm thick TiN layer respectively. The roughness is given as the root mean square (RMS) value determined on an area of  $(5 \times 5) \mu\text{m}^2$ . It suggests a linear dependency on thickness (Fig. (4.1 d)).

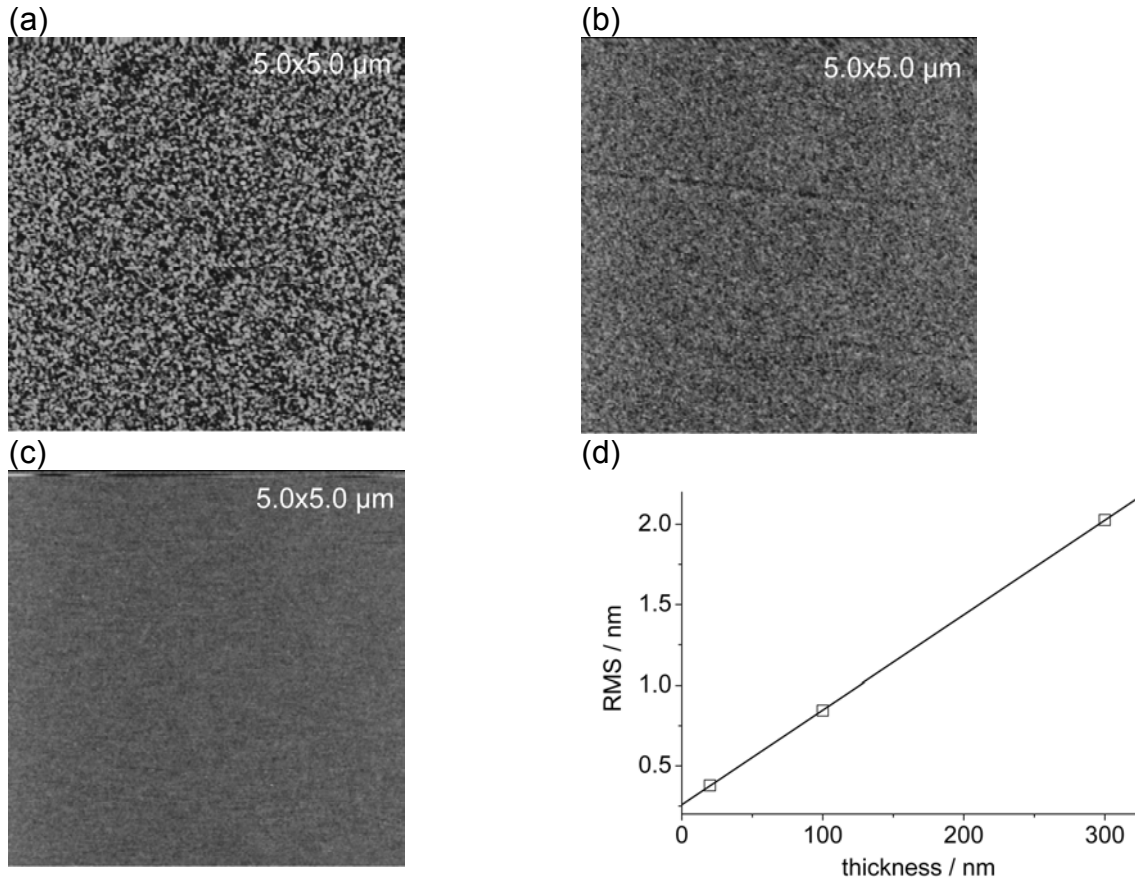


**Figure 4.1.** Scanning force microscopy of TiN layer. Image of (a) a 300 nm, (b) 100 nm and (c) 20 nm TiN thick layer. (d) RMS values determined on an  $(5 \times 5) \mu\text{m}^2$  area on different TiN samples as function of layer thickness.

**X-ray photoelectron spectroscopy (XPS):** XPS spectra were recorded and analyzed by Dr. K. H. Hallmeier from the University of Leipzig. Signals for Ti, N, O and C were found in XPS spectra and were analyzed in more detail. On native samples the high-resolution Ti 2p signal shows three components (Fig. (4.2a)). Because the Ti  $2p_{1/2}$  signal is superimposed with a complicated background including also a possible energy-loss structure, attention should be directed only to the Ti  $2p_{3/2}$  signal at binding energies (BE) of 454-460 eV. The three components can be assigned to TiN (455.1 eV)<sup>[223]</sup>, titanium oxynitride (456.3 eV) and  $\text{TiO}_2$

(458.1 eV). This pattern is typical for TiN layers prepared in this way.<sup>[205, 211, 212]</sup> However, the relative intensities of the components are highly dependent on the preparation conditions. Interestingly, the bulk TiN material has the lowest TiN contribution at the surface layer. Therefore, also the energy loss structure associated with  $Ti^{3+}$  centers and expected at 455.7 eV<sup>[224, 225]</sup> has a lower importance for this sample.

The main component of the N 1s spectra at 397.3 eV (Fig. (4.2c)) agrees very well with literature references for the nitride.<sup>[223, 225]</sup> In addition, there is a higher energy contribution that may result from nitrogen-oxygen compounds at the surface. The origin of two low-energy components at 395.8 eV and 396.5 eV is presently unclear. The BE values are unusually low for N 1s signals.

The O 1s spectra (Fig. (4.2d)) are formed by a contribution of oxidic oxygen atoms (529.6 eV) and a hydroxylic component at 531.4 eV due to OH<sup>-</sup> groups from the humidity during the sample treatment in air. The C 1s spectra (Fig. (4.2b)) have a main component of  $sp^2$ -hybridized carbon at 286.4 eV. The BE corresponds to that of graphite, but this assignment has not been further verified. Carbides were not detected. Two components at higher BE are typical for organic contaminations that must be expected after prolonged storage in air (286.0 eV, 288.2 eV).

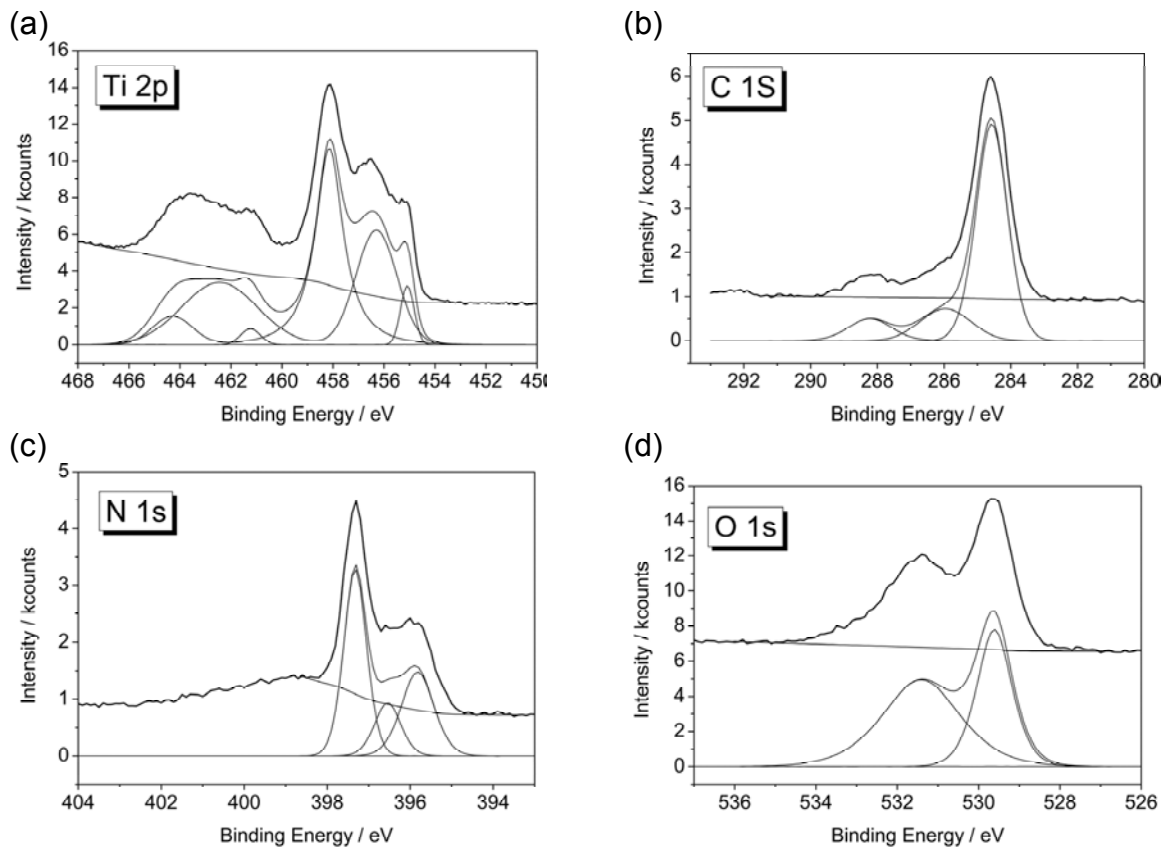


**Figure 4.2.** XPS spectra of native TiN layers after prolonged storage in air. a) Ti 2p, b) C 1s, c) N 1s, d) O 1s.

The assignments are supported by a moderate sputtering of the sample by 5 min  $\text{Ar}^+$  bombardment intended to remove the topmost contamination layer (Fig. (4.3)). The total amount of carbon was drastically reduced. The main component is now located at 285.0 eV, a value expected for  $\text{sp}^3$ -hybridized carbon not connected to electronegative elements (Fig. (4.3b)). The N 1s component at 395.8 eV was completely removed (Fig. (4.3c)). This suggests that this unknown component is present only at the very surface of the sample and probably results from a contamination. The total amount of oxygen was decreased, whereby in particular the oxygen bound in organic contaminants (531.4 eV) was reduced (Fig. (4.3d)). In the Ti  $2\text{p}_{3/2}$  spectra the intensity of the bulk component at 455.0 eV has a much higher intensity and the associated energy-loss structure at 455.7 eV had to be considered in the spectral analysis (Fig. (4.3a)).

The UV/ozone treatment of the samples leads to a partial removal of the carbon contamination and an almost negligible increase in the  $\text{TiO}_2$  and oxidic oxygen component.

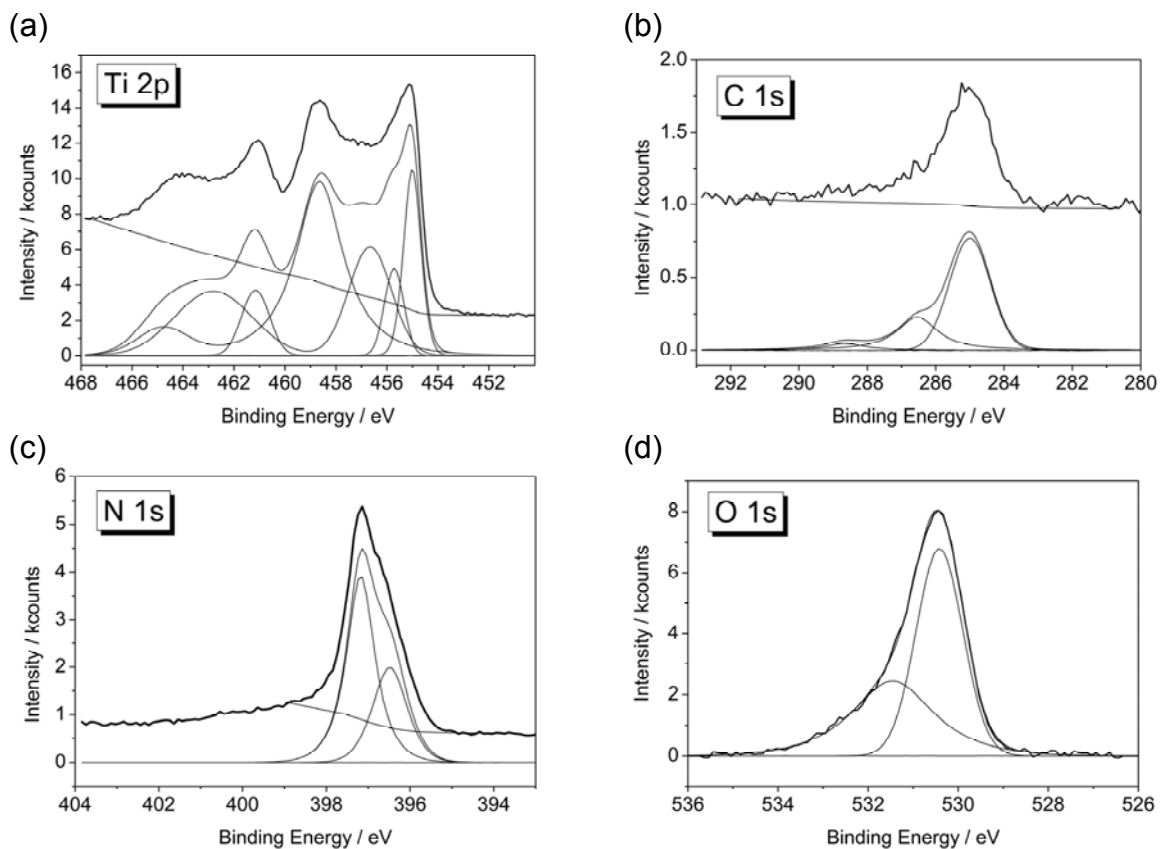


**Figure 4.3.** XPS spectra of native TiN layers after 5 min  $\text{Ar}^+$  sputtering. a) Ti 2p, b) C 1s, c) N 1s, d) O 1s.

### 4.1.3 Electrical and basic electrochemical characteristics

**Four point resistance measurement:** The resistivity of the TiN layers were measured using the four point resistance measurement and were carried out by Dr. A. Kittel from the University of Oldenburg. The measured resistance ( $R$ ) was 0.88  $\Omega$ , 1.98  $\Omega$  and 13.49  $\Omega$  for 300 nm 100 nm and 20 nm TiN respectively. It is usual to express the resistance as surface resistance. Since the TiN is a smooth sample, one can assume that the current density distribution transverse to the direction of the current has a Gauss shape (follows the solution of the Laplace equation). Thus the surface resistance resulting from an equidistant four point resistance measurement can be described by Eq. (4.1):

$$R_s = \frac{U}{i} \cdot \frac{\pi}{\ln 2} \quad (4.1)$$

where  $R_s$  is the surface resistance,  $U$  the voltage and  $i$  the current. It has the unit  $\Omega/\text{quad}$  (actually only  $\Omega$ , because the dimensions for length and width of the layer shorten themselves).

In order to calculate the resistivity, one has to multiply  $R_s$  with the thickness of the TiN layer. However, these calculations are only valid if the thicknesses of the samples are much smaller than the distance of the points of contact (assumption fulfilled by the measurement). Thus the calculated resistivity is 122.3  $\mu\Omega \text{ cm}$ , 90.1  $\mu\Omega \text{ cm}$  and 119.9  $\mu\Omega \text{ cm}$  for 20 nm 100 nm and 300 nm TiN respectively. The values are in agreement with literature.<sup>[202]</sup>

**Double layer charging currents and potential window:** A working electrode will only function within a potential window defined by electrode dissolution/decomposition or solvent electrolysis. Therefore the potential window of the TiN was explored and compared with gold electrodes, being very often used as electrode material in electroanalytical applications. The potential windows were tested as a function of the TiN layer thickness in different media. Fig. (4.4) shows the potential window of the 20, 100 and 300 nm TiN electrodes in neutral (a), alkaline (b), and acidic (c) solution and compares with the typical CV of a gold sample.



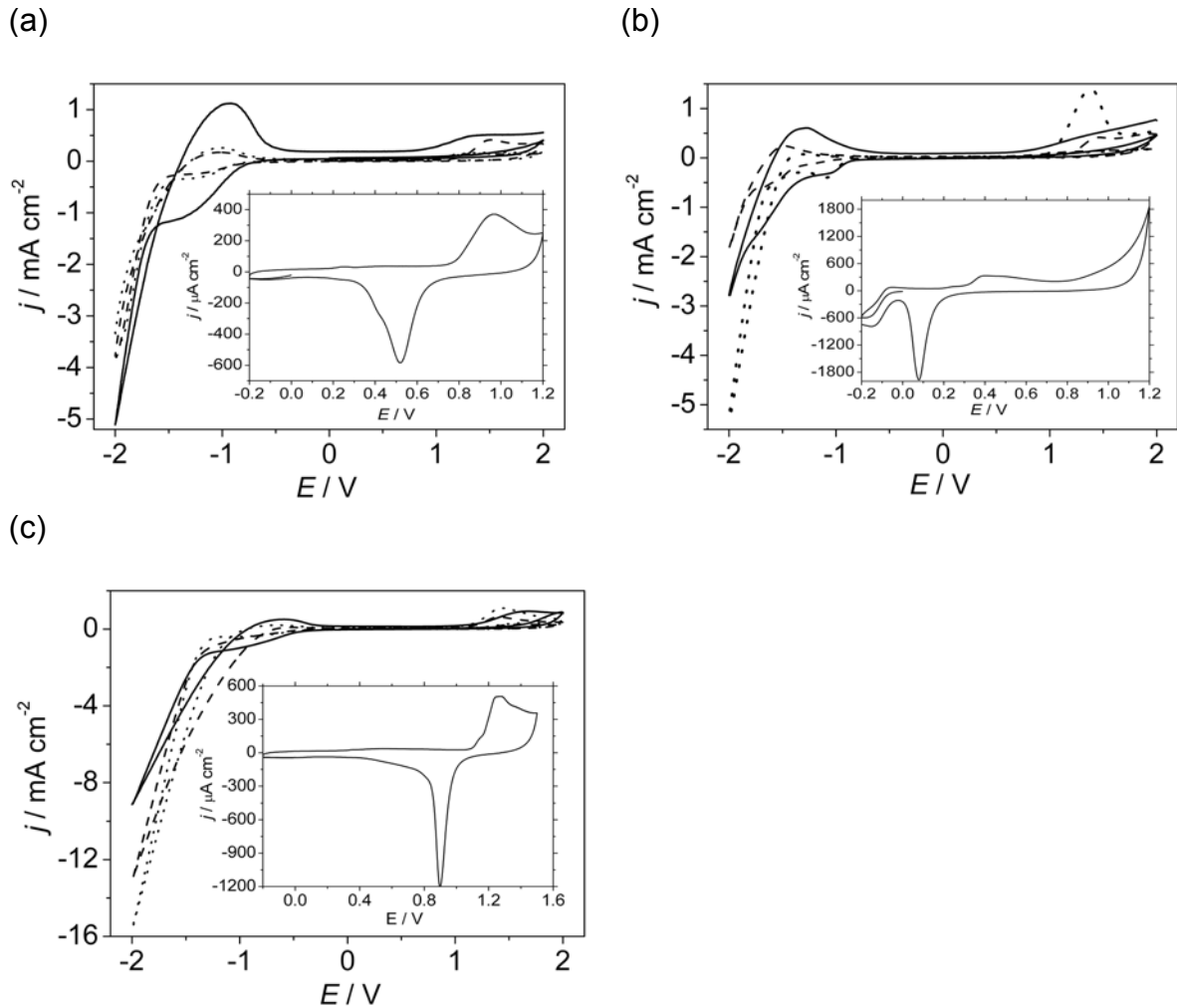


**Figure 4.4.** Study of potential window at 20 nm TiN (solid line), 100 nm TiN (dashed line), 300 nmTiN (dotted line) in (a) 0.1 M phosphate buffer, (b) 0.1 M NaOH and (c) 0.05 M H<sub>2</sub>SO<sub>4</sub>. The CV of a gold electrode is shown in the inset for the corresponding media.

The potential window shown in Fig. (4.4) ranges from -2 V to 2 V. A large increase in the current density begins around 1 V in the anodic side and is associated with titanium oxide (TiO<sub>2</sub>) and oxynitride (TiN<sub>x</sub>O<sub>y</sub>) formation, and at higher potentials (above 2 V), the increase in the current density is associated with the process of oxygen evolution.<sup>[226]</sup> A large increase in the cathodic current indicates proton reduction around -1 V. A closer view in a smaller potential range leads to a better recognition of the redox processes because the redox currents are not masked by the large currents. An example of a smaller potential range for a 100 nm TiN thin film electrode in acidic (Fig. (4.5), curve 1), in neutral (Fig. (4.5), curve 2) and in alkaline solutions (Fig. (4.5), curve 3) is illustrated in Fig. (4.5). The potential range useful for electroanalytical applications is limited by proton reduction at the negative side (Eq. (4.2)) and formation of passive films at the positive side (Eq. (4.3)<sup>[226]</sup>).

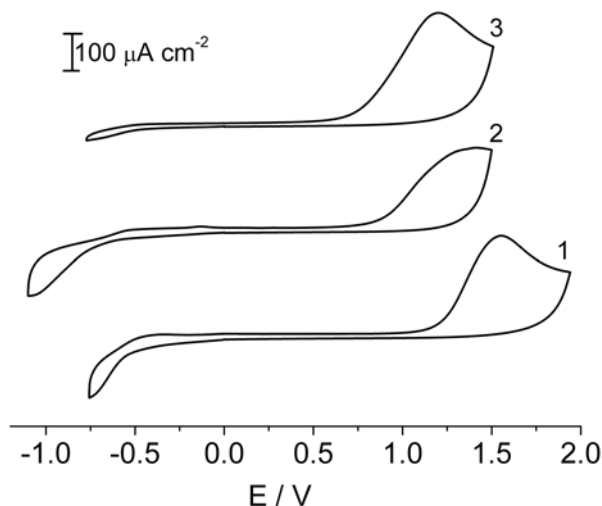


**Figure 4.5.** Comparison of the useful potential ranges for a 100 nm TiN electrode in (1) 0.05 M  $\text{H}_2\text{SO}_4$ , (2) 0.1 M phosphate buffer, and (3) 0.1 M NaOH.

The values quoted in Table (4.1) were taken as those values when the current exceeded the capacitive current observed between 0 and +0.3 V by more than 30 % (Fig. (4.4)). The negative limits were taken from CVs starting from 0 V in negative direction. Since the current rises gradually, there is some variation in the exact potential when the criterion is met. After the negative limit was established, the positive limit was tested by successively increasing the positive potential limit. The values in Table (4.1) varied only slightly with the tendency that the useful potential window increased with the TiN layer thickness (Table 4.1)). The upper limits of the potential range compare well to the useful potential range of noble metal electrodes such as gold. The voltammograms of Fig. (4.5) were recorded afterwards to include the onsets of proton reduction and the formation of a passive film for an illustrative overview.

**Table 4.1:** Negative and positive potential windows of the TiN electrode in different electrolytes.

Layer thickness / nm	0.05 M $\text{H}_2\text{SO}_4$		0.1 M phosphate buffer		0.1 M NaOH	
	negative limit / V	positive limit / V	negative limit / V	positive limit / V	negative limit / V	positive limit / V
20	-0.24	0.86	-0.31	0.60	-0.35	0.43
100	-0.23	0.87	-0.30	0.60	-0.26	0.43
300	-0.23	0.94	-0.32	0.66	-0.37	0.51

While TiN electrodes used for pacemaker electrodes were optimized with the aim of obtaining a large surface area, a large charging current caused by an internal surface would be undesirable for electroanalytical application as it contributes to the background signal. The charging current densities at TiN investigated depend on the TiN thickness and are 3-8 times larger than that on gold electrodes of the same geometric area (Fig. (4.6)). Most likely, the signal at TiN is also influenced by pseudo-capacitances. They result from the electrochemical conversion of surface-bound functional groups. However, it seems that these contributions can be kept under control.

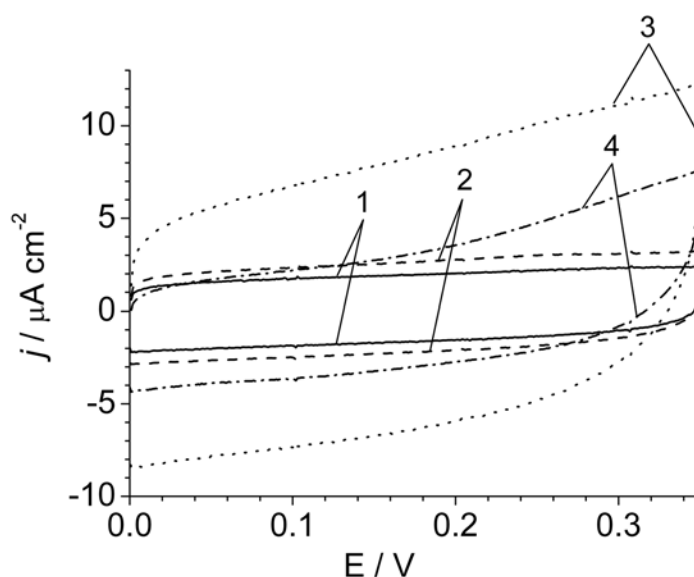


**Figure 4.6.** Comparison of the cyclic voltammograms in 0.1 M  $\text{Na}_2\text{SO}_4$ . Curve 1 (solid line) was recorded at a 20 nm TiN electrode, curve 2 (dashed line) at a 100 nm TiN electrode, curve 3 (dotted line) at a 300 nm TiN electrode and curve 4 (dash-dotted line) at a gold thin film electrode.  $\nu = 50 \text{ mV s}^{-1}$ .

Fig. (4.7) compares the CVs of Fc at gold and at TiN. At the gold electrode the difference of the peak potentials is close to the value of 59 mV expected for a reversible one-electron couple. The response at the TiN exhibited larger peak separations shown in Table (4.2). Assuming the equality of the diffusion coefficients for the oxidized and reduced form and taking the experimentally determined diffusion coefficient for Fc of  $6 \times 10^{-6} \text{ cm}^2 \text{ s}^{-1}$ , the standard heterogeneous rate constant can be estimated (Table (4.2)).<sup>[227]</sup>

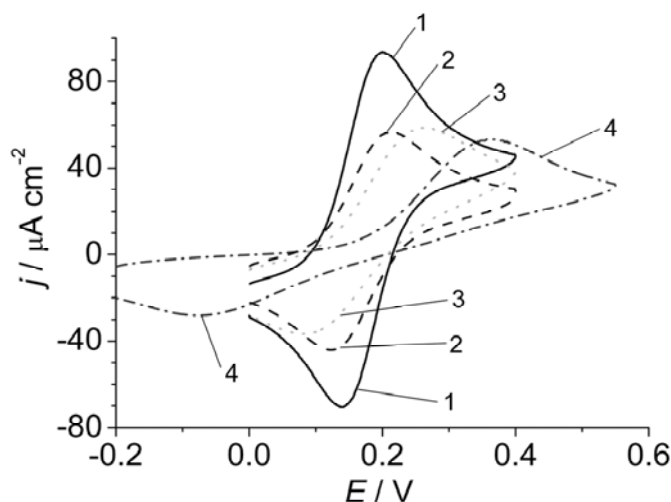


**Figure 4.7.** Cyclic voltammograms of 1 mM Fc in 0.1 M Na<sub>2</sub>SO<sub>4</sub> solution. Curve 1 at gold (solid line), curve 2 at 300 nm TiN (dashed line), curve 3 at 100 nm TiN (dotted line), and curve 4 at 20 nm TiN (dash-dotted line).  $\nu = 20 \text{ mV s}^{-1}$ .

**Table 4.2:** Peak potential difference  $\Delta E_p$  of gold and TiN in different thicknesses and their corresponding standard heterogeneous rate constant.

Electrode	$\Delta E_p = (E_{pa} - E_{pc}) / V$	$k^0 / \text{cm s}^{-1}$
20 nm TiN	0.436	$3.98 \times 10^{-5}$
100 nm TiN	0.181	$5.48 \times 10^{-4}$
300 nm TiN	0.094	$2.61 \times 10^{-3}$
Au	0.061	$4.48 \times 10^{-2}$

The low value for the usually fast redox kinetics results from the internal resistivity of the TiN layers and/or slow electron transfer kinetics at the TiN surface. In view of the low resistance obtained from the four-point resistance measurements it seems that the heterogeneous electron transfer kinetics have the dominating influence, furthermore as the thicknesses of TiN increases, the heterogeneous ET becomes faster. Despite this effect, the CV is well-developed and for a number of electroanalytical applications such a response might be sufficient.

#### 4.1.4 SECM investigation of electron transfer kinetics

The kinetics of the electron transfer were studied using SECM approach curves in the FB mode. This offers the advantage, that a very low total current is passing through the sample. If the sample is externally polarized, resistive effects inside the electrode material are

less important than for instance in CV. A batch of approach curves were recorded for TiN with 20, 100 and 300nm thicknesses in order to extract the  $k_{\text{eff}}$  values. The approaches were carried out in Fc solution in different concentrations (1, 2, and 3 mM) in 0.1 M  $\text{Na}_2\text{SO}_4$  as supporting electrolyte. Two different samples of each thickness were probed: (i) the native sample, cleaned with ethanol and without further treatment, and (ii) ozone-cleaned samples that were cleaned with ethanol and with UV light, to cause the generation of ozone (in order to remove organic adsorbates) for 5 minutes. The approach curves were obtained by moving the UME toward the TiN surface and recording  $i_T$  as a function of  $d$ . Fc was oxidized at the UME at a potential  $E_T = 0.4 \text{ V}$  (Fig. (4.10)) under diffusion-controlled conditions. The generated hydroxymethylferrocinium ( $\text{Fc}^+$ ) diffused towards the samples (TiN, or glass as reference). The externally biased TiN sample reduced  $\text{Fc}^+$  to Fc. The rate of Fc recycling at the TiN was controlled by adjusting  $E_S$ . Fig. (4.8) shows a sketch of the mediator recycling caused by application of different overpotentials at the sample.

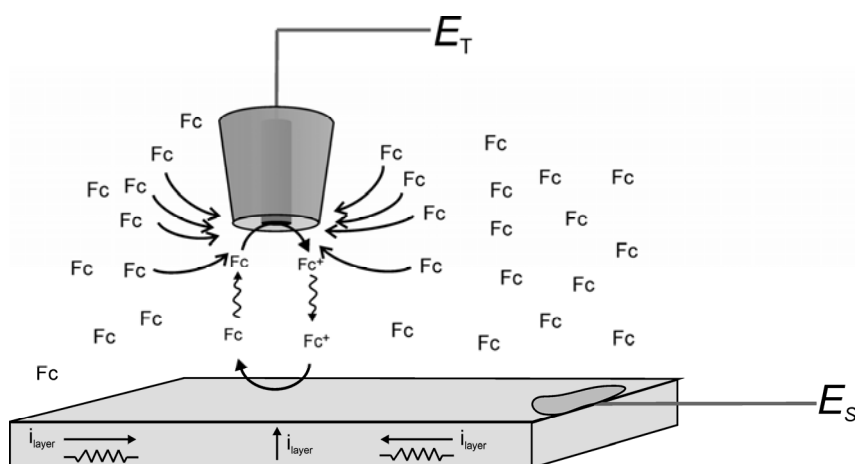


**Figure 4.8.** Sketch of the mediator feedback at the sample. The feedback can be controlled by applying an overpotential to the TiN layer.

Initially, an approach curve was recorded towards a smooth glass surface until the mechanical contact between the glass sheath of the UME and the sample surface was detected as a suddenly established constant current at the vertical coordinate  $z_0$  (Fig. (4.9)). A fit of this curve to Eq. (2.3) gives the effective distance between the active electrode area and the sample surface  $d_{\text{offset}}$  (point of closest approach).

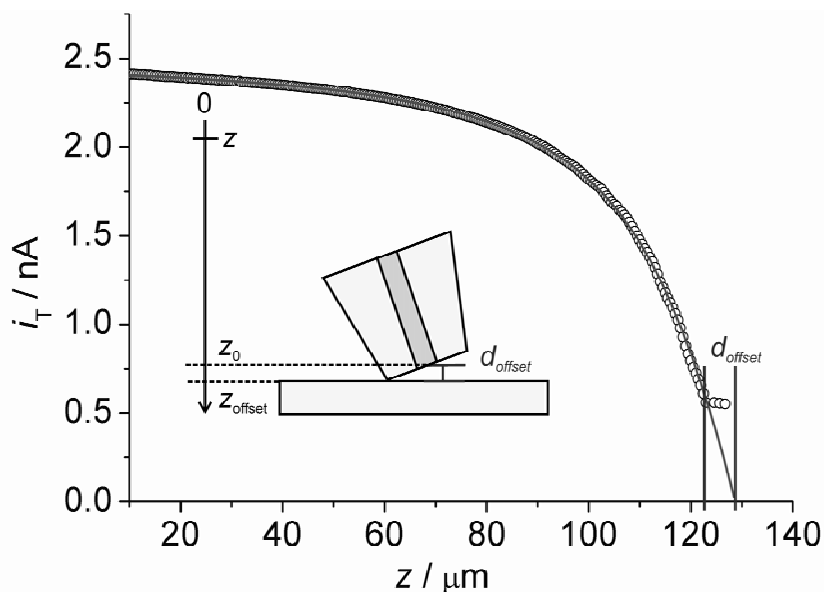


**Figure 4.9.** An experimental approach curve for a 25  $\mu\text{m}$  diameter Pt UME towards glass. The illustration shows the distance  $d_{\text{offset}} = z_{\text{offset}} - z_0$  between the active electrode surface and the sample in the moment of the mechanical touch by the insulating sheath. The  $z$  arrow illustrates the relation to the laboratory coordinate system in which the movement of the UME is measured.  $z = 0$  corresponds to the start point of the approach curve,  $z_0$  is the coordinate of the active electrode area, when the insulating sheath touches the surface,  $z_{\text{offset}}$  is the coordinate of the surface. Note: The tilt of the UME is greatly exaggerated in order to illustrate the principle, while the radius of the glass sheath is smaller in the sketch than in the real experiment ( $RG = 10.2$ ). The theoretical curve (solid line) was calculated according to Eq. (2.3) with the following coordinate transformations:  $r_T = 12.84 \mu\text{m}$ ,  $z_{\text{offset}} = 201.52 \mu\text{m}$ ,  $i_{T,\infty} = 5.554 \text{ nA}$ .

The obtained curves (approach to glass) were first normalized to  $i_{T,\infty}$  and  $r_T$  respectively (Eq. (2.10)). The normalized current  $I_T$  is the distance-dependent steady-state current  $i_T$  normalized by the experimental current  $i_{T,\infty}$  recorded far away ( $> 20 r_T$ ) from the sample surface. The vertical coordinate  $z$  is converted to a normalized distance  $L$  (Eq. (4.4)) using the experimentally determined coordinate  $z_{\text{offset}} = z_0 + d_{\text{offset}}$  at which a mechanical touch between the insulating glass sheath of the UME and the surface occurred. The  $d_{\text{offset}}$  and the exact  $r_T$  are determined by fitting to Eq. (2.3) an experimental approach curve towards a glass sample with the same UME and the same UME mounting.

$$L = \frac{z - z_{\text{offset}}}{-r_T} \quad (4.4)$$

Afterwards, the glass sample was exchanged against the TiN sample without changing the mounting of the UME. After detecting the mechanical touch between UME sheath and the TiN sample in the same way as on the glass electrode, the zero distance point could be

established for the samples with finite kinetics. This procedure was found necessary for high accuracy because otherwise several sets of  $d_{\text{offset}}$  and normalized rate constants  $\kappa$  could reasonably describe the experimental approach curve in the limited  $L$  interval for which an analytical approximation is available.

The experimental approach curves to TiN were fitted to the expression derived for approach curves towards samples with finite kinetics at the sample and diffusion-limited current at the UME (Eq. (2.8)).<sup>[72]</sup> The contributions to this current,  $I_T^{\text{ins}}(L)$ ,  $I_S^{\text{kin}}(L)$  and  $I_T^{\text{cond}}(L)$  were obtained from different approximations (Chapter 2, Section 2.2). The contribution for the normalized current for an insulator  $I_T^{\text{ins}}$  was taken from Ref. <sup>[88]</sup> for  $RG = 10.2$ . From the normalized curves,  $\kappa$  and  $k_{\text{eff}}$  could be determined by a least-square procedure detailed in Chapter 2, Section 2.2.

The UME potential  $E_T$  allowed the diffusion-controlled oxidation of the Fc to  $\text{Fc}^+$ . Different potentials were applied at the TiN layer in order to monitor changes in surface kinetics through variation of the overpotential ( $E_S - E^\circ$ ). The overpotential serves to provide the activation energy required to drive the heterogeneous process at the rate reflected by the effective heterogeneous first order rate constant. The choice of the potentials applied to the substrate at which the oxidized mediator is reduced back was determined observing the CV of the mediator (Fig. (4.10)).

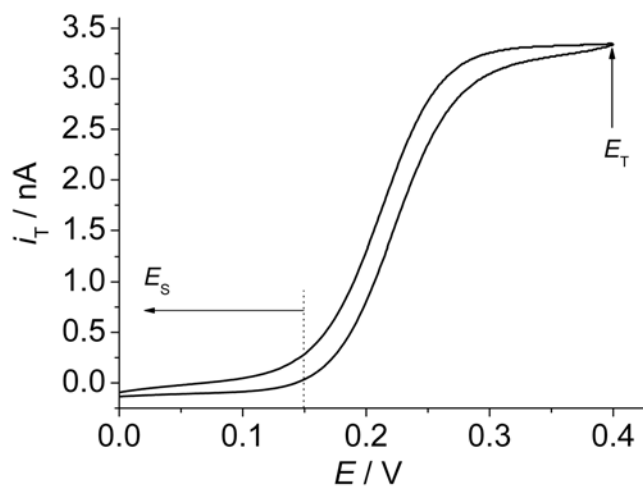


**Figure 4.10.** Potential applied to UME ( $E_T = 0.4$  V) and sample ( $E_S = 0.15, 0.1, 0.05, 0, -0.05, -0.1$  and  $-0.15$  V). UME potential: diffusion-controlled mass transfer. Sample potential negative to formal potential: fast recycling of the mediator.  $E^\circ = 0.224$  V. The CV was performed in 1 mM Fc in 0.1 M  $\text{Na}_2\text{SO}_4$  at an UME with  $r_T = 12.5$   $\mu\text{m}$  and  $RG \sim 10$ .  $\nu = 20$   $\text{mV s}^{-1}$ .

Fig. (4.11) shows the fitted experimental approach curves for native (a, b and c) and UV-ozone treated (d, e and f) TiN in different thicknesses in a solution containing 1 mM Fc. It shows already qualitatively clear differences in the rate constant with the applied sample potential and pretreatment. For calculation of  $k_{\text{eff}}$ ,  $D_{\text{O}} = D_{\text{R}}$  was assumed. The value  $D = 6 \times 10^{-6} \text{ cm}^2 \text{ s}^{-1}$  was obtained from chronoamperometric measurements of Fc. The  $i_{\text{T}}$  increased with increasing overpotential at the sample due to an enhanced rate of mediator regeneration. The thicker the TiN layer, the faster is the ET at the sample. The approach curves in other mediator concentrations yielded the same tendency but with higher current values. The conductivity and the electrochemical reactivity is highly influenced by the oxide film formed on the TiN after ozone treatment, hence the regeneration of Fc at the oxidized sample is slower although it is free of organic contamination. The oxide film grown by the ozone treatment increased the resistivity considerably and acted as a blocking film. However the rate of ET could still be controlled by applying potential to the sample.



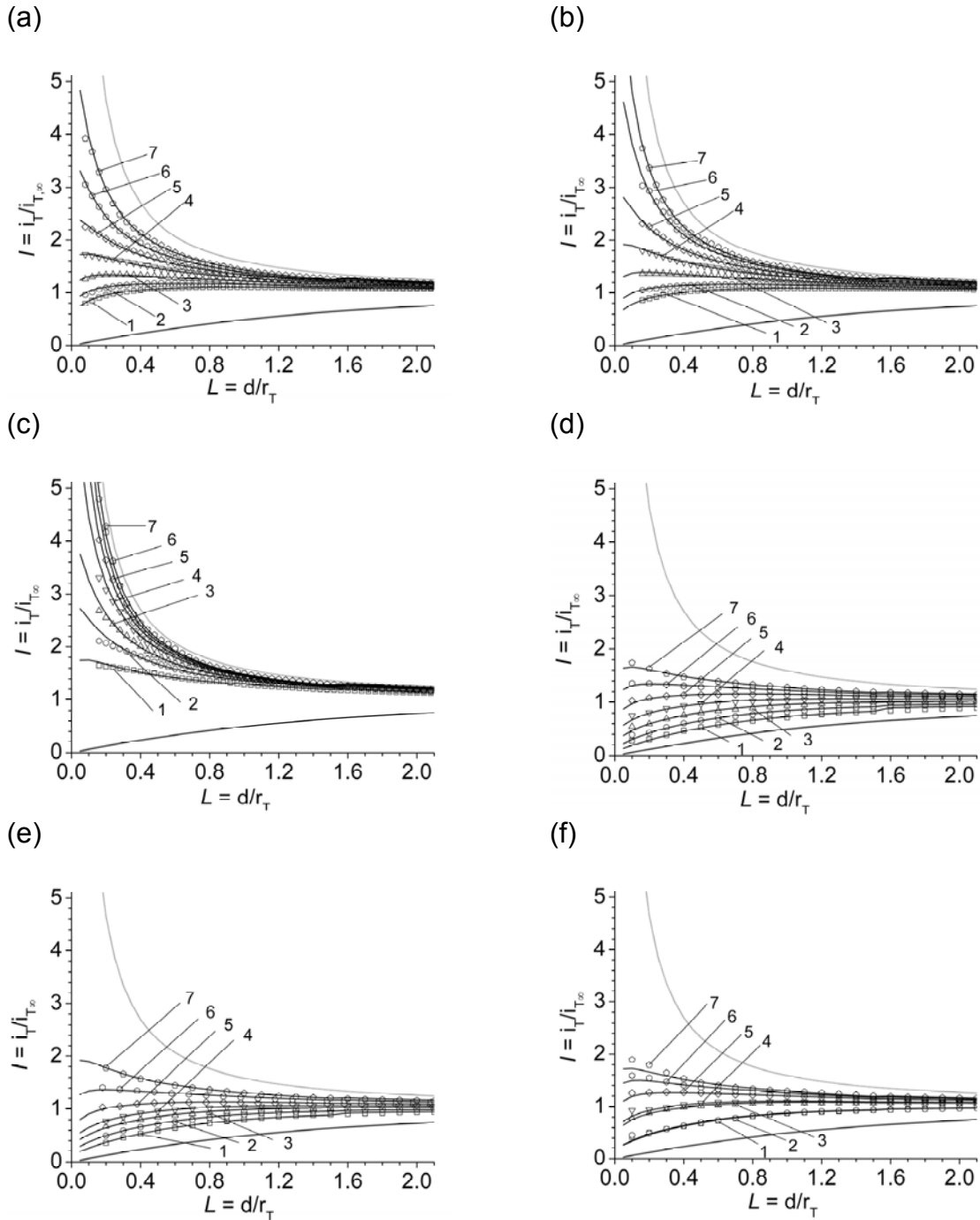


**Figure 4.11.** Normalized approach curves in 1mM Fc towards a (a) 20 nm, (b) 100 nm, and (c) 300 nm thick TiN layer before ozone treatment. Curves d, e and f show the approach curves to 20, 100, and 300 nm thick TiN samples, respectively, after ozone treatment. The experimental curves (open symbols) at different sample potentials  $E_S$  were fitted to the theory giving the corresponding  $\kappa$  values (lines). Thick lines (upper and lower lines) show the expected behavior for hindered diffusion ( $\kappa = 0$ ) and diffusion-controlled Fc recycling ( $\kappa = \infty$ ). The curves numbering stands for the applied sample potential  $E_S$ .  $E_S$  (1) = 150 mV,  $E_S$  (2) = 100 mV,  $E_S$  (3) = 50 mV,  $E_S$  (4) = 0 mV,  $E_S$  (5) = -50 mV,  $E_S$  (6) = -100 mV,  $E_S$  (7) = -150 mV. The corresponding calculated effective heterogeneous rate constants value are shown in Table (4.3).

A summary of the  $k_{\text{eff}}$  values derived from the various  $\kappa$  values (Eq. (2.19)) extracted from the fit of the approach curves to native and ozone-treated TiN performed in 1 mM Fc solution are shown in Table (4.3). The rate of  $\text{Fc}^+$  regeneration at the TiN surface depends upon the overpotential. At large negative overpotential in the native TiN, the  $k_{\text{eff}}$  increases and approaches the values of a pure conducting sample, however for the ozone-treated samples the  $k_{\text{eff}}$  becomes larger (at larger negative overpotentials) but does not approach such high values. This behavior follows the kinetics prediction described by the Butler-Volmer equation (Eq. (2.20)) where the perturbation applied to the system, i.e. overpotential, controls the rate of the ET reaction at the sample leading to higher effective rate constants.

**Table 4.3:** Effective heterogeneous rate constants of the  $\text{Fc}/\text{Fc}^+$  couple as a function of sample overpotential of different TiN layer thicknesses for native TiN and UV/ozone-treated TiN calculated from the curve fitting of approach curves in a 1 mM Fc mediator solution.

$(E_S - E^{\circ'}) / V$	$k_{\text{eff}} / 10^{-3} \text{ cm s}^{-1}$ (20 nm)		$k_{\text{eff}} / 10^{-3} \text{ cm s}^{-1}$ (100 nm)		$k_{\text{eff}} / 10^{-3} \text{ cm s}^{-1}$ (300 nm)	
	native TiN	UV/ozone-treated TiN	native TiN	UV/ozone-treated TiN	native TiN	UV/ozone-treated TiN
	-0.074	3.5	1.20	3.17	1.80	9.59
-0.124	4.56	2.28	4.36	3.00	16.80	2.76
-0.174	6.38	4.02	6.81	4.62	25.90	7.49
-0.224	9.40	6.47	10.80	6.23	48.00	8.39
-0.274	14.10	10.60	17.50	9.59	76.70	13.90
-0.324	21.80	15.90	34.90	16.40	125.00	19.10
-0.374	37.40	22.20	57.50	27.00	240.00	23.50

With knowledge of  $k_{\text{eff}}$  for every  $(E_S - E^{\circ'})$ , an apparent heterogeneous standard rate constant  $k^{\circ}$  can be extracted using the Butler-Volmer (Eq. (2.20)) for sufficiently high overpotentials. The plots of the logarithm of  $k_{\text{eff}}$  versus  $E_S - E^{\circ'}$  for three different Fc concentrations at the TiN samples are shown in Fig. (4.12). The mean value of the apparent standard rate constants obtained from the linear regression from the plots for TiN layers of 20 nm, 100 nm and 300 nm thickness before and after UV/ozone treatment are given in Table (4.4). The UV/ozone treatment turned out to be not beneficial for the redox kinetics although XPS had shown an effective removal of organic contamination. Most likely, the thin surface layer of  $\text{TiO}_2$  on the TiN samples was enlarged and decreased the electron transfer kinetics even more effectively than the organic contamination layer present after storage in air. There is a clear effect of the thickness of the TiN layers on the effective ET kinetics. This could be a

consequence of the increased surface area for thicker TiN layers. The SFM images of the TiN layers showed that the roughness increases with the thickness of TiN layer, thus the actual surface area is enhanced. This result agrees with a recent publication,<sup>[228]</sup> in which an increased ET rate was observed for TiN in comparison to Au and Si due to enhanced roughness.

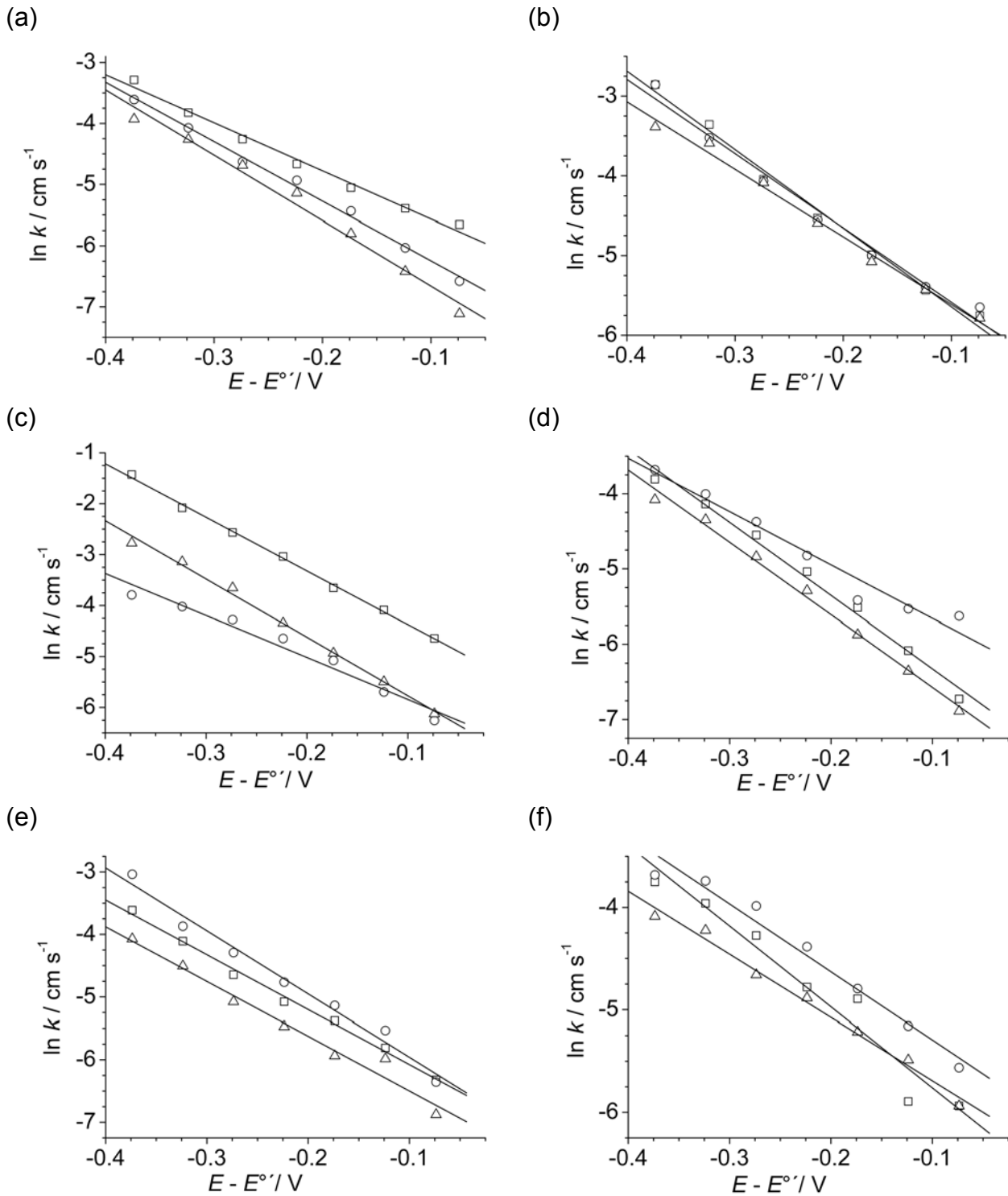


**Figure 4.12.** Plot of the effective rate constants obtained from approach curves towards (a) 20 nm, (b) 100 nm, and (c) 300 nm thick TiN layer before ozone treatment and (d) 20 nm, (e) 100 nm, and (f) 300 nm thick TiN sample after ozone treatment. ( $\square$ ) 1.0 mM, ( $\circ$ ) 2.0 mM and ( $\triangle$ ) 3.0 mM Fc solutions.

**Table 4.4:** Apparent standard rate constants of the Fc/Fc<sup>+</sup> couple as a function of the TiN layer thickness for native TiN and UV/ozone-treated TiN.

TiN thickness / nm	$k^{\circ} / (10^{-3} \text{ cm s}^{-1})^*$	
	native TiN	UV/ozone-treated TiN
20	(0.97 ± 0.68)	(0.97 ± 0.65)
100	(1.45 ± 0.12)	(0.84 ± 0.18)
300	(2.22 ± 1.89)	(1.95 ± 0.59)

\* averaged from three different Fc concentrations.

Comparing the  $k^{\circ}$  values of the native TiN, the  $k^{\circ}$  of the 20 nm thick film determined by the SECM approach curves is more than two orders of magnitude larger than the  $k^{\circ}$  value determined from the peak separations of the cyclic voltammogram. For the 100 nm thick TiN the difference falls to one order of magnitude, while for the 300 nm thick TiN the difference is negligible. The cyclic voltammetric values are probably low because the ohmic drop contributed to the measured peak potentials. The  $k^{\circ}$  values obtained by the CV and by the SECM approach curves indicate that the thickness of the TiN layer influences the rate of heterogeneous electron transfer being faster at thicker layers and slower at thinner layers.

#### 4.1.5 Conclusions

Thin films of TiN were tested for their direct use as electrodes in electroanalytical measurements, i.e. without previous coating by another metal. These electrodes offer advantages by their mechanical hardness and relative inertness to organic contaminations during prolonged storage. This can be in particular interesting for microstructured devices. It can be produced in well-adhering thin layers by an established technology that opens possibilities for mass-producing nanometer-sized electrodes.

The potential range in aqueous solutions is large enough for many compounds used for instance in electrochemical detections of immunoassays. The ET kinetics of redox couples that are considered reversible at conventional noble metal electrodes are clearly slower at TiN, however, still in a useful range if some overpotential can be applied without causing interference problems. This situation might be encountered in read-out procedures for electrochemical immunoassays or DNA assays. The double layer capacity is higher than at gold electrodes. It can to some extent be tuned by controlling the crystal morphology of the TiN films and the film thickness. Nevertheless, the charging currents suggest that TiN electrodes may be better applied in amperometric (at constant potential) than in voltammetric detection schemes. A passive layer of TiO<sub>2</sub> and oxidic oxygen component have been

spontaneously grown on the TiN as seen in the XP spectra. The UV/ozone treatment removed partially the carbon contamination of the sample without significant increase of the passive layer components.

The heterogeneous ET kinetics analysis was studied by recording SECM approach curves without contribution of ohmic potential drop in solution and double layer charging current because the rate of ET is measured by the UME and not directly by the polarized TiN sample as in cyclic voltammetry. It was shown that the local electrochemical reactivity depends on the thickness of the TiN and passive layer. A similar tendency was observed on the biomedical implant material Ti6Al4V, in which showed that the local electrochemical reactivity depends on the relative position of the band edges of the passive layer and  $E^\circ$  of the mediator.<sup>[A8]</sup>

## 4.2 Electrochemical investigation of the influence of thin SiO<sub>x</sub> films deposited on gold on charge transfer characteristics

The electrochemical behavior of a thin gold film electrode coated with silicon dioxide (SiO<sub>x</sub>) layers of increasing thickness will be discussed in this Section.<sup>[A1]</sup> Stable thin films of amorphous silica (SiO<sub>x</sub>) were deposited on glass slides coated with a 5 nm adhesion layer of titanium and 50 nm of gold, using a plasma-enhanced chemical vapor deposition (PECVD) technique by Prof. Dr. S. Szunerits from Laboratoire d'Electrochimie et de Physicochimie des Matériaux et des Interfaces (LEPMI).

SECM and electrochemical impedance spectroscopy (EIS, measured and analyzed by Prof. Dr. S. Szunerits) were used to investigate the electrochemical behavior of the interfaces. In the case of SECM, the influence of the SiO<sub>x</sub> thicknesses on the electron transfer kinetics of three redox mediators was investigated. Normalized current-distance curves (approach curves) were fitted to the theoretical model in order to find the effective heterogeneous first order rate constant at the sample. EIS was in addition used to confirm the diffusion barrier character of the SiO<sub>x</sub> interlayer.

### 4.2.1 Introduction

Self-assembled monolayers and Langmuir-Blodgett films deposited on metals and semiconductors have been extensively used and studied due to their fundamental importance in fine-tuning the bulk material properties. They enable to cause drastic and controlled changes in biophysics and to wetting, adhesion, corrosion and electron transfer properties and have many applications in several areas of science and technology. Next to these organic materials, silica-based materials have attracted considerable attention as effective barrier layers as well as for chemical and biological sensing due to the high reactivity of their surface silanol groups, enabling the immobilization of different molecules through silane coupling chemistry.<sup>[229-234]</sup> In this study, controlled SiO<sub>2</sub> thin films on Si are produced through plasma-enhanced chemical vapor deposition (PECVD) (Appendix Section 8.1.2). SiO<sub>2</sub> is an important insulating material in the fabrication of semiconductor devices,<sup>[235]</sup> and is used as an intermetallic dielectric material and as a transistor gate dielectric layer.<sup>[236]</sup> The formation of silica films on gold could be achieved by thermal evaporation of silicon dioxide in the presence of oxygen at low pressure,<sup>[237]</sup> using a multitarget magnetron sputtering system,<sup>[238]</sup>

or low temperature sol-gel chemistry.<sup>[230, 231, 234, 237, 239-242]</sup> Due to the instability of the SiO<sub>2</sub>/Au interfaces upon immersion in water,<sup>[237]</sup> an adhesion layer of 2 nm titanium between gold and the silicon dioxide film was added.<sup>[243-246]</sup> Recently, it was shown that thin layers of SiO<sub>x</sub> deposited on gold films (with no intervening adhesion layer) by PECVD are chemically and mechanically stable under various conditions.<sup>[247]</sup> In addition these interfaces were adaptable for surface plasmon resonance (SPR) detection. While SPR signals could be detected for SiO<sub>2</sub> thicknesses ranging from 7 - 40 nm, the use of these interfaces for electrochemical detection schemes depends strongly on the thickness of the oxide film. CV could be performed only on films thinner than 9 nm. EIS has shown to be highly useful to understand the packing density and distribution of pinhole defects in monolayers. The technique shows that the dynamics of charge transfer at the electrochemical interface is strongly influenced by the nature of the electrode surface and the structure of the electrical double layer. In addition, SECM is powerful technique for investigation of mass transport as it combines high-resolution visualization of surface topography with interfacial chemical and electrochemical reactivity information.<sup>[248]</sup> It is thus adapted to investigate the molecular transport of different electrochemical mediators through the nanostructured or porous layers.<sup>[249, 250]</sup> The kinetics of the heterogeneous ET of semiconductors have been studied using SECM approach curves in the feedback mode<sup>[32]</sup> and showed that the ET rate can be controlled by applying different overpotentials ( $E_S - E^\circ$ ) to the sample (Section 4.2.4). Pust et al.<sup>[32]</sup> and Neufeld et al.<sup>[251]</sup> showed that the ET kinetics at the semiconductor/liquid interfaces may change strongly depending on the redox potential of the mediator with respect to the energetic position of the bandgap of the semiconductor. An advantage in using SECM to analyze the kinetics of ET at the sample is that contributions due to ohmic potential drop in solution and double layer charging currents are negligible.

A detailed investigation on the effect of silicon oxide layer thickness deposited on gold on the ET using EIS is described in Section 4.2.5. In fact most EIS studies have been performed on a Si/SiO<sub>2</sub> interface where space charge layer of the semiconductor will influence the electrochemical response. Here only the Helmholtz double layer capacitance on the gold interface is taken into account. It is shown that by performing EIS measurements at high frequencies information about the insulating SiO<sub>2</sub> layer can be obtained. Furthermore the feedback mode of SECM was used to record the approach curves to SiO<sub>x</sub> layers of different thicknesses to extract the corresponding  $k_{\text{eff}}$  values.



## 4.2.2 Deposition of SiO<sub>x</sub> thin films on gold

Silica films of three different thicknesses between 7 nm and 40 nm were deposited on gold thin films using the PECVD technique. The process is based on the chemical decomposition of a gas mixture of SiH<sub>4</sub> and N<sub>2</sub>O in a plasma reaction at 300 °C.<sup>[247, 252, 253]</sup> The thickness of the silica layer on gold was evaluated using ellipsometry and  $6.6 \pm 0.5$  nm,  $19.5 \pm 0.5$  nm and  $40.2 \pm 0.5$  nm were obtained. These results were corroborated using SPR in the scanning mode where the variation of the reflected light as a function of the angle of incidence of the light beam is monitored. The critical angle under which the light beam hits the interface and thus the angle of resonance  $\Theta$  are characteristic to the system under study. Any change in the refractive index or the thickness of the dielectric medium will cause the resonance angle to shift. Fig. (4.13) shows the shift in the resonance angle after SiO<sub>x</sub> films of three different thicknesses have been deposited *ex situ* on the gold-covered glass slide.

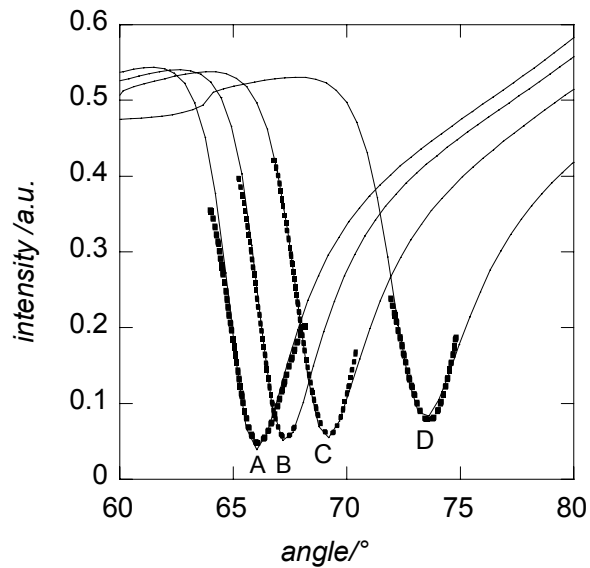


**Figure 4.13.** Reflected light intensity versus incident angle curves for different thicknesses of deposited SiO<sub>x</sub> on 50 nm thick gold layers on glass with an adhering layer of 5 nm titanium. Dashed lines are experimental results; full lines are fitted curves: (A) 0 nm, (B) 7.5 nm, (C) 20.00 nm, (D) 44.20 nm: fitting parameters:  $n_{(\text{prism})} = 1.58$ ,  $n_{(\text{gold})} = 0.197 + i 3.442$  with  $d = 53$  nm,  $n_{(\text{titanium})} = 2.36 + i 3.112$  with  $d = 5$  nm,  $n_{(\text{SiO}_2)} = 1.48$  (fitting program: Winspall 2.01). Where  $i$  is the intensity.

While the critical angle is not shifting during the experiment as water was used as the solvent in all experiments, the angle where the surface plasmon minimum occurs is shifted to higher angles with increasing SiO<sub>x</sub> thickness. The determination of the SiO<sub>x</sub> layer thickness was achieved by fitting the SPR curves to theoretical working curves and the corresponding

thicknesses were determined using the following parameters:  $n_{(\text{prism})} = 1.58$ ,  $n_{(\text{gold})} = 0.197 + i3.442$  with  $d = 53$  nm,  $n_{(\text{titanium})} = 2.36 + i3.112$  with  $d = 5$  nm,  $n_{(\text{SiO}_2)} = 1.48$ . The obtained thicknesses of  $\text{SiO}_2$  are in good agreement with the expected values according to the experimental conditions and are comparable to those obtained from ellipsometric measurements. Gold-silicon dioxide interfaces with a  $\text{SiO}_x$  thickness higher than 60 nm did not show any SPR minimum on the glass prism ( $n = 1.58$ ).

### 4.2.3 Characterization of the gold/ $\text{SiO}_x$ films

**Scanning force microscopy:** The morphology of the gold interface before and after silica coating was investigated using SFM. Fig. (4.14a) displays the tapping mode SFM of a cleaned gold surface. The gold substrate displays a RMS surface roughness of 0.546 nm on an area of  $1 \mu\text{m}^2$ . Chemical deposition of silica films on the surface did not induce any topographical changes to the surface. SFM images of the surfaces covered with 6 - 40 nm thick  $\text{SiO}_x$  films (Fig. (4.14b-d)) exhibit similar features with increasing surface roughness (6.6 nm, RMS = 0.956 nm; 19.5 nm, RMS = 1.155 nm; 40.2 nm, RMS = 1.68 nm; area of  $1 \mu\text{m}^2$ ). With the limit of the SFM resolution, no defects or pinholes were observed. After leaving the interfaces in water for 2 h, there was no evidence for morphology changes in the SFM images. This is characteristic of a free-pinhole surface.

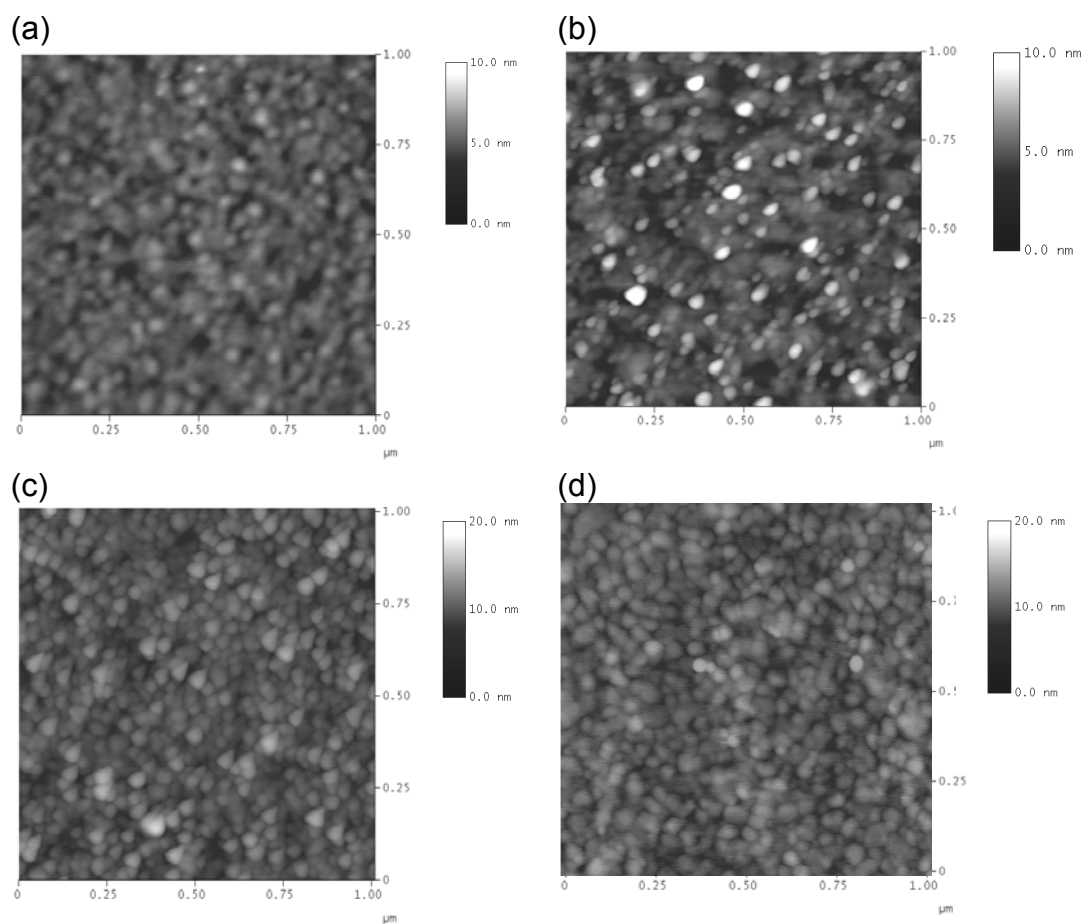


**Figure 4.14.** Tapping mode<sup>TM</sup> SFM images of a Au surface before (a) and after coating with (b) 7.1 nm, (c) 19.5 nm, (d) 40.2 nm thick SiO<sub>x</sub> layers.

**Cyclic voltammetry measurements:** CV of an electroactive redox couple is a valuable tool for testing the kinetic barrier properties of surface-modified electrodes. Fig. (4.15) compares the voltammetric responses obtained prior to the SiO<sub>x</sub> film deposition and after PECVD deposition of SiO<sub>x</sub> layers with different thicknesses. Fe(CN)<sub>6</sub><sup>4-</sup> is oxidized as expected on the bare gold thin film electrode in a one-electron process. A higher peak separation ( $\Delta E_p = 130$  mV) compared to a massive gold electrode ( $\Delta E_p = 60$  mV) is observed, due to higher resistivity of the thin gold film. For the SiO<sub>x</sub> films with a thickness of 19.5 and 40.2 nm the behavior is characteristic for highly efficient barriers for the redox probe. The capacitive currents as well as the redox currents detected are largely suppressed. This blocking effect was maintained during storage of the interface for more than 4 h in an aqueous redox mediator solution, in agreement with the existence of a highly dense oxide film, preventing the degradation of the hydrophilic SiO<sub>x</sub> thin layer with time. The capacitive current of SiO<sub>x</sub> is less intense than that recorded on bare electrodes. This behavior is characteristic for barriers with a high concentration of defect sites. The shape of the *i*-*E* signal

remained sigmoidal suggesting that the interface can be considered as an assembly of ultramicroelectrodes.

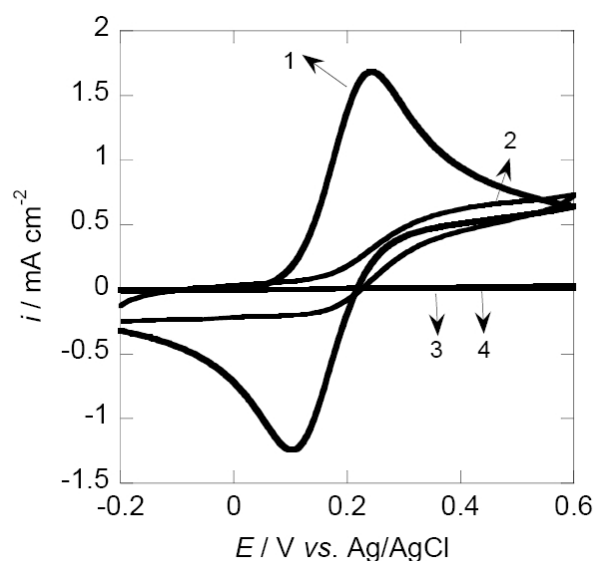


**Figure 4.15.** CV curves for a 50 nm thick polycrystalline gold film on glass with a 5 nm titanium adhesion layer (1) and the same electrode covered with 6.9 nm SiO<sub>x</sub> (2), 19.5 nm SiO<sub>x</sub> (3), 40.2 nm SiO<sub>x</sub> (4). Redox solution: 10 mM Fe(CN)<sub>6</sub><sup>4-</sup> in 0.1 M KCl,  $\nu = 0.05 \text{ V s}^{-1}$ . Curves 3 and 4 overlap.

#### 4.2.4 SECM investigation of SiO<sub>x</sub>

A series of SECM approach curves was recorded with three different redox mediators: K<sub>3</sub>[IrCl<sub>6</sub>], Fc and [Ru(NH<sub>3</sub>)<sub>6</sub>]Cl<sub>3</sub>. The redox mediator concentrations were 1 mM and were diluted in aqueous 0.1 M KCl being the supporting electrolyte. Prior to the SECM experiment, all SiO<sub>x</sub> samples were rinsed with ethanol, deionized water and dried under a stream of Ar. The potentials applied to the UME and SiO<sub>x</sub> thin film were determined by CV of the redox mediator on the UME and are given in Table (4.5):

**Table 4.5:** Redox mediators used for approach curves with their respective diffusion coefficients, formal potentials and UME and sample potentials applied during approach curves.

Redox mediator	$D / 10^{-5} \text{ cm}^2 \text{ s}^{-1}$ [32]	$E^\circ / \text{V}$ [32]	$E_T / \text{V}^*$	$E_S / \text{V}^*$
[IrCl <sub>6</sub> ] <sup>3-/2-</sup>	$1.0 \pm 0.2$	$+0.724 \pm 0.001$	0.9	OCP, 0.6, 0.5, 0.4
Fc/Fc <sup>+</sup>	$0.6 \pm 0.1$	$+0.228 \pm 0.004$	0.4	OCP, 0.1, 0, -0.1
[Ru(NH <sub>3</sub> ) <sub>6</sub> ] <sup>3+/2+</sup>	$0.74 \pm 0.08$	$-0.150 \pm 0.001$	-0.4	OCP, -0.1, 0, 0.1

\* Potential refers to Ag/AgCl/3 M KCl

The experimental approach curves were fitted to a new expression derived for approach curves (Eq. (2.11)) towards samples with finite kinetics as described in detail in Section 4.1.4.

Fig. (4.16a) shows the normalized approach curves on gold/SiO<sub>x</sub> (6.9 nm) interface using three different redox mediators while the interface was not biased (OCP). The calculated  $k_{\text{eff}}$  for the three mediators gave a negative feedback,  $3.8 \times 10^{-4} \text{ cm s}^{-1}$ ,  $3.0 \times 10^{-4} \text{ cm s}^{-1}$ ,  $6.2 \times 10^{-4} \text{ cm s}^{-1}$  for  $[\text{IrCl}_6]^{3-}$ ,  $[\text{Ru}(\text{NH}_3)_6]^{3+}$ , and Fc, respectively. The positively and negatively charged mediators showed lower rates of regeneration than the neutral mediator. However, as the thickness of the SiO<sub>x</sub> increases, this difference becomes negligible (Fig. (4.16b)). A dependence of  $k_{\text{eff}}$  on the thickness of SiO<sub>x</sub> is shown in Fig. (4.16b) (sample at OCP). The rate of ET decreases with the increase of SiO<sub>x</sub> thickness. For the thinnest layer (6.9 nm) clear differences between the used mediators were recorded.

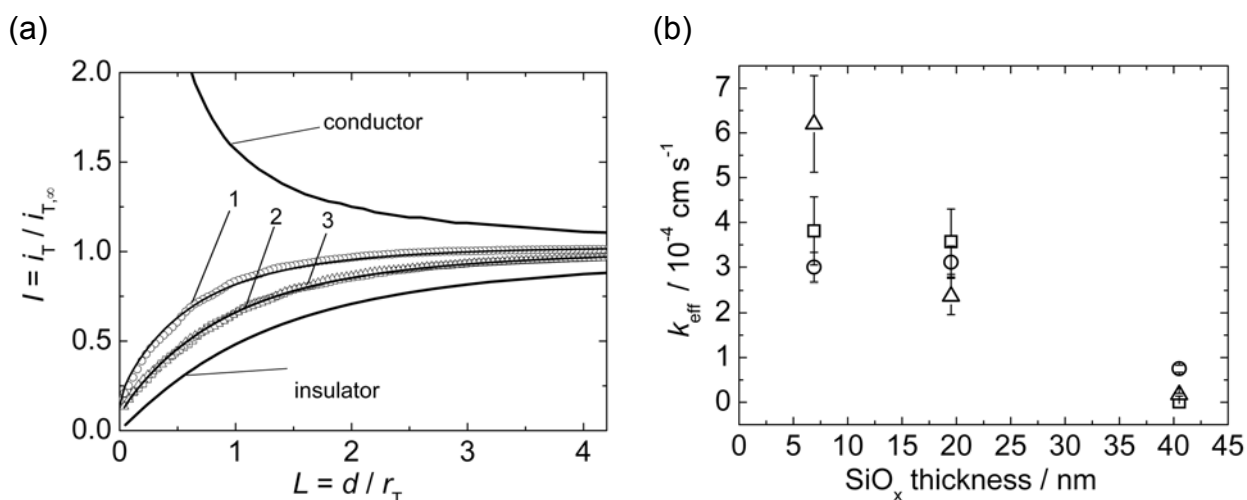


**Figure 4.16.** (a) Normalized approach curves towards 6.9 nm SiO<sub>x</sub> deposited on gold using different redox mediators: (1) Fc/Fc<sup>+</sup>, (2)  $[\text{Ru}(\text{NH}_3)_6]^{3+/2+}$ , (3)  $[\text{IrCl}_6]^{3-/2-}$ . The applied UME potential was  $E_T = 0.4$ ,  $-0.4$  and  $0.9$  V, respectively, and the sample was left at OCP. The corresponding  $\kappa$  value extracted from the curve fitting were: (1) 0.136, (2) 0.050 and (3) 0.049. The open symbols correspond to experimental curves and the lines to theoretical fittings from Ref. [115]. The thick lines represent the theoretical approach curves for an UME over a conductive and an insulating substrate from Ref. [115]. (b) Dependence of  $k_{\text{eff}}$  on SiO<sub>x</sub> layer thickness. ( $\square$ )  $[\text{IrCl}_6]^{3-}$ , ( $\circ$ )  $[\text{Ru}(\text{NH}_3)_6]^{3+}$ , ( $\triangle$ ) Fc.  $E_S = \text{OCP}$ .

Furthermore, the influence of the overpotential applied to the substrate on the rate of the heterogeneous ET was investigated. Negative feedback was observed in all three cases. The applied potentials to the substrate were not sufficiently negative (in the case of Fc and  $[\text{IrCl}_6]^{3-}$ ) or positive ( $[\text{Ru}(\text{NH}_3)_6]^{3+}$ ) to influence the SiO<sub>x</sub> electronic structure, thus the  $k_{\text{eff}}$  values extracted from the curve fittings were rather constant. Table (4.6) is summarizing the obtained  $k_{\text{eff}}$  using the different mediators with different applied potentials and interfaces. The 6.9 nm SiO<sub>x</sub> interface showed a slightly faster rate of ET than 19.5 and 40.2 nm indicating that it has more defect sites, and thus the mediator could diffuse through these sites and be regenerated at the underlying gold substrate. Among the interfaces, 40.2 nm SiO<sub>x</sub> showed the

best insulating features providing  $k_{\text{eff}}$  values close to that of insulating layers, even when an overpotential was applied. Fig. (4.17) shows the normalized approaches curves for 6.9, 19.5 and 40.2 nm thick  $\text{SiO}_x$  films at OCP using  $[\text{IrCl}_6]^{3-}$  as redox mediator. The gold/ $\text{SiO}_x$  (40.2 nm) interface approach curve is overlapping the limiting case of a totally inert and insulating surface with  $k_{\text{eff}} = 1 \times 10^{-6} \text{ cm s}^{-1}$ , while the other interfaces showed higher  $k_{\text{eff}}$ . The same behavior was observed using the other mediators.

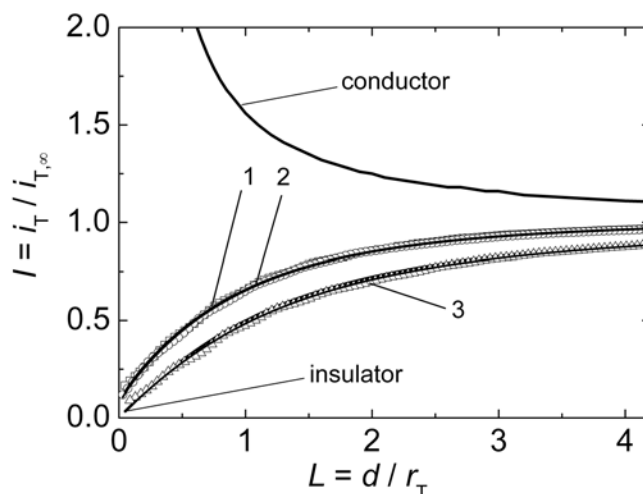


**Figure 4.17.** Normalized approach curves for  $[\text{IrCl}_6]^{3-/2-}$  towards  $\text{SiO}_x$  in different thicknesses: (1) 6.9 nm, (2) 19.5 nm, and (3) 40.2 nm.  $E_T = 0.9 \text{ V}$  and sample at OCP. The corresponding  $\kappa$  value extracted from the curve fitting were: (1) 0.0486, (2) 0.0446 and (3) 0.0001. The open symbols correspond to experimental curves and the lines correspond to theoretical fittings. The thick lines represent the theoretical approach curves for an UME over a conductive and an insulating substrate from Ref. <sup>[88]</sup>

**Table 4.6:** Calculated  $k_{\text{eff}}$  from SECM approach curves on 6.9, 19.5 and 40.5 nm SiO<sub>x</sub> layers for [IrCl<sub>6</sub>]<sup>3-</sup>, [Ru(NH<sub>3</sub>)<sub>6</sub>]<sup>3+</sup>, and Fc redox mediators.

$E_T / \text{V}$	$E_s / \text{V}$	$k_{\text{eff}} / 10^{-4} \text{ cm s}^{-1}$		
		6.9 nm	19.5 nm	40.5 nm
<b>[IrCl<sub>6</sub>]<sup>3-</sup></b>				
0.9	OCP	$3.8 \pm 0.76$	$3.57 \pm 0.73$	$0.01 \pm 0$
	0.6	$3.42 \pm 0.68$	$3.26 \pm 0.67$	$0.01 \pm 0$
	0.5	$4.22 \pm 0.84$	$2.38 \pm 0.49$	$0.01 \pm 0$
	0.4	$5.11 \pm 1.02$	$3.00 \pm 0.61$	$0.01 \pm 0$
<b>[Ru(NH<sub>3</sub>)<sub>6</sub>]<sup>3+</sup></b>				
-0.4	OCP	$3.00 \pm 0.33$	$3.11 \pm 0.36$	$0.75 \pm 0.08$
	-0.1	$3.37 \pm 0.37$	$1.43 \pm 0.17$	$0.85 \pm 0.09$
	0	$3.51 \pm 0.38$	$2.55 \pm 2.93$	$0.73 \pm 0.08$
	0.1	$3.85 \pm 0.42$	$2.55 \pm 0.29$	$0.73 \pm 0.08$
<b>Fc</b>				
0.4	OCP	$6.20 \pm 1.08$	$2.37 \pm 0.41$	$0.17 \pm 0.03$
	0.1	$6.94 \pm 1.21$	$2.64 \pm 0.29$	$0.01 \pm 0$
	0	$6.59 \pm 1.14$	$2.77 \pm 0.67$	$0 \pm 0$
	-0.1	$6.72 \pm 1.17$	$2.66 \pm 0.64$	$0.08 \pm 0.01$

#### 4.2.5 Electrochemical impedance analysis

EIS analysis was performed on the gold/SiO<sub>x</sub> interfaces in aqueous solutions containing different concentrations of KCl as supporting electrolyte. Fig. (4.18) shows the evolution of the impedance behavior of the interfaces with increasing SiO<sub>x</sub> thickness (Fig. (4.18a)) and at different electrolyte concentrations keeping the thickness of SiO<sub>x</sub> constant (Fig. (4.18b)).

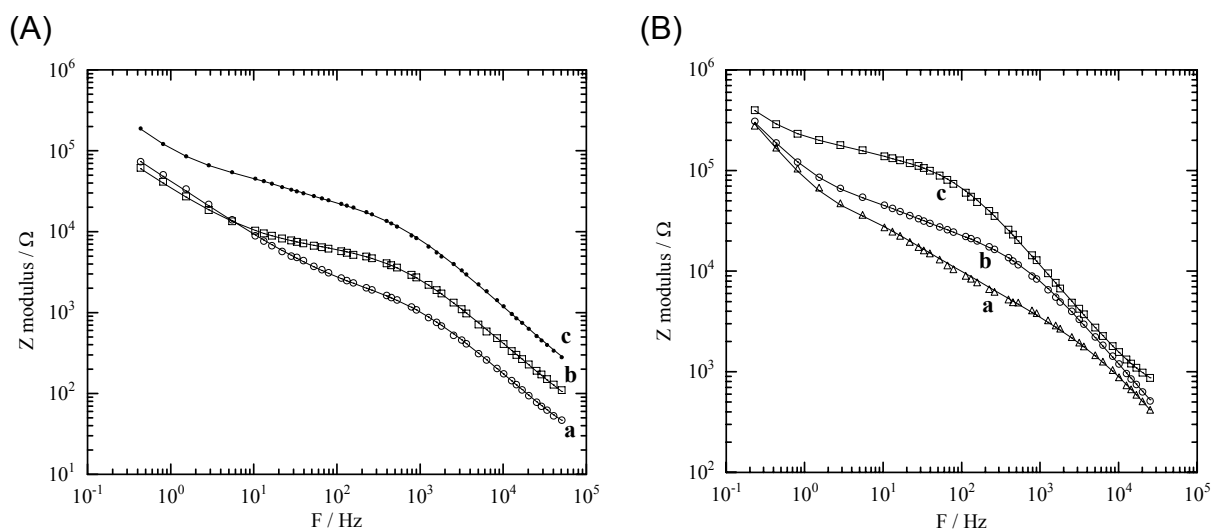


**Figure 4.18.** Bode plot for (A) gold/SiO<sub>x</sub> interfaces: (a) 6.9 nm, (b) 19.5 nm, (c) 40.5 nm in 0.1 M KCl and (B) on gold/SiO<sub>x</sub> (40.5 nm) in aqueous (a) 1 M KCl, (b) 0.1 M KCl and (c) 0.01 M KCl; experimental data (symbols), fitted data (solid line), the measured frequency range is 100 kHz - 1 Hz with a 10 mV RMS signal applied under open circuit conditions

An equivalent circuit was designed in order to fit the impedance spectra obtained (Fig (4.19)). For the high frequency domain, the circuit includes the ohmic resistance of the electrolyte solution; for intermediary and low frequency domains, a resistance  $R_{\text{int}}$  in series with a finite length Warburg impedance and in parallel with interface capacitance  $C_{\text{int}}$  were used. The resistance  $R_{\text{int}}$  was globally attributed to the Au/SiO<sub>x</sub> interface, the SiO<sub>x</sub> layer and the SiO<sub>x</sub>/electrolyte interface. In a first approximation, the capacity  $C_{\text{int}}$  was also attributed to these three parts of the interface. The lines in Fig. (4.18) correspond to the fit using the equivalent circuit model.

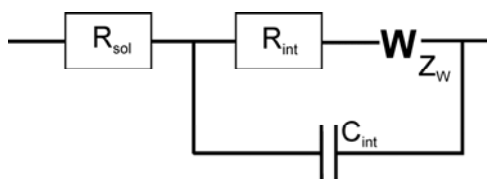


**Figure 4.19.** Scheme of used equivalent circuit.

Table (4.7) shows values of the circuit elements obtained by fitting of the experimental data. The capacitance  $C_{\text{int}}$  obtained is in the order of  $10^8$  F, which is too low to be attributed to a solid/solution interface. Moreover, it was observed that  $C_{\text{int}}$  is independent of the electrolyte concentration. It can be thus concluded that  $C_{\text{int}}$  is principally governed by the thickness of the layer of SiO<sub>x</sub>. Similar results have been shown for SiO<sub>2</sub> layers on silicon.<sup>[254, 255]</sup> In addition,



the thickness of thin oxide layers has been determined by impedance spectroscopy with the calculation of capacitance.<sup>[256]</sup>

**Table 4.7:** Values of equivalent circuit elements obtained by fitting the experimental data for gold/SiO<sub>x</sub> interfaces 6.9 nm, 19.5 nm, 40.5 nm in 0.1 M KCl.

interface	$R_{\text{int}} / \Omega$	$C_{\text{int}} / 10^{-8}\text{F}$	$F_{\text{int}} / \text{Hz}$	$n_{\text{int}}$	$W-R / \Omega$	$W-T / \text{s}$	$W-P$
6.9 nm	$775 \pm 24$	$9.8 \pm 0.3$	2106	0.943	$3130 \pm 90$	0.003	0.34
19.5 nm	$4070 \pm 130$	$4.9 \pm 0.2$	804	0.903	$6950 \pm 200$	0.018	0.35
40.5 nm	$14200 \pm 400$	$1.6 \pm 0.1$	685	0.923	$101000 \pm 3000$	0.197	0.41

The resistance  $R_{\text{int}}$  changes with the SiO<sub>x</sub> thickness and with the electrolyte concentration. This resistance is thus indeed the sum of three resistors in series related to the Au/SiO<sub>x</sub> interface, the SiO<sub>x</sub> layer and the SiO<sub>x</sub>/electrolyte interface. The parameters related to the Warburg impedance are given in the last three columns in Table (4.7). The resistance  $W-R$  associated with the particle diffusion is large when the SiO<sub>x</sub> layer is thick or when the electrolyte concentration is low. The time constant  $W-T$  is also related to the thickness of SiO<sub>x</sub>. However, it is independent of the concentration of the solution (Table (4.8)). As  $W-T = \delta^2/D$  with  $\delta$  being the diffusion layer thickness and  $D$  the diffusion coefficient, this suggests that the diffusion layer thickness is related to the thickness of the SiO<sub>x</sub> layer. The SiO<sub>x</sub> layer acts as a diffusion barrier. These results confirm those obtained by cyclic voltammetry and SECM.

**Table 4.8:** Values of equivalent circuit elements obtained by fitting the experimental data for gold/SiO<sub>x</sub> (40.5 nm) in aqueous 1 M KCl, 0.1 M KCl and 0.01 M KCl.

solution	$R_{\text{int}} / \Omega$	$C_{\text{int}} / 10^{-8}\text{F}$	$F_{\text{int}} / \text{Hz}$	$n_{\text{int}}$	$W-R / \Omega$	$W-T / \text{s}$	$W-P$
1 M KCl	$1360 \pm 40$	$1.5 \pm 0.1$	8048	0.974	$88500 \pm 2700$	0.193	0.46
0.1 M KCl	$14200 \pm 400$	$1.6 \pm 0.1$	685	0.923	$101000 \pm 3000$	0.197	0.41
0.01 M KCl	$98000 \pm 3000$	$1.7 \pm 0.1$	98	0.917	$154000 \pm 4600$	0.245	0.37

## 4.2.6 Conclusions

The electrochemical behavior of thin gold film electrodes coated with silicon dioxide layers of different thicknesses was investigated using CV, SECM and EIS. SECM images showed no resolvable pinholes in agreement with the absence of detectable pinholes using SFM. However, SECM approach curves allowed determining the presence of very small pinholes by recording changes in the heterogeneous rate constant of different redox mediators

to the gold/SiO<sub>x</sub> interfaces. The 6.6 nm thick SiO<sub>x</sub> interface showed slightly faster electron transfer (due to the presence of pinholes), while an insulating behavior was observed on the 40.2 nm SiO<sub>x</sub> interface (pinhole-free surface). EIS and cyclic voltammetry measurements confirmed the barrier effect of the SiO<sub>x</sub> layer. It was in particular observed that the interface capacitance is governed by the thickness of the oxide layer.

# 5 Study of diffusion and reaction in microbead agglomerates

## 5.1 Introduction

Immobilization of enzymes has been studied since the second half of the last century.<sup>[2, 257, 258]</sup> Since then much effort has been put to study the activity of immobilized enzymes for a wide range of applications such as immunoassays,<sup>[259-261]</sup> biosensing<sup>[262, 263]</sup> and chemical separation.<sup>[264-266]</sup> The advantage in immobilizing enzymes for biosensing applications are fast response time, improved selectivity and sensitivity, and the possibility to prepare a stable and reusable system which is economically interesting.<sup>[267]</sup>

The effect of enzyme stability upon immobilization has been widely studied and it was found that the stability of the enzyme may be enhanced when the immobilization processes occur unstrained.<sup>[268]</sup> The reasons for the increased stability are: conformational changes within the enzyme are prevented by the immobilization procedure, prevention of interaction between enzyme molecules, and protection against microbiological and proteolytic attack. A maximum stabilization is achieved when the enzyme and the support are complimentary forming many unstrained interactions such as covalent and non-covalent interactions. Nevertheless, immobilization alters the kinetic constants of the enzymes (e.g.  $K_M$ ,  $v_{max}$ ) due to internal structural changes and restricted access to the active site. The intrinsic parameters<sup>1</sup> of the soluble enzyme are different from those of the immobilized enzymes, which in turn differs from the apparent parameters of the immobilized enzyme due to mass transport limitation, mainly by diffusion, and partitioning.

For a general treatment,<sup>[269-274]</sup> one may consider an enzyme E that follows Michaelis-Menten kinetics. This enzyme is immobilized on and inside a macroporous support. The support may allow partitioning of the enzyme substrate S between the aqueous phase and the support material. If S is converted in an enzyme-catalyzed reaction, it will be resupplied by diffusion. For the treatment, it is useful to distinguish between external and internal diffusion. External diffusion is the diffusion outside the porous support and internal diffusion is the diffusion of S in the pore volume of the macroporous support. Fig. (5.1) shows a sketch of the external and internal diffusion to and within a macroporous support.

---

<sup>1</sup> The intrinsic parameters are those observed in absence of mass transfer limitation. Apparent parameters are observed in the presence of mass transfer limitations.

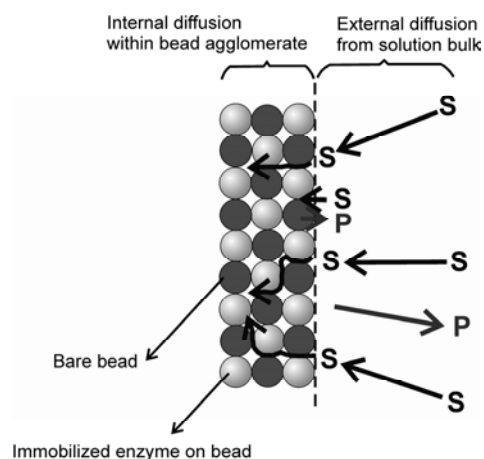


**Figure 5.1.** Sketch of the external and internal substrate (S) diffusion toward and inside a macroporous support containing immobilized enzyme.

Under these conditions the conversion of the enzymatic reaction depends on the properties of the enzyme, substrate, and support. There are several factors that affect the kinetics of immobilized enzymes:

- internal and external diffusional limitations,
- substrate partitioning between support and solution bulk,
- presence of competitive and noncompetitive inhibition,
- reversible reactions catalyzed by the immobilized enzyme,
- release or consumption of  $H^+$  by the immobilized enzyme,
- steric, spatial, and conformational effects, and
- microenvironmental interactions of the support with the enzyme and substrate.<sup>[268]</sup>

Kinetic studies of immobilized enzymes are of great interest because the reaction rate and the amount of substrate are crucial for immunoassays and biosensor optimization. Consequently, intensive research was devoted to study the kinetics of enzymes after different immobilization methods using a variety of detection methods.<sup>[267, 273, 275-289]</sup> Mass transport effects have been considered in order to understand and elucidate the influence of this process upon the biocatalyst kinetics. Engasser and Horvarth<sup>[269]</sup> evaluated the effect of internal diffusion on the kinetic parameters and substrate diffusivity in heterogeneous systems by a mathematical model. Later they published a study where dimensionless parameters were introduced in order to treat the external and internal diffusional effects.<sup>[270]</sup> Several mathematic models describing the kinetics of immobilized enzymes have been developed in order to support the experimental data. This study builds on these concepts and relates them to SECM experiments which provide a very good characterization of external diffusion. The experimental system allowed to vary systematically the internal diffusion.

### 5.1.1 Use of magnetic microbeads as bioreceptor support

The most common techniques of enzyme immobilization are noncovalent adsorption, covalent attachment, entrapment in a polymeric gel, membrane, or capsule, and cross-linking of enzymes.<sup>[290]</sup> Among other immobilization techniques, the use of colloidal particles composed of different composite materials and different surface chemistries has received much attention in the biosensor community<sup>[289, 291-295]</sup> for the immobilization of biomolecules and the study of their kinetic parameters. Paramagnetic surface-modified beads have gained popularity as a solid, yet mobile support surface of heterogeneous immunoassays.<sup>[141, 296, 297]</sup> Magnetic beads have the advantage that they can possess different surface chemistry making possible the collection of different biomolecules on its surface either by adsorption or by covalent immobilization. Suspension of beads can be dosed like liquid solutions. In addition to the advantage of a higher surface-to-volume ratio compared to the smooth walls of a microtiter plate, they can be dispersed into a sample solution during the binding step. This accelerates the binding step because the dependence on molecular diffusion over macroscopic distances is eliminated. The beads can be concentrated in an external magnetic field and separated easily from the analyte solution or washing solutions. Furthermore the beads can be transferred from a large volume sample into a small detection volume.<sup>[33]</sup> This enables sensitive electrochemical detection of products generated by an enzyme label. Examples include immunoassays with detection by a rotating disk electrode (Fig. (5.2a)) put on the surface of a drop of bead suspension.<sup>[296]</sup> In this case the enzyme alkaline phosphatase (ALP) generated *p*-aminophenol (PAP) which was electrochemically detected. In a further development the sampled beads were transported into a small detection chamber of a microfluidic device and captured by a magnetic bead trap,<sup>[35, 298]</sup> the PAP was generated and detected amperometrically (Fig. (5.2b)). The batch of beads used for one assay could be released making room for the next analysis.<sup>[33]</sup>

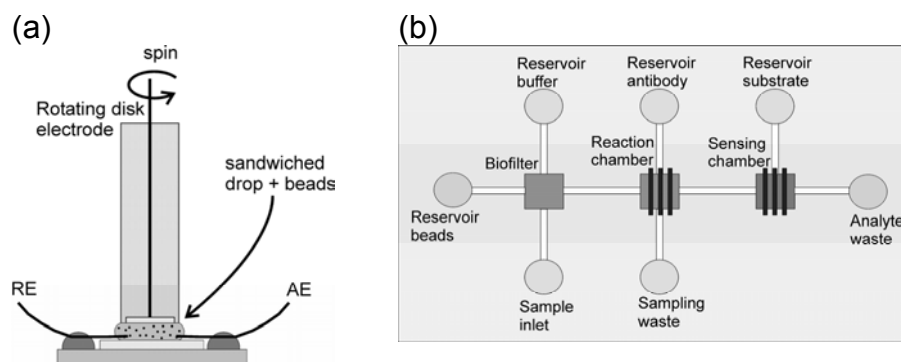


**Figure 5.2.** Microbead immunoassays: (a) electrochemical detection by a rotating disk electrode<sup>[296]</sup> and (b) sketch of a microfluidic device with an amperometric detection chamber.<sup>[35, 298]</sup>

The possibility to preconcentrate the beads in an external magnetic field can also be used to form microscopic agglomerates on solid surfaces.<sup>[299]</sup> Such agglomerates on solid surfaces have been used to carry out model sandwich immunoassays by depositing the beads on surfaces after they had captured the analyte.<sup>[141]</sup> Detection was performed by SECM using the oxidation of PAP that was formed by the ALP-catalyzed reaction in the sandwich assay. The use of agglomerates of enzyme-modified beads has been constantly used in the Wittstock group as one possibility to prepare micropatterned and microcompartmentalized surfaces.<sup>[15, 19, 120, 140]</sup> The enzyme  $\beta$ -galactosidase was investigated as an alternative to ALP in immunoassays.<sup>[141]</sup> It converts *p*-aminophenyl- $\beta$ -D-galactopyranoside (PAPG) to PAP and galactopyranoside. Magnetic microbeads were used to optimize detection conditions for this enzyme.<sup>[120]</sup> Magnetic beads were also used to optimize imaging conditions and to quantify reaction rates of pyrroloquinoline quinone (PQQ)-dependent glucose dehydrogenase.<sup>[140]</sup> Surface-modified microbeads offer the attractive opportunity to mix suspensions of beads with different surface modifications to generate more complex functionalities.<sup>[19]</sup> Unless competitive adsorption or covalent binding processes to the same solid support, mixing of bead suspensions allows a precise adjustment of the amount of both functional units. Demonstrations of this concept are bead agglomerates containing beads modified with PQQ-dependent glucose dehydrogenase and beads modified with  $\beta$ -galactosidase. In this system, galactosidase-generated PAP was oxidized at the UME of SECM in a GC scheme to *p*-iminoquinone (PIQ). PIQ is an electron acceptor for PQQ-dependent glucosedehydrogenase and was reduced in the enzymatic reaction to PAP. This established an electrochemical feedback. The combination of GC and FB modes provided excellent detection limits (typical for the GC mode) and lateral resolution close to that expected for the feedback mode.<sup>[19]</sup> Using digital simulation and GC experiments the possibilities of detection of biochips with  $\beta$ -galactosidase were elucidated and design recommendations with respect to layout and activity ranges could be derived.<sup>[300]</sup> The described bioanalytical applications aimed for the quantification of the amount of bound enzyme labels via the detection of concentrations or fluxes of a dissolved reaction product.

In this chapter, the streptavidin-biotin interaction was used to immobilize the biotin-labeled enzyme on a streptavidin-coated magnetic bead surface, the support. This system is forming a highly stable conjugate with an affinity constant of  $K_d = 10^{-15} \text{ mol}^{-1} \text{ L}^{-1}$ .<sup>[301]</sup> The morphology and organization of the microbead microstructures determines the accessibility of the active site of the enzyme for the binding of substrate and release of product. Within bead agglomerates not all beads contribute in the same way to the

total flux that can be detected outside the agglomerate due to the hindrance of diffusion towards and from modified beads located inside the agglomerate. While the immobilization of enzymes on surface-modified microbeads has become a popular procedure to sense enzymatic reactions, the significance of substrate and product diffusion through the microbead microstructure was unclear. Although the substrate transport towards the biomolecule plays a critical role on the overall rate of reaction and hence on the performance of the biosensor, there is a lack of scientific work regarding this problem.<sup>[274]</sup> Understanding the mass transport mechanisms that are taking place and more importantly which regime is governing, e.g. reaction-limited or diffusion-limited, helps to develop and optimize biosensors.

Studies concerning the diffusional effects and kinetics of immobilized enzymes on porous and non-porous particles have been done. Backer and Baron<sup>[302]</sup> used a porous glass particle as immobilization matrix for *saccharomyces cerevisiae* to determine the effective intraparticle diffusivity of the substrate and found that the intraparticle diffusivity is lower than the diffusivity in bulk due to a reduction of the available volume in the bead (porosity) and due to an increase in the path length for diffusion (tortuosity). Krishnan et al.<sup>[303]</sup> developed a mathematical model to evaluate the performance of an amperometric sensor of glucose oxidase immobilized on glass beads attached to a platinum electrode as function of the bead radius. The influence of external mass transfer limitation on apparent kinetic parameters using non-porous silica particles as enzyme carrier was studied by Kheirloom et al.<sup>[271]</sup> Bozhinova et al.<sup>[304]</sup> investigated the kinetic and stereoselectivity behavior of enzymes immobilized on non-porous magnetic microbeads and recently Magario et al.<sup>[272]</sup> evaluated the applicability of using non-porous magnetic beads as enzyme immobilization carrier for diffusion rate-limited reactions in an emulsion. However, these studies consider single beads as a porous (or non-porous) support, while here an agglomerate of non-porous beads is considered as a porous support, moreover the main scope of those studies are the industrial application of immobilized enzymes (e.g. bioreactors), being the support (e.g. beads containing immobilized enzyme) placed inside a packed bed enzyme reactor. Nevertheless, a study concerning the availability of enzyme embedded in a bead agglomerate as well as mass transport toward the spot and through the spot have not been done yet.

Thus the understanding of interfacial kinetics between microbeads aggregates containing immobilized enzymes and substrate solution is of great importance. This phenomenon is studied in this chapter by a combination of experimental investigations and digital simulations using the boundary element method (BEM). Another concern specific to amperometric GC measurements in SECM is related to the fact that an amperometric UME is

not a truly passive sensor and flux determinations might be susceptible to errors introduced by intersection of the UME and sample diffusion layers or, in the case of conducting support surfaces, additional feedback contributions discussed in Chapter 6.<sup>[A6]</sup>

### 5.1.2 Design of the experiment

In order to investigate the phenomenon of mass transport inside the microbeads agglomerates, an experiment was designed so that different bead suspensions were mixed in defined ratios (Fig. (5.3)). The biotin-labeled  $\beta$ -galactosidase was captured on streptavidin-coated magnetic microbeads through the biotin-streptavidin interaction. The  $\beta$ -galactosidase-modified beads were mixed with bare beads and were deposited on a hydrophobic surface in a defined mound-shape spot. Several spots were created on a glass slide forming an array of microbead spots.<sup>[299]</sup> By varying the content of bare beads, the shielding in a statistically mixed agglomerate of both bead types is systematically varied and the resulting flux from such agglomerates is detected in the SECM GC mode and evaluated according to the routines of Scott et al.<sup>[124]</sup> The routine for simulations of SECM experiments using the BEM has been expanded from initial demonstrations<sup>[305-308]</sup> to allow finite first order kinetics at the boundaries,<sup>[309-311]</sup> to consider more than one independent diffusing species which is necessary to describe GC experiments with enzymes.<sup>[300]</sup>

While the earlier papers of the Wittstock group had to use linear first order or zero order approximations to describe the enzyme kinetics, the consideration of non-linear boundary conditions for the reaction rate at the enzyme-modified surfaces in electrochemical BEM simulations was recently introduced by Träuble et al.<sup>[A5]</sup> and is used here. This allows treating the experiments without the assumption of a non-interacting probe and facilitates comparison to real UME measurements.



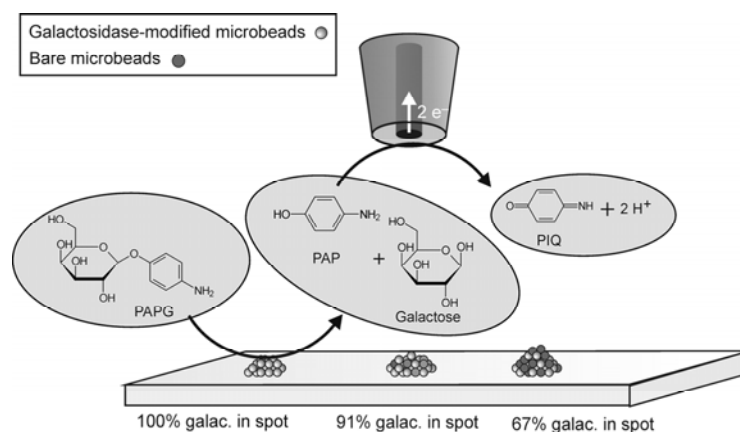
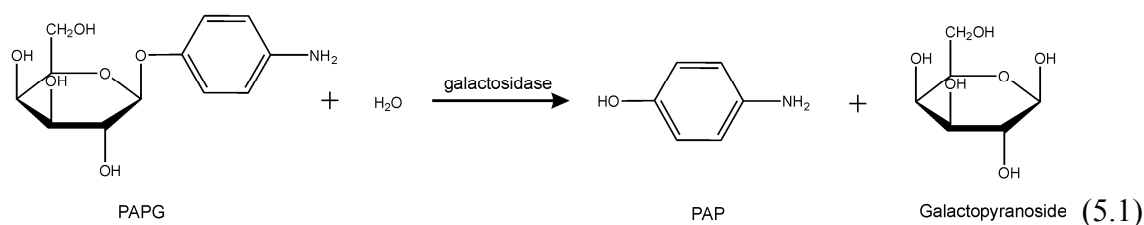


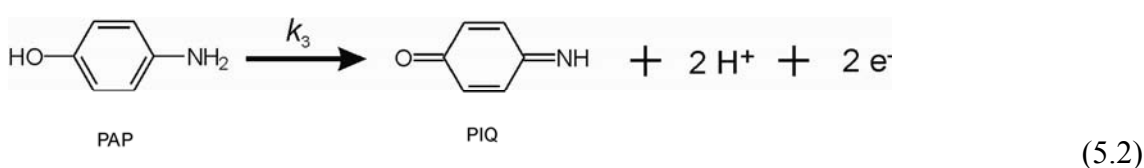
**Figure 5.3.** Schematic of the GC detection of  $\beta$ -galactosidase activity by SECM above spots that contain different ratios of  $\beta$ -galactosidase-modified (bright) and bare (dark) beads. The sketch is not to scale.

The immobilized  $\beta$ -galactosidase breaks the strong ether bond of the redox-inactive substrate PAPG to form the electrochemically active PAP and galactopyranoside (Eq. (5.1)). The PAP is then oxidized at the UME to PIQ when the UME is poised to a positive overpotential,<sup>[120]</sup> hence the enzymatic activity is imaged by the GC mode of the SECM. The PAP has excellent electrochemical properties such as low oxidation potential, quasi-reversible electrochemical behavior and negligible electrode fouling.<sup>[312]</sup> The oxidation of the PAP is governed by a two-electron transfer process (Eq. (5.2)). At the potential at which oxidation of PAP occurs, PAPG is electrochemically inactive and the observed UME current is due to oxidation of PAP, a compound that is not initially present in solution, yielding a very sensitive measurement.<sup>[120]</sup>

At the sample:



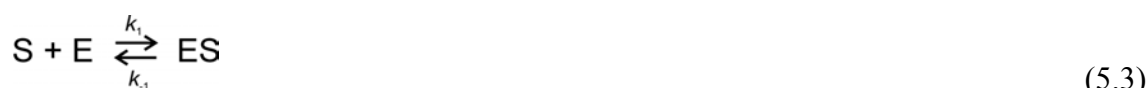
At the UME:



The PAP flux formed on the surface of the bead agglomerate depends on the amount of bare beads present in the spot which “shield” the  $\beta$ -galactosidase-modified beads from the diffusion of PAPG to the enzyme. Open questions regarding shielding effects of the beads on each other are studied and discussed in this Chapter.

## 5.2 Kinetics of immobilized enzymes

In an enzymatic reaction, the enzyme (E) increases the rate of chemical reactions, i.e. catalyzes the reaction, without suffering any change. The reactant in an enzymatic reaction is called substrate<sup>1</sup> (S) and is specific for each enzyme. All enzymes are proteins that have an active site where the substrate is bound. The active site is substrate-specific, however some substrates with similar structure can also be used to participate in the enzymatic reaction. The activity of many enzymes can be described in terms of Michaelis-Menten kinetics. A simplified mechanism for a single substrate and an enzyme can be written as following:



where S is PAPG, E is  $\beta$ -galactosidase, ES is  $\beta$ -galactosidase-PAPG complex, P<sub>1</sub> is PAP, P<sub>2</sub> is galactopyranoside and  $k_1$ ,  $k_{-1}$ , and  $k_2$  is reaction rate constants.

In this process the immobilized enzyme E ( $\beta$ -galactosidase) catalyses the hydrolysis of S (PAPG) by a two step mechanism through an enzyme-substrate complex ES ( $\beta$ -galactosidase-PAPG) intermediate<sup>[313]</sup> as shown in Eq. (5.3) and (5.4). In this study, only P<sub>1</sub> (PAP) which is redox-active is of interest, the galactopyranoside is not redox-active at the applied potential and does not need to be considered for SECM signal calculations. In further discussions on the enzymatic reaction the reaction product P refers to PAP.

A generalized single-substrate rate law for the steady-state substrate consumption introduced by Briggs and Haldane<sup>[314]</sup> based on the original proposal by Michaelis and Menten<sup>[315]</sup> can be derived from Eqs. (5.3) and (5.4):

$$v = \frac{d[P]}{dt} = \frac{v_{\max} [S]}{K_M + [S]} \quad (5.5)$$

<sup>1</sup> Do not to confuse the biochemical term “substrate” used as one of the reagents in an enzymatic reaction with “substrate” commonly used to term “sample”, “specimen” and “support”. To avoid confusion the term substrate is used here only as the reagent in enzymatic reaction.

where

$$K_M = \frac{k_{-1} + k_2}{k_1} \quad (5.6)$$

and

$$v_{\max} = k_2[E] \quad (5.7)$$

and  $v$  is the reaction rate of product formation  $v = d[P]/dt$ ,  $v_{\max}$  is the maximum rate for the catalytic process, and  $K_M$  is the Michaelis-Menten constant.  $K_M$  denotes the affinity of an enzyme with a particular substrate and reveals abnormalities (e.g. mutations, structural changes, etc.) in an enzyme as an altered  $K_M$  reflects changes in the enzyme-substrate binding. In this study a single-substrate reaction with one substrate-binding site per enzyme is used, hence  $k_2 = k_{\text{cat}}$ . The turnover number ( $k_{\text{cat}}$ ) describes the maximum amount of substrate that an enzyme can convert to the product per catalytic site per unit time and is unique for a particular enzyme and the substrate.

The Eq. (5.5) leads to two limiting cases:

$$\frac{d[P]}{dt} = v_{\max}, \quad [S] \gg K_M \quad (5.8)$$

$$\frac{d[P]}{dt} = \frac{v_{\max}[S]}{K_M}, \quad [S] \ll K_M \quad (5.9)$$

These cases describe zero-order (Eq. (5.8)) and first-order (Eq. (5.9)) limiting cases of the rate law. A typical Michaelis-Menten plot containing these two quasi-linear regions is shown in Fig. (5.4). There is a region of intermediate  $[S]$  showing a non-linear relation between rate and substrate concentrations (intermediate regime).

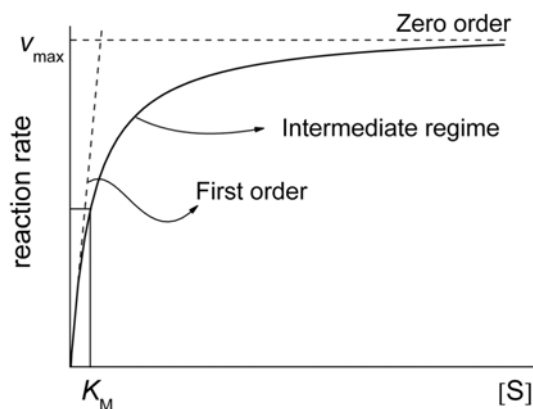


**Figure 5.4.** Michaelis-Menten kinetics curve indicating the first-order, intermediate regime and the zero-order kinetics region.

Considering the average flux per enzyme  $r$ , one can derive the average number of products produced per enzyme per unit time with units of  $s^{-1}$ , thus the Eq. (5.5) can be modified to:

$$r = \frac{v}{[E]} = \frac{k_{\text{cat}}[S]}{K_M + [S]} \quad (5.10)$$

As the enzymes used in this study are immobilized, the Eq. (5.10) should be modified in order to consider the enzyme surface concentration  $\Gamma_{\text{enz}}$  and the concentration of S at the surface  $[S]_S$ :<sup>1</sup>

$$J = \frac{k_{\text{cat}}\Gamma_{\text{enz}}[S]_S}{K_M + [S]_S} \quad (5.11)$$

The Eq. (5.11) describes the heterogeneous reaction rate for the formation of product produced per unit time and area [ $\text{mol cm}^{-2} \text{s}^{-1}$ ] and characterizes the effective kinetics of the enzymatic reaction.

In this work, the GC mode was used to study the activity of immobilized enzymes. The enzymes generated the redox-active molecules (sample generation) that were then collected by the UME (tip collection) by a diffusion-limited reaction at the UME. The magnitude of the UME current depends on the kinetics of the enzymatic reaction (Eq. (5.11)) and the diffusion rate of the product to the UME (Eq. (2.21)). As the sample region is a microscopic region itself (spot), a steady-state concentration for S and P is established in the solution. At the UME, P (PAP) is oxidized to O (PIQ) under steady-state diffusion-controlled conditions. Fig. (5.5) shows a sketch of the system being considered.

---

<sup>1</sup> The subscript S in  $[S]_S$  means the substrate concentration at the spot surface. For substrate concentration at the solution bulk,  $[S]^*$  is used.

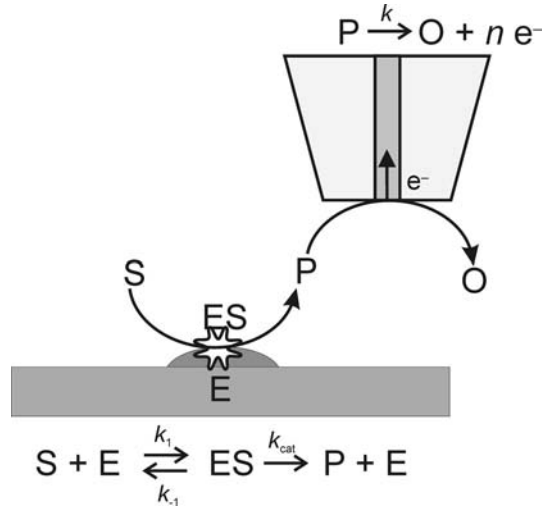


**Figure 5.5.** Reaction at the immobilized enzyme and detection of product at the UME. Here the product of the enzymatic reaction is oxidized to O at the UME by diffusion-controlled reaction. S corresponds to PAPG, E to  $\beta$ -galactosidase, ES to  $\beta$ -galactosidase-PAPG complex, P to PAP, and O to PIQ.

An approach suggested by Scott et al.<sup>[93, 124]</sup> has been used to quantify molecular flux generated by the microscopic sample. Quantification of the recorded signal is possible because a steady-state hemispherical diffusion field is formed over the spot. This approach assumes the UME acts as a passive probe (i.e. a sensor that does not consume the analyte) and does not disturb the local diffusion field attained above the microscopic sample. The equations used to describe the UME current suggested by Scott et al.<sup>[93, 124]</sup> have been discussed in Chapter 2, Section 2.3 (Eqs. (2.21) and (2.22)).

The magnitude of  $i_T$  is proportional to the local concentration of the redox-active molecules P. The  $i_T$  dependence on the dilution factor  $\theta$  from Eq. (2.22) is related to the concentration decrease of the released redox-active product as function of the lateral ( $\Delta x$ ) and vertical ( $d$ ) distances from the center of the active region, and  $r_s$ . When the UME is positioned over the center of the active region (where the peak current occurs), the lateral distance equals to zero ( $\Delta x = x - x_0 = 0$ ), hence the Eq. (2.21) can be simplified to:

$$i_T = gnFD r_T [P]_s \frac{2}{\pi} \arctan \frac{r_s}{d} \quad (5.12)$$

It is straightforward to measure the peak current due to the simplifications that can be made, moreover  $i_T$  ( $\Delta x = 0$ ) is proportional to the rate of molecular diffusion at any point across the active region of the sample due to steady-state conditions.<sup>[148]</sup>

A comparison between the flux of Michaelis-Menten kinetics (Eq. (5.11)) and the flux of product over the entire active region (Eq. (2.25)) leads to an equation that describes the concentration of detected species  $[P]_S$  at the sample surface<sup>1</sup>:

$$[P]_S = \frac{\pi \cdot r_S \cdot (k_{\text{cat}} \cdot \Gamma_{\text{enz}} \cdot [S]_S)}{4 \cdot D \cdot (K_M + [S]_S)} \quad (5.13)$$

Replacing  $[P]_S$  in Eq. (5.12) and considering  $g = 4$  (infinitely large insulator), the current at the UME can be calculated using Eq. (5.14). This equation considers the Michaelis-Menten kinetics at the sample and the diffusion of the product to the UME, and was used in this work to describe the peak current measured when the UME was placed above the center of the spot:

$$i_{T,\text{peak}} = 2 \cdot n \cdot F \cdot r_T \cdot r_S \cdot \arctan\left(\frac{r_S}{d}\right) \cdot \left(\frac{k_{\text{cat}} \cdot \Gamma_{\text{enz}} \cdot [S]_S}{K_M + [S]_S}\right) \quad (5.14)$$

### 5.2.1 Effects of substrate diffusion on the kinetics of immobilized enzyme in porous support

The study of internal and external diffusion on immobilized enzymes plays an important role since it can influence the kinetics of a reaction. Moreover, with the knowledge of these effects, one can optimize the system where the enzyme is immobilized, saving high-cost material such as enzyme, substrate, and support. The net diffusive process occurs due to the steady state concentration gradients of solutes (substrate and products) formed outside and inside the spot.

The catalytic conversion of substrate to products occurs in series with the external diffusion of substrate towards the spot surface and product away from the surface, however, inside the spot the catalytic conversion as well as the diffusion of substrate and product is in parallel. A system where all the beads are saturated with enzyme and the substrate utilized in the system is much greater than  $K_M$ , has a concentration gradient shown in Fig. (5.6). The concentration gradient formed outside the spot is a combination of partition and diffusion effects.

<sup>1</sup> Here  $[P]_S$  is the concentration of PAP at the spot surface.

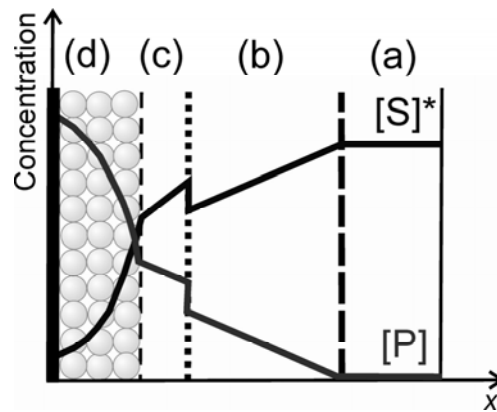


**Figure 5.6.** Concentration gradient at steady-state caused by diffusion and partition at the spot surface (macroporous support containing immobilized enzymes). The substrate concentration within the spot microenvironment is lower than that in the bulk solution due to its depletion by the enzymatic reaction. (a) Initially only S is present at the bulk at a concentration  $[S]^*$ , hence  $[P]$  is zero. (b) S is catalytically consumed by E forming P. (c) Due to partition  $[S]$  is increased as well as  $[P]$ . (d) S diffuses inside the macroporous substrate where it will be fully consumed by E forming P.

The system under investigation are agglomerates of magnetic beads. The amount of microbeads that were completely saturated with  $\beta$ -galactosidase were constant in the spot, while the amount of non-modified beads was modified. Fig. (5.7) shows a schematic representation of three spots formed with the same amount of enzyme-modified bead and varied amount of bare beads.

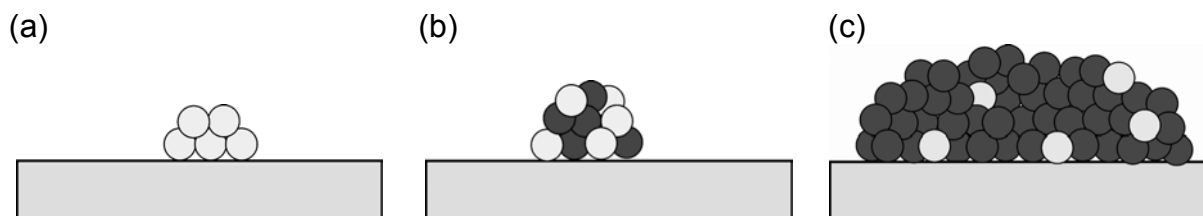


**Figure 5.7.** Schematic of bead spots with different amount of bare beads and constant amount of enzyme-saturated beads. (a) 100% enzyme-saturated bead (no bare beads present), (b) 50% enzyme-saturated beads and 50% bare beads, (c) 10% enzyme-saturated beads and 90% bare beads. Not to scale.

The bead spot microenvironment consists of the internal solution plus the surrounding solution which is influenced by surface characteristics of the bead surface and the immobilized enzyme. It is unknown if the substrate can diffuse toward the immobilized enzyme encountered inside the bead agglomerate (Fig. (5.8b)). In order to investigate it, there are some phenomena that must be considered. Partition between the bead spot microenvironment and the bulk macroenvironment may occur due to hydrophobic interaction. The substrate must diffuse from the bulk of the solution toward the spot surface where it will

be converted to the product, forming a diffusion gradient outside the spot. If there is enough substrate on the surface of the spot, i.e. not all substrate is consumed by the enzyme found on the spot surface, an internal diffusion gradient is formed within the spot due to diffusion of substrate into the agglomerate. In the spot microenvironment, the substrate must diffuse within the pores in order to reach the enzyme active site. Under steady-state conditions the rate of substrate diffusion to the spot surface, the overall rate of enzymatic conversion and the rate product of diffusion away from the spot surface are equal.

There are two extreme cases that should be considered:

- only beads located at the surface of the bead agglomerate (e.g. first and second uppermost layer) contribute to the PAP flux (Fig. (5.8a)).
- all beads in the spot contribute to the PAP flux (Fig. (5.8b)).

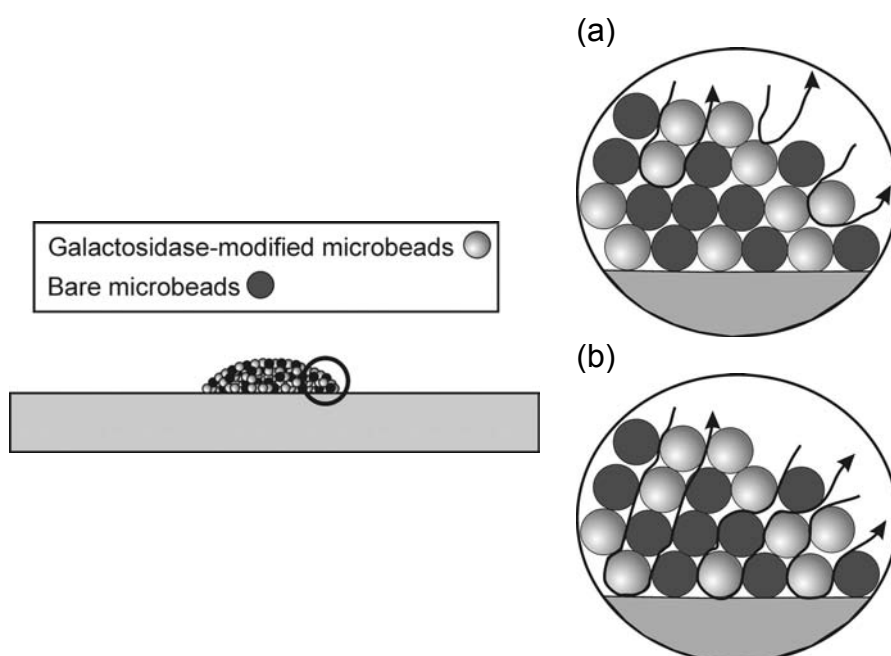


**Figure 5.8.** Sketch of the diffusion pathway through microbead spot. (a) The PAPG and PAP can only diffuse through the first and second bead layer of the spot. (b) the PAPG and PAP diffuse through the whole spot.

Analyzing the flux of the enzymatic reaction product by SECM and comparing with the study of external and internal diffusion, one can answer the following questions:

- How many modified-beads contribute to the overall external flux?
- Do all modified-beads inside the spot contribute to the overall flux or just the uppermost bead layer of the spot?
- Is there enough PAPG inside the spot?
- How big is the influence on shielding inside the bead agglomerate if enough PAPG is provided?



**Effects of external diffusion:** In order to investigate the effects of external diffusion, a model system containing 100% enzyme-saturated beads forming a bead agglomerate was used. Some assumptions have to be made in order to derive the equation describing the effect of external diffusion on the rate of the enzyme-catalyzed reaction:

- Michaelis-Menten kinetics hold,
- enzyme immobilization on a disk-shaped support,
- no partitioning or electrostatic effects,
- the substrate concentration at the bulk is unchanged throughout the experiment (steady-state condition).

At steady-state, the overall rate of the enzymatic reaction is equal to the rate of substrate diffusion to the enzyme surface and equal to the rate of product diffusion away from the enzyme surface. Assuming that all enzymes at the surface are equally accessible to the substrate and the reaction obeys the Michaelis-Menten kinetics: <sup>[270]</sup>

$$k_L ([S]^* - [S]_s) = \frac{v_{\max} [S]_s}{K_M + [S]_s} \quad (5.15)$$

The left-hand side of the equation describes the rate of substrate diffusion to the catalytic surface and the right-hand side the Michaelis-Menten kinetics, where  $k_L$  is the proportionality constant also known as mass transfer coefficient.<sup>[116]</sup> This equation shows that the rate of substrate flow to the spot surface is proportional to the spot area and the difference in substrate concentration between the bulk of solution and the spot surface (under assumption that all enzymes at the spot surface are equally accessible for reaction).

The functional form of the proportionality constant depends on the geometry of the system under study. In this study, a bead agglomerate was considered as a porous support for enzyme immobilization and it was assumed that the bead spot has a disk shape. As the spot is a microscopic structure and a steady-state hemispherical diffusion layer is built over the spot, Eq. (5.16) may be used.<sup>[116]</sup>

$$k_L = \frac{4D_s}{\pi \cdot r_s} \quad (5.16)$$

The ratio between reaction rate and the mass transport rate defines the dimensionless Damköhler number  $\mu$ :

$$\mu = \frac{v_{\max}}{k_L K_M} \quad (5.17)$$

where  $v_{\max}$  is the maximum rate of enzymatic reaction by unit surface area. The term  $v_{\max}/K_M$  is related to the enzymatic reaction and  $k_L$  to the mass transport rate. The dimensionless concentration  $\beta$  is given by:

$$\beta = \frac{[S]}{K_M} \quad (5.18)$$

Substituting the dimensionless parameters from Eqs. (5.18) and (5.17) into Eq. (5.15) leads to Eq. (5.19):<sup>[270]</sup>

$$\beta^* - \beta_s = \mu \frac{\beta_s}{1 + \beta_s} \quad (5.19)$$

where  $\beta^*$  and  $\beta_s$  are the dimensionless substrate concentration at the bulk and at the spot surface respectively. Eq. (5.19) leads to two limiting cases. If the diffusion rate is much greater than the enzyme reaction rate (at  $\mu \rightarrow 0$ ) and the substrate concentration at the spot surface is practically equal to the bulk concentration, and if the overall rate of the process is kinetically controlled by the enzyme and is as effective as for the free enzyme in solution,  $\mu = 1$ . Thus at a given substrate concentration the reaction rate is equal to the maximum possible rate of enzymatic reaction and is given by Eq. (5.5) for  $k_L \gg v_{\max}/K_M$ .

However, if the overall rate of the process is diffusion-controlled for a slow diffusion rate and a fast rate of enzymatic reaction (large  $\mu$ ), the substrate concentration at the spot surface approaches zero because all substrate molecules that reach the spot surface are immediately converted by the enzyme. Hence the rate of reaction is equal to the maximum possible rate of external transport:<sup>[270]</sup>

$$v_{diff} = k_L [S]^* \quad \text{for } k_L \ll v_{\max}/K_M \quad (5.20)$$

Eqs. (5.5) and (5.20) propose two different cases. If the reaction is diffusion-controlled and Eq. (5.20) is held, this means that the overall rate of reaction is independent of enzyme activity, thus changes in pH, temperatures, and ionic strength do not affect the reaction rate. However, if the Eq. (5.5) is held and the overall rate of reaction is kinetically controlled, the pH, temperature and ionic strength influences the rate of reaction. The external diffusion control over the rate of enzyme reaction is produced by

- high enzyme loading on the spot surface,
- low substrate bulk concentration,
- low substrate diffusion coefficients,
- low  $K_M$ ,

- high enzyme specificity,
- low rate of stirring, and
- flat surfaces.

The Eq. (5.19) may be simplified to Eq. (5.21) for low  $\beta^*$ , when  $\beta_s$  approaches zero:

$$\beta_s = \frac{\beta^*}{1 + \mu} \quad (5.21)$$

Thus:

$$[S]_s = \frac{[S]^*}{1 + \mu} \quad (5.22)$$

For low substrate bulk concentration and knowing  $\mu$ , one can estimate the concentration of the substrate at the spot surface.<sup>[268]</sup> Another way to estimate  $[S]_s$  is to use the  $[P]_s$  estimated from the fit of the SECM line profile and  $[S]^*$ , for  $D_s = D_p$ :

$$[S]_s = [S]^* - [P]_s \quad (5.23)$$

In this study, Eq. (5.23) was used to calculate  $[S]_s$  rather than Eq. (5.22) because  $[S]^*$  given to the system was high compared to  $[P]_s$ .

**Effects of internal diffusion:** The analysis of internal diffusion is influenced by several factors such as the shape of particles, route through the pores that the substrate encounters (tortuosity,  $\tau$ ), total volume of the pores with respect to the particle volume (porosity,  $\zeta$ ), effective diffusion coefficient of substrate  $D_{\text{eff}}$  and products within the pores, and uniformity of enzyme distribution within the particles.<sup>[316]</sup> A concentration gradient is formed within the spots and was found to be non-linear.<sup>[268]</sup> The non-linear concentration profile formed on spherical particles is due to substrate molecules diffusing toward the bead surface through convergent or divergent pathways.

The analysis of diffusional effects within the spots leads to two cases. One is when the beads spot is 100% saturated with enzymes and the other case is when the bead spot also contains bare beads. In the case of a spot containing 100% enzyme-saturated beads, and the reaction being diffusion-controlled (e.g. low substrate concentration), the effect of internal diffusion may be neglected because the substrate concentration on the spot surface is effectively zero being not available for penetration into the spot. However, when the bead spot has different amounts of enzyme-modified beads or are 100% saturated and the substrate is given in excess, enough substrate may be available to diffuse through the pores of the spot

reaching the enzyme-modified beads encountered within the spot. Hence analysis of internal diffusional resistance and its influence on the overall kinetics must be made in order to find out if the beads found inside the spot contribute to the overall reaction.

Three processes are occurring in parallel within the porous spot: diffusion of S toward the enzyme, enzyme catalysis and diffusion of P away from the enzyme. The substrate concentration gradient between the bead agglomerate and the bulk is enhanced by substrate consumption by the enzyme reaction taking place in the spot. The reaction inside the spot results in decrease of substrate concentration on the spot surface, leading to a depletion of substrate deep inside the spot and increase of product concentration within the spot.

In order to analyze the effect of diffusion within the spots some assumptions have to be made:

- the galactosidase-modified beads are uniformly distributed within the spot,
- the enzyme kinetics are described by the Michalis-Menten model,
- the system is under steady-state and isothermal conditions,
- substrate and product diffusion obeys the Fick's law,
- there is no inhibition by substrate or product, and
- no electrostatic effects are present.<sup>[269]</sup>

In 1939 Thiele<sup>[317]</sup> suggested an equation that combined the parameters responsible for concentration profiles within a porous particle such as size of the particle, facility for the substrate to diffuse through the support and the intrinsic activity of the catalyst. This equation introduces the term  $\phi$  known as Thiele modulus:

$$\phi = \Lambda \sqrt{\left( \frac{v_{\max}}{K_M D_{\text{eff}}} \right)} \quad (5.24)$$

where  $\Lambda$  is taken as the characteristic length of the system. Because the Thiele modulus is reciprocal to the pore utilization level, generally  $\Lambda$  is the ratio of the sphere volume and its external surface.<sup>[269]</sup> The modulus allows the characterization of the system (spot microenvironment) when the internal diffusion perturbs the reaction and  $K_M$  and  $v_{\max}$  do not describe the rate of the system alone.  $D_{\text{eff}}$  is proportional to the diffusion coefficient in the bulk solution  $D^*$ , to the tortuosity of the pore geometry  $\tau$  and inversely proportional to the particle porosity  $\zeta$ :

$$D_{\text{eff}} = D^* \frac{\zeta}{\tau} \quad (5.25)$$

To calculate the penetration depth of the substrate into the bead spot, a closed packing of the beads is assumed. The porosity  $\zeta$  of such packing is:<sup>[318]</sup>

$$\zeta = 1 - \frac{\pi}{3\sqrt{2}} \quad (5.26)$$

and the tortuosity  $\tau$  can be estimated from the mean value of the angles between pore-direction and transport.<sup>[319]</sup>

$$\tau = \frac{\pi}{2} \quad (5.27)$$

A model for internal diffusion can be established assuming that the porosity and the tortuosity affect the effective diffusion coefficient, the spot is homogeneous and the enzyme-modified beads are uniformly distributed throughout the spot. It is also assumed that  $[S]_s$  is equal at all locations. This assumption is critical, because in geometries with different layer thickness as the layer-cap geometry or elliptical geometries, the concentration of product is expected to be higher at parts with higher thickness, if internal diffusion plays a role. Nevertheless, this assumption gives the possibility to establish a quite easy model.

Under steady state conditions, a balance between diffusion and reaction exists, so a general description of the mass transport inside the spot is:

$$D_{\text{eff}} \nabla^2 [S]_s = \frac{v_{\text{max}} [S]_s}{K_M + [S]_s} \quad (5.28)$$

The enzymatic reaction in a spot depends on several conditions, mainly on the geometry of the spot, the number of enzyme-saturated beads and the depth of penetration of S into the spot. Assuming that the amount of  $\beta$ -galactosidase-modified beads in the spot in % is kept after spot deposition and that the total number of beads in the spot is increased, the relevant conditions are geometry and penetration.

Differential equations describing the concentration profile of the substrate in the spot have been given for two distinct geometry-dependent models: one considers the spot as a uniform bead layer (Fig (5.9a)), the other model considers the spot as a half-sphere (Fig (5.9b)). These two models were used in order to simplify the partial differential equations (PDE) from Eq. (5.28) to ordinary differential equations (ODE) and make the equation solvable. Moreover these geometries approach the experimental spot geometry.

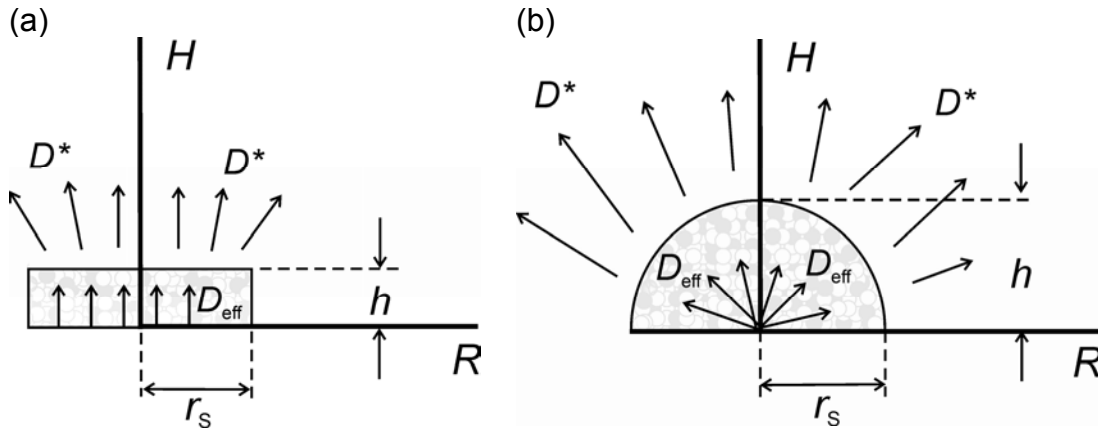


**Figure 5.9.** Schematic of the spot geometry considered for the numerical simulation of the internal diffusion. (a) Model 1: uniform bead layer (layer-cap), (b) Model 2: half-sphere. The two orthogonal coordinates are given as  $H$  and  $R$  in order to characterize the position inside the spot toward  $h$  and  $r_s$  respectively. The arrows inside the spot symbolize the diffusion pathway of  $P$  with  $D_{\text{eff}}$ , and arrows outside the spots symbolize the diffusion pathway of  $P$  with  $D^*$ .

There are several issues that affect the reproducibility of the deposition process such as formation of a droplet, position of the droplet with respect to the magnet, adhesion of beads on the glass slide, hydrophobic forces, magnetic force and environment. It is a problem when one has to calculate the real amount of beads deposited to form one spot in order to simulate the concentration profile of the substrate in the spot. Therefore, in order to investigate the internal diffusion of Models 1 and 2, four cases were simulated, in which the total amount of beads present in one spot could be estimated.

**Model 1:** (Fig. (5.10a)) considers the spot as a uniform bead layer (layer-cap) with the spot height  $h$  calculated from the estimated adhesion angle  $\alpha = (12.5 \pm 3.5)^\circ$  according to Eq. (5.29), and the spot radius  $r_s$  being the one extracted from microscope pictures. The  $\alpha$  was estimated from the height obtained from the SCLM of similarly prepared but not identical spots.<sup>1</sup> For this Model,  $A$  is equal to  $h$ . This choice does not affect the differential equation, but makes the values of  $\phi$  comparable.

$$h = r_s \cdot \tan\left(\frac{\alpha}{2}\right) \quad (5.29)$$

The area of the spot  $A_{\text{spot}}$  is estimated with the help of the experimental  $r_s$  as:

$$A_{\text{spot}} = 2\pi r_s^2 \left(1 - \cos\left(\frac{\alpha}{2}\right)\right) \quad (5.30)$$

<sup>1</sup> It was found that measurements with SCLM deactivated the enzyme. Therefore, SCLM images were recorded on spots prepared to identical procedures, hence a representative value of  $\alpha$  could be estimated.  $r_s$  could be obtained from standard microscopic pictures.

The volume of the layer-cap-type spot can be calculated using the height and the radius of the spot:

$$V_{\text{spot}} = \pi h^2 r_s - \frac{\pi}{3} h^3 \quad (5.31)$$

Since  $V_{\text{spot}}$  and  $h$  can be estimated from Eqs. (5.31) and (5.29) respectively, the total number of beads in the spot  $N_{\text{tot}}$  can be calculated according to:

$$N_{\text{tot}} = \frac{V_{\text{spot}}(1-\zeta)}{V_{\text{bead}}} \quad (5.32)$$

where  $V_{\text{bead}}$  is the volume of a microbead  $V_{\text{bead}} = 4/3 * (\pi r_{\text{bead}}^3)$ . The bead radius is taken from the microbead description from the supplier ( $r_{\text{bead}} = 1.4 \mu\text{m}$ ).<sup>[320]</sup>

Multiplying the total number of beads in the spot  $N_{\text{tot}}$  with the fraction  $\chi$  of  $\beta$ -galactosidase-modified beads in the spot yields  $N_{\text{tot,gal}}$  (Eq. (5.33)):

$$N_{\text{tot,gal}} = \chi \cdot N_{\text{tot}} \quad (5.33)$$

The ordinary differential Eq. (5.34) describes the concentration profile of the substrate in a flat layer of uniform thickness as shown in Fig. (5.9a). This case is sufficiently simple to treat instead of the complex geometry shown in Fig. (5.10a) and was used to describe the concentration profile of Model 1.

$$\frac{\delta^2 \varphi}{\delta^2 \rho} = \phi^2 \frac{\varphi}{1 + \beta_s \varphi} \quad (5.34)$$

where  $\varphi$  is the dimensionless concentration that is the ratio of the substrate concentration at a certain distance  $h'$  inside the spot normalized to the substrate concentration at the spot surface (Eq. (5.35)),  $\rho$  is the dimensionless radial position (Eq. (5.36)),  $\beta_s$  is the dimensionless substrate concentration at the spot surface given by Eq. (5.18), and  $A$  is equal to  $h$ .

$$\varphi = \frac{[S]_{h'}}{[S]_s} = \frac{[\text{PAPG}]_{h'}}{[\text{PAPG}]_s} \quad h = h', [\text{PAPG}]_{h'} = [\text{PAPG}]_s \quad (5.35)$$

$$\rho = \frac{h'}{r_s} \quad (5.36)$$

Because the normal flux at the glass slide (where the spots were deposited) is equal to zero and the normalized concentration at the surface is equal to 1, the following boundary conditions hold:

$\varphi = 1$  at  $\rho = 1$ , and

$$\frac{d\varphi}{d\rho} = 0 \text{ at } \rho = 0$$

**Model 2:** considers the spot as a half-sphere, however the size of the half-sphere is varied. The calculated area corresponds to the area of a half-sphere given by  $A_{\text{spot}} = 2\pi r_S^2$  and  $V_{\text{spot}}$  is the volume of a half-sphere calculated as following:

$$V_{\text{spot}} = \frac{2}{3}\pi r_S^3 \quad (5.37)$$

For this model, the ODE describing the concentration profile in the half-sphere is given by Eq. (5.38):

$$\frac{\delta^2 \varphi}{\delta^2 \rho} + \frac{2}{\rho} \frac{\delta \varphi}{\delta \rho} = r_S^2 \frac{1}{\Lambda} \phi^2 \frac{\varphi}{1 + \beta_S \varphi} \quad (5.38)$$

where  $\Lambda$  is equal to the ratio of the volume  $V_{\text{spot}}$  to surface area  $A_{\text{spot}}$ :

$$\Lambda = \frac{V_{\text{spot}}}{A_{\text{spot}}} = \frac{r_S}{3} \quad (5.39)$$

Three cases can be analyzed using Model 2:

- Case 1 (Fig. (5.10b)) considers the spot as a half-sphere with the height  $h$  being the same as the  $r_S$  extracted from the microscope picture (big half-sphere). It leads to an overestimation of the spot height, but gives an upper boundary for the conversion rate.  $V_{\text{spot}}$  is calculated from Eq. (5.37),  $N_{\text{tot}}$  was calculated from Eq. (5.32),  $N_{\text{tot,gal}}$  was calculated according to Eq. (5.33),  $\Lambda$  from Eq. (5.39) and  $\phi$  from Eq. (5.24).
- Case 2 (Fig. (5.10c)) considers the spot as a half-sphere, however with the spot height  $h$  being the one calculated from Eq. (5.29) of Model 1, and  $r_S = h$  (small half-sphere). This leads to an underestimation of the spot giving a lower boundary for the conversion rate.  $V_{\text{spot}}$ ,  $N_{\text{tot}}$ ,  $N_{\text{tot,gal}}$ ,  $\Lambda$  and  $\phi$  were calculated as in the previous case.
- Case 3 considers the spot as a half-sphere, but here the  $N_{\text{tot}}$  calculated for Model 1, i.e., the one that approaches most to the "real" experimental spot, is given as initial parameter. Knowing  $N_{\text{tot}}$  and  $V_{\text{bead}}$ , one can estimate  $V_{\text{spot}}$  (Eq. (5.32)) leading to  $r_S$  using Eq. (5.37), and hence  $h$  ( $r_S = h$ ). This case gives a "medium" half-sphere, and is the intermediate case between case 1 and 2 (not shown as a sketch).



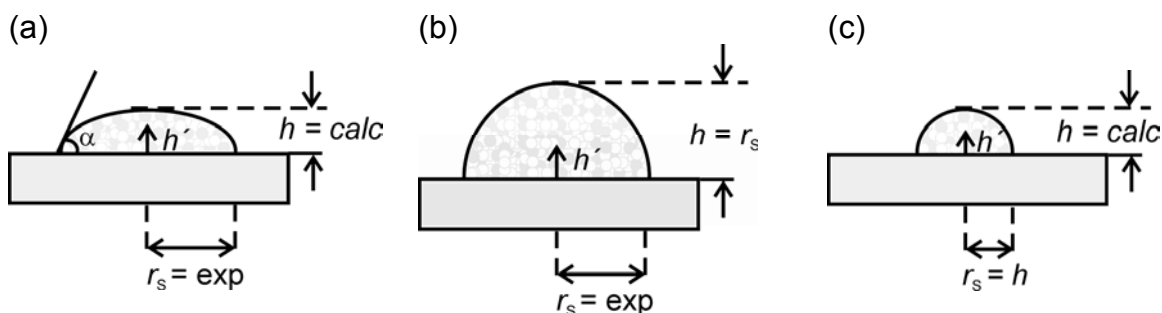


**Figure 5.10.** Schematic of the spot geometry considered for the numerical simulation of the internal diffusion. (a) Model 1: layer cap, where  $r_s$  is extracted from microscope pictures and  $h$  is calculated according to Eq. (5.29), (b) Model 2, case 1: big half sphere, where  $r_s$  is extracted from microscope pictures and is equal to  $h$ , and (c) Model 2, case 2: small half-sphere, where  $r_s$  is equal to  $h$  which is calculated according to Eq. (5.29).

The ODE were solved using a shooting method in order to solve the appropriate initial value problem as boundary value problem with variable concentration at  $\rho = 0$  with a fourth order Runge-Kutta method and minimizing the difference of the solution  $\varphi$  at  $\rho = 1$  and the boundary condition  $\varphi = 1$  at  $\rho = 1$ . Results are discussed in Section 5.5.3.

### 5.3 Digital simulation of external diffusion

The current measured at the UME is influenced by the geometries of the sample and the probe, as well as by the diffusional flux of oxidizable (or reducible) molecules to the UME and by the interfacial kinetics at the sample. The rather complex SECM experiments have been quantitatively analyzed by analytical approximations and by digital simulations. Digital simulations have accompanied SECM development since its beginning<sup>[79, 83, 86, 90, 92, 300, 308, 321]</sup> and have been used to deliver kinetics constants.<sup>[300]</sup> The finite difference method (FDM) has been used most often,<sup>[88-90]</sup> however its difficulty in treating three-dimensional (3D) coordinates limits the calculations to simplified geometries in two-dimensional (2D) coordinates. After Fulian et al.<sup>[305-307, 322]</sup> introduced the boundary element method (BEM) for the numerical solutions of SECM problems, extensions of BEM have been developed and extended to 3D coordinates.<sup>[300, 308-310, 323]</sup> Sklyar et al.<sup>[300]</sup> developed an extension of BEM that described a real<sup>1</sup> SG/TC experiment in true 3D space. However, this model considered only the two quasi-linear regions of the Michaelis-Menten kinetics curve (Fig. (5.4)). As the Michaelis-Menten kinetics are described by a non-linear equation, further extension for the BEM have been implemented by Träuble et al.<sup>[A5]</sup> This model used the BEM to solve the

<sup>1</sup> A system with more than one independent concentration variable.

steady-state diffusion equation with nonlinear boundary conditions and was used here to estimate the concentration of the product of the enzymatic reaction  $[PAP]_S$  and was compared with the concentration extracted from the fitting of Eq. (2.21). Moreover, the simulation could reveal the local kinetics, imaging conditions, interrelation of sample layout and the quality of the obtained image.

The parameters that must be given to the simulation as initial parameters are:  $r_T$ ,  $RG$ ,  $r_S$ ,  $d$ , spot height, PAPG bulk concentration  $[PAPG]^*$ ,  $D$ ,  $K_M'$  and  $k_{cat}\Gamma_{enz}$ . The  $r_T$ ,  $RG$ ,  $r_S$  and  $h$  can be extracted from SCLM images,  $[PAPG]^*$  is known from the experimental set up,  $D$  is either known from literature or calculated from chronoamperometric experiments, and  $K_M$  and  $k_{cat}\Gamma_{enz}$  are estimated values extracted from the fitting of  $i_T$  (Eq. (5.14)) versus  $[PAPG]^*$  according to Eq. (5.11).

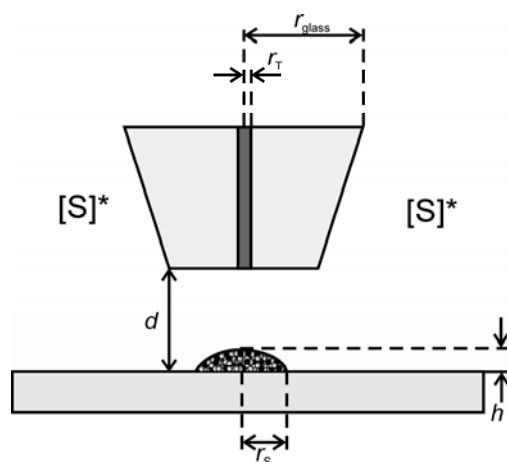


**Figure 5.11.** Schematic of SECM experiment and the associated known parameters that are used in the digital simulation.

## 5.4 Optimization of SECM imaging conditions

### 5.4.1 Hindered diffusion

The assumption that the UME does not interfere within the molecular diffusion from the spot has been questioned. It is known that when  $r_T \ll r_S$  this assumption may be considered, however if  $r_T$  is comparable to or larger than  $r_S$ , the UME can not be treated as a non-interacting probe.<sup>[148]</sup> In this work  $r_T \ll r_S$ . A sketch of the steady-state diffusion layer of the UME and sample is shown in Fig. (5.12) (not to scale). At the sample a hemispherical steady-state diffusion field of PAP is formed within few minutes after the substrate solution is

added. When the UME is brought in the close proximity to the sample a hemispherical steady-state diffusion layer of PIQ around the UME is set up.

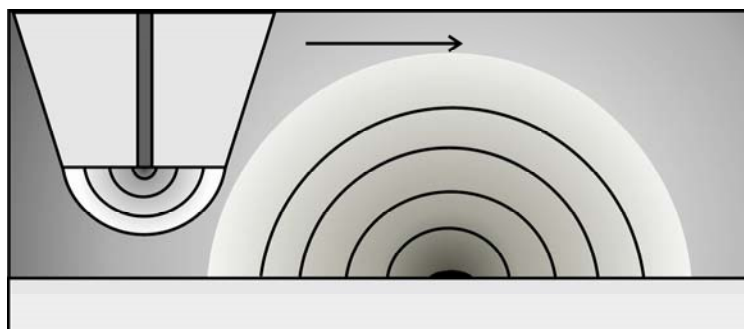


**Figure 5.12.** Diffusion field intersection. At the UME a hemispherical steady-state diffusion layer of PIQ is formed and at the sample a hemispherical steady-state diffusion layer of PAP is formed. The diffusion of PAPG to the sample is not shown.

The presence of the UME may hinder the substrate diffusion toward the sample surface (Fig. (5.13)). This diffusional shielding of the substrate due to the UME body is similar to the conventional negative feedback and has been shown by Horrocks et al.<sup>[324]</sup> by approach curves and by Zhao and Wittstock<sup>[15]</sup> by imaging experiments. This problem is obvious if the enzymes have high activity and the substrate concentration is low. Nevertheless, this problem may be solved by providing the enzyme a substrate concentration that is much larger than the  $K_M$  of the enzyme. Zhao and Wittstock<sup>[15]</sup> demonstrated that when providing a sufficiently high substrate concentration to saturate the enzymes, diffusional shielding is avoided even at smaller  $d$ .

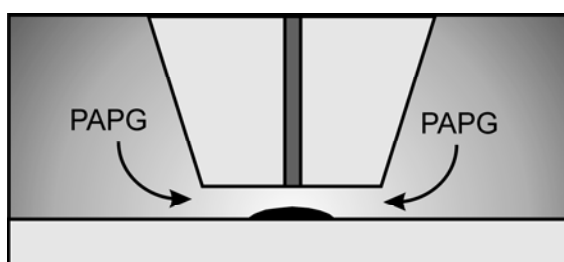


**Figure 5.13.** Hindered diffusion of PAPG towards the sample surface.

Fig. (5.14) shows a GC image of a spot of  $\beta$ -galactosidase-saturated microbeads in a 2 mM PAPG solution. The  $\beta$ -galactosidase activity was mapped by translating the UME in  $x$  and  $y$  plane at a constant  $d$ , monitoring the oxidation of PAP, formed by the galactosidase catalyzed hydrolysis of PAPG. Fig. (5.3) shows the sketch of the  $\beta$ -galactosidase activity imaging. The magnetic beads were deposited onto a hydrophobic surface placed on a magnet.

The magnetic beads were attracted by the magnetic field and formed a well defined mound-shaped bead agglomerate spot. The size of the mound-shaped spot is determined by the concentration of the beads in the bead suspension, and the spherical mound-shape is assured by the magnetic field that attracts the magnetic beads (Fig. (8.1)). The bead spot can be considered as a smooth spherical cap as the diameter of the magnetic bead ( $2.8 \mu\text{m}$ ) is much smaller than the bead spot ( $r_s = 150 - 250 \mu\text{m}$ ) and smaller than the imaging distances ( $d = 40 - 100 \mu\text{m}$ ), hence the diffusion layers of different beads overlap completely and cannot be distinguished at the working distance.<sup>[141]</sup>

The spot size in this example (Fig. (5.14)) is relatively large ( $r_s = 185 \mu\text{m}$ ,  $d = 70 \mu\text{m}$  and  $r_T = 12.5 \mu\text{m}$ ). A current decrease can be seen at the center of the spot resulting from the presence of the UME (Fig (5.14a)). The UME hindered the PAPG diffusion towards the spot. If the UME-to-sample separation is increased ( $d = 100 \mu\text{m}$ ), the PAPG can diffuse through the gap between UME and spot (Fig (5.14b)), and an increased current is observed at the center of the spot, however broad peaks and decreased signals are observed as a consequence of enlarged  $d$ . Since some substrates have limited solubility and are expensive or rare, a compromise must be found between  $d$  and  $[S]^*$  in order to have the optimum conditions for a SECM measurement and its quantification. In the next section these parameters are analyzed and the optimum parameters are found for the system under study.

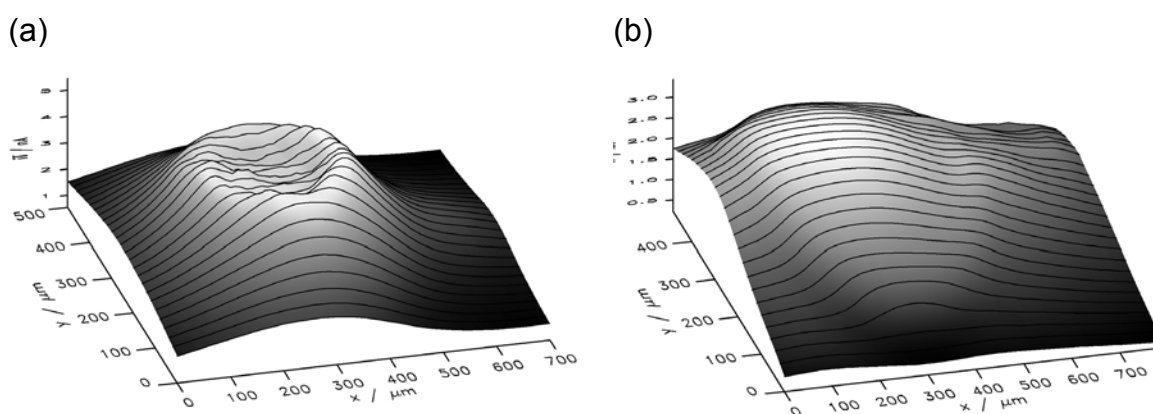


**Figure 5.14.** GC image of immobilized  $\beta$ -galactosidase on magnetic microbeads. The streptavidin-coated microbeads were saturated with biotin-labeled  $\beta$ -galactosidase and a spot was formed ( $r_s = 185 \mu\text{m}$ ). A 2 mM PAPG substrate solution was added to the system and an image was recorded with a Pt UME,  $r_T = 12.5 \mu\text{m}$  at (a)  $d = 70 \mu\text{m}$  and (b)  $d = 100 \mu\text{m}$ .

## 5.4.2 Experimental determination and simulation of the Michaelis-Menten curve

Studies on the optimization of pH, temperature, ionic environment and working potential were done by Zhao et al.<sup>[120]</sup> The Michaelis-Menten constant was also studied, but for a spot with 23% of the binding-sites saturated with  $\beta$ -galactosidase. As in this approach spots with 100% binding-sites saturation were used, and a Michaelis-Menten study was performed in order to define a PAPG concentration where an optimum activity is reached by the enzyme and the enzymatic reaction occurs under substrate saturation. This test is important because a deficiency of enzyme substrate as well as the UME shielding over the spot (due to short UME-to-sample separation) limits the PAPG diffusion to the enzyme spot and can cause distortion of recorded images and underestimation of enzyme activity (Fig. (5.14)).

In order to verify the Michaelis-Menten type dependence of the enzymatic conversion on the availability of PAPG, one bead agglomerate was prepared according to the procedure shown in the Appendix (Section 8.1.4) containing 100% of the bead binding sites saturated with biotinylated  $\beta$ -galactosidase. Substrate solutions in different concentrations were prepared (Table (8.2)) in order to perform the Michaelis-Menten study and plot the Michaelis-Menten curve. After depositing the bead spot on the hydrophobic surface, a solution containing the  $\beta$ -galactosidase substrate PAPG ( $[PAPG]^* = 0.01 \text{ mM}$ ) was added to the electrochemical cell (Table (8.2)). The UME was then positioned at several hundred micrometers laterally of the spot and an approach curve was measured by observing the  $O_2$  reduction current ( $E_T = -0.6 \text{ V}$ ). When the current decreased and the UME touched the insulating hydrophobic surface, the approach was interrupted and the UME was retracted  $40 \mu\text{m}$ . This distance was chosen because UME should move freely over the spot, without destroying the protruding bead mound and preventing the UME from shielding the diffusion of PAPG to the spot surface. Furthermore, it was assumed that the spot height was  $20 \mu\text{m}$ ,<sup>[299]</sup> hence the distance between the UME and the topmost layer of the spot was  $20 \mu\text{m}$ . It avoided a dipping of the  $i_T$  on the top of the line scan as shown in Fig. (5.14). According to Wijayawardhana et al.<sup>[299]</sup> the shape of the bead agglomeration changes with the number of beads, a bead spot has a hemispherical shape when the spot is formed from suspensions containing  $6.7 \times 10^8 \text{ beads mL}^{-1}$  and  $6.8 \times 10^6 \text{ beads mL}^{-1}$ , however for more diluted suspensions of  $4.0 \times 10^5 \text{ beads mL}^{-1}$  a bilayer (two layers of beads) is formed. In this study, a

bead suspension of  $4.7 \times 10^7$  beads  $\text{mL}^{-1}$  was used to prepare the bead spot and almost hemispherical shapes were observed.

A SECM GC image of the activity of the  $\beta$ -galactosidase-saturated bead spot was performed in order to find the center of the bead spot. At the spot center the highest current is observed. Then the substrate solution was exchanged to solution 1 and a line scan across the point of maximum current was carried out. This procedure was repeated until the highest PAPG concentration ( $[\text{PAPG}]^* = 10 \text{ mM}$ ) was used. Fig. (5.15a) shows the line scans over the spot for the different substrate concentrations. Background currents (2.8 - 23.2 pA) resulting from current offset of the potentiostat and slow accumulation of PAP in the solution bulk were subtracted. The peak currents were extracted and plotted versus  $[\text{PAPG}]^*$ . Fig. (5.15b) shows the Michaelis-Menten curve with the experimental values (open squares), the fit to the Michaelis-Menten equation (solid line) and the digital simulation (open circles). A good agreement between the experimental and the simulated values (Fig (5.15b)) can be observed.

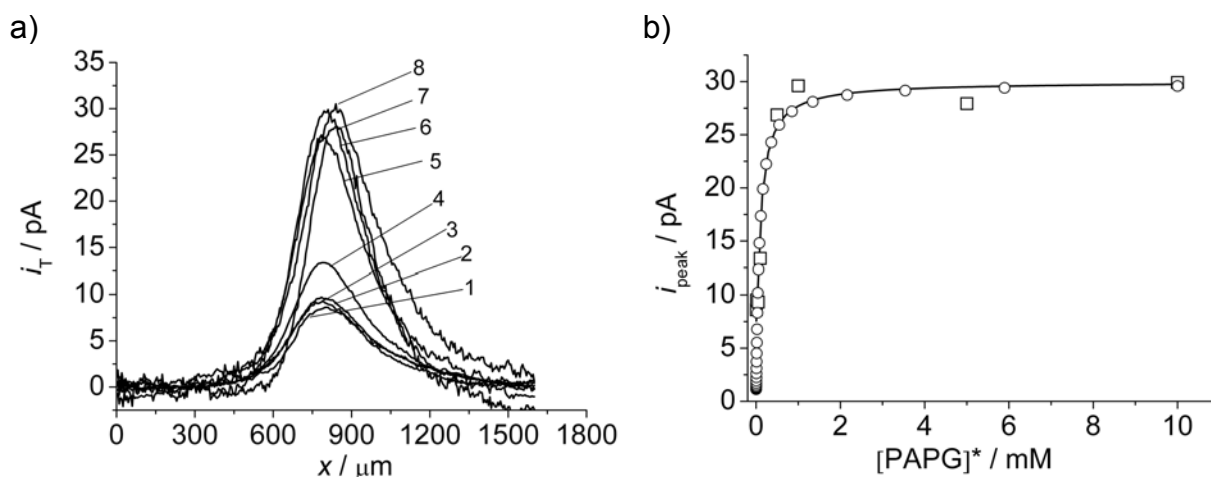


**Figure 5.15.** (a) Line scans over a bead spot saturated with  $\beta$ -galactosidase with different  $[\text{PAPG}]^*$ : 1) 0.005 mM, 2) 0.01 mM, 3) 0.05 mM, 4) 0.1 mM, 5) 0.5 mM, 6) 1.0 mM, 7) 5.0 mM, and 8) 10 mM,  $v = 10 \mu\text{m s}^{-1}$ ,  $r_T = 5 \mu\text{m}$ ,  $d = 40 \mu\text{m}$ . Constant background currents were subtracted. (b)  $\square$  experimental peak currents taken from Fig. (5.15a),  $\circ$  digital simulation, and — least square fit to experimental data with  $K_M' = (0.08 \pm 0.03) \text{ mM}$ ,  $i_{\text{peak, max}} = (30 \pm 2) \text{ pA}$

The Eq. (5.14) was fitted to the experimental peak currents  $i_{T,\text{peak}} = f([\text{PAPG}]^*)$  with  $d = 40 \mu\text{m}$ ,  $r_S = 145 \mu\text{m}$ ,  $r_T = 5 \mu\text{m}$ . The  $i_{T,\text{peak,max}} = (30 \pm 2) \text{ pA}$  and  $K_M' = (0.08 \pm 0.03) \text{ mM}$  were obtained as adjustable parameters. The  $K_M'$  was obtained as an apparent parameter because it changes according to experimental setup (e.g. amount of saturated beads and volume of bead spot) and it may be under influence of diffusional limitations, thus it is not identical to the intrinsic Michaelis-Menten constant  $K_M$  observed for dissolved enzymes. The apparent Michaelis-Menten constant  $K_M'$  is lower than the literature value of intrinsic

$K_M = 0.179 \text{ mM}^{[325]}$  reported for the native enzyme. The  $K_M'$  value of the immobilized enzyme was expected to be different from the  $K_M$  value of the native enzyme because of the conformational changes that may occur on immobilization and due to changes in affinity between enzyme and substrate. Moreover, a reason for the decrease in the apparent  $K_M'$  are the hydrophobic interactions that may influence the solution behavior present within a few molecular diameters (1 - 10 nm) from the spot surface. The enzyme is immobilized on hydrophobic microbeads which in turn are forming an agglomerate of hydrophobic enzyme-modified beads. Hydrophobic interactions may cause partition of molecules between the bulk phase and the spot microenvironment. The partition causes an increase of local PAPG concentration, reflected in an apparent decrease of  $K_M$ . Due to the neutral character of PAPG, the effect of electrostatic partition may be neglected.

The experiment was also modeled with the BEM assuming  $k_{\text{cat}}\Gamma_{\text{enz}} = 4.9 \times 10^{-12} \text{ mol cm}^{-2} \text{ s}^{-1}$  for  $K_M' = 0.082 \text{ mM}$ . The results are shown in Fig. (5.15b) as open circles. Note that no assumption regarding a non-interacting probe was made in the simulation. The diffusion of PAPG and PAP are truly modeled in 3D. The data agree almost perfectly with the function fitted to the experimental data (Eq. (5.14)). This provides evidence that the assumption made in treating the experimental data (non-interacting probe) is a reasonable approximation for the experimental situation. Furthermore it was seen that with  $[\text{PAPG}]^* = 2 \text{ mM}$  the experiment is carried out under conditions of substrate saturation, i.e. the presence of the SECM probe does not block the flux of PAPG so that a noticeable effect can be detected in the flux of PAP coming from the sample.

In order to study the effects of external diffusion,  $k_L$  was calculated from Eq. (5.16). Assuming that  $D_{\text{PAPG}} = D_{\text{PAP}} = 9.2 \times 10^{-6} \text{ cm}^2 \text{ s}^{-1}[326]$  and  $r_S = 145 \times 10^{-4} \text{ cm}$ , this results in  $k_L = 8.1 \times 10^{-4} \text{ cm s}^{-1}$ . The  $v_{\text{max}}$  can be calculated from Eq. (5.14), considering  $v_{\text{max}} = k_{\text{cat}}\Gamma_{\text{enz}}$  and taking  $i_{T,\text{peak}}$  as the maximum value extracted from the fitting of the experimental data in Fig. (5.15b) to a Michaelis-Menten curve gives  $v_{\text{max}} = 3.29 \times 10^{-12} \text{ mol s}^{-1} \text{ cm}^{-2}$ . Substituting  $k_L$ ,  $K_M$  and  $v_{\text{max}}$  in Eq. (5.17) leads to  $\mu = 0.05$ . The Damköhler number was found to be  $\mu \ll 1$  meaning that the rate of substrate diffusion (expressed by  $k_L$ ) is higher than the rate of enzymatic substrate conversion (expressed by  $v_{\text{max}}/K_M$ ) and the overall rate of the process is under kinetic control of the enzyme (no external diffusion control), thus Eq. (5.5) prevails.

For investigation of mass transport through the bead spots,  $[\text{PAPG}]^*$  is the bulk concentration of PAPG and was added in excess ( $[\text{PAPG}]^* \gg K_M$ ), the product of the enzymatic reaction is PAP and is initially zero in the bulk phase. The enzyme surface

concentration  $\Gamma_{enz}$  can be estimated according to experimental conditions, and  $d$ ,  $r_T$ ,  $r_S$  and  $n$  are known parameters.

For the study of internal diffusion limitation within the spot the effect of external diffusion limitation may be neglected by the fact that the substrate is given in excess, the reaction on the spot surface is kinetically controlled, hence the substrate is available for diffusion within the spot pores in order to be converted by the enzyme. Therefore an investigation of the effects of internal substrate diffusion within the spots is described in Section 5.5.

### 5.4.3 Study of the bead spot height

A spot array formed according to the dilutions shown in Table (8.1) was formed and the height of bead spots was investigated. The analysis of the spot height is very important for the experimental setup because the  $d$  must be chosen to avoid diffusional shielding and collision of the UME and the protruding bead spot. SCLM was used to record image stacks (3-dimensional data sets, intensity =  $f(x, y, z)$ ) of each bead spot dilution to measure the spot height.

In order to record a 3D data set of a bead spot with SCLM, stacks of single images was recorded at different planes of the bead spot by moving the sample along the optical axis ( $z$ ) by controlled step sizes. The number of recorded single images depends on the step sizes (distance between the single images) and on the total height of the image stack. Here step sizes of  $1.4 \mu\text{m}$  (bead diameter =  $2.8 \mu\text{m}$ ) were used leading to well resolved images. A 3D reconstruction of the sample provided information about the spatial structure of the sample, such as bead spot height. The profile function of SCLM was used to calculate the bead spot height after reconstruction of the sample (Table (5.1) and Fig. (5.16)). The uncertainties given in Table (5.1) arise from the mean value calculated from two line profiles of each spot.

**Table 5.1:** Bead spot heights and radii.

Spot	% Gal. in spot	$r_S / \mu\text{m}$	$h / \mu\text{m}$
1	100	$217 \pm 18$	$19 \pm 3$
2	91	$241 \pm 6$	$16 \pm 2$
3	67	$226 \pm 8$	$19 \pm 2$
4	50	$290 \pm 12$	$23 \pm 2$
5	20	$311 \pm 8$	$37 \pm 3$
6	10	$492 \pm 64$	$38 \pm 4$



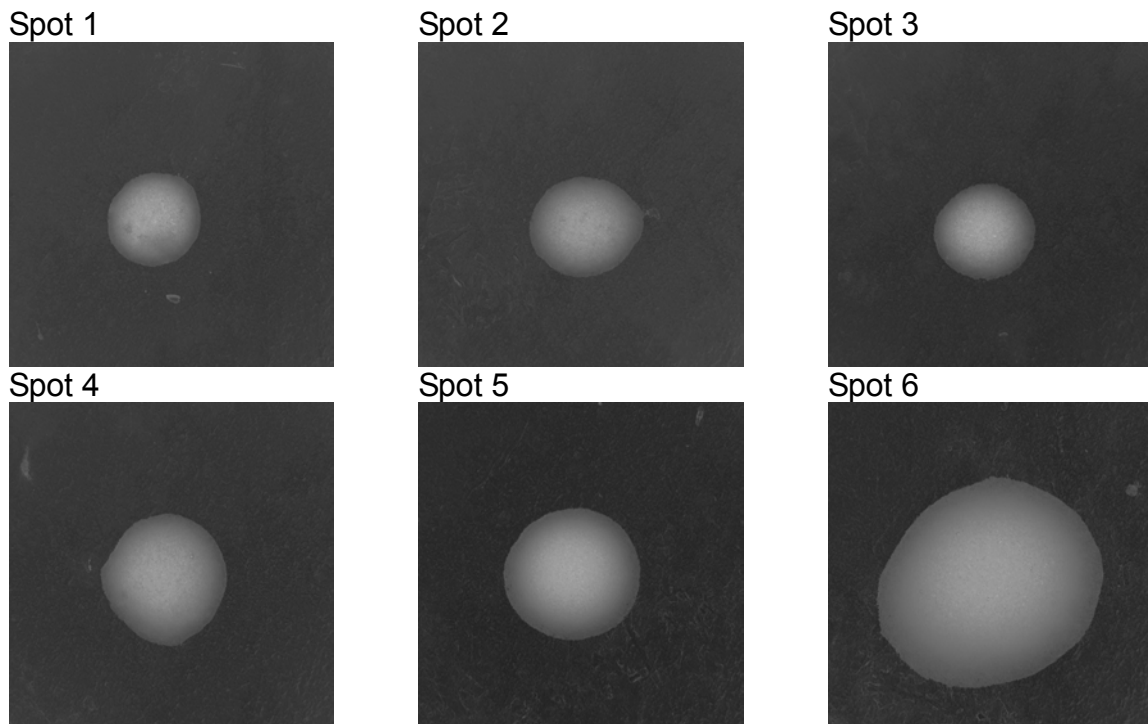


**Figure 5.16.** 3D reconstruction of stacks (topography) recorded on SCLM. The bead spots were prepared according to Table (8.1).

From Table (5.1) one can see that the radius of the spots increases with the increase of amount of bare beads in the spot, reflecting also in the height. The spots have hemispherical shapes that are more similar to the spot shape proposed by Model 1 represented by Fig. (5.10a). The height of the spot is much smaller than the radius, so the Model 2 is not appropriate to estimate the diffusion inside the experimental spots, however it gives an upper and lower boundary. An example of a line profile extracted from Spot 5 after 3D reconstruction is shown in Fig. (5.17). One can see that the bead spot has a sharp edge and a smooth layer-cap shape rather than a half-sphere shape. Two perpendicular line profiles were extracted from each spot, thus  $h$  and  $r_s$  could be estimated from the mean value of these two line profiles.

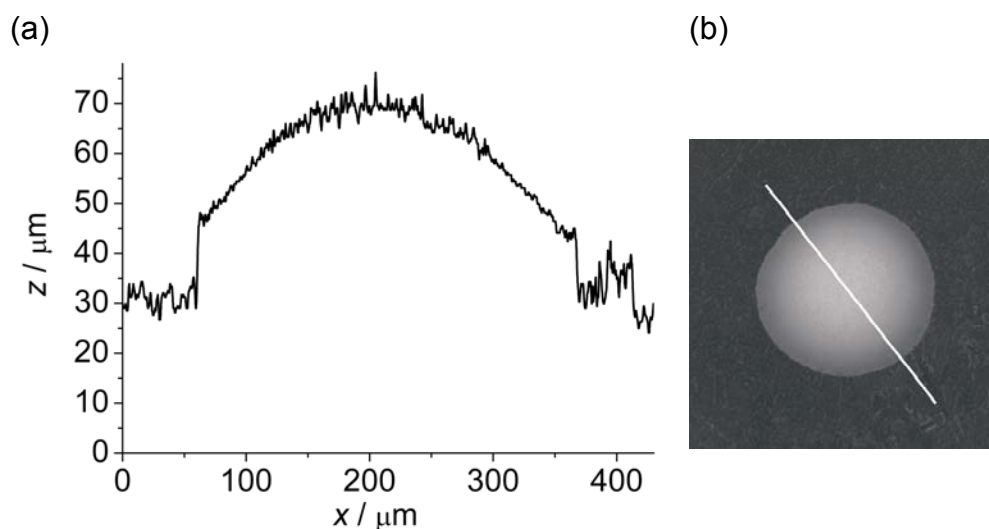


**Figure 5.17.** Line profile (a) extracted from Spot 5. (b) After 3D reconstruction, the profile was extracted giving the height and the radius of the spot.

The measurements made here with the SCLM give the representative values of  $h$  that were used to estimate an adhesion angle  $\alpha = (12.5 \pm 3.5)^\circ$  used in the simulations of Models 1 and 2. The profile of the other spots (not shown here) had the same shape, although  $h$  varied according to the total number of beads present in the agglomerate. This variation is understood as the lateral force acting on an individual bead compared with the vertical magnetic force imposed by the magnet. Wijayawardhana et al.<sup>[299]</sup> showed that the lateral force grows as the total number of beads contained in an agglomerate increases, eventually leading to agglomerates with shapes close to a hemisphere as shown here.

For the investigation of shielding effects inside bead spots, two shapes have been considered for the calculation of the PAP fluxes of coming from individual beads from the SECM measurement: \* disk-shaped spots (exp - disk\*) in which only the superficial beads are considered, and layer-cap-shaped spots (exp - volume\*) in which all the beads present in the volume of the spots are considered. The digital simulation used to investigate the internal diffusion of PAPG inside the spots considered two different spot geometries, uniform bead layer and half-sphere, and among the half-sphere three cases were analyzed regarding the amount of beads in the spot. A block diagram (Fig. (5.18)) shows the considered spot shapes for the experimental and simulation data.

\* The abbreviations, exp - disk and exp - volume, are given to the experimental spot geometries in order to differentiate the experimental from simulation spot shapes.

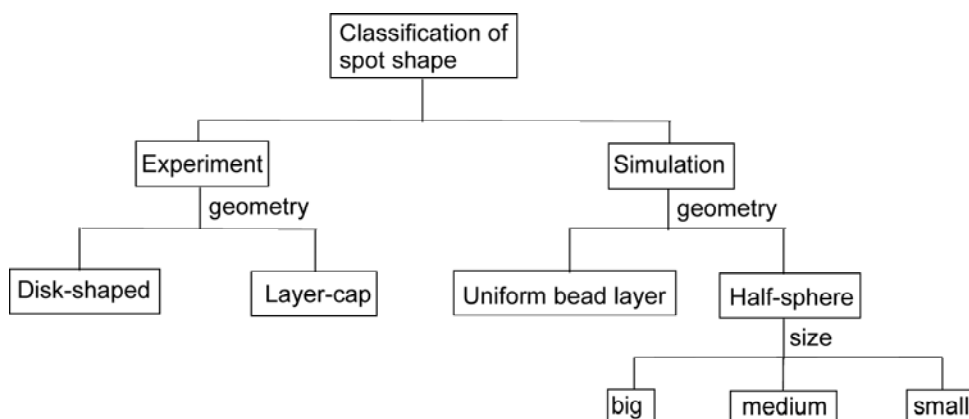


**Figure 5.18.** Classification of spot shape.

## 5.5 Investigation of the shielding inside the bead spot

### 5.5.1 Experimental data

Two batches of  $\beta$ -galactosidase-modified beads and bare beads were prepared. From them, mixtures containing  $\beta$ -galactosidase-modified and bare beads in different ratios (Table (8.1)) were made. From these suspensions, bead spots were formed (according to Section 8.1.6). A random distribution of the bare beads and the  $\beta$ -galactosidase-modified beads in the reagent glasses and consequently in the spot was expected.

Since the total amount of beads in each spot is different, the resulting agglomerates have different sizes. Furthermore, there is a variability on the size coming from the preparation of the beads and from the deposition. Optical microphotographs of the six investigated bead spots are given in Fig. (5.19). The spots were arranged on two microscope slides from which GC images were recorded (Fig. (5.20)). The bead spots had increasing bead numbers and therefore spots with increasing sizes were formed, so the UME-substrate distance had to be large enough to scan over the spots avoiding a collision of the UME and the protruding bead mound. Furthermore smaller UME-substrate distances may limit the diffusion of PAPG to the spot misleading the recorded image and causing a false result interpretation as shown in Fig. (5.14a).

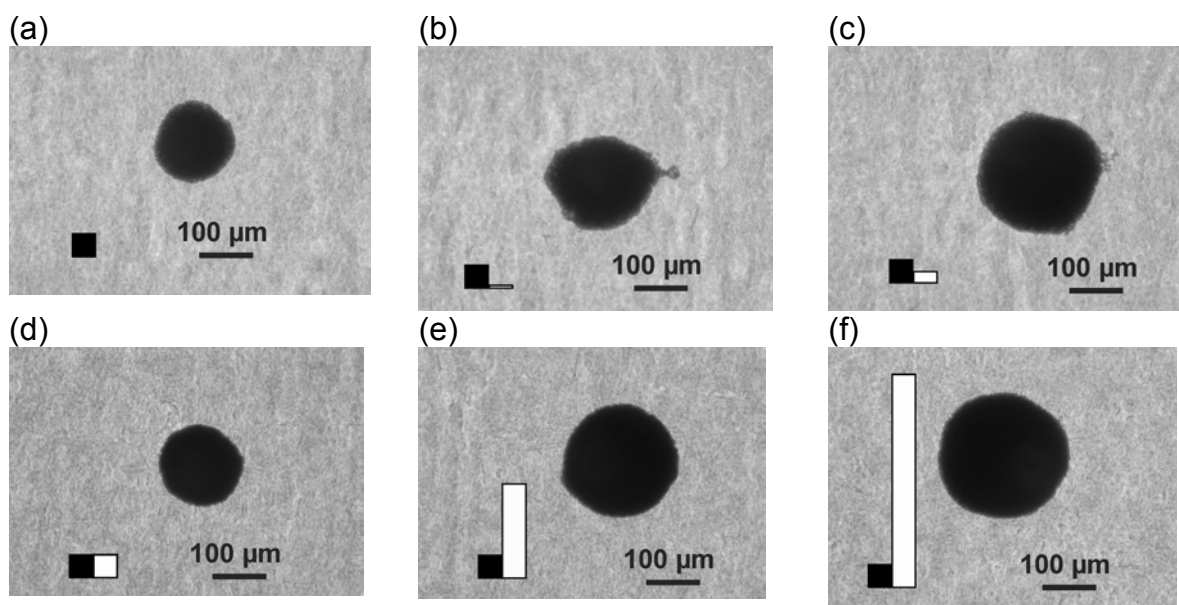


**Figure 5.19.** Microscope pictures of the spotted microbeads. (a) Spot 1 (100% immobilized  $\beta$ -galactosidase in spot), (b) spot 2 (91% immobilized  $\beta$ -galactosidase in spot), (c) spot 3 (67% immobilized  $\beta$ -galactosidase in spot), (d) spot 4 (50% immobilized  $\beta$ -galactosidase in spot), (e) spot 5 (20% immobilized  $\beta$ -galactosidase in spot) and (f) spot 6 (10% immobilized  $\beta$ -galactosidase in spot). The columns in the picture represent the amount of galactosidase-modified beads (black column) and the amount of bare beads (white column) present in the bead spot.

The SECM images (Fig. (5.20)) are a function of the different overall catalytic conversion by the bead spots. Each spot contains the same amount of the  $\beta$ -galactosidase but the amounts of bare beads are different. A qualitative inspection of the figures reveals that the number of added bare beads has a significant influence on the recorded UME currents. The recorded faradaic current at the UME caused by oxidation of PAP that diffused from the bead spot surface are different because of the different amount of bare beads present in the spots, leading to different shielding of PAPG flux to the enzymes.

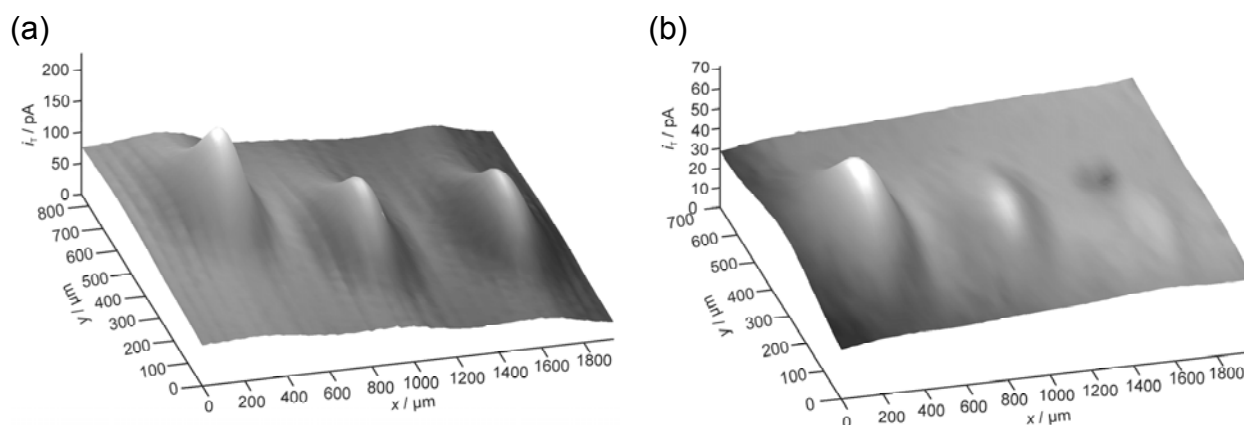


**Figure 5.20.** GC image of enzyme activity of (a) spot 1, spot 2, and spot 3 from left to right; and (b) spot 4, spot 5, and spot 6 from left to right.

Profiles for each spot passing across the center of the spot were extracted from Fig. (5.20) and a constant offset due to instrumental offsets of the potentiostat and the data acquisition board, and slow accumulation of traces of PAP in the solution were subtracted (Fig. (5.21)). An average behavior of all immobilized enzymes was considered.

The data points were fitted to Eqs. (2.21) and (2.22) yielding the exact working distance  $d$ , the spot size  $r_s$ , and  $[PAP]_s$ . However, the initial parameters for the fittings must be input and can either be set as variable or fixed values in order to provide an accurate result. The values of the spot radii determined from the microphotographs (Fig. (5.19) and Table (5.2)) were given as start parameters and were fixed (no variation for the fit was allowed). The working distances  $d$  were also given as fixed values and were 100  $\mu\text{m}$  for spots 1, 2, and 3 and 90  $\mu\text{m}$  for spots 4, 5, and 6. These values were the distances the UME was retracted after approach. After setting the initial parameters, the line scans extracted from the bead spot images (Fig. (5.21)) that passed through the highest current value were fitted to Eqs. (2.21) and (2.22). Fig. (5.22) shows an example of a line scan extracted from the image that passes through the highest current value of spot 1. The image cross section diagonal gives a symmetric profile, thus the theoretical curve (line) fits to experimental curve (open squares) perfectly. From the fit  $[PAP]_s$  is obtained. The results for all 6 spots are collected in Table (5.2). The uncertainty ranges are calculated from the uncertainty interval of the non-linear least-square fitting used.

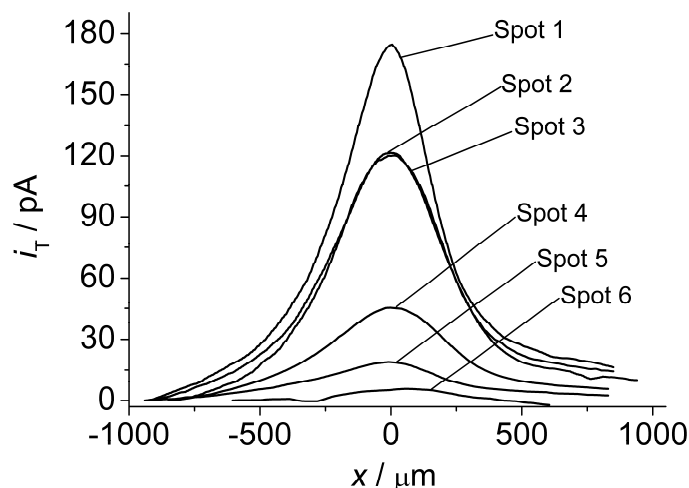


**Figure 5.21.** Experimental line scan profiles of the bead spots extracted from GC images. Constant offset currents were subtracted from the experimental curves for comparison. Spot 1:  $i_{\text{off}} = 51.34$  pA, spot 2:  $i_{\text{off}} = 44.4$  pA, spot 3:  $i_{\text{off}} = 27.94$  pA, spot 4:  $i_{\text{off}} = 26.62$  pA, spot 5:  $i_{\text{off}} = 33.21$  pA, and spot 6:  $i_{\text{off}} = 37.4$  pA.

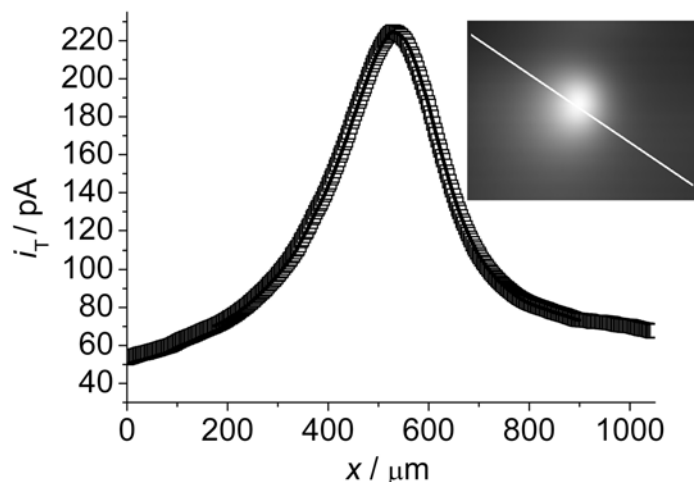


**Figure 5.22.** Line scan profile of the GC mode image of  $\beta$ -galactosidase activity of spot 1. The profile across the experimental image is shown as open squares and the fitted curve as solid line.  $[\text{PAPG}]^* = 2$  mM,  $r_T = 12.5$   $\mu\text{m}$ , and  $v = 30$   $\mu\text{m s}^{-1}$ . Fitting parameters:  $r_T = 12.5$   $\mu\text{m}$ ,  $r_S = 75.64$   $\mu\text{m}$ ,  $d = 100$   $\mu\text{m}$ , and  $D_{\text{PAP}} = 9.2 \times 10^{-6}$   $\text{cm}^2 \text{s}^{-1}$ .

## 5.5.2 Calculation of PAP fluxes

Using the obtained  $r_S$ ,  $[\text{PAP}]_S$  ( $d=0$ ), and  $D_{\text{PAP}} = 9.2 \times 10^{-6}$   $\text{cm}^2 \text{s}^{-1}$ ,<sup>[326]</sup> one obtains the integrated external flux  $\Omega$  of PAP from the entire bead spot according to Eq. (2.24). Assuming a uniform flux over the entire area of the bead agglomerate, an estimate of the generation rate  $J$  is obtained using Eq. (2.25). The PAP flux is related to the concentration profile of the

enzymatic reaction over the spot and two limiting cases can be distinguished according to the distribution of the flux across the spot surface.<sup>[147]</sup> One case is when the substrate diffusion limits the enzymatic reaction causing a non-uniform flux across the spot. Alternatively, if the substrate concentration is above  $K_M$  and the diffusion-limited flux of substrate to enzyme is greater than the flux of the enzyme-catalyzed reaction, and a uniform flux over the spot is set up. Such a uniform flux of PAP over the microspot area was assumed ( $[PAPG]^* \gg K_M$ ). As discussed in Section 5.4.2, the enzymatic reaction is kinetically-controlled, hence the substrate concentration at the spot surface is not effectively zero, i.e. PAPG may be available for penetration into the spot reaching the  $\beta$ -galactosidase-modified beads encountered inside the spot. Moreover, in the case of more diluted spots, one may find more  $\beta$ -galactosidase-modified beads inside the spot than outside. Nevertheless, inside the spots the enzymatic reaction occurs simultaneously with the substrate and product diffusion and not all enzyme molecules within the spot are in contact with the same substrate concentration as the enzymes present in the outer part of the spot.

The results calculated from the profile fitting are given in Table (5.2). Larger bead spots were formed due to increasing quantity of bare beads added to the suspension containing a constant number of  $\beta$ -galactosidase-modified beads. It is clearly evident that both  $\Omega$  and  $J$  values decrease with increasing amount of bare beads in the agglomerate, although the  $\beta$ -galactosidase-modified bead amount is constant in all spots. This illustrates that the presence of bare beads shields the  $\beta$ -galactosidase-modified beads from the flux of PAPG.

**Table 5.2:** Quantification of kinetic parameters:

Spot	$\chi^{(a)}$	$d / \mu\text{m}$	$r_s / \mu\text{m}^{(b)}$	$[PAP]_s / 10^{-8} \text{ mol cm}^{-3}$	$\Omega / 10^{-14} \text{ mol s}^{-1}$	$J / 10^{-11} \text{ mol s}^{-1} \text{ cm}^{-2}$
1	100	$100 \pm 10$	75.6	$5.9 \pm 0.5$	$1.6 \pm 0.1$	$9.1 \pm 0.7$
2	91	$100 \pm 10$	95.5	$4.6 \pm 0.3$	$1.4 \pm 0.1$	$5.0 \pm 0.4$
3	67	$100 \pm 10$	116.2	$3.5 \pm 0.3$	$1.5 \pm 0.1$	$3.5 \pm 0.3$
4	50	$90 \pm 10$	78.1	$1.3 \pm 0.1$	$0.4 \pm 0.03$	$2.0 \pm 0.2$
5	20	$90 \pm 10$	109.7	$0.5 \pm 0.1$	$0.2 \pm 0.02$	$0.5 \pm 0.04$
6	10	$90 \pm 10$	121.7	$0.2 \pm 0.1$	$0.1 \pm 0.01$	$0.2 \pm 0.02$

(a) saturation of  $\beta$ -galactosidase in the spot in %

(b) from scanning confocal laser micrographs in reflection mode

Fig. (5.23) shows a plot of (a)  $[PAP]_s$  and (b)  $J$  versus  $\chi$ . The contribution of the buried  $\beta$ -galactosidase-modified beads to the PAP production decreased with the increase of the total amount of bare beads. The bare beads that are at the outer surface block the diffusion of PAPG to the  $\beta$ -galactosidase saturated microbeads that are buried in the spot, hence they

hinder the PAP formation in the inner  $\beta$ -galactosidase saturated microbeads. Moreover, the decrease in the PAP production can be caused by the progressive depletion of the PAPG toward the center of the spot. Here one has a situation in which the substrate diffusion to the inner part of the microspot is limited so the conversion rate is not uniform within the spot. If this is true, the reaction inside the spot is partially diffusion-controlled and does not obey the Michaelis-Menten kinetics. The steric conformation of the immobilized enzyme on the microbead encountered in the down part of the bead<sup>1</sup> can also contribute to the hindrance of PAP formation because the enzymes are not in favorable positions to catalyze the reaction and the PAPG may not reach the active site of the enzyme. If all  $\beta$ -galactosidase modified beads would equally contribute to the PAP formation, the generation rate should be constant. One can conclude that even with the same amount of  $\beta$ -galactosidase-modified beads in the spot, the real contribution to the PAP flux comes from the saturated beads that are encountered in the outer layers of the spot, thus only the first and maybe the second bead layer contribute to the PAP formation (Fig. (5.8a)). Spot 1 shows a relatively high  $J$  indicating that all the saturated beads contained in the outer surface contribute to the PAP formation, however this value deviates from the  $J$  values obtained for other spots.

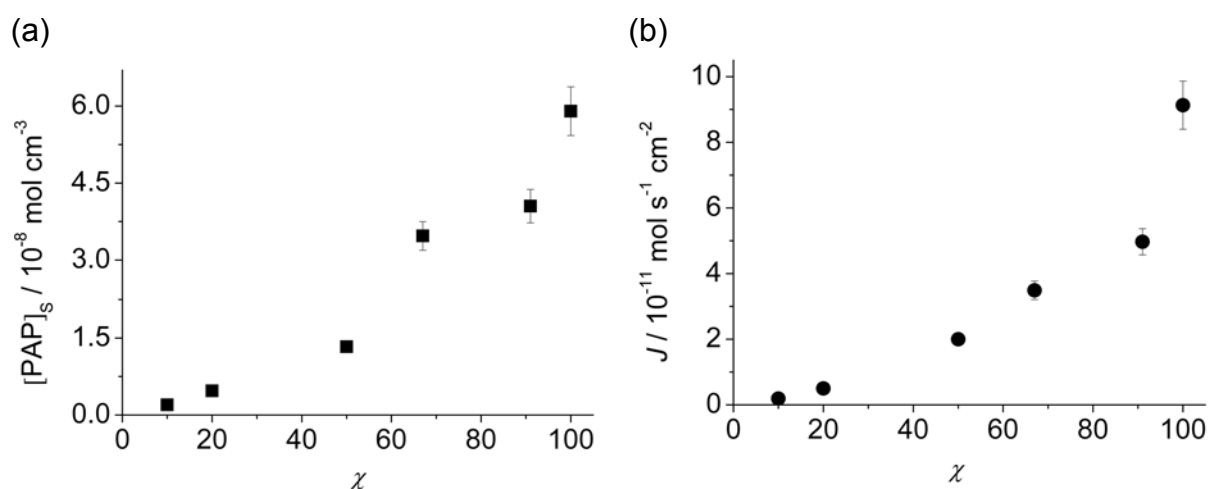


**Figure 5.23.** Plot of (a)  $[PAP]_s$  of the spots extracted from the fit to the image profile, and (b) PAP generation rate related to the projected area of the spot  $J$  versus  $\chi$ .

If all modified beads would contribute to the formation of PAP, a constant value should be found, if the integrated flux  $\Omega$  is related to the number of  $\beta$ -galactosidase-modified beads at the surface of the agglomerate. For this treatment an upper boundary of the value  $k_{\text{cat}}\Gamma_{\text{enz}}$  of the modified beads is estimated. For this purpose all the contributing enzymes are projected to

<sup>1</sup> Down part of the bead refers to the side of the bead that is not in contact with the solution, but in direct contact to another bead.



an area of  $A_{\text{spot}} = \pi \cdot r_s^2$ . Assuming the bead spot as a disk where only the modified-bead at the surface contribute to the PAP flux (exp - disk), the effective number of beads  $N_{\text{b,eff}}$  at the surface of the bead spot can be calculated assuming that the ratio between the cross-section of the individual beads  $A_{\text{cross,bead}} = \pi \cdot r_{\text{bead}}^2$  and the cross section of the spot  $A_{\text{spot}}$  results in an effective number of:

$$N_{\text{b,eff}} = \frac{r_s^2}{r_{\text{bead}}^2} \quad (5.40)$$

Multiplying the effective number of beads at the spot surface with the fraction  $\chi$  of  $\beta$ -galactosidase-modified beads yields  $N_{\text{b,eff,gal}}$  as described by Eq. (5.33). Thus, the flux of PAP produced per individual bead can be evaluated:

$$\Omega_{\text{bead}} = \frac{\Omega}{N_{\text{b,eff,gal}}} \quad (5.41)$$

The flux from an individual bead can be expressed in number of PAP molecules produced per second by a single bead  $M_{\text{PAP}}$  by multiplying  $\Omega_{\text{bead}}$  with the Avogadro number  $N_A$ .

$$M_{\text{PAP}} = \Omega_{\text{bead}} \cdot N_A \quad (5.42)$$

Table (5.3) shows  $N_{\text{b,eff}}$ ,  $N_{\text{b,eff,gal}}$ ,  $\Omega_{\text{bead}}$ ,  $M_{\text{PAP}}$  of each spot. Considering the flux of PAP produced per each bead  $\Omega_{\text{bead}}$  and the total number of PAP molecules per bead  $M_{\text{PAP}}$ , one can see that the contribution of a single bead varies and is dependent on the amount of bare beads in the spot. The value of  $\Omega_{\text{bead}}$  and  $M_{\text{PAP}}$  should be constant if all modified beads contributed equally to the PAP flux, however one can see that this is not the case and the calculated flux per bead is not a constant value. A variation in  $\Omega_{\text{bead}}$  and  $M_{\text{PAP}}$  of a factor up to 4.5 was observed. As these values decrease, it shows that beads that are accessible at the spot surface contribute significantly more to the flux, and thus  $N_{\text{b,eff,gal}}$  is effectively smaller. The uncertainty ranges are calculated from the error propagation of the parameters calculated in Table (5.2).

**Table 5.3:** Calculated values of  $N_{b,eff}$ ,  $N_{b,eff,gal}$ ,  $\Omega_{bead}$ , and  $M_{PAP}$ :

Spot	$\chi$	$N_{b,eff}$	$N_{b,eff,gal}^{(a)}$	$\Omega_{bead} / 10^{-18} \text{ mol s}^{-1}$	$M_{PAP} / 10^6 \text{ molecules s}^{-1}$
1	100	2919	2919	$5.6 \pm 0.5$	$3.4 \pm 0.3$
2	91	4648	4230	$3.4 \pm 0.3$	$2.0 \pm 0.2$
3	67	6888	4615	$3.2 \pm 0.3$	$1.9 \pm 0.2$
4	50	3108	1554	$2.5 \pm 0.2$	$1.5 \pm 0.1$
5	20	6143	1229	$1.6 \pm 0.1$	$0.9 \pm 0.1$
6	10	7560	756	$1.2 \pm 0.1$	$0.7 \pm 0.1$

(a) The microbead radius is  $1.4 \mu\text{m}$

Fig. (5.24) shows a plot of  $\Omega_{bead}$  and  $M_{PAP}$  versus  $\chi$ . From this plot it is evident that the number of generated PAP molecules per bead as well as the flux generated per bead decreases with the increase of unmodified beads in the spot.

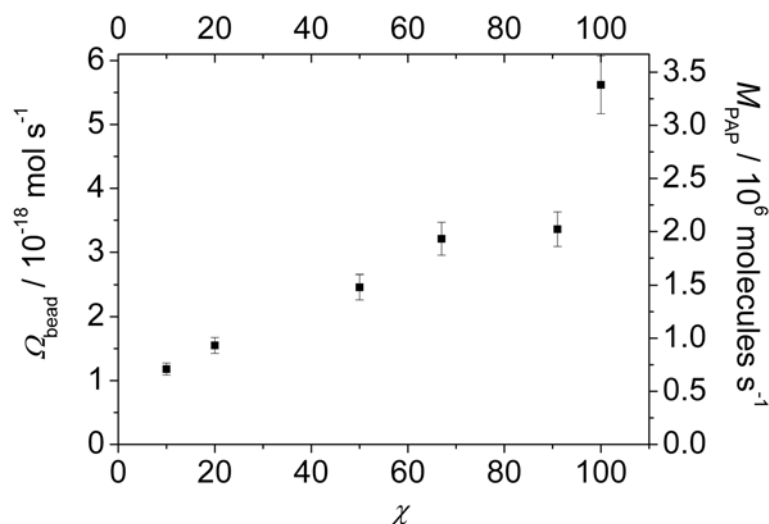


**Figure 5.24.** Plot of PAP flux produced per bead ( $\Omega_{bead}$ ) and number of molecules produced per second by a single bead ( $M_{PAP}$ ) versus  $\chi$ .

Considering the spot as a layer-cap as shown in Fig. (5.10a), and assuming that the beads present in the spot volume contribute to the PAP flux (exp - volume), one can estimate the total number of beads in the spot (Eq. (5.32)) using the equations of Model 1. Thus, one can estimate the total number of modified beads present in the volume of the spot (Eq. (5.33)). It leads to other values of  $\Omega_{bead}$  and  $M_{PAP}$  as shown in Table (5.4):

**Table 5.4:** Calculated values of  $N_{tot}$ ,  $N_{tot,gal}$ ,  $\Omega_{bead}$ , and  $M_{PAP}$  for the case that the beads that are inside the spot also contribute to the overall PAP flux:

Spot	$\chi$	$N_{tot}$	$N_{tot,gal}$	$\Omega_{bead} / 10^{-18} \text{ mol s}^{-1}$	$M_{PAP} / 10^6 \text{ molecules s}^{-1}$
1	100	4815	4815	3.4	2.1
2	91	9676	8797	1.6	1.0
3	67	17454	11636	1.3	0.8
4	50	5291	2645	1.4	0.9
5	20	14701	2938	0.6	0.4
6	10	20071	2006	0.4	0.3

Comparing the values of  $\Omega_{bead}$  and  $M_{PAP}$  for a disk-shaped spot (Table (5.3)) and a layer-cap-shaped spot (Table (5.4)), one can see a decrease of the PAP flow contributed by one bead in dependence of  $\chi$ . The disk-shaped model showed a decrease in  $\Omega_{bead}$  and  $M_{PAP}$  with  $\chi$ , however these values were up to 3-fold higher than the values calculated for the layer-cap-shaped spots even though the beads present in the spot volume were considered for this approach. This can be explained because the  $\beta$ -galactosidase-modified beads of the layer-cap-shaped spot are distributed inside the spot volume suffering the influence of internal diffusional shielding, what is not considered in the disk-shaped model. It is an evidence that the main contribution is coming from the beads at the surface, although the inner layers do have some influence on the PAP flux. In the next Section the internal diffusion problem of the Models 1 and 2 introduced in Section 5.2.1 is analyzed and compared with the experimental data.

### 5.5.3 Analysis of the internal diffusion

In order to analyze the internal diffusion, one has to obtain  $v_{max}$  and  $K_M'$  of  $\beta$ -galactosidase immobilized on a bead surface free in solution. In contrast to the previously discussed results, the beads are suspended in solution. This gives the kinetic parameters without the effect of diffusion limitation inside the agglomerates. In order to find this value,  $\beta$ -galactosidase was immobilized on the bead surface according to the Appendix (Section 8.1.4). Differential pulse voltammetry (DPV) was used to measure the conversion from which  $v_{max}$  and  $K_M'$  were calculated (Appendix, Section 8.1.8).  $v_{max} = 1.56 \times 10^{-4} \text{ mM s}^{-1}$  and  $K_M = 0.418 \text{ mM}$  were obtained for modified beads free in solution. Thus, the flux of PAP generated per bead free in the solution  $\Omega_{bead,free}$  can be calculated:

$$\Omega_{\text{bead,free}} = \frac{v_{\text{max}} V_{\text{sol}}}{N_{\text{bead}}} \quad (5.43)$$

where  $v_{\text{max}}$  is the maximum rate obtained from DPV experiment of the beads free in solution ( $1.56 \times 10^{-4} \text{ mM s}^{-1}$ ),  $V_{\text{sol}}$  is the total volume of the solution used in the DPV measurement ( $120 \mu\text{L}$ ), and  $N_{\text{bead}}$  is the total number of beads added to the DPV experiment (934000). Hence,  $\Omega_{\text{bead,free}} = 2.0 \times 10^{-17} \text{ mol s}^{-1}$ . This value is about one order of magnitude higher than the value found within bead spots.

The numerical integration of Eqs. (5.34) and (5.38) gives the radial concentration profile  $\varphi$  ( $\rho$ ) of the substrate as function of  $\phi$ , allowing the computation of the overall rate of substrate consumption within the spot  $v$ .<sup>[269]</sup>  $\varphi$  has been plotted as a function of  $\rho$  with  $\phi$  as parameter (Figs. (5.25), (5.26), (5.27)). The four cases mentioned in Section 5.2.1 were analyzed in order to be compared with the results obtained with the SECM measurement and find out which type of diffusion occurs inside the microbead agglomerate system. The next Sections (5.5.4, 5.5.5, 5.5.6, 5.5.7) shows the qualitative diffusion behaviors of distinct systems leading to an estimative of fundamental quantities such as fluxes and collection rates.

#### 5.5.4 Diffusion Model 1: uniform layer of beads

The spot is treated as a layer of beads with a thickness  $h$  calculated according to Eq. (5.29) (Fig. (5.10a)). The  $V_{\text{spot}}$  is estimated with the help of the experimental  $r_s$  and the estimated  $h$  using Eq. (5.31). The total number of beads in the spot  $N_{\text{tot}}$  can be estimated from the  $V_{\text{spot}}$ ,  $V_{\text{bead}}$  and  $\zeta$  (Eq. (5.32)), leading to the total number of active beads in the spots  $N_{\text{tot,gal}}$ . The overall maximum rate of reaction  $v_{\text{max}}$  (Eq. (5.44)) was used to calculate the  $\phi$  (Eq. (5.24)), with  $A = h/2$ :

$$v_{\text{max}} = \frac{N_{\text{tot,gal}} \Omega_{\text{bead,free}}}{V_{\text{spot}}} \quad (5.44)$$

**Table 5.5:** Calculated parameters for uniform layer of beads of Model1 for the numerical solution of the differential equation (5.34).

$\chi$	$r_s / \mu\text{m}$	$h / \mu\text{m}$	$V_{\text{spot}} / 10^{-7} \text{cm}^3$	$N_{\text{tot}}$	$N_{\text{tot,gal}}$	$v_{\text{max}} / 10^{-6} \frac{\text{mol}}{\text{cm}^3 \text{s}^{-1}}$	$\lambda / \mu\text{m}$	$\phi$
100	75.6	8.3	0.7	4815	4815	1.3	4.1	0.59
91	95.5	10.5	1.5	9676	8797	1.2	5.2	0.70
67	116.2	12.7	2.7	17454	11636	0.9	6.3	0.73
50	78.1	8.5	0.8	5291	2645	0.6	4.2	0.43
20	109.7	12.0	2.3	14701	2938	0.3	6.0	0.38
10	121.7	13.3	3.1	20071	2006	0.1	6.6	0.30

The numerical solution of the differential Eq. (5.34) gives a concentration profile of PAPG within the spot (Fig. (5.25)) and considers the spot as bead layers. Considering that  $D_{\text{PAP}} = D_{\text{PAPG}}$  one can estimate the  $[\text{PAPG}]_s$  necessary to calculate  $\phi$  as following:

$$[\text{PAPG}]_s = [\text{PAPG}]^* - [\text{PAP}]_s \quad (5.45)$$

where  $[\text{PAP}]_s$  was obtained from the fit of the line profiles of the experimental SECM image. This assumption was used to have the  $[\text{PAPG}]_s$  for all Models.

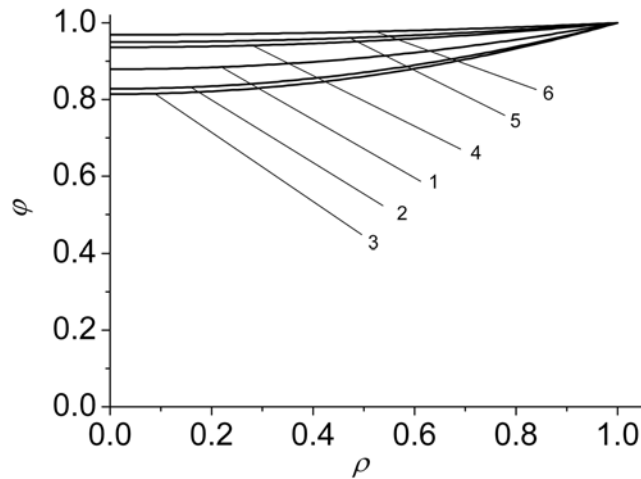


**Figure 5.25.** Concentration profile of PAPG within a bead layer with different saturation of active spots  $\chi$  and different thickness  $h$ . 1)  $\chi = 100\%$ ,  $h = 8.24 \mu\text{m}$ ; 2)  $\chi = 91\%$ ,  $h = 10.05 \mu\text{m}$ ; 3)  $\chi = 67\%$ ,  $h = 12.70 \mu\text{m}$ ; 4)  $\chi = 50\%$ ,  $h = 8.55 \mu\text{m}$ ; 5)  $\chi = 20\%$ ,  $h = 12.0 \mu\text{m}$ ; 6)  $\chi = 10\%$ ,  $h = 13.3 \mu\text{m}$ .

The concentration profiles from Fig. (5.25) show that for this geometry the substrate can diffuse within the spot, although a small amount of PAPG is consumed throughout the spot. If the PAPG is available, it can be converted into PAP by the immobilized enzyme encountered

deep in the spot. The small value of  $\phi$  is an evidence that the reaction in the spot is not diffusion-controlled and follows the Michaelis-Menten scheme.

Table (5.6) gives the calculated  $\nu$  from the numerical solution where  $D_{\text{eff}} = 1.52 \times 10^{-6} \text{ cm}^2 \text{ s}^{-1}$  (Eq. (5.25)),  $J = \nu \cdot D$ ,  $\Omega_{\text{spot}}$  according to Eq. (2.25), and  $\Omega_{\text{bead}}$  according to Eq. (5.41). The ratio of  $\Omega_{\text{bead}}$  to  $\Omega_{\text{bead,free}}$  compares the PAP flux per bead obtained from the theoretical models with the PAP flux per bead obtained from the DPV experiment giving an estimative of collection efficiency. Although PAPG is available throughout the spot, the single bead fluxes decrease for more "diluted" beads giving an evidence of shielding effects of the bead agglomerates. Moreover the ratio shows that not more than 29.7% of the modified-beads inside the spot can contribute to the PAP flux.

**Table 5.6:** Estimation of flux and conversion from simulation of internal diffusion at bead layers and using the resulting flux for uniform bead layer geometry.

$\chi$	$\nu / 10^{-5} \text{ mol cm}^4$	$\Omega_{\text{spot}} / 10^{-14} \text{ mol s}^{-1}$	$\Omega_{\text{bead}} / 10^{-18} \text{ mol s}^{-1}$	$\Omega_{\text{bead}} / \Omega_{\text{bead,free}} [\%]$
100	1.71	2.86	5.95	29.66
91	1.33	3.54	4.02	20.07
67	1.01	3.99	3.43	17.09
50	0.20	0.35	1.33	6.63
20	0.04	0.14	0.47	2.34
10	0.01	0.04	0.20	0.99

### 5.5.5 Diffusion Model 2, Case 1: big half-sphere with $h = r_s$ (exp)

The spot is treated as a "big" half-sphere (Fig. (5.10b)), in which  $h$  is the same as  $r_s$  from the microscope picture (Fig. (5.19)) used for the SECM measurements.  $N_{\text{tot}}$  was calculated from Eq. (5.32),  $N_{\text{tot,gal}}$  was calculated according to Eq. (5.33),  $\nu_{\text{max}}$  from Eq. (5.44),  $\Lambda$  from Eq. (5.39) and  $\phi$  from Eq. (5.24).

**Table 5.7:** Calculated parameters for big half-spheres with radius  $r_s$  equal to  $h$  for numerical solution of the differential equation (5.38).

$\chi$	$r_s / \mu\text{m}$	$h / \mu\text{m}$	$V_{\text{spot}} / 10^{-7} \text{cm}^3$	$N_{\text{tot}}$	$N_{\text{tot,gal}}$	$v_{\text{max}} / 10^{-6} \text{mol cm}^{-3} \text{s}^{-1}$	$\Delta / \mu\text{m}$	$\phi$
100	75.64	75.64	9.1	58392	58392	1.3	25	3.59
91	95.45	95.45	18.2	117335	106668	1.2	32	4.32
67	116.19	116.19	32.9	211644	141096	0.9	39	4.51
50	78.05	78.05	10.0	64153	32077	0.7	26	2.62
20	109.73	109.73	27.7	178269	35623	0.3	37	2.33
10	121.73	121.73	37.8	243384	24328	0.1	41	1.83

The numerical solution of Eq. (5.38) for large half-sphere spots using the parameters from Table (5.7) gives the concentration profile of PAPG as  $\varphi = (\rho, \phi)$  illustrated in Fig. (5.26).

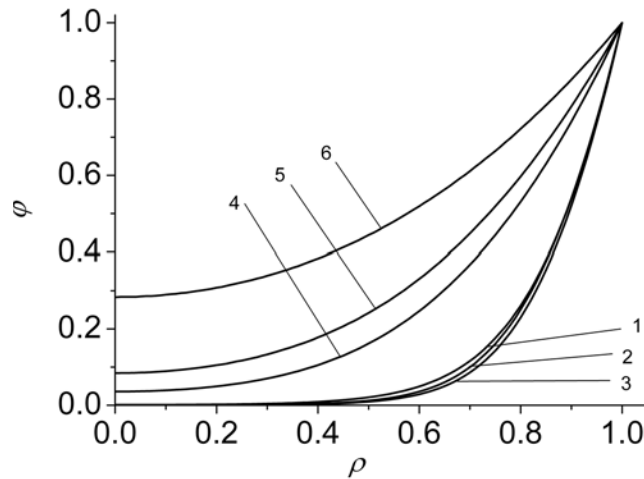


**Fig.5.26.** Concentration profiles of substrate in a half-sphere bead spot with radius  $r_s = h$  and different saturation of active beads. 1)  $\chi = 100\%$ , 2)  $\chi = 91\%$ , 3)  $\chi = 67\%$ , 4)  $\chi = 50\%$ , 5)  $\chi = 20\%$ , 6)  $\chi = 10\%$ .

A sharp decrease of  $\varphi$  was observed for  $\phi$  larger than 2.6 which means that the reaction inside the spot is diffusion-limited. In this case, only the enzymes encountered in the outer layer are exposed to the substrate and participate in the reaction. As inside the spot the biochemical reaction occurs simultaneously with the mass transfer, not all enzyme molecules inside the bead agglomerate are in contact with the same amount of PAPG as the enzymes bounded to the beads that are on the outer surface of the spot. Hence, under diffusion-controlled conditions, the overall reaction rate is lower due to a decreased substrate concentration within the spot. Table (5.8) gives the calculated  $\nu$  from the numerical solution and the respective fluxes. This case shows that the modified-beads that are at the outer surface

of the spot consume the substrate, hence the penetration of substrate inside the bead spots is depleted. One can see that  $\Omega_{\text{bead}}$  is 3-fold lower than that predicted by Model 1. Moreover, the ratio of  $\Omega_{\text{bead}}/\Omega_{\text{bead,free}}$  gives a maximum of 6.2% conversion. Here, only the modified-beads at the surface contribute to the PAP flow because PAPG is depleted inside the spot.

**Table 5.8:** Estimation of flux and conversion from simulation of internal diffusion at big half-sphere spots with radius  $R_S$ .

$\chi$	$v / 10^{-5} \text{ mol s}^{-1}$	$\Omega_{\text{spot}} / 10^{-14} \text{ mol s}^{-1}$	$\Omega_{\text{bead}} / 10^{-18} \text{ mol s}^{-1}$	$\Omega_{\text{bead}} / \Omega_{\text{bead,free}} [\%]$
100	2.21	7.29	1.25	6.23
91	1.17	6.16	0.58	2.88
67	0.86	6.74	0.48	2.38
50	0.24	0.85	0.27	1.33
20	0.05	0.35	0.10	0.50
10	0.01	0.11	0.05	0.23

### 5.5.6 Diffusion Model 2, Case 2: small half-sphere with $r_S = h$ (exp)

The spot is treated as a "small" half-sphere (Fig. (5.10c)), with the spot height  $h$  being the one calculated from Eq. (5.29), and  $r_S$  the same as  $h$ . As in the previous case,  $A_{\text{spot}} = 2\pi r_S^2$ ,  $V_{\text{spot}}$  was calculated Eq. (5.37),  $N_{\text{tot}}$  from Eq. (5.32),  $N_{\text{tot,gal}}$  from Eq. (5.33),  $v_{\text{max}}$  from Eq. (5.44),  $\Lambda$  from Eq. (5.39) and  $\phi$  from Eq. (5.24). The values resulting for small half-spheres with radius  $h$  are shown in Table (5.9).

**Table 5.9:** Calculated parameters for small half-spheres with  $r_S$  equal to  $h$  of experiment for numerical solution of the differential equation (5.38).

$\chi$	$h / \mu\text{m}$	$r_S / \mu\text{m}$	$V_{\text{spot}} / 10^{-9} \text{ cm}^3$	$N_{\text{tot}}$	$N_{\text{tot,gal}}$	$v_{\text{max}} / 10^{-6} \text{ mol cm}^{-3} \text{ s}^{-1}$	$\Lambda / \mu\text{m}$	$\phi$
100	8	8	1.2	77	77	1.3	2.8	0.39
91	10	10	2.4	154	140	1.2	3.5	0.47
67	13	13	4.3	278	185	0.9	4.2	0.49
50	9	9	1.3	84	42	0.6	2.8	0.29
20	12	12	3.6	234	47	0.3	4.0	0.26
10	13	13	5.0	320	32	0.1	4.4	0.20

The numerical solution of Eq. (5.38) for small half-sphere spots using the parameters from Table (5.9) gives the concentration profile of PAPG illustrated in Fig. (5.27).



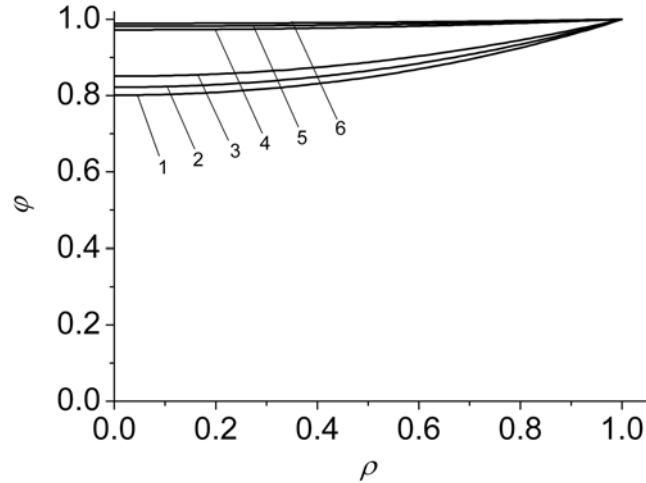


**Fig. 5.27.** Concentration profiles of substrate in a half-sphere bead spot with radius  $r_s = h$  and different saturation of active beads. 1)  $\chi = 100\%$ , 2)  $\chi = 91\%$ , 3)  $\chi = 67\%$ , 4)  $\chi = 50\%$ , 5)  $\chi = 20\%$ , 6)  $\chi = 10\%$ .

The concentration profile of Fig. 5.27 is quite similar to that of Model 1. A slight decrease in the PAPG concentration inside the spot shows that enough substrate penetrates the spot being available for conversion. An evidence of this behavior are the low  $\phi$  values for the spots. It is evident that the spot height plays an important role in the overall rate of reaction. Larger  $h$  lead to depletion of substrate inside the spot and thus hindrance of catalytic reaction inside it. This effect does not occur for smaller  $h$  as for Model 1 and Model 2, Case 2. Table (5.10) gives the calculated  $v$  from the numerical solution and the respective fluxes. The ratio of the fluxes are very large because the simulated  $\Omega_{\text{bead}}$  has to be high enough in order to produce  $[\text{PAP}]_s$  given as initial parameter. This case shows that all modified beads present in the spot contribute the overall PAP flow.

**Table 5.10:** Estimation of flux and conversion from simulation of internal diffusion at small half-sphere spots with radius  $h$ .

$\chi$	$v / 10^{-6}$ $\text{mol s}^{-1}$	$\Omega_{\text{spot}} / 10^{-17}$ $\text{mol s}^{-1}$	$\Omega_{\text{bead}} / 10^{-16}$ $\text{mol s}^{-1}$	$\Omega_{\text{bead}} / \Omega_{\text{bead,free}}$ [%]
100	12.63	5.01	6.53	3258.92
91	5.96	3.77	2.69	1341.16
67	3.47	3.25	1.75	874.09
50	0.36	0.15	0.36	180.11
20	0.06	0.05	0.11	53.33
10	0.01	0.01	0.04	21.43

### 5.5.7 Diffusion Model 2, Case 3: medium half-sphere, with $N_{\text{tot}}$ from experiment

The spot is treated as a "medium" half-sphere, with  $N_{\text{tot}}$  being the same as calculated in Model 1 using Eq. (5.32) and  $N_{\text{tot,gal}}$  from Eq. (5.33). This  $N_{\text{tot}}$  approximates to that of the "real" experiment, and therefore was used here to calculate the other parameter of the half-sphere-shaped spot. Knowing  $N_{\text{tot}}$  one can calculate  $V_{\text{spot}}$  (Eq. (5.32)),  $r_S$  (Eq. (5.37)), and  $h$  ( $r_S = h$ ).  $v_{\text{max}}$  from Eq. (5.44),  $\lambda$  from Eq. (5.39) and  $\phi$  from Eq. (5.24). The values resulting for medium half-spheres with radius  $h$  are shown in Table (5.11).

**Table 5.11:** Calculated parameters for medium half-spheres with radius  $r_S$  equal to  $h$  for numerical solution of the differential equation (5.38).

$\chi$	$h / \mu\text{m}$	$V_{\text{spot}} / 10^{-8} \text{cm}^3$	$r_S / \mu\text{m}$	$N_{\text{tot}}$	$N_{\text{tot,gal}}$	$v_{\text{max}} / 10^{-6} \text{mol cm}^{-3} \text{s}^{-1}$	$\lambda / \mu\text{m}$	$\phi$
100	8	7.5	32.9	4815	4815	1.3	11.0	1.56
91	10	15.0	41.5	9676	8797	1.2	13.8	1.88
67	13	27.1	50.6	17454	11636	0.9	16.9	1.96
50	9	8.2	34.0	5291	2645	0.6	11.3	1.14
20	12	22.8	47.8	14701	2938	0.3	15.9	1.01
10	13	31.2	53.0	20071	2006	0.1	17.7	0.80

The numerical solution of Eq. (5.38) for medium half-sphere spots using the parameters from Table (5.11) gives the concentration profile of PAPG illustrated in Fig. (5.28).

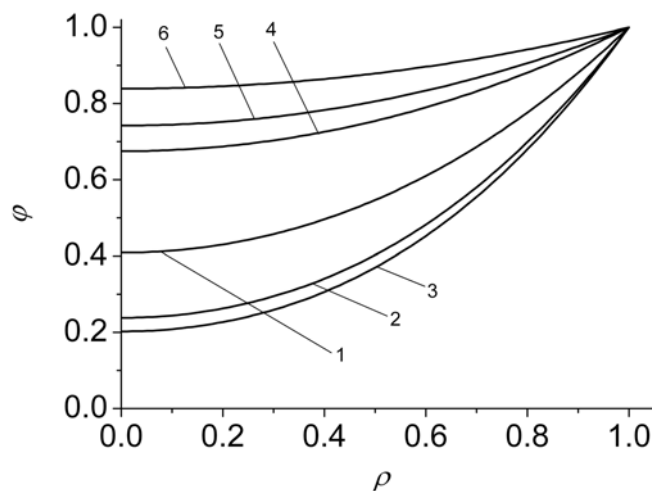


**Fig. 5.28.** Concentration profiles of substrate in a medium half-sphere bead spot with radius  $r_S = h$  and different saturation of active beads. 1)  $\chi = 100\%$ , 2)  $\chi = 91\%$ , 3)  $\chi = 67\%$ , 4)  $\chi = 50\%$ , 5)  $\chi = 20\%$ , 6)  $\chi = 10\%$ .

The concentration profile of Fig. (5.28) shows that [PAPG] is drastically decreased inside the spot, however no complete depletion is observed. A diffusion-controlled reaction may take place inside the spot rather than a kinetically-controlled reaction. This may lead to a behavior that does not follow the Michaelis-Menten kinetics inside the spot. The contributions of the beads inside the spots are hindered by the substrate depletion. In this case, major contributions to the PAP flow come from the modified-beads that are at the outermost layer. Table (5.12) gives the calculated  $v$  from the numerical solution and the respective fluxes. The ratio  $\Omega_{\text{bead}}/\Omega_{\text{bead,free}}$  calculated here are very close to those of Model 1. It shows that the conversion rate of the modified beads in the spots is much smaller than for free modified beads, reaching a maximum of 38.94%. The beads inside the spots have some contribution to the overall rate of reaction, but the modified beads at the spot surface have the main contribution.

**Table 5.12:** Estimation of flux and conversion from simulation of internal diffusion at medium half-sphere spots with radius  $h$ .

$\chi$	$v / 10^{-6} \text{ mol s}^{-1}$	$\Omega_{\text{spot}} / 10^{-14} \text{ mol s}^{-1}$	$\Omega_{\text{bead}} / 10^{-18} \text{ mol s}^{-1}$	$\Omega_{\text{bead}} / \Omega_{\text{bead,free}} [\%]$
100	60.0	3.8	7.8	38.94
91	44.6	4.4	5.1	25.23
67	33.5	4.9	4.3	21.21
50	6.9	0.5	1.7	8.69
20	1.4	0.2	0.6	3.06
10	0.3	0.1	0.3	1.30

### 5.5.8 Comparison of the fluxes for the three models

The comparison of the ratios of conversion rates of modified-beads in spots to free modified-beads resulting from the four models described above and the two experimental types, the disk-shaped spot (exp - disk, Table (5.3)) and layer-cap-shaped spot (exp - volume, Table (5.4)) are given in Table (5.13). The experimental  $\Omega_{\text{bead}}/\Omega_{\text{bead,free}}$  values of the disk-shaped spots are comparable to those of Model 1 (simulated uniform bead layer, Table (5.6)) and Model 2, Case 3 (medium half-sphere, Table (5.12)), most likely due to  $N_{\text{tot}}$  and  $N_{\text{tot,bead}}$  amounts considered for the simulation and "real" experiment. The  $\Omega_{\text{bead}}/\Omega_{\text{bead,free}}$  of Model 2, Case 2 (small half-sphere, Table (5.10)) deviates strongly from the other results most likely due to the small radius considered. The underestimation of the number of beads in a spherical spot with  $r_s$  equal to the plausible  $h$  leads to a grave overestimation of conversion

rate per single bead. The  $\Omega_{\text{bead}}/\Omega_{\text{bead,free}}$  of Model 2, Case 1 (big half-sphere, Table (5.8)) leads to an underestimation of conversion rate per single bead. One can conclude that the bead spot conversion rate depends strongly on the height and radius of the spot.

**Table 5.13:** Comparison of ratios of  $\Omega$  at spots with different saturation of active beads for different models.

$\chi$	$\Omega_{\text{bead}} / \Omega_{\text{bead,free}}$ [%]	$\Omega_{\text{bead}} / \Omega_{\text{bead,free}}$ [%]	$\Omega_{\text{bead}} / \Omega_{\text{bead,free}}$ [%]	$\Omega_{\text{bead}} / \Omega_{\text{bead,free}}$ [%]	$\Omega_{\text{bead}} / \Omega_{\text{bead,free}}$ [%]	$\Omega_{\text{bead}} / \Omega_{\text{bead,free}}$ [%]
	(exp - disk)	(exp - volume)	(uniform bead layer)	(big sphere)	(small sphere)	(medium sphere)
100	27.94	16.96	29.66	6.23	3258.92	38.94
91	16.96	7.98	20.07	2.88	1341.16	25.23
67	15.97	6.49	17.09	2.38	874.09	21.21
50	12.47	6.99	6.63	1.33	180.11	8.69
20	7.98	2.99	2.34	0.50	53.33	3.06
10	5.99	2.00	0.99	0.23	21.43	1.30

Fig. (5.29) shows a plot of the ratio of the fluxes versus of the experimental values and the simulated values that are comparable to the experimental, i.e. uniform bead layer and medium half-sphere. For most concentrated spots ( $\chi = 100, 91, 67$ ) the  $\Omega_{\text{bead}}/\Omega_{\text{bead,free}}$  of simulated layer-cap matches the values of the experimental disk-shaped spots indicating a large contribution of the beads at the surface. A reason for that is that the modified-beads that are at the surface have the main contribution to the overall conversion rate. While the experimental disk-shaped spots consider only the beads at the spot surface, and the simulated uniform bead layer considers the total number of beads in the spot volume, one can conclude that for higher  $\chi$  the main contribution is coming from the modified beads at the spot surface.

However, for lower  $\chi$ , the ratios differ by a factor of 6. This can be explained by the effects of internal diffusion. For more diluted spots ( $\chi = 50, 20, 10$ ) most modified beads are buried inside the spot, and have a lower contribution to the overall rate of conversion than those modified beads that are at the spot surface due to diffusional shielding. As observed in Fig. 5.25 the substrate can diffuse through the spots although a slight depletion occurs. Since the disk-shaped spots (exp - disk) consider that only the beads that are at the spot surface contribute to the overall rate of conversion and ignore the effects of internal diffusion, the  $\Omega_{\text{bead}}/\Omega_{\text{bead,free}}$  of the experimental disk-shaped spots is much larger than the ratio of the simulated uniform bead layer. However, the ratios of the layer-cap-shaped spot (exp - volume) are similar to the ratios of the simulated uniform bead layer, in which the effects of internal

diffusion were considered. It shows that for lower  $\chi$ , one has to consider the effects of internal diffusion for quantitative analysis, while for higher  $\chi$  these effects can be neglected.

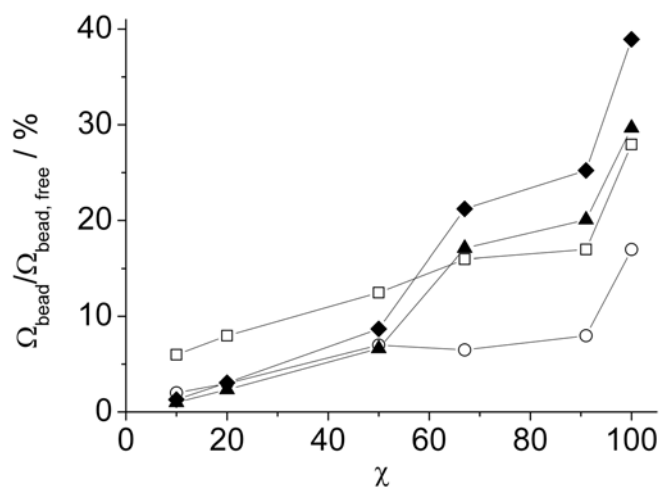


**Fig. 5.29.** Comparison of the ratios of  $\Omega_{\text{bead}}/\Omega_{\text{bead, free}}$  for (□) experimental results considering a disk-shaped spot geometry, (○) experimental results considering the total volume of the spot, (▲) simulated uniform bead layer-shaped spot, and (◆) simulated medium half-sphere-shaped spot.

Transferring the PDE to systems of ODE is only possible for such symmetric geometries shown above. For more realistic geometry, like the sphere-cap geometry, the non-linear PDE has to be solved. This needs much more additional numerical effort.

## 5.6 Conclusions

Studies of internal and external diffusion and reaction in microbead agglomerates have been elucidated in this Chapter. The biotinylated  $\beta$ -galactosidase was immobilized to streptavidin-coated beads and suspensions with different total bead concentration were prepared. Initially a spot containing only  $\beta$ -galactosidase-modified beads was formed in order to optimize the experimental conditions by analyzing the  $K_M'$  and effects of external diffusion. The study of the  $K_M'$  resulted in a value smaller than the intrinsic  $K_M$ , due to partition of the substrate that occurred in the proximity of the spot. The partition was caused by the hydrophobic forces between the substrate and the microbeads. The experimental data were compared with the fitted values from the previously used theory and with BEM simulations using non-linear boundary conditions. It showed that the theory developed by Scott et al.<sup>[93, 124]</sup> is a good approximation for systems that are not necessarily disk-shaped, such as bead spots. The analysis of the external diffusion in terms of Damköhler number, showed that the

external diffusion was kinetically controlled and there was enough substrate at the surface of the spot to diffuse inside it.

After analyzing the external diffusion a system has been prepared to analyze the effects of internal diffusion. Representative experiments were made in order to determine the spot geometry (radius and height). The spot shape has been found to be a hemispherical cap. An estimate of the total number of beads could then be calculated for the real experimental spot. Bead agglomerates with constant concentration of  $\beta$ -galactosidase-modified beads and increasing bare bead concentrations were formed in an array. The enzyme activity was mapped using the SECM by monitoring the oxidation of PAP, formed by the galactosidase-catalyzed hydrolysis of PAPG. Line profiles were extracted from the SECM images. The fit of these line profiles to the SECM theory provide the PAP concentration at the spot surface, thus the overall flux of PAP generated by the spot could be estimated. The PAP fluxes and concentrations at the surface decreased with the increase of the amount of bare beads added to the spot indicating that the beads buried in the spot experience internal diffusion limitation and shielding. The PAP flux generated by an individual bead has been calculated considering the spot as a disk following the theory (Table (5.3)), and considering the spot as a hemispherical cap (Table (5.4)). The fluxes of both cases decreased with the increase of the number of bare beads in the spot. The shielding effect of the beads on each other blocks the PAPG diffusion to the immobilized  $\beta$ -galactosidase and the hydrolysis product PAP out of the spot to the UME, so the  $\beta$ -galactosidase-saturated microbeads found buried into the spots do not contribute to the total PAP flux but only that ones that are in the first or second layer (outermost layer).

In order to investigate the internal diffusion more precisely, ODEs describing the internal PAPG concentration profiles were developed for two distinct models: uniform bead layer-shaped spots and half-sphere-shaped spots. From these models the concentration profiles of systems with varied amount of beads were simulated. A complete PAPG depletion within the spot was calculated for the big half-sphere (Model 2, Case 1), in which the number of beads is too large in comparison to the number of beads contained in the experimental spots. Analyzing the fluxes resulting from this simulation, one can see that this case leads to an underestimation of the fluxes. The concentration profile of small half-sphere (Model 2, Case 2) showed small depletion of substrate, however lead to an overestimation of the PAP fluxes due to the small amount of beads considered. The concentration profile of medium half-sphere (Model 2, Case 3) showed a partial depletion of substrate. The uniform bead layer model (Model 1) is the one that is more similar to the experimental spots because it used the

parameters of the experiment, such as radius and total number of beads. The concentration profile of this model showed that enough substrate can diffuse inside the spots although some substrate consumption has been observed at the spot surface.

The analysis of the PAP fluxes resulting from the concentration profiles of these models, showed that the fluxes of PAP decrease with the increase of the dilution of enzyme-modified beads by bare beads, indicating that PAPG is consumed by the beads encountered at the outer shell of the spot, although for Model 1 and Model 2, Case 2, there is still enough substrate available.

The ratios of the fluxes of PAP generated per bead to the fluxes of PAP of free beads have been used as comparison for the analysis of the shielding effects of the proposed model and the experiments. The Model 1 is the one that approximates most to the disk-shaped experimental value, however, for more diluted beads, the layer-cap shaped experimental data suits better. An explanation for this behavior is the influence of internal diffusion. There is a slight depletion of PAPG inside the spot, leading to inhomogeneous kinetics inside the spot and decreased contribution of the beads inside the spot. A major contribution is shown to come from the beads at the spot surface, while the beads buried in the spot do not contribute, or contribute to a lesser extent.

As the experimental disk-shaped spots consider only the contribution of beads at the surface, an overestimation of the fluxes of individual beads is made, ignoring the contribution of the buried beads. The assumption of a disk-shaped spot is good for more concentrated spots, due to higher concentration of modified beads at the spot surface. However, when the number of the modified beads at the surface is decreased and most of the modified beads are buried inside the spot, the influence of internal diffusion must be considered. For more diluted spots the experimental layer-cap shaped spots lead to more realistic values of individual fluxes that agree with the simulated fluxes. As a result, the comparison of the models with the experiments shows that the SECM model used to describe the fluxes are suitable for more concentrated spots, however, for more diluted spots the internal diffusion limitation should not be ignored. The influence of shielding effects inside the spots are stronger for more diluted spots.

As a consequence, the SECM theory that has been used up to date, still can be used to calculate the overall fluxes of spots. However, one should not calculate the contribution of individual beads for diluted systems due to the influence of internal diffusion. In this case, one has to consider the volume of the spot. In microfluidic systems, the influences of internal diffusion limitation are of great importance. The geometry of the aggregates formed into the

microfluidic chambers determinates the diffusion of analyte within the agglomerate, affecting the reaction inside the agglomerate. Thus, the analysis of the reaction product will depend on how the bead agglomerate is formed and cannot be attributed to all bioreceptors present in the chamber. The effects of mass-transport limitation should be included in the calculation of uncertainty of such systems. A way to optimize these systems is to use the proposed mathematical model in order to estimate the effects of internal diffusion and the optimum number of bioreceptors.



## 6 Polymerization of polypyrrole and detection of hybridization events

This chapter presents the use of the direct mode of SECM for the local deposition of oligonucleotide (ODN) patterns on thin gold films and the GC mode for the determination of the amount of surface-accessible ODN.<sup>[A6]</sup> This work was done in cooperation with Prof. Dr. S. Szunerits.

### 6.1 Introduction

DNA recognition, based on its hybridization with surface-immobilized oligonucleotide probes, has become increasingly important for gene mapping, DNA sequencing, disease diagnosis and analysis of DNA-ligand interactions. Motivated by the aim of nucleic acid sequencing via hybridization, the development of DNA sensors and arrays has received a considerable attention.<sup>[327-338]</sup> In general, two main problems must be addressed in the development of DNA chips: one being the development of strategies for the stable and reproducible immobilization of a variety of ODN probes onto specific locations on the surface; the other being the use of a sensitive, real-time and multiparametric detection method for hybridization.

The local immobilization of ODN probes has been achieved using mechanical spotting techniques,<sup>[339, 340]</sup> lithographic approaches such as microcontact printing<sup>[341, 342]</sup> and photolithography<sup>[343, 344]</sup> or simply by site-selective supply of biomolecules via microfluidic networks.<sup>[345]</sup> Next to these approaches, SECM has attracted much attention for the site-directed patterning of surfaces due to its simplicity.<sup>[346, 347]</sup> Recently, it was shown that the local deposition of ODN strands is possible using the direct mode of SECM.<sup>[28, 348-350]</sup> The approach is based on the copolymerization of ODN-substituted pyrrole and unsubstituted pyrrole. This necessitates the synthesis of the pyrrole-ODN precursor, which is based on the preparation of a nucleoside phosphoramidite bearing a pyrrole with a spacer arm, where the ODN was tethered at its 5' end to the pyrrole unit.<sup>[351-355]</sup> The advantages of this direct immobilization strategy are numerous. Firstly, the solubility of pyrrole in water together with the possibility of electropolymerization in aqueous medium allows the polymerization of pyrrole-ODN without destroying the biological activity of the ODN probes. Secondly, the pre-synthesis of ODN-pyrrole probes allows purification of the product. The electrochemically

induced formation of polypyrrole films onto an electrode surface is, however, a rather complex process and involves a number of steps which are critical for the formation of polymer films.

The hybridization capacity depends largely on the density of ODN groups on the polymer surface. In fact, the ODN groups buried in the polymer film will most likely not participate in the hybridization event due to steric hindrance. Several surface analytical techniques such as surface plasmon resonance (SPR),<sup>[356-358]</sup> quartz crystal microbalance (QCM),<sup>[358, 359]</sup> and fluorescence measurements<sup>[338, 360, 361]</sup> have been used to obtain information about surface grafting densities, which should be kept below a limiting value for attaining the maximum hybridization efficiency and thus the maximum sensitivity and selectivity.

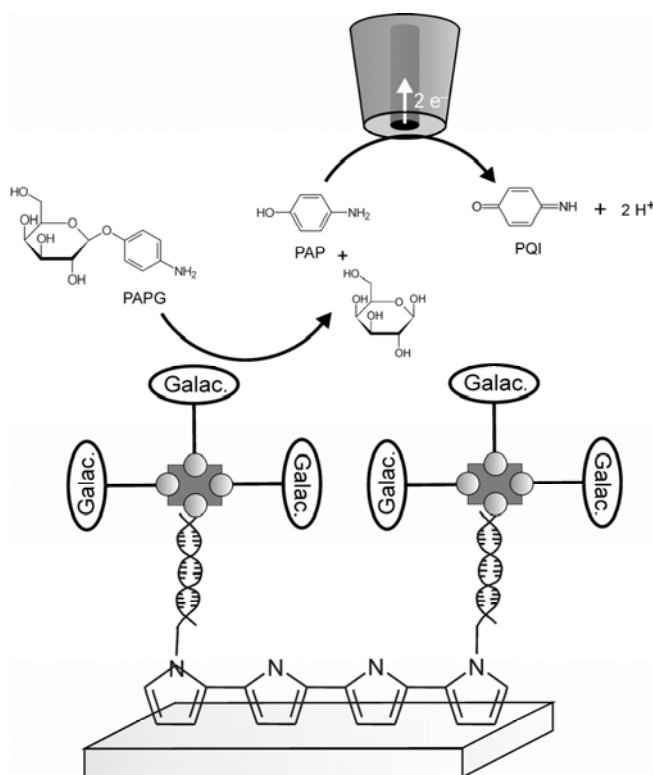


**Figure 6.1.** Schematic representation of the molecular assembly based on ODN hybridization together with a schematic of the imaging principle (The scheme is not to scale).

While SECM has been used to study polypyrrole deposition,<sup>[26, 36-38]</sup> ion transport and electron transfer at polypyrrole films,<sup>[39]</sup> immobilization of glucose oxidase via direct electrochemical microspotting of polypyrrole-biotin film,<sup>[16]</sup> and DNA hybridization,<sup>[20, 27, 28, 40-42]</sup> quantification of hybridization events has not been reported using the SECM. This chapter demonstrates how SECM in the GC mode allows the determination of the surface concentration of ODN strands accessible for hybridization. The approach is based on

monitoring the activity of biotin-labeled  $\beta$ -galactosidase, linked through a molecular assembly to a hybridized complimentary strand (Fig. (6.1)) and takes into account feedback effects arising from redox recycling at the supporting gold surface.

## 6.2 Localized immobilization of oligonucleotides onto thin gold films and hybridization

The local grafting of  $15^{\text{mer}}$  oligonucleotide strands on thin gold films was achieved through an electrochemical copolymerization process using pyrrole and pyrrole-oligonucleotide as monomer units using the direct mode of SECM (Fig. 2.8). The nucleotide sequence was taken as a model. There is no relation of this particular sequence to a specific diagnostic application. As demonstrated firstly by Kranz et al.,<sup>[36, 37]</sup> the use of a pulse sequence is critical in order to generate sufficiently high concentrations of pyrrole radical cations for local deposition of the conducting polymer. This approach was followed by using a copolymerization of pyrrole/pyrrole-ODN to link the oligonucleotides locally and irreversibly to the gold substrate.<sup>[28, 349]</sup> Although the mechanisms of polypyrrole electropolymerization has been widely studied,<sup>[362-371]</sup> there is still no agreement regarding the initiation step.<sup>[371]</sup> The formation of polypyrrole films involves several steps: diffusion of the monomer to the electrode surface, oxidation of the monomer at the electrode surface to form the radical cations, coupling between the radical cation and monomeric (or oligomeric) radical cation (or neutral monomer), loss of protons, electrochemical oxidation of the formed copolymers, chain propagation due to further coupling reactions and precipitation of the polycationic polymers at the anode surface when the specific solubility of the polymer has been achieved.<sup>[350]</sup> Fortin et al.<sup>[350]</sup> studied the construction of a DNA array involving the electropolymerization of a mixture of pyrrole and ODN-pyrrole.

The choice of the pulsing time  $\tau$  as well as the potential  $E_{\text{pulse}}$  at which the copolymerization takes place and the distance between UME and gold surface  $d$  has been found to be crucial for the formation of pyrrole-ODN deposits. The optimal conditions for the local deposition of pyrrole-ODN films from a solution of pyrrole-ODN (10  $\mu\text{M}$ ) and pyrrole (200 mM) in  $\text{LiClO}_4$  (0.1 M) using a UME with  $r_{\text{T}} = 5 \mu\text{m}$  were established as (i)  $E_{\text{pulse}} = 0.7 \text{ V}$ , (ii)  $\tau = 20 \text{ ms}$ , (iii)  $d = 60 \mu\text{m}$ .<sup>[349]</sup> While the use of a larger UME ( $r_{\text{T}} = 12.5 \mu\text{m}$ ) in this study leads to larger deposits, the other parameters turned out to be not affected significantly, most likely because of the comparable size of the insulating sheath that

mainly determines the monomer diffusion into the interelectrode space. An example of a pulse for the local deposition of pyrrole-ODN film is shown in Fig. (6.2):

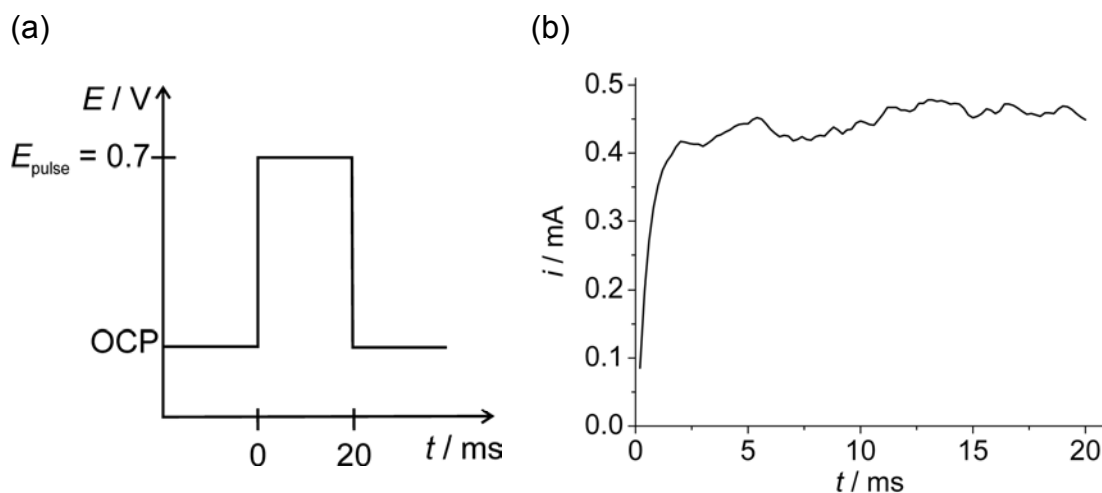


**Figure 6.2.** (a) Pulse for the electrochemical formation of polypyrrole film.  $E_{\text{pulse}}$  is determined by the oxidation potential of the pyrrole monomer. (b) The faradaic current response due to oxidation of the monomer.

Fig (6.3a) shows a SCLM reflection image of an array of six polypyrrole/polypyrrole-ODN spots. The contrast in the image is provided by the more intense light absorption of the black polypyrrole spots compared to highly reflecting gold. The diameter of the polymer spots varies between 206 - 270  $\mu\text{m}$  and depends on the number of potential pulses applied (between one and three pulses of 20 ms) and also on the amount of electrical charges passed between UME and substrate. The electrical charge consumed in the polypyrrole/polypyrrole-ODN spot formation was determined in the following way: a pulse was performed in a PBS solution without pyrrole monomers. The currents were integrated and provided a background charge (used to charge the double layer of the substrate). This value was subtracted from the integrated currents measured at the substrate during one pulse in monomers solution. The corrected charges for the polypyrrole/polypyrrole-ODN formation are shown in Table( 6.1). The good resolution of Fig (6.3a) allows the identification of four zones on the spots (Fig (6.3b)): (I) a darker inner part of  $(40 \pm 10) \mu\text{m}$  which corresponds to the size of the active part of the UME used (diameter = 25  $\mu\text{m}$ ), (II) a brighter region of  $(85 \pm 15) \mu\text{m}$  in diameter surrounded by a darker ring (III) with a total diameter of  $(150 \pm 20) \mu\text{m}$ , and finally an area with fading intensity (IV). The size of the polymer spot including all the 4 zones is about  $(270 \pm 10) \mu\text{m}$  for spots 1-5 (two and three pulses) and 206  $\mu\text{m}$  for spot 1 (one pulse). In the case of spots 1-5 the size corresponds to the diameter of the glass sheath  $r_{\text{glass}}$  of the UME being 300  $\mu\text{m}$ , while for spot 6 it is slightly smaller.

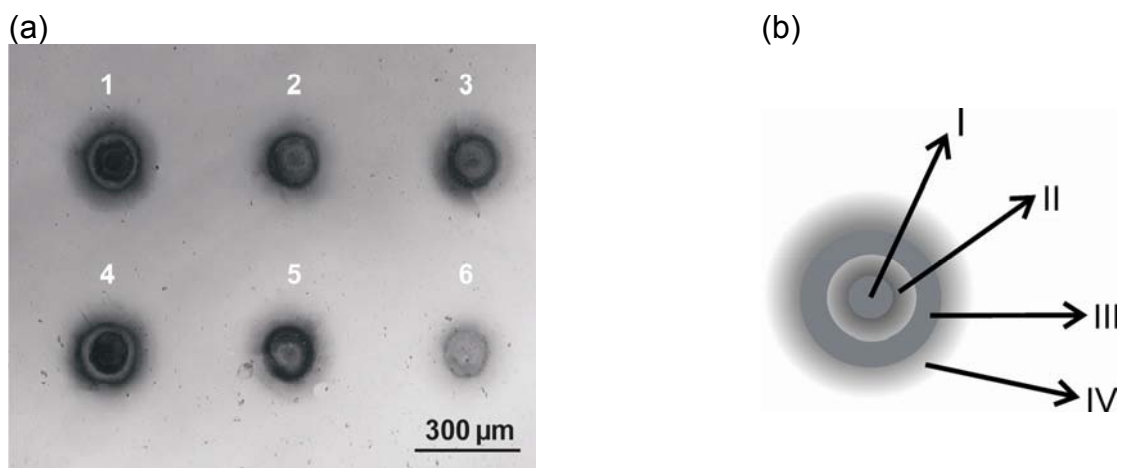


**Figure 6.3.** (a) SCLM reflection image of an array of pyrrole-ODN spots, Spotting conditions:  $c_{\text{pyrrole}} = 200 \text{ mM}$ ,  $c_{\text{pyrrole-ODN}} = 10 \text{ μM}$  in  $0.1 \text{ M LiClO}_4$  in water,  $d = 60 \text{ μm}$ ,  $E_{\text{pulse}} = 0.7 \text{ V}$ ,  $\tau = 20 \text{ ms}$ ; spots 1 and 4 = 3 pulses, spots 2, 3 and 5 = 2 pulses, spot 6 = 1 pulse; (b) Sketch of the four zones that are formed inside a pyrrole-ODN spot.

**Table 6.1:** Summary of thickness obtained for the different spots in Fig. (6.3).

Spot	$Q / 10^{-5} \text{ C}^{(a)}$	$r_s / \text{μm}^{(b)}$	Thickness / nm <sup>(c)</sup>
1	2.04	135	122
2	1.04	130	62
3	1.13	130	67
4	2.12	130	127
5	1.10	135	66
6	0.06	103	4

<sup>a)</sup> corrected by charging currents

<sup>b)</sup> estimated from SCLM images in Figure (6.3)

<sup>c)</sup> calculated from equation (6.1)

SFM images were recorded in order to confirm the ring structure and to measure variations of the film thickness within a spot. Fig. (6.4) shows a SFM image of the spots 1, 2, and 6. The image size was limited to the translation range of the SFM scanner thus only one half of the spot could be measured. From the images it is possible to recognize the height variations in the different zones of the spots (Table (6.2)). Table (6.2) lists the mean height in regions I, II, III, and IV taken from Fig (6.4). The morphology of the deposition is a consequence of the uneven current densities of pyrrole oxidation at the sample surface and the diffusion of monomers from the bulk solution into the interelectrode gap and possible homogeneous coupling reactions between radical cations and neutral monomers (or oligomers) and other (oligomeric) radical cations. It seems that the reaction of radical ions with

monomers diffusing from the bulk into the interelectrode gap causes the ring-shaped zones observed in the SCLM images. In all the six cases the area where polymer is deposited is not larger than the total size of the UME probe including the insulating glass sheath. While this is not the focus on this study, the influence of the glass sheath on the deposition dimensions is under investigation using optical fiber-based electrodes by the group of Prof. Szunerits.

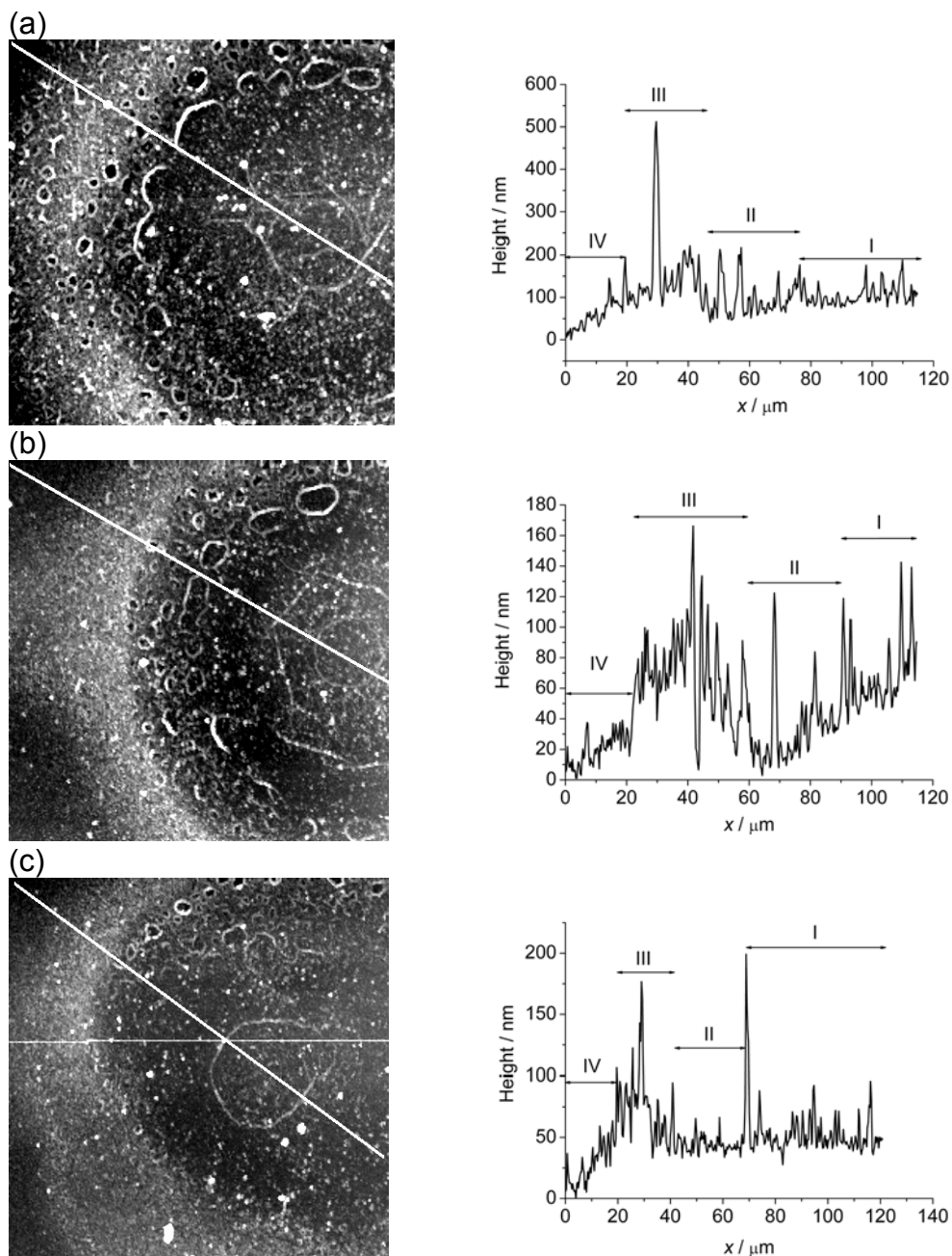


**Figure 6.4.** SFM image of polypyrrole spots after the enzyme assembly. The image shows the ring structure of (a) spot 1 formed through 3 pulses of 20 ms, (b) spot 2 formed through 2 pulses of 20 ms, and (c) spot 6 formed through 1 pulse of 20 ms. The profile extracted from the SFM shows the variations of the spot height.

**Table 6.2:** Height of ring regions at spot 1, 2 and 6 (described in Fig. (6.3)). The heights are calculated from the cross section extracted from SFM images.

Spot	I / nm	II / nm	III / nm	IV / nm
1	105.1 ± 22.9	95.4 ± 39.8	32.6 ± 86.8	58.8 ± 37.2
2	67.0 ± 20.8	36.7 ± 24.9	40.1 ± 28.3	20.7 ± 11.1
6	52.0 ± 14.5	47.1 ± 21.1	30.5 ± 27.6	29.2 ± 18.8

From the corrected electrical charge used for the polymer formation ( $Q$ ) and the total size of the polymer spot, the effective thickness of the polymer film before the enzyme assembly can be estimated according to Eq. (6.1):<sup>[372]</sup>

$$d_{film} = \frac{(M_{py} + \delta \cdot M_{ClO_4^-}) \cdot Q}{(2 + \delta) \cdot F \cdot A \cdot q_{py}} \quad (6.1)$$

where  $d_{film}$  corresponds to the thickness of the film,  $M_{PY}$  and  $M_{ClO_4^-}$  to the molecular mass of the monomer and dopant respectively,  $\delta$  to the doping level (0.33 assumed in this case<sup>[373]</sup>),  $F$  to the Faraday constant,  $A$  to the surface of the polymer spot,  $q_{PY}$  to the density of polypyrrole (1.51 g cm<sup>-3</sup>) and  $Q$  to the electrical charge. The thickness of the local deposited film under conditions used in this study varied between 4 nm to 127 nm (Table (6.1)).

While the success of the polymer deposition can be verified using SCLM reflection imaging, it does not give direct information about the concentration of ODN accessible on the polymer films. From previous results it is known that the realization of hybridization is possible.<sup>[28, 349]</sup> However, part of the oligonucleotide might not be accessible to hybridization as it might be buried in the polymer matrix. An estimation of accessible ODN may provide not only a deeper insight into the co-polymerization process, but might help to optimize the local polymerization procedure. In order to perform SECM investigation, a spot array was prepared using the polymerization conditions described above (Fig. (6.5)). The spots were prepared with four pulses (spot 1), three pulses (spot 2) and two pulses (spot 3) of 20 ms with a lateral separation of 500  $\mu$ m. The thicknesses estimated from Eq. (6.1) are shown in Table (6.3).

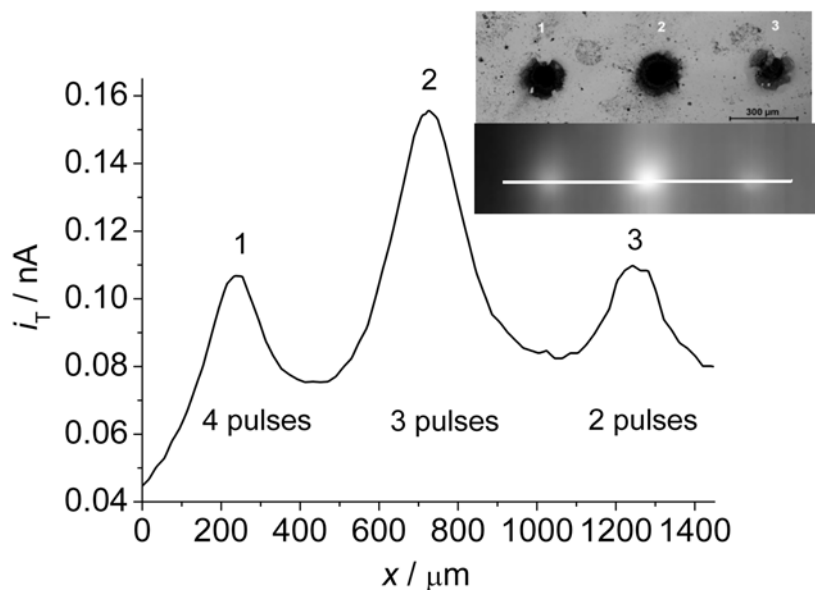


**Figure 6.5.** GC image of galactosidase activity of a hybridized polypyrrole/polypyrrole-ODN spot array, SCLM reflectance image and a line profile across the GC image passing through the highest current value. Experimental parameters for polypyrrole/polypyrrole-ODN formation:  $c_{\text{pyrrole}} = 200 \text{ mM}$ ,  $c_{\text{pyrrole-ODN}} = 10 \text{ } \mu\text{M}$  in  $0.1 \text{ M LiClO}_4$  in water,  $d = 60 \text{ } \mu\text{m}$ ,  $E_{\text{pulse}} = 0.7 \text{ V}$ ,  $\tau = 20 \text{ ms}$ ; spots 1 = 4 pulses, spots 2 = 3 pulses, spot 3 = 2 pulses, for the GC image:  $c_{\text{PAPG}} = 2 \text{ mM}$ ,  $r_{\text{T}} = 12.5 \text{ } \mu\text{m}$ ,  $d = 20 \text{ } \mu\text{m}$ ,  $v_{\text{T}} = 40 \text{ } \mu\text{m s}^{-1}$ .

**Table 6.3:** Summary of thickness obtained for three different spots used for SECM imaging.

Spot	$Q / 10^{-5} \text{ C}^{(a)}$	$r_s / \mu\text{m}^{(b)}$	Thickness / nm <sup>(c)</sup>
1	1.65	114.7	117.5
2	1.73	115.2	122.1
3	1.16	116.0	80.76

<sup>a)</sup> corrected by charging currents

<sup>b)</sup> estimated from SCLM images (6.5)

<sup>c)</sup> calculated from equation (6.1)

### 6.3 Determination of the accessible ODN concentration using the GC mode of SECM

A schematic of the GC imaging experiment is shown in Fig. 6.1. After local deposition of polypyrrole/polypyrrole-ODN, the immobilized ODN strands were hybridized using biotin-labeled complimentary strands. Streptavidin was bound to the biotin labels. The biotin-labeled  $\beta$ -galactosidase was attached to the streptavidin that marks hybridized ODN at the surface in such a way that the three remaining streptavidin binding sites were saturated



with enzyme. This system is forming a highly stable conjugate with an affinity constant of  $K_d = 10^{-15} \text{ mol}^{-1} \text{ L}^{-1}$ <sup>[301]</sup> and is stable for the SECM detection (Fig. (6.1)). As explained in Chapter 5, the enzymatic hydrolysis of PAPG in the presence of  $\beta$ -galactosidase at the substrate surface leads to local formation of PAP that is detected by amperometric oxidation at the UME in the GC mode.<sup>[120]</sup> Because the ODN-enzyme assembly was formed on gold, the GC mode has to be used in order to avoid the influence of SECM feedback effects by electrochemical recycling of the mediator by electron transfer reactions at the gold surface and the unmodified conducting polymer. The higher sensitivity of the GC mode (compared to the FB mode) represents another advantage of the GC mode for this study.<sup>[15]</sup> Quantification of GC mode is only possible if the enzymes are immobilized in well-separated microscopic regions that form steady-state concentration profiles. The SECM deposition of an ODN-polymer in the direct mode results in microspots (Fig. (6.5)) with rather well-defined size and separation, for which such a quantitative analysis is possible.

Galactosidase has a broad operational pH for PAPG and the activity does not fall below 60 % of the optimum in the pH range of 6-9. This range must also be maintained in order to avoid breaking the DNA double helix. In order to work in the regime of substrate saturation, different PAPG bulk concentrations were tested. The best results were obtained with a PAPG bulk concentration of 2 mM. Higher concentrations (5 mM, 10 mM) did not lead to an increase of the SECM signal but showed higher background currents. Lower concentrations (0.5 mM, 1 mM) showed relatively low overall currents and were not further investigated here.

Although the GC mode seems to be a straightforward measurement, the oxidation product PIQ formed at the UME can diffuse toward the gold substrate and can be recycled to PAP resulting in an enhancement of the total UME current (Fig. (6.6)).

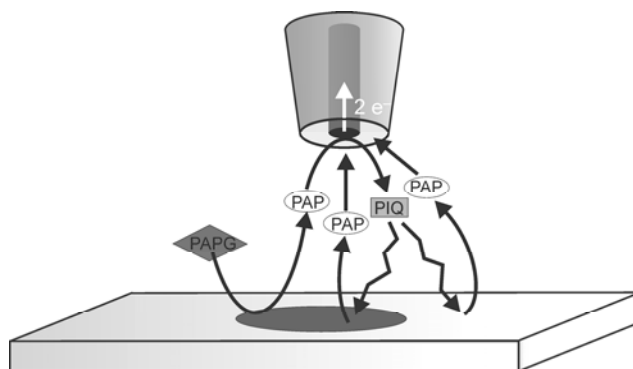


**Figure 6.6.** Recycling of PIQ at the gold surface.

The magnitude of the feedback enhancement is distance-dependent and may depend on the polymer coverage on gold. An optimal working distance for GC imaging had to be determined that provides high sensitivity but avoids signal contributions from feedback effects. In order to find the spot center, an image of the spot array was recorded with  $d = 20 \mu\text{m}$  (Fig. 6.5). The PAP oxidation current at the UME is plotted as gray scale and as line scan through the spot center. The location of the current maxima matches the layout as deduced from SCLM images. Separate control experiments were performed on pure gold surfaces and on non-hybridized polypyrrole/polypyrrole-ODN spots after molecular assembly. No faradaic currents due to the PAP oxidation were recorded under these conditions. A hemispherical quasi-stationary diffusion field developed within 3 min and diffusive fluxes did not increase at longer imaging times. After the spots were localized, the UME was moved along a line that crosses the middle of the spots where the current maximum had been observed. Horizontal line scans were recorded at different distances subsequently. The initial  $d$  was  $10 \mu\text{m}$  and the distance was incremented by  $2 \mu\text{m}$  until  $d = 88 \mu\text{m}$  (Fig. 6.7a). Fig. 6.7b shows the image as a three dimensional representation. Please note, that the space coordinates are horizontal ( $x$ ) and vertical ( $z$ ) to the substrate. As expected the current decreases with the increasing  $d$  according to the local PAP concentration established over the spot.

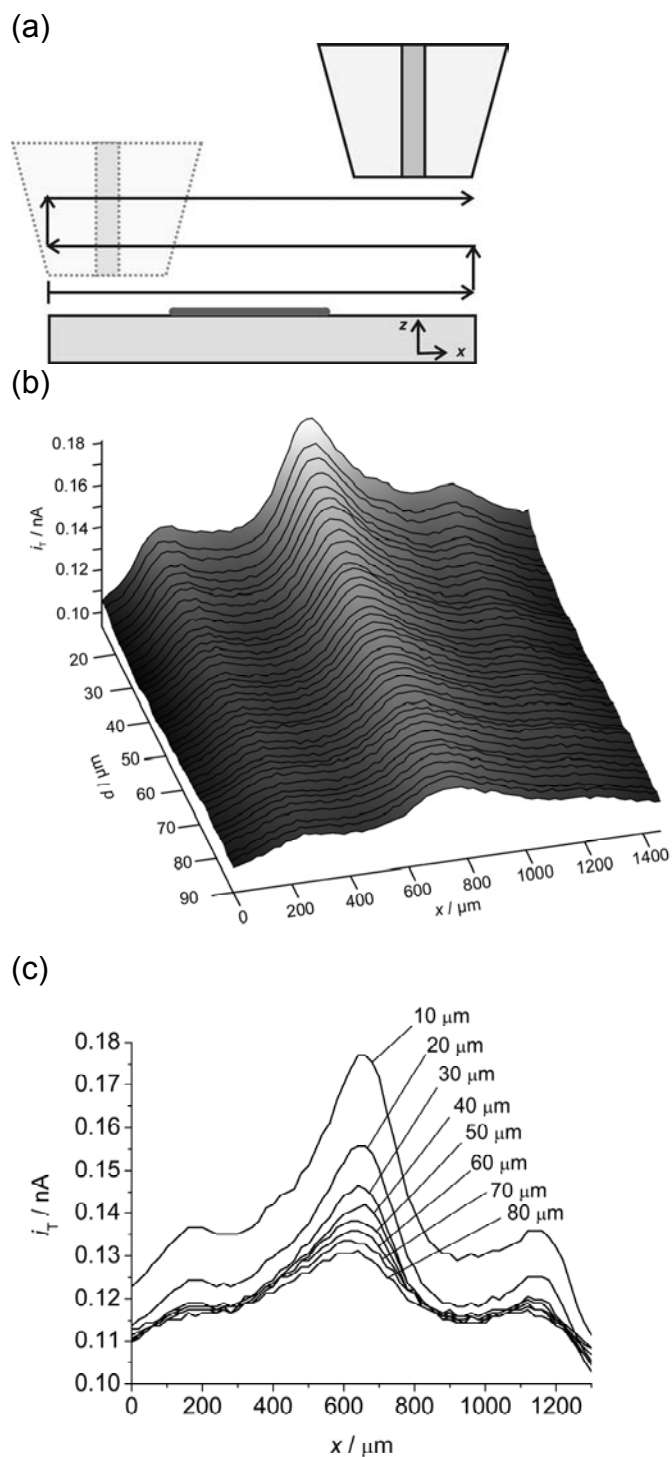


**Figure 6.7.** (a) Sketch of the  $x$ - $z$  SECM imaging. (b) GC image of the activity of galactosidase linked through streptavidin to the hybridized assembly. The UME ( $r_T = 12.5 \mu\text{m}$ ) translated in horizontal ( $x$ ) versus vertical ( $d$ ) direction with a  $v_T = 40 \mu\text{m s}^{-1}$ . Initial  $d = 10 \mu\text{m}$ ,  $d$  increment =  $2 \mu\text{m}$ ,  $c_{\text{PAPG}} = 2 \text{mM}$ . (c) 2D plot of UME current versus horizontal UME translation over the spot array. It is indicated in the plot the  $d$  at which the curve was extracted ( $d = 10$  to  $d = 80 \mu\text{m}$ ).

In order to obtain information about a possible contribution from feedback effects the observed background currents were analyzed. The background current was extracted from the

line scan as the current value that is besides the peaks, e.g. the current at  $x = 0$  in Fig (6.7c). Alternatively, the background current that was found by applying a fitting routine to the signals in Fig (6.7c) could be used with essentially the same result. The background current of each line scan was plotted versus  $d$  for each scan. As an example, Fig. (6.8) shows a plot of background current versus vertical distance of spot 2. The background currents of the other spots exhibited the same tendency (not shown). It is evident that at distances smaller than 30  $\mu\text{m}$  the background current increases with the decrease of  $d$ . The increase of the background current is due to the feedback effect coming from the recycling of PIQ on the gold surface. At  $d > 30 \mu\text{m}$  the background current becomes rather constant indicating that the feedback effect has no influence on the UME current. Thus quantitative studies must be done at  $d > 30 \mu\text{m}$ . Another problem of small  $d$  such as the disturbance of the diffusion layer of the spot caused by the translation of the UME over the surface can also be avoided by recording the SECM image at larger distances. Hence the quantitative measurements were performed at distances larger than 30  $\mu\text{m}$ .

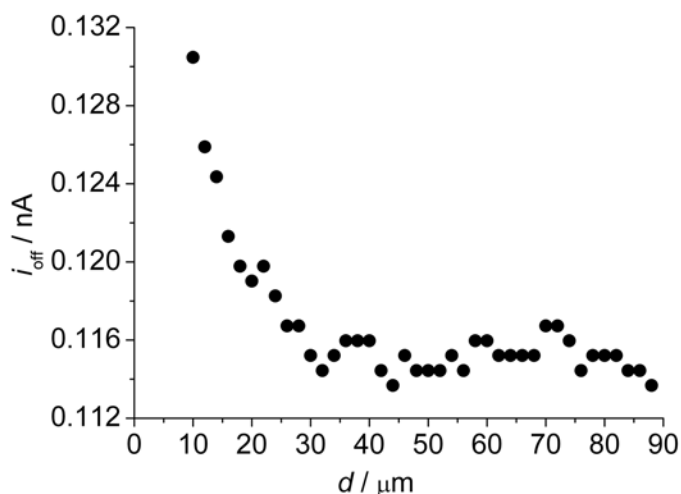


**Figure 6.8.** Plot of the offset current extracted from line scans across of spot 2 of Fig. (6.5) versus UME-substrate separation.

The signal over the polymer spot can be described by a model developed for diffusion to an isolated disk-shaped pore<sup>[108, 374]</sup> as discussed in Chapter 2, Section 2.3. This model was used in this study to fit the extracted line profiles from Fig. (6.7b). Fittings were made using two different conditions: (i) the spot radius  $r_S$  was fixed to the value found in the SCLM image, (ii)  $r_S$  was also fitted. The solid line in Fig. 6.9 was obtained after fitting Eq. (2.21) to the experimental data obtaining  $c_{S,\text{PAP}} = (4.1 \pm 0.1) \times 10^{-6} \text{ mol L}^{-1}$ ,  $d = 80 \mu\text{m}$  and a fixed spot radius  $r_S = 115.2 \mu\text{m}$ . The value of  $c_{S,\text{PAP}}$  confirms that only a small fraction of the enzyme

substrate PAPG provided ( $c^*_{\text{PAPG}} = 2 \times 10^{-3} \text{ mol L}^{-1}$ ) is converted. Therefore, the enzyme reaction follows the regime of substrate saturation. At  $d = 80 \text{ }\mu\text{m}$  the diffusion layer is naturally larger than the measured spot size itself, however  $r_s$  obtained by the fitting procedure at  $d = 80 \text{ }\mu\text{m}$  is similar to the value measured by SCLM ( $r_s = 105.4 \text{ }\mu\text{m}$ ). This underlines that the theory describes sufficiently well the experimental data.

Line scan profiles were extracted and subsequent fitting was done for  $d = 30, 40, 50, 60, 70$  and  $80 \text{ }\mu\text{m}$  for the three spots. The obtained  $c_{\text{S,PAP}}$  were similar for each curve. Table 6.4 summarizes the surface concentrations of PAP extracted from the fittings with (a) fixed  $r_s$  (values from SCLM) and (b) fitted  $r_s$ . The  $c_{\text{S,PAP}}$  values were averaged from the line scans at different  $d$ . The variations are the variations between the results for one spot obtained at different distances. The uncertainties of the other quantities are estimated from the uncertainty of the  $c_{\text{S,PAP}}$  values.

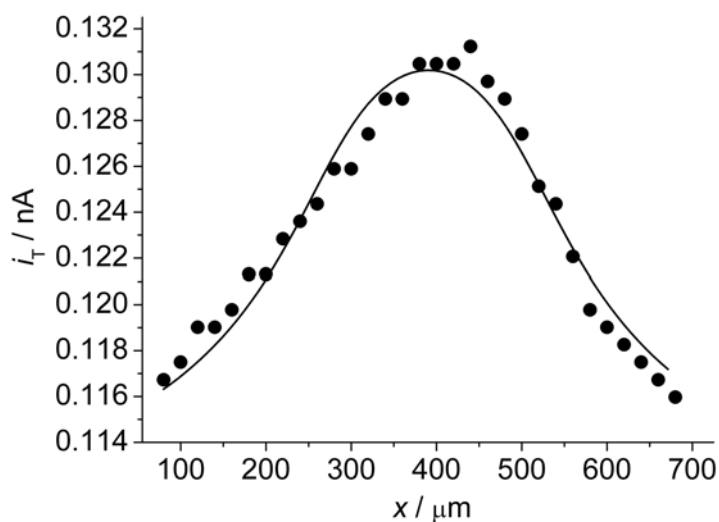


**Figure 6.9.** Line profile of spot 2 extracted from the x-z image and its fit to the theory. The experimental parameters are:  $c_{\text{PAPG}} = 2 \text{ mM}$ ,  $r_T = 12.5 \text{ }\mu\text{m}$ ,  $d = 80 \text{ }\mu\text{m}$ ,  $v_T = 40 \text{ }\mu\text{m s}^{-1}$ . Fitting parameters:  $d = 80 \text{ }\mu\text{m}$ ,  $D_{\text{PAP}} = 9.2 \times 10^{-6} \text{ cm s}^{-1}$ ,  $r_s = 115.2 \text{ }\mu\text{m}$ , and  $i_{\text{offset}} = 0.107 \text{ nA}$ .

**Table 6.4:** Summary of results obtained for the spots 1, 2, and 3. The PAP concentrations were estimated from the line scan fitting according to Eq. (2.21). (a) The spot radius was fixed to the value determined from the SCLM images in Fig. (6.5). (b) The spot radii were estimated from the curve fit.

(a)

Spot	$r_s / \mu\text{m}$	$c_{\text{S,PAP}} / \mu\text{M}$	$\Omega / 10^{-15} \text{ mol s}^{-1}$	$J / 10^{-12} \text{ mol s}^{-1} \text{ cm}^{-2}$	$\Gamma_{\text{enz}} / 10^{-13} \text{ mol cm}^{-2}$	$\Gamma_{\text{DNA}} / 10^{-13} \text{ mol cm}^{-2}$	$\Gamma_{\text{DNA}} / 10^{10} \text{ molecules cm}^{-2}$
1	114.7	$3.8 \pm 0.4$	$1.6 \pm 0.2$	$3.8 \pm 0.4$	$4.9 \pm 0.5$	$1.6 \pm 0.2$	$9.9 \pm 1.0$
2	115.2	$4.4 \pm 0.3$	$1.9 \pm 0.1$	$4.5 \pm 0.3$	$5.8 \pm 0.5$	$1.9 \pm 0.2$	$11.6 \pm 0.9$
3	116.0	$2.2 \pm 0.1$	$0.9 \pm 0.1$	$2.2 \pm 0.1$	$2.8 \pm 0.2$	$0.9 \pm 0.1$	$5.7 \pm 0.3$

(b)

Spot	$r_s / \mu\text{m}$	$c_{\text{S,PAP}} / \mu\text{M}$	$\Omega / 10^{-15} \text{ mol s}^{-1}$	$J / 10^{-12} \text{ mol s}^{-1} \text{ cm}^{-2}$	$\Gamma_{\text{enz}} / 10^{-13} \text{ mol cm}^{-2}$	$\Gamma_{\text{DNA}} / 10^{-13} \text{ mol cm}^{-2}$	$\Gamma_{\text{DNA}} / 10^{10} \text{ molecules cm}^{-2}$
1	$126.6 \pm 11.9$	$3.9 \pm 0.6$	$1.8 \pm 0.2$	$3.6 \pm 0.8$	$4.7 \pm 1.0$	$1.6 \pm 0.4$	$9.4 \pm 2.1$
2	$105.4 \pm 4.9$	$4.4 \pm 0.3$	$1.7 \pm 0.2$	$4.9 \pm 0.6$	$6.3 \pm 0.8$	$2.1 \pm 0.3$	$12.7 \pm 1.6$
3	$123.2 \pm 53.3$	$2.2 \pm 0.3$	$1.0 \pm 0.5$	$2.1 \pm 2.1$	$2.7 \pm 2.7$	$0.9 \pm 0.9$	$5.5 \pm 5.4$

According to Eq. (2.24) the fluxes  $\Omega$  of PAP molecules formed via the  $\beta$ -galactosidase immobilized on the hybridized polypyrrole-ODN spots can be calculated (Table (6.4)). By assuming a uniform flux over the whole polymer spot, a generation rate  $J$  can be determined according to Eq. (2.25). The amount of enzymes  $\Gamma_{\text{enz}}$  linked to the hybridized sample can be finally calculated from the generation rate  $J$  by Eq. (6.2):

$$J = k_{\text{cat}} \cdot \Gamma_{\text{enz}} \quad (6.2)$$

where  $k_{\text{cat}}$  is the turnover number for  $\beta$ -galactosidase using PAPG as substrate. The turnover number can be determined by measuring the flux  $\Omega$  of PAP molecules produced from a well-defined number of  $\beta$ -galactosidase molecules in the regime of substrate saturation.

Such a system was created by the use of a microbead spot, similar to Section 5.4 of Chapter 5. The microbead spot consisted of streptavidin-modified polymeric microbeads saturated with  $\beta$ -galactosidase. This model system uses the same biotinylated galactosidase preparation as in the case of the polypyrrole/polypyrrole-ODN spots. In both experiments biotinylated galactosidase is bound to streptavidin *after* the polymer structure (spot or bead) was created. In case of the beads the enzyme is bound to the outer surface of the microbeads. The investigations are carried out in the same buffer. It was supposed that the model experiment using microbeads can provide a reasonable estimation of the turnover number of the biotinylated  $\beta$ -galactosidase also for the experiment with the polypyrrole/polypyrrole-

ODN spots. However, it is impossible to rule out slight variations based on changes of the enzyme environment on the microbeads and on the polypyrrole/polypyrrole-ODN spot. Fig. (6.10) shows the GC image of a microbead spot of comparable size as the DNA polymer spot. From the line profile (Fig. (6.10b)) the concentration of PAP was determined being  $c_{S,PAP} = 8.5 \times 10^{-6} \text{ mol L}^{-1}$  resulting in  $\Omega = 2.13 \times 10^{-14} \text{ mol s}^{-1}$ . Assuming a disk-shaped profile a flux per area of  $J = 1.48 \times 10^{-10} \text{ mol s}^{-1} \text{ cm}^{-2}$  could be calculated ( $A = 1.43 \times 10^{-4} \text{ cm}^2$ ). As each bead is coated with an estimated number of  $7 \times 10^5$  streptavidin molecules<sup>[320]</sup> and each streptavidin accepts four biotin molecules,  $2.8 \times 10^6$  active binding sites are present on each bead.<sup>[320]</sup> In the case of full saturation of the streptavidin beads with  $\beta$ -galactosidase and with a bead radius of  $1.4 \text{ }\mu\text{m}$ , an enzyme surface concentration of  $\Gamma_{\text{enz}} = 1.8 \times 10^{-11} \text{ mol cm}^{-2}$  can be calculated and a turnover number of  $7.85 \text{ s}^{-1}$  is obtained from Eq. (6.2).

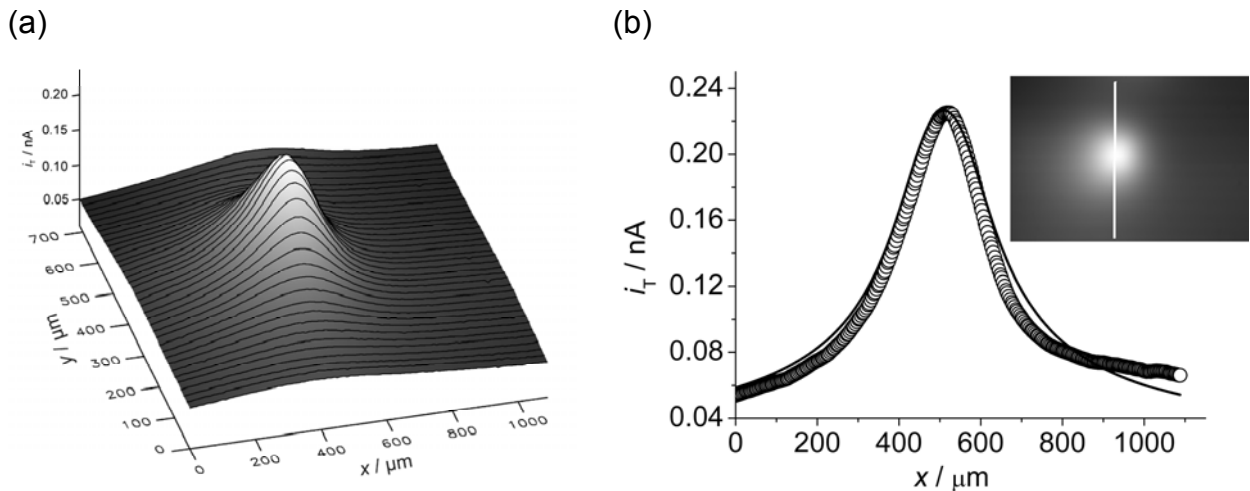


**Figure 6.10.** (a) GC image of  $\beta$ -galactosidase activity in a microspot; (b) experimental line profile across image (open circles); Experimental parameters:  $c_{\text{PAPG}} = 2 \text{ mM}$ ,  $r_T = 5 \text{ }\mu\text{m}$ ,  $d = 50 \text{ }\mu\text{m}$ ,  $v_T = 30 \text{ }\mu\text{m s}^{-1}$ . The solid line was calculated using equation (2.21) with  $r_T = 5 \text{ }\mu\text{m}$ ,  $d = 47 \text{ }\mu\text{m}$ ,  $D_{\text{PAP}} = 9.2 \times 10^{-6} \text{ cm}^2 \text{ s}^{-1}$ ,  $r_{\text{spot}} = 67.6 \text{ }\mu\text{m}$ ,  $c_{S,PAP} = 8.5 \times 10^{-5} \text{ M}$  and a constant current offset of  $0.0361 \text{ nA}$ .

Knowing  $J$ , the total amount of enzyme linked to the hybridized double helix  $\Gamma_{\text{enz}}$  was calculated for the galactosidase bound to ODN-polymer spots. Table (6.4) shows the determined values for the two different conditions of (a) fixed  $r_s$  and (b) fitted  $r_s$ . Surface concentrations of  $\beta$ -galactosidase ranging from  $2.72 \times 10^{-13} \text{ mol cm}^{-2}$  to  $6.32 \times 10^{-13} \text{ mol cm}^{-2}$  are obtained. From the surface concentration of the enzyme and the fact that all the biotinylated complements are bound to one of the three free binding sites of streptavidin (Fig. 6.1), an average surface concentration for the accessible biotinylated complementary DNA is

estimated to be  $\Gamma_{\text{DNA-comp}} = \Gamma_{\text{enz}}/3$ . This leads to  $\Gamma_{\text{DNA-comp}}$  of  $(1.64 \pm 0.16) \times 10^{-13}$ ,  $(1.93 \pm 0.15) \times 10^{-13}$  and  $(0.94 \pm 0.05) \times 10^{-13}$  mol cm<sup>-2</sup> for spot 1, 2, and 3 respectively in the case of fixed  $r_s$ , and  $(1.56 \pm 0.35) \times 10^{-13}$ ,  $(2.11 \pm 0.27) \times 10^{-13}$  and  $(0.91 \pm 0.89) \times 10^{-13}$  mol cm<sup>-2</sup> for spot 1, 2, and 3 respectively in the case of fitted  $r_s$ . Assuming 100% hybridization, this value corresponds to the surface concentration of accessible ODN for hybridization with complementary strands labeled by an enzyme. In the case of the often-observed hybridization efficiency of  $(60 \pm 20)\%$ ,<sup>[375]</sup> the accessible surface concentration is  $5.46 \times 10^{10} - 1.27 \times 10^{11}$  molecules cm<sup>-2</sup>. This is lower than the reported surface coverage for other ODN systems ranging between  $3 \times 10^{12}$  to  $1.5 \times 10^{13}$  molecules cm<sup>-2</sup>.<sup>[358, 375]</sup> However, our deposition procedure is not comparable to that used in the references.<sup>[338, 358, 375]</sup>

The lower values of accessible ODN surface concentration at the pyrrole/pyrrole-ODN spots can have several reasons:

- it can be a consequence of a low ratio of ODN-substituted pyrrole units in the polymer, which can differ significantly from the ratio of the monomers in solution,
- it can be a consequence of the deposition procedure in which ODN stands will be buried inside the polymer matrix so that they become inaccessible to streptavidin and the biotinylated enzyme due to steric constraints,
- it can be that although ODN strands are available at the outside of the polymer deposit, hybridization cannot occur.

Such situations have been found in cases where the grafting density is too high and the negatively charged immobilized ODN prevent the approach of the negatively charged oligonucleotides from solution. It is quite difficult to access the contribution of all these mechanisms to the observed numbers. The observation that the ODN surface concentration does not increase with the number of pulses indicates that at least the pyrrole/pyrrole-ODN ratio inside the film does not seem to be the limiting factor. Furthermore, the low overall number of accessible nucleotides suggests that the grafting density is not too high. Therefore, there is a tendency to interpret the result as a consequence of burying ODNs inside the polymer spots so that they are not accessible for streptavidin and biotin. The hybridization time of 20 min was taken from an existing protocol<sup>[28]</sup> in which it was found to be sufficient for a similar system (Figure 6 of Ref. <sup>[350]</sup>).



## 6.4 Conclusion

SECM can be used in different ways for developing and improving DNA chips: (i) local deposition of DNA, (ii) detection of hybridization, (iii) parallel determination of grafting density. The detection of the enzyme activity using the GC mode of SECM can be very useful for the determination of the surface concentration of oligonucleotides in polymer layers. The contribution of feedback effects to the UME current can be avoided by using working distances  $d \geq 3 r_T$ . This method is valuable for any other surface where ODNs were immobilized. A combination of the direct mode of SECM to deposit ODNs locally on metallic surfaces and the GC mode for the parallel detection of the hybridization event via enzyme activity shows the large application spectrum of SECM, which can be used for the fabrication as well as the detection and quantification of hybridization events. It could be shown that thicker pyrrole/ODN-pyrrole polymer films do not lead to a significantly increased accessible ODN surface concentration.



## 7 General Concluding Remarks and Outlook

The SECM has been established as a method to analyze and optimize biosensors. The advantages in utilizing SECM are several: it can measure local solute concentrations, map local electrochemical reactivities, to induce localized electrochemical modifications, and to investigate heterogeneous and homogeneous kinetics. In this thesis the SECM was used to analyze the kinetics of electrochemical reactions taking place at the solid-liquid interface. Firstly, electrode materials were electrochemically characterized. This was followed by a kinetic analysis of enzymatic reactions of immobilized enzymes in microbead agglomerates. The emphasis was on the evaluation of transport processes that take place, and its influence on the overall reaction rate. Finally, the accessibility of ODNs on microscopic DNA spots was determined after hybridization with enzyme-labeled ODNs. Other instrumental methods such as CV, SFM, XPS, EIS, SCLM, and DPV were also used in order to corroborate and complement the results obtained with the SECM.

In order to realize the experiments of this thesis, four SECM systems were constructed and tested. Therefore, piezo actuator, piezo motor, and stepper motor positioning systems were assembled with ADDA cards, potentiostats and computers. The signal-to-noise ratio of all systems was analyzed and optimized. The systems reveal to be very stable and throughout these years, did not show any problem and did not have to be recalibrated. Images of a grid patterned on plastic (topography) and micro-contact printing of hexadecanethiol on gold (reactivity) showed that the SECM systems give a good reproducibility. The combination of SECM with other (electro)analytical techniques are being developed and showed to be ideal for certain investigations such as topography with reactivity.

Titanium nitride is a hard and inert conducting material that has yet not been widely used as electrode material for electroanalytical applications although there are highly developed protocols available to produce well-adherent micro and nanostructured electrodes. The possibilities of using TiN thin films for electroanalytical applications were investigated. Three different layers of TiN were characterized by SFM, and showed that the sample roughness increased linearly with the increase of TiN thickness. The XP spectra of native TiN after 5 years of storage showed a high carbon and oxygen (bound in organic compounds) contamination on the topmost layer. UV/ozone treatment successfully removed the organic contamination layer, but at the same time a passive layer of TiO<sub>2</sub> was grown. This passive

layer decreased the ET rate even more than the organic contamination layer as shown by the SECM feedback measurements with  $\text{Fc}/\text{Fc}^+$  as redox mediator.

The double layer capacity was analyzed and is higher than at gold electrodes. It suggests that TiN electrodes are more appropriate to be used in amperometric rather than in voltammetric detection schemes. In addition, the potential window in acidic, neutral and alkaline aqueous solutions were shown to be large enough for many compounds used for instance in the electrochemical detection of immunoassays. Many electrochemical biosensors, immunoassays and DNA assays function under application of overpotential, thus TiN electrodes can be used in most of these cases to perform amperometric measurements without interference problems. Since it is known that nanoscopic TiN structures can be produced by established technologies, this is an attractive material for producing miniaturized detectors, e.g. interdigitated electrode arrays.

Besides electrode material, also reliable covering materials are of importance. The electrochemical behavior of a thin gold film electrode coated with PECVD  $\text{SiO}_x$  layers of increasing thickness has been investigated. The SFM images of the  $\text{SiO}_x$  layers suggested that the layers do not have pinholes (resolvable by SFM) and showed increasing surface roughness with increasing layer thickness. CVs of reversible redox couples were recorded for testing the kinetic barrier properties of the  $\text{SiO}_x$ -modified electrodes. The 6.6 nm thick  $\text{SiO}_x$  interface showed slightly faster electron transfer rates due to the presence of pinholes, which was not evident at larger  $\text{SiO}_x$  thicknesses. The positively and negatively charged mediators showed lower regeneration rates than the neutral mediator, however this difference becomes negligible with the increase of the  $\text{SiO}_x$  thicknesses. EIS and CV measurements confirmed a diffusion barrier character of the  $\text{SiO}_x$  layer. The interface capacitance is governed by the thickness of the oxide layer. As a conclusion, PECVD- $\text{SiO}_x$  layers for electrochemical applications must have thicknesses of around 20 nm to be pinhole-free.

Although the analyte transport towards the bioreceptor plays a critical role on the overall rate of reaction and hence on the performance of the biosensor, there is a lack of quantitative experimental work regarding this problem.<sup>[274]</sup> Understanding the mass transport that is taking place and more importantly which regime is governing, e.g. reaction-limited or diffusion-limited, helps to develop and optimize biosensors. A quantitative analysis of the interplay between reaction and diffusion of the substrate towards the surface of the bioreceptor and through the bioreceptor has been performed. These relations were

investigated using model system agglomerates of paramagnetic microbeads that were coated with the enzyme  $\beta$ -galactosidase. By variation of the ratio between modified and unmodified beads, the size of the bead agglomerates and the solution composition, the internal and external diffusion of reagents and products was varied independently and product fluxes were measured by the generation-collection mode of SECM.

The  $\beta$ -galactosidase-catalyzed PAPG hydrolysis was used as a model system for investigation of diffusion through magnetic microbead spots because its reaction product (PAP) is electrochemically active and can be detected at the UME by recording the oxidation current. This magnetic microbead system was used because it provides a way to control the amount of immobilized enzymes within the spot and it forms well-defined spots. Moreover magnetic microbeads are widely used for immunoassays and as already mentioned, there are not many studies regarding the diffusion problems in such systems although they are of great importance. The SECM was used to measure the enzymatic activity by recording the oxidation current of PAP at the UME

The apparent Michaelis-Menten constant and the effects of external diffusion were analyzed in order to optimize the experimental parameters, such as [PAPG] and  $d$ . The  $K_M'$  of the system under study was found to be lower than the intrinsic  $K_M$  for homogeneous systems. It can be explained by the external diffusion pathway of PAPG. The PAPG diffuses toward the bead spot, but at the proximity of the spot partition occurs, increasing the PAPG concentration close to the spot surface. The partition occurs due to hydrophobic interactions between the microbeads and the PAPG. A digital simulation was used to evaluate the theory used to quantify the external PAP fluxes that assumes the bead spot as a disc-shaped spot. It showed that the size of the protruding bead spot does not influence the result, thus the previously used theory from Scott et al.<sup>[93, 124]</sup> is still a valuable approximation that can be used to quantify the bead spot system in the GC mode.

The analysis of the external diffusion has been made in terms of the Damköhler number  $\mu$ . The  $\mu$  was 0.05, indicating that the external diffusion is kinetically controlled rather than diffusion-controlled, thus enough substrate is available to diffuse inside the bead agglomerate. Spot dimensions, such as height and radius, were analyzed by representative experiments using SCLM. The height of the spots increased with increasing number of beads. Hemispherical-cap shape was observed for all bead dilutions.

In order to analyze the shielding effects of beads on each other, bead agglomerates with constant concentration of  $\beta$ -galactosidase-modified beads and increasing bare bead concentrations were formed and SECM imaging was performed. The fluxes obtained from the

evaluation of experimental SECM line scans decreased with the increase of the amount of bare beads added to the spot. It is a qualitative evidence that the shielding effect of the beads on each other blocks the PAPG diffusion to the immobilized  $\beta$ -galactosidase inside the spot and the PAP diffusion out of the spot. Thus, the  $\beta$ -galactosidase-saturated beads buried into the spots do not contribute equally to the total PAP flux. This applies naturally if all PAPG is consumed in the outer layers, but the statement even holds if there is enough PAPG inside the agglomerate. In this case the less effective mass transport prevents an equal contribution to the overall conversion.

The total number of beads inside the spot has been estimated by the geometrical parameters of the spot, e.g. height and radius, with two different assumptions: the disk-shaped spot as considered in the SECM GC theory, and the layer-cap-shaped spot considering the total volume of beads estimated from the geometry. With the total number of beads, the ratio of enzyme-modified beads, and the experimental flux values, the average PAP flux per enzyme-modified bead was determined. These values showed that the PAP flux generated per bead decreases with the increase of unmodified beads in the spot, quantifying the influence of the internal PAPG diffusion. A deeper insight in the internal diffusion in bead spot systems was investigated by comparing the experimental data with simulated data.

In order to express the effect of internal diffusion limitation quantitatively, ODE describing the internal PAPG concentration profile were proposed assuming that  $D_{\text{eff}}$  inside the spot is affected by the porosity and tortuosity. For simplicity of the ODE, two models were used to describe the internal concentration profile under the influence of spot geometry and number of beads: uniform bead layer-shaped spot and half-sphere-shaped spot. Four cases were analyzed varying the shape and the number of beads: uniform bead layer model, big half-sphere, small half-sphere, medium half-sphere. The numerical solution of the proposed models gave the radial concentration profile of the substrate as function of the Thiele modulus  $\phi$ . This approach yields an overall flow of PAP that represents an ensemble average of the random behavior of the individual modified beads inside the spot. The analysis the PAP fluxes resulting from the concentration profile of these models, showed that the flux of PAP decreases with increasing dilution of enzyme-modified beads by bare beads. This proves that the individual beads inside the spot contribute differently to the overall PAP flux.

The comparison of the ratio between the fluxes of PAP generated per bead and the fluxes of PAP generated by freely suspended beads showed that the uniform bead layer model is the most approximate one for the experimental situation. The more concentrated experimental disk-shaped spots agree well to the simulated uniform bead layer model,

however the ratios of the more diluted spots deviate from the uniform bead layer model. In this case, the uniform bead layer model agrees better to the experimental values. As the experimental disk-shaped spot theory considers only the beads that are at the spot surface, it neglects the contribution coming from the buried beads. This leads to higher values of fluxes of individual beads, wrongly attributed to the modified beads at the spot surface. On the other hand, the experimental layer-cap-shaped spots consider all modified beads present in the spot volume, leading to more realistic values of individual fluxes. As a result, the comparison of the models with the experiments shows that the SECM model used to describe the fluxes are suitable for more concentrated spots, however, for more diluted spots the internal diffusion limitation must be considered. It was proved, by comparing the experimental data to the simulated data, that the shielding effects inside of the more diluted bead agglomerates play a role in the quantification of the fluxes, while for more concentrated bead agglomerates it can be neglected.

Further developments of SECM theory of GC mode considering the diffusional effects of macroporous systems should be encouraged, because its influence on the results was proved. The shielding effects and internal diffusion may have an influence in microfluidic analytical systems in which enzymes are immobilized on beads that form aggregates. The analysis of the reaction product is affected by the geometry of the formed agglomerates, external and internal diffusion, and by the enzyme-catalyzed reaction. The shielding effects of microfluidic systems may increase the uncertainty of the measurement. Understanding these effects promotes an improvement of such systems. The height and the shape of the bead agglomerate have a large influence on the response. Packed systems may suffer complete depletion of substrate and the immobilized enzymes inside the pack may not participate in the reaction. In order to improve those systems and decrease costs, one can use the mathematical model proposed here to estimate the effects of internal diffusion and optimum number of beads.

For many immobilization procedures of biomolecules in polymer matrices it is unclear to which extent bioreceptors can be reached by the analyte. As an example, ODN immobilized to polypyrrole spots was investigated. The direct mode of SECM was used for the local deposition achieved through the micrometer-sized formation of a conducting polymer bearing 15mer single-stranded ODN strands. After the interaction of the ODN with its biotin-labeled complementary strand, streptavidin was bound. The molecular assembly was completed by linking biotin-labeled  $\beta$ -galactosidase to the streptavidin. The activity of the linked

$\beta$ -galactosidase was mapped as in the study of bead-immobilized enzymes. It was shown experimentally that the SECM feedback effect becomes insignificant at UME-sample distances larger than 3 UME radii. The flux of formed PAP allowed the determination of the surface density of accessible ODN strands in the functionalized polymer after calibrating with values of bead-immobilized galactosidase. It was shown that thicker pyrrole/ODN-pyrrole polymer films do not lead to a significantly increased accessible ODN surface concentration. The results in this thesis showed for the first time the quantification of hybridization events after ODN immobilization into the polypyrrole film using the SECM, illustrating the versatility of the approach for any other surface where ODNs can be immobilized. A combination of the direct mode of SECM to deposit ODNs locally on metallic surfaces and the GC mode for the parallel detection of the hybridization event via enzyme activity shows the large application spectrum of SECM, which can be used for the fabrication as well as the detection and quantification of hybridization events.

From a more general point of view, this work showed that a detailed kinetic analysis can be obtained by recording approach curves and line scans, and by fitting the data to models of the interfacial reaction and mass transfer processes. This analysis can provide quantitative results because the mass transport between the UME and the sample is usually controlled by diffusion, a theoretically well understood phenomenon that can be described by continuum models. This has been illustrated in the thesis by a variety of rather complex surface architectures.

Further work on complex samples will benefit from increased availability of combined microscopic techniques that can gain morphological information simultaneously with reactivity data, thereby decreasing the uncertainties in estimating parameters of the sample, e.g. the total amount of bead in an agglomerate (Section 5.5.2). Digital simulations become increasingly able to deal with complex geometric objects, interrelated fluxes, and interfacial reactions. The combinations of such new developments will allow new insights into the properties of functional sensor materials and form a rational basis for their optimization.



## 8 Appendix

### 8.1 Procedures

#### 8.1.1 Preparation of the TiN layers

TiN layers were deposited on boron-doped p-Si(100) samples with a resistivity of 12 - 20  $\Omega$  cm. The samples were cleaned and 100 nm thermal oxide was grown on them. TiN was applied by reactively sputtering Ti in a gas atmosphere consisting of Ar and N<sub>2</sub> at a total pressure of 0.2 Pa using a DC magnetron system (HZSN-03, Hochvakuum Dresden, Germany) at 2 kW. The gas atmosphere was formed by adjusting the gas volume fluxes  $F_{N_2}$  and  $F_{Ar}$  to  $F_{N_2}/(F_{N_2} + F_{Ar}) = 0.2$ . The sputter rate was 0.47 nm s<sup>-1</sup>. The atomic ratio is influenced by the composition of the gas atmosphere and by the transmitted power at the sample. The N/Ti atomic ratio in the sample was 1.01 as determined by Rutherford backscattering spectroscopy and elastic backscattering detection. In addition depth profiles were recorded by Auger electron spectroscopy (AES). The layers had thicknesses of 20 nm, 100 nm and 300 nm. An extensive account of the preparation and analysis is available.<sup>[376]</sup>

The TiN electrodes were stored for prolonged time in air (1 month to 5 years). They were washed in ethanol, deionized water and then dried with Ar gas before the measurements. The reported data in this thesis are for electrodes aged 5 years (native samples). Results for electrodes tested after 1 month and 3 years were identical. One sample set was cleaned by a 5 min treatment with UV light (UV tip cleaner, Bioforce Nanoscience, Ames, Iowa, USA) that causes the generation of ozone (UV/ozone-treated samples). Contact to TiN was made with silver epoxy joint to copper wires.

#### 8.1.2 Preparation of the gold/SiO<sub>2</sub> composite slides

Substrate electrodes were prepared by vacuum deposition of 5 nm of titanium and 50 nm of gold onto cleaned glass slides ( $76 \times 26 \times 1$  mm<sup>3</sup>,  $n = 1.58$  at  $\lambda = 633$  nm CML, France). Prior to silica film deposition, the gold samples were first degreased in isopropanol and acetone in an ultrasound bath at room temperature, rinsed copiously with Milli-Q water and dried under a stream of nitrogen. The gold slides were then heated in the plasma chamber at 300°C at a pressure of 0.005 Torr for 1 hour. SiO<sub>x</sub> layers were synthesized by plasma

enhanced chemical vapor deposition in a Plasmalab 800Plus (Oxford Instruments, UK). The growth conditions used were as follows: substrate temperature: 300°C; gas mixture: SiH<sub>4</sub> (3% in N<sub>2</sub>) and N<sub>2</sub>O (the gas flow was 260 sccm and 700 sccm for SiH<sub>4</sub> and N<sub>2</sub>O, respectively); total pressure in the reactor: 1 Torr; power: 10 W at 13.56 MHz. Under these experimental conditions, the deposition rate was 41.4 nm min<sup>-1</sup> and the silica films display a refractive index of 1.48. The silica film thicknesses were adjusted by varying the deposition time.

### 8.1.3 Gold evaporation on glass

Glass slides (Menzel-Gläser, Braunschweig, Germany) were washed throughout with water and ethanol and subsequently cleaned in an ultrasonic bath for 5 minutes with pure ethanol and 5 minutes with distilled water. The slides were then dried in argon stream. Substrate electrodes were prepared by vacuum deposition of 5 nm of chromium and 30 nm of gold onto cleaned glass slides using a Tectra Mini-Coater (Tectra, Frankfurt, Germany). The thicknesses of chromium and gold layers were controlled observing the thickness shown in a quartz crystal microbalance (QCM).

### 8.1.4 Modification of magnetic microbeads

Two microbead suspensions were prepared, one with  $\beta$ -galactosidase-modified beads and another with bare beads. For the preparation of  $\beta$ -galactosidase-modified beads, 10  $\mu$ L of streptavidin-coated M-280 microbead suspension ( $7 \times 10^8$  bead mL<sup>-1</sup>)<sup>[320]</sup> was mixed with 100  $\mu$ L of biotinylated  $\beta$ -galactosidase diluted to 500  $\mu$ g mL<sup>-1</sup> in 0.1 mol L<sup>-1</sup> phosphate buffer solution (pH 7.0). The amount of biotinylated  $\beta$ -galactosidase required to saturate all the biotin binding sites of the streptavidin-coated microbeads can be calculated from the volume of the bead suspension (0.01 mL), the number of beads per microliter ( $7 \times 10^8$  bead mL<sup>-1</sup>), the number of streptavidin molecules per bead ( $7 \times 10^5$ ), the number of biotin binding sites per streptavidin molecule (4), and the molar mass of galactosidase ( $5.3 \times 10^5$  g mol<sup>-1</sup>).<sup>[377]</sup> Hence the amount of  $\beta$ -galactosidase required to saturate all the binding sites is 17.22  $\mu$ g, while 500  $\mu$ g mL<sup>-1</sup> were added. The added amount is sufficient for complete saturation. The streptavidin-coated microbead suspension was mixed with the biotinylated  $\beta$ -galactosidase in a plate shaker for 40 min. The supernatant solution was removed while a strong magnet was pressed against the test tube thus keeping the magnetic microbeads fixed on the test tube wall.

This procedure was used to wash the beads. After removal of the magnet, the beads were resuspended. The beads were washed three times with 100  $\mu\text{L}$  phosphate buffer solution containing 0.5 % v/v Tween 20. After the washing the beads were re-suspended in 150  $\mu\text{L}$  phosphate buffer solution (pH 7.0) yielding a final bead concentration of  $4.7 \times 10^7$  beads  $\text{mL}^{-1}$ .

The same procedure was used to prepare the bare bead solution but instead of using biotinylated  $\beta$ -galactosidase solution, 0.1 M phosphate buffer solution was added to the bare beads.

### 8.1.5 Preparation of modified beads solution in different concentrations

Six suspensions with different ratios of  $\beta$ -galactosidase-modified and bare beads were prepared according to the data given in Table (8.1). The required volume of the bare beads was pipetted into a test tube and a magnet was pressed against the test tube wall, attracting the beads to the wall. The supernatant solution was removed completely, hence only the bare beads were left into the test tube. A constant volume of  $\beta$ -galactosidase-modified bead suspension was added to the test tube and the suspension was thoroughly mixed resulting in constant total solution volume (20  $\mu\text{L}$ ) with increasing number of beads in the suspension but constant number of  $\beta$ -galactosidase saturated beads. The test tubes were gently mixed and used for spotting the bead mounds. The final suspensions amounted in 10, 20, 50, 67, 91, and 100% of beads saturated with  $\beta$ -galactosidase in the suspension volume as shown in Table (8.1).

**Table 8.1:** Bead suspension formation:

Spot Nr.	Volume of bare bead suspension / $\mu\text{L}$	Volume of gal-modified bead suspension / $\mu\text{L}$	Ratio of bare vs. modified bead	Percentage of immobilized enzyme in the spot
1	0	20	0 : 1	100%
2	2	20	0.1 : 1	91%
3	10	20	0.5 : 1	67%
4	20	20	1 : 1	50%
5	80	20	4 : 1	20%
6	180	20	9 : 1	10%

### 8.1.6 Formation of microbeads microspot array

After preparation of modified bead suspensions in different concentrations (Table (8.1)), the magnetic microbeads were deposited on a hydrophobic surface forming a microspot array. The deposition of microbeads spots was performed according to Refs. [120, 299]. 1  $\mu\text{L}$  of bead suspension was taken up in a variable volume micropipette, the micropipette was then placed on a SECM UME holder and positioned over a Parafilm-coated microscope slide placed on a permanent magnet. A hanging drop of 0.7  $\mu\text{L}$  was extruded and held for 30 s in a distance of 1 mm over the Parafilm. The magnetic microbeads were attracted to the bottom of the hanging drop due to the magnetic field. Subsequently, the drop volume was reduced to 0.3  $\mu\text{L}$  and brought into contact with the Parafilm-covered glass slide. After contact, the micropipette was retracted and a well-defined bead mound was left on the Parafilm. An array could be formed by repeating the deposition procedure after moving horizontally the UME holder. Fig. (8.1) shows the spot deposition procedure.

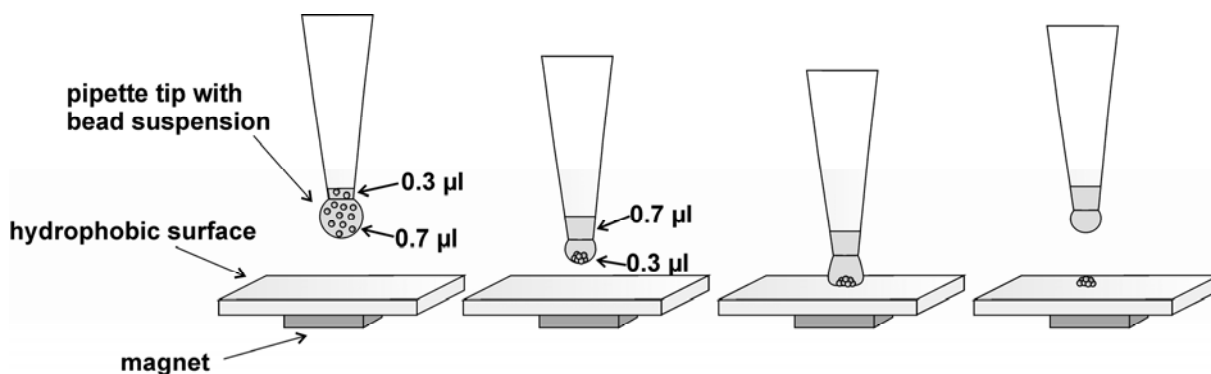


**Figure 8.1.** Sketch of formation of microbeads spot array.

Two slides were prepared, each containing 3 spots of different suspensions. Slide 1 had spots of suspensions 1, 2, and 3 and slide 2 had spots of suspensions 4, 5, and 6. The distance between the spots were 500  $\mu\text{m}$  with a positional uncertainty of about 70  $\mu\text{m}$  due to the pipette tilt in the electrode holder. The optical images of the deposited bead spots were then captured with a Nikon Coolpix 5000 digital camera combined with an optical microscope Nikon TS 100 - F using a transparent scale (100  $\mu\text{m}$  graduations) as reference.

### 8.1.7 Experimental set up for Michaelis-Menten study

A spot with 100 % of the streptavidin binding sites saturated with biotinylated  $\beta$ -galactosidase was formed and 8 solutions were prepared from a concentrated stock solution:

**Table 8.2:** PAPG concentrations used in the Michaelis-Menten study.

Solution number	[PAPG] / mM
1	0.005
2	0.01
3	0.05
4	0.1
5	0.5
6	1
7	5
8	10

Initially a solution containing 0.01 mM PAPG was given into the electrochemical cell. Within few seconds after addition of PAPG, a quasi-stationary, hemispherical diffusion layer was established over the spot. The UME was positioned in a lateral distance of several hundred micrometers to the deposited bead spot. An approach curve was performed observing the negative feedback during oxygen reduction ( $E_T = -0.6$  V). After the UME touched the glass slide surface it was retracted to 40  $\mu\text{m}$  away from the surface. The UME potential was switched to 0.4 V to cause the oxidation of PAP into PIQ. The spot images and line scans were performed by translating the UME horizontally at a translation speed  $v = 10 \mu\text{m s}^{-1}$  in different substrate concentrations.

### 8.1.8 Preparation of modified beads suspensions for analysis of $K_M'$ and $v_{\text{max}}$ of modified bead free in solution

A calibration curve of peak current in dependence of PAP concentration was done by preparing 6 PAP solutions: 2, 1, 0.5, 0.1, 0.05, and 0.005 mM PAP in 0.1 M phosphate buffer pH = 7.2 containing 0.01 M  $\text{MgCl}_2$ . An Ar stream was passed into the solution in order to remove  $\text{O}_2$ . Differential pulse voltammograms (DPV) were recorded for each solution concentration, using a Pt UME with  $r_T = 12.5 \mu\text{m}$ , a Pt wire as CE, and an Ag wire as quasi-reference electrode. The  $i_{\text{peak}}$  was extracted from the voltammogram and was plotted versus the concentration (Fig. (8.2)). The linear fit is  $i_{\text{peak}} (\text{A}) = 9.88 \times 10^{-11} + 3.54 \times 10^{-9} [\text{PAP}] (\text{mM})$ .

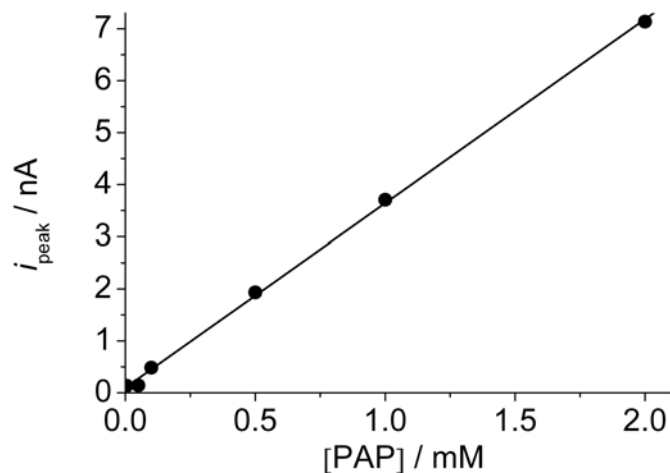


**Figure 8.2.** Calibration curve recorded from the dependence of  $i_{\text{peak}}$  on the PAP concentration extracted from the differential pulse voltammograms.

The streptavidin-coated microbeads were saturated with biotin-labeled  $\beta$ -galactosidase according to the procedure described in Appendix, Section 8.1.4 in order to have all binding sites saturated with the enzyme. Seven substrate solutions with the following concentration were prepared: 10, 5, 1, 0.5, 0.1, 0.05 and 0.01 mM PAPG in 0.1 M phosphate buffer pH = 7.2 containing 0.01 M  $\text{MgCl}_2$ . An Ar stream was passed into the solution in order to remove  $\text{O}_2$ . A Pt UME with  $r_{\text{T}} = 12.5 \mu\text{m}$  was used as WE, a Pt wire as CE, and an Ag wire as quasi-reference electrode.

In order to measure the DPV of the PAP produced by the conversion of PAPG through the immobilized enzyme, 20  $\mu\text{L}$  bead suspension was given to 100  $\mu\text{L}$  PAPG solution, and a sequence of DPV was measured over about 30 min. The  $i_{\text{peak}}$  of PAP increased with time. The measured  $i_{\text{peak}}$  was transferred to [PAP] using the calibration curve. Thus a plot of [PAP] versus time was obtained for each PAPG concentration leading to the slope:  $\Delta[\text{PAP}]/\Delta t$ . The plot of  $\Delta[\text{PAP}]/\Delta t$  versus [PAPG] (Fig. (8.3)) gave a saturation curve and hence the maximum rate  $v_{\text{max}}$  of PAP produced by the modified beads free in the solution.

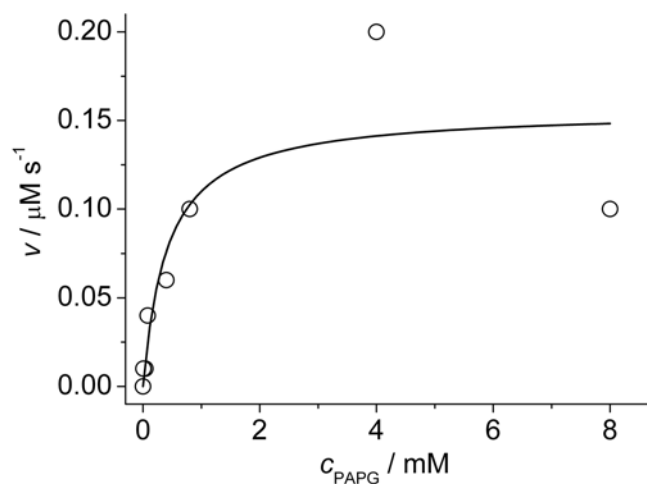


**Figure 8.3.** Saturation curve for modified beads free in solution.  $K_M' = 0.418 \text{ mM}$  and  $v_{\text{max}} = 1.56 \times 10^{-4} \text{ mM s}^{-1}$ .

### 8.1.9 Experiment setup for investigation of the shielding effect inside the bead spot

In order to record the GC image the slides containing the spots were placed in the electrochemical cell, where the substrate solution was added. The substrate solution was 2.0 mM PAPG and 10 mM  $\text{MgCl}_2$  in 0.1 M phosphate buffer (pH 7.2). The divalent cation  $\text{Mg}^{2+}$  was added to the substrate solution in order to provide a stimulatory environment to the enzyme and thus obtain high activity of the enzyme. A quasi-stationary diffusion layer was formed over the bead mounds and hemispherical diffusion was observed. This steady state condition occurs because the diffusion rate of PAPG towards the spot is the same as the rate of the enzymatic catalysis, and the same as rate of PAP formation and diffusion towards the solution bulk. The distance between the bead spots was 500  $\mu\text{m}$  thus the diffusion layers from the single spots did not overlay, hence the spots could be resolved and imaged.

Prior to GC imaging, the UME was positioned about 1 mm away from the bead spots. An approach curve was performed at this position by applying a potential to the UME sufficient to reduce  $\text{O}_2$  at the UME ( $E_T = -0.6 \text{ V}$ ). At this distance the UME has no danger to smash the spot and thus destroy it. The images were recorded after positioning the UME at  $d = 100 \mu\text{m}$  for spots 1, 2 and 3 and  $d = 90 \mu\text{m}$  for spots 4, 5 and 6. The UME potential  $E_T = 0.4 \text{ V}$  versus  $\text{Ag}|\text{AgCl}|3 \text{ M KCl}$  as RE, and a Pt wire was used as AE.

### 8.1.10 Local deposition of polypyrrole-ODN spots

Approach curves for the positioning of the microelectrode to the gold substrate were performed in the monomer solution by poisoning the UME at  $E_T = -0.6$  V where the reduction of oxygen is diffusion-controlled. The substrate was left at OCP. By recording the UME current while approaching the gold substrate ( $v_T = 3 \mu\text{m s}^{-1}$ ), the distance between the two electrodes can be determined precisely. The UME was then retracted to the desired distance  $d$ . The copolymerization of pyrrole/pyrrole-ODN was carried out in 200 mM pyrrole + 10  $\mu\text{M}$  pyrrole-ODN + 0.1 M  $\text{LiClO}_4$  in water at a UME-substrate distance  $d = 60 \mu\text{m}$ . A potential pulse sequence was applied to the gold substrate which consisted of a polymerization pulse at  $E_{\text{pulse}} = 0.7$  V ( $\tau = 20$  ms) and a delay time of  $\tau_{\text{delay}} = 1$  min at OCP. The UME acted as auxiliary electrode as explained in Chapter 2, Section 2.4.

### 8.1.11 Hybridization and construction of biological assembly for the determination of the DNA density grafted

Before hybridization, the gold surface was incubated for 10 min in PBS containing BSA (1%) to minimize non-complementary interactions with the gold surface. The sample was hybridized at room temperature for 20 min in biotinylated complementary ODN (1  $\mu\text{M}$ ) in PBS and then washed with PBS. The modified gold slide was incubated for 15 min in 0.5  $\text{mg mL}^{-1}$  streptavidin solution in PBS, rinsed, and then incubated in biotin-labeled  $\beta$ -galactosidase (500  $\mu\text{g mL}^{-1}$  in PBS) for 30 min. After thoroughly rinsing the sample in order to remove any traces of unspecifically adsorbed  $\beta$ -galactosidase, the galactosidase activity was imaged using the SECM GC mode according to Ref. [120]. The substrate solution contained 2 mM PAPG and 10 mM  $\text{MgCl}_2$  in 0.1 M phosphate buffer (pH 7.0). In order to locate the spots, a SECM image was obtained in the GC mode by translating the UME in  $x$  and  $y$  direction at  $d = 20 \mu\text{m}$  above the polymer spots with  $v_T = 40 \mu\text{m s}^{-1}$  and  $E_T = 0.35$  V to detect PAP. After positioning the UME on a line across the spot center, an  $x$ - $z$  image was recorded where the UME performed line scans along the horizontal direction ( $x$ ) and  $d$  was increased from 10  $\mu\text{m}$  to 88  $\mu\text{m}$  in 2  $\mu\text{m}$  steps. The gold surface was left at OCP during GC imaging.



## 8.2 Material and chemicals

All chemicals were analytical grade and were used as received. All solutions were prepared with deionized water.

- Sodium sulfate ( $\text{Na}_2\text{SO}_4$ , Carl Roth GmbH & Co, Karlsruhe, Germany)
- Sodium hydroxide ( $\text{NaOH}$ , Carl Roth GmbH & Co, Karlsruhe, Germany)
- Potassium chloride ( $\text{KCl}$ ) (Sigma–Aldrich Chemie GmbH, Schnelldorf, Germany)
- Di-sodium hydrogen phosphate dihydrate ( $\text{Na}_2\text{HPO}_4 \cdot 2\text{H}_2\text{O}$ , Scharlau Chemie S. A., Barcelona, Spain)
- Sodium dihydrogen phosphate dihydrate ( $\text{NaH}_2\text{PO}_4 \cdot \text{H}_2\text{O}$  Fluka Chemie GmbH, Buchs, Switzerland)
- Sulfuric acid ( $\text{H}_2\text{SO}_4$ , Merck KGaA, Darmstadt, Germany)
- Ferrocenemethanol (Fc, ABCR GmbH & Co. KG, Karlsruhe, Germany)
- Potassium hexacyanoferrate-II trihydrate ( $\text{K}_4[\text{Fe}(\text{CN})_6] \cdot 3\text{H}_2\text{O}$ , Merck KGaA, Darmstadt, Germany)
- Potassium hexacyanoferrate-III ( $\text{K}_3[\text{Fe}(\text{CN})_6]$ , Sigma–Aldrich Chemie GmbH, Schnelldorf, Germany)
- Potassium hexachloroiridate ( $\text{K}_3[\text{IrCl}_6]$ , Sigma–Aldrich Chemie GmbH, Schnelldorf, Germany)
- Ruthenium hexamine chloride ( $[\text{Ru}(\text{NH}_3)_6]\text{Cl}_3$ , ABCR GmbH & Co. KG, Karlsruhe, Germany)
- Magnesium chloride ( $\text{MgCl}_2$ , Fluka Chemie GmbH, Buchs, Switzerland)
- Biotin-labeled  $\beta$ -galactosidase (Catalog No. G5025, from *Escherichia coli*, 680 U  $\text{mg}^{-1}$ , one unit will hydrolyze 1.0  $\mu\text{mole}$  of *o*-nitrophenyl-  $\beta$ -D-galactoside per min at pH 7.3 at 37 °C - Sigma–Aldrich Chemie GmbH, Schnelldorf, Germany)
- *p*-aminophenyl- $\beta$ -D-galactopyranoside (PAPG, Sigma–Aldrich Chemie GmbH, Schnelldorf, Germany)
- *p*-aminophenol (PAP, Sigma–Aldrich Chemie GmbH, Schnelldorf, Germany)
- Streptavidin-coated M-280 Dynabeads (2.8  $\mu\text{m}$  diameter, monodisperse suspension of  $6.7 \times 10^8$  beads  $\text{mL}^{-1}$  and  $7 \times 10^5$  strepavidin molecules per bead - Invitrogen GmbH, Karlsruhe, Germany)
- Tween<sup>®</sup> 20 (Sigma – Aldrich Chemie GmbH, Steinheim Germany)
- Bovine serum albumin (BSA, Sigma – Aldrich Chemie GmbH, Schnelldorf, Germany)

- Streptavidin (IBA GmbH, Göttingen, Germany)
- Lithium perchlorate ( $\text{LiClO}_4$ , Fluka Chemie GmbH, Buchs, Switzerland)
- Acetonitrile HPLC grade ( $\text{CH}_3\text{CN}$ , Fluka Chemie GmbH, Buchs, Switzerland)
- Pyrrole ( $\text{C}_4\text{H}_5\text{N}$ , Acros, Geel, Belgium)
- Pyrrole-oligonucleotides (5'-Pyrrole-(T)<sub>10</sub> ACG CCA GCA GCT CCA-3', BioMérieux (former Apibio), CEA Grenoble, France)
- Complimentary biotinylated ODNs (5'-biotin-TGG AGC TGC TGG CGT-3', BioMérieux (former Apibio), CEA Grenoble, France)
- Platin wire (Pt, Goodfellow GmbH, Bad Nauheim, Germany)
- Silver wire (Ag, Goodfellow GmbH, Bad Nauheim, Germany)
- $\text{Ag}|\text{AgCl}||3\text{ M KCl}$  (CH Instruments, Austin, TX, USA)
- Gold (Au, Goodfellow GmbH, Bad Nauheim, Germany)
- Micropolish<sup>®</sup> II: 0.3  $\mu\text{m}$  deagglomerated alpha alumina and 0.05  $\mu\text{m}$  deagglomerated gamma alumina, Buehler, Lake Bluff, IL, USA)
- Silver paint (SPI Flash-Dry<sup>™</sup> Ag colloidal suspension, SPI # 04998-AB, SPI Supplies Division, Structure Probe, West Chester, PA, USA)
- Microscope slides (76×26×1 mm,  $n = 1.58$  at  $\lambda = 633$  nm) (Menzel – Gläser, Braunschweig, Germany)
- Parafilm<sup>®</sup> (American National Can, Chicago, IL, USA)
- UME borosilicate glass capillaries (Hilgenberg GmbH, Malsfeld, Germany)
- Nikon Coolpix 5000 digital camera (Nikon GmbH, Düsseldorf, Germany)
- Nikon TS 100 - F (Nikon GmbH, Düsseldorf, Germany)
- Transparent scale, 100  $\mu\text{m}$  graduation (Gretag Ltd., Tonbridge, UK)

### 8.3 Standard solutions

solution	compound	concentration	volume	add. mass
Phosphate buffer pH 7.0 <sup>(a)</sup>	Na <sub>2</sub> HPO <sub>4</sub> ·2H <sub>2</sub> O	0.056 M	500 mL	4.9837 g
	NaH <sub>2</sub> PO <sub>4</sub> ·H <sub>2</sub> O	0.044 M		3.4322 g
Sodium hydroxide	NaOH	1 M	500 mL	20.0050 g
Potassium chloride	KCl	0.1 M	100 mL	0.7456 g
Sodium sulfate	Na <sub>2</sub> SO <sub>4</sub>	0.1 M	100 mL	1.4204 g
Lithium perchlorate	LiClO <sub>4</sub>	0.1 M	100 mL	1.0639 g
Ferrocenemethanol <sup>(b)</sup>	Fc	1 mM	25 mL	0.0054 g
Potassium hexacyanoferrate-(II) <sup>(b)</sup>	K <sub>4</sub> [Fe(CN) <sub>6</sub> ]·3H <sub>2</sub> O	1 mM	25 mL	0.0106 g
Potassium hexacyanoferrate-(III) <sup>(b)</sup>	K <sub>3</sub> [Fe(CN) <sub>6</sub> ]	1 mM	25 mL	0.0082 g
Potassium hexachloroiridate <sup>(b)</sup>	K <sub>3</sub> [IrCl <sub>6</sub> ]	1 mM	25 mL	0.0131 g
Ruthenium hexamine chloride <sup>(b)</sup>	[Ru(NH <sub>3</sub> ) <sub>6</sub> ]Cl <sub>3</sub>	1 mM	25 mL	0.0031 g
<i>p</i> -aminophenyl-β-D-galactopyranoside	PAPG	2 mM	25 mL	0.0136 g
Magnesium chloride	MgCl <sub>2</sub>	0.01 M	25 mL	0.0238 g
Tween	Tween <sup>®</sup> 20	0.5% v/v	1.5 mL	7.5 μL

<sup>(a)</sup> adjust the pH with 1 M NaOH

<sup>(b)</sup> can be diluted in KCl or Na<sub>2</sub>SO<sub>4</sub> electrolyte solutions

### 8.4 Equipments

#### Potentiostats

- bipotentiostat CHI 7001B and monopentiostat CHI 660A (CH Instruments, Austin, TX, USA)
- Monopentiostat μ-P3 (Schramm, Heinrich Heine University, Düsseldorf, Germany)
- Bipotentiostat Ivium Compactstat (Ivium Technologies, Eindhoven, The Netherlands)
- Autolab potentiostat 100 (Eco Chemie, Utrecht, The Netherlands).
  - The cyclic voltammetric experiments were carried out with a three electrode setup, where Pt wire acted as AE, Ag|AgCl|3 M KCl or Ag wire as RE. All potentials in this thesis are referred to Ag|AgCl|3 M KCl.

**SECM**Positioning system

- Marzhäuser (Marzhäuser Wetzlar GmbH & Co KG, Wetzlar, Germany)
  - $x$  and  $y$  scan table - special version (travel range: 100 mm each axis)
  - $z$  scan table - special version (travel range: 50 mm)
  - MR - measuring system for closed loop
  - Corvus motor controller for 3 axis
- PI - HERA (PI GmbH & Co KG, Karlsruhe, Germany)
  - P - 625.2CD - piezo nano positioning system (travel range: 500  $\mu\text{m}$ )
  - P - 625.1CD - piezo nano positioning system (travel range: 500  $\mu\text{m}$ )
  - Controller: E - 500K012, E - 503.00 and E - 509.C3A
- OWIS (OWIS GmbH, Staufen, Germany)
  - $x$ ,  $y$  and  $z$  measuring stage MT 60 (travel range: 25 mm)
  - DIGI-MIC 2 phase stepper motor
  - PC - SM 32 stepper motor controlling card
- Mechnics (Mechonics AG, Munich, Germany)
  - $x$ ,  $y$  and  $z$  miniature translation stage with piezo electric inertial drive (travel range: 18 mm)
  - CU 30 closed loop controller

ADDA card

- PCI-DAS 1602/16 (Plug-in Electronic GmbH, Eichenau, Germany)
- PCI-DDA 04/16 and PCI-DDA 08/16 (Plug-in Electronic GmbH, Eichenau, Germany)
- Cable P50E 100 STG (Plug-in Electronic GmbH, Eichenau, Germany)
- Universal library (Plug-in Electronic GmbH, Eichenau, Germany)

SECM program language

- C++ language (Borland Software Corporation, California, USA)

**SFM**

- Veeco Dimension 3100 microscope and Nanoscope IIIA controller (Veeco Instruments Inc., Santa Barbara, CA, USA) for measurements of TiN and pyrrole-ODN spots

- Dimension 3100 model AFM (Veeco, Santa Barbara, CA) equipped with a Nanoscope IV controller (Digital Instruments) for measurements of the SiO<sub>x</sub> layers
  - All SFM micrographs were recorded in Tapping Mode™

#### ***UV/ozone tip cleaner***

- UV tip cleaner (Bioforce Nanoscience, Ames, Iowa, USA)

#### ***XPS***

- ESCALAB 220 iXL (VG, East Grinstead, UK)
  - XP spectra of Ti, N, C and O were obtained with a hemispherical analyzer at a pressure  $< 5 \times 10^{-8}$  Pa using monochromatized Al K $\alpha$  radiation for excitation. A pass energy of 50 eV and 10 eV was used for survey scans and individual lines. The binding energy (BE) scale of the spectrometer was calibrated by Au 4f<sub>1/2</sub> (84.0 eV), Ag 3d<sub>5/2</sub> (368.3 eV) and Cu 2p<sub>3/2</sub> (932.7 eV). The BE energy scales showed no charging effects, giving in the case of the untreated sample a value of 284.6 eV for the main C 1s component (sp<sup>2</sup> carbon – graphite-like) and 285 eV for the spectrum of the sputtered samples (sp<sup>3</sup> carbon – the well known aliphatic contamination). Spectra were recorded immediately after introduction into the ultra high vacuum and after sputtering 5 min with Ar<sup>+</sup> ion of 3 keV kinetic energy. The spectra were decomposed into individual contributions using the program UNIFIT 2006.<sup>[378]</sup> The graphs show in the upper parts the measured spectrum and the baseline, the lower sections show the fitted components and their sum.

#### ***SCLM***

- SCLM (Leica TCS SP AOBS, Leica Microsystems GmbH, Wetzlar, Germany) with a Leica HC PL FLUOTAR 10 × objective (numerical aperture NA = 0.3)
  - All SCLM micrographs were done in reflection mode.

#### ***Deionized water***

- Seralpur PRO 90C (Seral, Ransbach-Baumbach, Germany)

#### ***Ultrasonic bath***

- SONOREX (Bandelin electronic GmbH & Co. Kg, Berlin, Germany)

**Shaker**

- KS 125 basic (Ika Werke GmbH & Co. KG, Staufen, Germany)

**Vortex**

- Vortex genie K 550-GE (Bender & Hobein AG, Zurich, Switzerland)

**pH meter**

- pH meter 605 (Deutsche Metrohm GmbH & Co. KG, Filderstadt, Germany)

**Balance**

- CP124S analytical balance (Sartorius AG, Göttingen, Germany)

**Variable pipettes**

- 1000  $\mu\text{L}$ , 100  $\mu\text{L}$ , 10  $\mu\text{L}$  and 2.  $\mu\text{L}$  variable pipettes (Eppendorf AG, Hamburg, Germany)

## 8.5 Abbreviations and symbols

### 8.5.1 Abbreviations

---

<b>Abbreviation</b>	<b>Meaning</b>
AD/DA	analog-to-digital/digital-to-analog board
AES	Auger Electron Spectroscopy
ADC	analog-to-digital converter
AE	auxiliary electrode
AFM	atomic force microscopy
BDD	boron-doped diamond
BE	binding energies
BEM	boundary element method
CV	cyclic voltammogram
DAC	digital-to-analog converter
DLL	dynamic link libraries
ECSTM	electrochemical scanning tunnelling microscopes (ECSTM)
EIS	electrochemical impedance spectroscopy
ET	electron transfer
FDM	finite difference methods
FB	feedback mode

---

---

<b>Abbreviation</b>	<b>Meaning</b>
GC	generation-collection mode
IDAs	interdigitated electrode arrays
MIRA	Microscopic Image Rapid Analysis
OCP	open circuit potential
ODN	oligonucleotide
PAP	<i>p</i> -aminophenol
PAPG	<i>p</i> -aminophenyl- $\beta$ -D-galactopyranoside
PECVD	plasma-enhanced chemical vapor deposition
PIQ	<i>p</i> -iminoquinone
PM	permanent magnet This type of motor is not appropriate stepper motor
PZT	lead (plumbum) zirconate titanate piezos positioning stages
RE	reference electrode
RMS	root mean square
SCLM	scanning confocal laser microscopy
SECM	scanning electrochemical microscopy
SEM	scanning electron microscopy
SFM	scanning force microscopy
SG/TC	sample-generation/tip-collection
SiO <sub>x</sub>	silicon dioxide
SNOM	scanning near-field optical microscopy
SNR	signal-to-noise ratio
SPM	Scanning probe microscopy
SPR	surface plasmon resonance
STM	scanning tunnelling microscopy
TG/SC	tip-generation/sample-collection
TiN	titanium nitride
UME	ultramicroelectrode
VR	variable reluctance stepper motor
WE	working electrode
WE2	second working electrode
XPS	x-ray photoelectron spectroscopy

---

## 8.5.2 Symbols

Symbol	Meaning
$A$	area
$c$ or $[ ]$	concentration
$c^*$ or $[ ]^*$	bulk concentration
$c'$	detection limit for the species observed at the UME
$C_{\text{int}}$	double layer capacitance
$c_{\text{O}}$ and $c_{\text{R}}$	concentrations of the oxidized and reduced form of the redox mediator
$[S]_{\text{S}}, [S]_{\text{r}}, [S]^*$	substrate concentration at the spot surface, internal substrate concentration at a radius $r$ , and the substrate concentration at the solution bulk respectively
$d$	UME-sample separation
$D$	diffusion coefficient
$D_{\text{eff}}$	effective diffusion coefficient
$D_{\text{O}}$ or $D_{\text{R}}$	diffusion coefficient of oxidized and reduced species
$d_{\text{offset}}$	point of closest approach
$E$	enzyme
$E$	potential
$E^{\circ'}$	formal potential
$E_{\text{S}}$	substrate potential
ES	enzyme-substrate complex
$E_{\text{T}}$	UME potential
$F$	Faraday constant
Fc	(Hydroxymethyl)ferrocen
$\text{Fc}^+$	(Hydroxymethyl)ferrocinium
$g$	geometry-dependent factor that assumes different values according to $RG$ value
$h$	height
$i$	current
$i_{\text{off}}$	offset current
$i_{\text{S}}$	substrate current
$I_{\text{S}}^{\text{kin}}$	normalized substrate current at the sample
$I_{\text{S}}^{\text{kin}}(L)$	kinetically controlled normalized substrate current.
$i_{\text{T}}$	UME current
$I_{\text{T}}$	normalized UME current ( $I_{\text{T}} = i_{\text{T}}/i_{\text{T},\infty}$ )
$i_{\text{T},\infty}$	infinity current measured at a quasi-infinite distance $d$ from the sample in the bulk solution
$I_{\text{T}}'(L)$	normalized UME current for finite substrate kinetics
$I_{\text{T}}^{\text{cond}}$	normalized current for a conductor
$I_{\text{T}}^{\text{cond},\cdot}$	normalized current for a conductor corrected for normalizations to $4nFD c^* r_{\text{T}}$



Symbol	Meaning
$I_T^{\text{cond}}(L)$	normalized UME current for diffusion controlled regeneration of a redox mediator
$I_T^{\text{ins}}$	normalized current for an insulator
$I_T^{\text{ins}'}$	normalized current for an insulator corrected by a factor $i_{T,\infty} / 4nFDc^*r_T$
$I_T^{\text{ins}}(L)$	normalized UME current for insulating sample
$J$	generation rate of species $c_S$ from the active region
$J$	average flux per enzyme
$j$	current density
$k$	first order heterogeneous rate constant
$k^\circ$	first order heterogeneous standard rate constant
$k_1, k_{-1}$ and $k_2$	reaction rate constants
$k_{\text{cat}}$	turnover number
$k_{\text{eff}}$	effective heterogeneous first order rate constant
$k_L$	proportionality constant
$K_M$	Michaelis-Menten constant
$K_M'$	apparent Michaelis-Menten constant
$L$	normalized UME-sample separation ( $L = d/r_T$ )
$M_{\text{PAP}}$	number of PAP molecules produced per second by a single bead
$n$	number of transferred electrons per molecule
$n$	refractive index
$N_{\text{bead}}$	total number of beads added to the DPV experiment
$N_{\text{b,eff}}$	effective number of beads at the spot surface
$N_{\text{b,eff,gal}}$	effective number of $\beta$ -galactosidase modified beads at the spot surface
$N_{\text{tot}}$	total number of beads in the spot
$N_{\text{tot,gal}}$	total number of $\beta$ -galactosidase modified beads in the spot
O	oxidized form of a quasi-reversible redox couple
P	product
Q	charge
R	reduced form of a quasi-reversible redox couple
$R$	gas constant
$R$	resistance
$R$	radius of the spot
$r$	radius at a certain distance from the spot center
$r$	average flux per enzyme
$R_{\text{int}}$	active charge transfer resistance
$r_S$	radius of the active region of the sample
$R_S$	surface resistance
$R_{\text{sol}}$	electrolyte resistance
$r_T$	radius of the disk-shaped active electrode area
$r_{\text{glass}}$	radius of the insulating sheath of the UME

---

Symbol	Meaning
S	substrate
$t$	time scale of the experiment
$T$	absolute temperature
$U$	voltage
$v$	linear potential scan rate
$v$	linear translation velocity
$v$	reaction rate
$V$	simulation domain
$V_{\text{bead}}$	volume of a bead
$v_{\text{free}}$	rate of enzyme reaction of free enzyme in solution
$v_{\text{max}}$	maximum rate for the catalytic process
$V_{\text{spot}}$	volume of a spot
$W$	Warburg element
$x$	parallel coordinate above a sample
$y$	parallel coordinate above a sample
$z$	vertical coordinate towards the sample
$z_0$	coordinate of the active electrode area, when the insulating sheath touches the surface
$z_{\text{offset}}$	coordinate of the surface
2D	two-dimensional
3D	three-dimensional
$\nabla^2$	Laplace operator
$\alpha$	transfer coefficient
$\alpha$	adhesion angle
$\beta$	dimensionless concentration
$\beta_{\text{B}}$ and $\beta_{\text{S}}$	dimensionless substrate concentration at the bulk and at the spot surface respectively
$\Gamma$	domain boundary
$\Gamma_{\text{enz}}$	enzyme surface concentration
$\mu$	Damköhler number
$\delta$	diffusion layer thickness
$\Delta E_{\text{peak}}$	peak potential difference (CV)
$\Delta x$	lateral distance from the center of the active sample region
$\theta$	dilution factor
$\varphi$	dimensionless concentration
$\zeta$	particle porosity
$\kappa$	dimensionless rate constant
$A$	characteristic length
$\lambda$	wavelength

---

<b>Symbol</b>	<b>Meaning</b>
$\rho$	dimensionless radial position
$\tau$	tortuosity of the pore geometry
$\phi$	Thiele modulus
$\chi$	percentage of $\beta$ -galactosidase modified beads in the spot
$\Omega$	total flux of species $c_S$ from the active region

---



## 9 Bibliography

- [1] T. Vo-Dinh, B. Cullum, *Fresenius J. Anal. Chem.* **2000**, 366, 540.
- [2] L. C. Clark, Jr., C. Lyons, *Ann. N. Y. Acad. Sci.* **1962**, 102, 29.
- [3] L. C. Clark, Jr., E. W. Clark, *Int. Anesthesiology Clinics* **1987**, 25, 1.
- [4] L. C. Clark, Jr., R. Wold, D. Granger, Z. Taylor, *J. App. Physiol.* **1953**, 6, 189.
- [5] D. Grieshaber, R. MacKenzie, J. Voros, E. Reimhult, *Sensors* **2008**, 8, 1400.
- [6] S. Zhang, G. Wright, Y. Yang, *Biosens. Bioelectron.* **2000**, 15, 273.
- [7] J. Evans, *Chemistry World* **2006**, 3, 42.
- [8] P. T. Kissinger, *Curr. Sep.* **1997**, 16, 101.
- [9] A. P. F. Turner, *Sens. Actuators* **1989**, 17, 433.
- [10] *IUPAC Compendium of Chemical Terminology*,  
<http://goldbook.iupac.org/B00663.html>.
- [11] W. Schuhmann, E. M. Bensen, in *Instrumentation and Electroanalytical Chemistry*,  
*Vol. 3* (Ed.: P. R. Unwin), Wiley-VCH, Weinheim, **2003**, p. 350.
- [12] F. Scheller, F. Schubert, D. Pfeiffer, R. Hintsche, I. Dransfeld, R. Renneberg, U.  
Wollenberger, K. Riedel, M. Pavlova, M. Kuhn, *The Analyst* **1989**, 114, 653.
- [13] J. Wang, L.-H. Wu, R. Li, *J. Electroanal. Chem.* **1989**, 272, 285.
- [14] A. J. Bard, X. Li, W. Zhan, *Biosens. Bioelectron.* **2006**, 22, 461.
- [15] C. Zhao, G. Wittstock, *Biosens. Bioelectron.* **2005**, 20, 1277.
- [16] S. A. G. Evans, K. Brakha, M. Billon, P. Mailley, G. Denuault, *Electrochem.*  
*Commun.* **2005**, 7, 135.
- [17] A. Kueng, C. Kranz, B. Mizaikoff, *Biosens. Bioelectron.* **2005**, 21, 346.
- [18] Y. Hirano, D. Oyamatsu, T. Yasukawa, H. Shiku, T. Matsue, *Electrochemistry (Tokyo,*  
*Jpn.)* **2004**, 72, 137.
- [19] C. Zhao, G. Wittstock, *Angew. Chem. Int. Ed.* **2004**, 43, 4170.
- [20] F. Turcu, A. Schulte, G. Hartwich, W. Schuhmann, *Biosens. Bioelectron.* **2004**, 20,  
925.
- [21] T. Kaya, Y.-s. Torisawa, D. Oyamatsu, M. Nishizawa, T. Matsue, *Biosens.*  
*Bioelectron.* **2003**, 18, 1379.
- [22] T. Kaya, K. Nagamine, D. Oyamatsu, M. Nishizawa, T. Matsue, *Chem. Sens.* **2002**,  
18, 187.
- [23] C. Kranz, T. Lötzbeyer, H.-L. Schmidt, W. Schuhmann, *Biosens. Bioelectron.* **1997**,  
12, 257.

- [24] H. Shiku, T. Takeda, H. Yamada, T. Matsue, I. Uchida, *Anal. Chem.* **1995**, *67*, 312.
- [25] T. Wilhelm, G. Wittstock, *Electrochim. Acta* **2001**, *47*, 275.
- [26] C. Kranz, H. E. Gaub, W. Schuhmann, *Adv. Mater.* **1996**, *8*, 634.
- [27] F. Turcu, A. Schulte, G. Hartwich, W. Schuhmann, *Angew. Chem. Int. Ed.* **2004**, *43*, 3482.
- [28] E. Fortin, P. Mailley, L. Lacroix, S. Szunerits, *Analyst (Cambridge, U.K.)* **2006**, *131*, 186.
- [29] C. Zhao, I. Witte, G. Wittstock, *Angew. Chem. Int. Ed.* **2006**, *45*, 5469.
- [30] M. Burchardt, G. Wittstock, *Bioelectrochemistry* **2008**, *72*, 66.
- [31] C. A. Nijhuis, J. K. Sinha, G. Wittstock, J. Huskens, B. J. Ravoo, D. N. Reinhoudt, *Langmuir* **2006**, *22*, 9770.
- [32] S. E. Pust, D. Scharnweber, S. Baunack, G. Wittstock, *J. Electrochem. Soc.* **2007**, *154*, C508.
- [33] H. Kuramitz, M. Dziewatkoski, B. Barnett, H. B. Halsall, W. R. Heineman, *Anal. Chim. Acta* **2006**, *561*, 69.
- [34] A. Bange, J. Tu, X. Zhu, C. Ahn, H. B. Halsall, W. R. Heineman, *Electroanalysis* **2007**, *19*, 2202.
- [35] J.-W. Choi, K. W. Oh, J. H. Thomas, W. R. Heineman, H. B. Halsall, J. H. Nevin, A. J. Helmicki, H. T. Henderson, C. H. Ahn, *Lab Chip* **2002**, *2*, 27.
- [36] C. Kranz, M. Ludwig, H. E. Gaub, W. Schuhmann, *Adv. Mater.* **1995**, *7*, 38.
- [37] C. Kranz, M. Ludwig, H. E. Gaub, W. Schuhmann, *Adv. Mater.* **1995**, *7*, 568.
- [38] W. Schuhmann, C. Kranz, H. Wohlschläger, J. Strohmeier, *Biosens. Bioelectron.* **1997**, *12*, 1157.
- [39] M. Arca, M. V. Mirkin, A. J. Bard, *J. Phys. Chem.* **1995**, *99*, 5040.
- [40] K. Yamashita, M. Takagi, K. Uchida, H. Kondo, S. Takenaka, *Analyst* **2001**, *126*, 1210.
- [41] J. Wang, F. Song, F. Zhou, *Langmuir* **2002**, *18*, 6653.
- [42] J. Wang, F. Zhou, *J. Electroanal. Chem.* **2002**, *537*, 95.
- [43] D. Bonnell (Ed.), *Scanning Probe Microscopy and Spectroscopy*, Wiley-VCH, New York, **2001**.
- [44] H. Takano, J. R. Kenseth, S.-S. Wong, J. C. O'Brien, M. D. Porter, *Chem. Rev.* **1999**, *99*, 2845.
- [45] P. Samori, M. Surin, V. Palermo, R. Lazzaroni, P. Leclere, *Phys. Chem. Chem. Phys.* **2006**, *8*, 3927.

- [46] P. Samori, *Chem. Soc. Rev.* **2005**, *34*, 551.
- [47] M. Bowker, *Chem. Soc. Rev.* **2007**, *36*, 1656.
- [48] G. Binnig, H. Rohrer, *IBM J. Res. Develop.* **2000**, *44*, 279.
- [49] D. A. Bonnell, *Prog. Surf. Sci.* **1998**, *57*, 187.
- [50] N. Garcia, *IBM J. Res. Develop.* **1986**, *30*, 533.
- [51] J. H. J. Scott, *Anal. Bioanal. Chem.* **2003**, *375*, 38.
- [52] J. Cazaux, *J. Microsc.* **2005**, *217*, 16.
- [53] O. C. Wells, D. C. Joy, *Surf. Interface Anal.* **2006**, *38*, 1738.
- [54] R. Reichelt, *Scanning electron microscopy*, Springer, New York, **2007**.
- [55] R. Zenobi, V. Deckert, *Angew. Chem. Int. Ed.* **2000**, *39*, 1747.
- [56] A. Dereux, C. Girard, J.-C. Weeber, *J. Chem. Phys.* **2000**, *112*, 7775.
- [57] A. J. Bard, M. V. Mirkin (Eds.), *Scanning Electrochemical Microscopy*, Marcel Dekker, Inc., New York, Basel, **2001**.
- [58] B. R. Horrocks, in *Instrumentation and Electroanalytical Chemistry, Vol. 3* (Ed.: P. R. Unwin), Wiley-VCH, Weinheim, **2003**, p. 444.
- [59] P. Sun, F. O. Laforge, M. V. Mirkin, *Phys. Chem. Chem. Phys.* **2007**, *9*, 802.
- [60] G. Wittstock, M. Burchardt, S. E. Pust, Y. Shen, C. Zhao, *Angew. Chem. Int. Ed.* **2007**, *46*, 1584.
- [61] A. J. Bard, D. E. Cliffel, C. Demaille, F.-R. F. Fan, M. Tsionsky, *Ann. Chim. (Rome, Italy)* **1997**, *87*, 15.
- [62] A. J. Bard, F.-R. F. Fan, M. V. Mirkin, in *Electroanalytical Chemistry, Vol. 18* (Ed.: A. J. Bard), Marcel Dekker, New York, Basel, Hong Kong, **1994**.
- [63] A. J. Bard, F.-R. F. Fan, M. V. Mirkin, in *Physical Electrochemistry: Principles, Methods and Applications* (Ed.: J. Rubinstein), Marcel Dekker, New York, **1995**.
- [64] A. L. Barker, M. Gonsalves, J. V. Macpherson, C. J. Slevin, P. R. Unwin, *Anal. Chim. Acta* **1999**, *385*, 223.
- [65] G. Wittstock, in *Solid-Liquid Interfaces, Macroscopic Phenomena - Microscopic Understanding* (Eds.: K. Wandelt, S. Thurgate), Springer-Verlag, Berlin, Heidelberg, **2003**, p. 335.
- [66] J. V. Macpherson, P. R. Unwin, in *Scanning Electrochemical Microscopy* (Eds.: A. J. Bard, M. V. Mirkin), Marcel Dekker, New York, Basel, **2001**, p. 521.
- [67] A. J. Bard, F.-R. F. Fan, *Faraday Discuss.* **1992**, *94*, 1.
- [68] M. V. Mirkin, in *Scanning Electrochemical Microscopy* (Eds.: A. J. Bard, M. V. Mirkin), Marcel Dekker, New York, Basel, **2001**, p. 299.

- [69] M. Tsionsky, A. J. Bard, M. V. Mirkin, *J. Phys. Chem.* **1996**, *100*, 17881.
- [70] Y. Shao, M. V. Mirkin, *J. Electroanal. Chem.* **1997**, *439*, 137.
- [71] S. Amemiya, Z. Ding, J. Zhou, A. J. Bard, *J. Electroanal. Chem.* **2000**, *483*, 7.
- [72] C. Wei, A. J. Bard, M. V. Mirkin, *J. Phys. Chem.* **1995**, *99*, 16033.
- [73] C. J. Slevin, S. Ryley, D. J. Walton, P. R. Unwin, *Langmuir* **1998**, *14*, 5331.
- [74] I. Ciani, D. P. Burt, S. Daniele, P. R. Unwin, *J. Phys. Chem. B* **2004**, *108*, 3801.
- [75] C. Gabrielli, F. Huet, M. Keddam, P. Rousseau, V. Vivier, *Electrochem. Solid State Lett.* **2003**, *6*, E23.
- [76] A. J. Bard, F.-R. F. Fan, J. Kwak, O. Lev, *Anal. Chem.* **1989**, *61*, 132.
- [77] R. C. Engstrom, M. Weber, D. J. Wunder, R. Burgess, S. Winkquist, *Anal. Chem.* **1986**, *58*, 844.
- [78] H.-Y. Liu, F.-R. F. Fan, C. W. Lin, A. J. Bard, *J. Am. Chem. Soc.* **1986**, *108*, 3838.
- [79] J. Kwak, A. J. Bard, *Anal. Chem.* **1989**, *61*, 1221.
- [80] A. L. Whitworth, D. Mandler, P. R. Unwin, *Phys. Chem. Chem. Phys.* **2005**, *7*, 356.
- [81] C. Combellas, A. Fuchs, F. Kanoufi, *Anal. Chem.* **2004**, *76*, 3612.
- [82] C. G. Zoski, B. Liu, A. J. Bard, *Anal. Chem.* **2004**, *76*, 3646.
- [83] P. Liljeroth, C. Johans, C. J. Slevin, B. M. Quinn, A.-K. Kontturi, *Anal. Chem.* **2002**, *74*, 1972.
- [84] Y. Lee, S. Amemiya, A. J. Bard, *Anal. Chem.* **2001**, *73*, 2261.
- [85] M. V. Mirkin, in *Scanning Electrochemical Microscopy* (Eds.: A. J. Bard, M. V. Mirkin), Marcel Dekker, New York, Basel, **2001**, p. 145.
- [86] Y. Selzer, D. Mandler, *Anal. Chem.* **2000**, *72*, 2383.
- [87] A. L. Barker, J. V. Macpherson, C. J. Slevin, P. R. Unwin, *J. Phys. Chem. B* **1998**, *102*, 1586.
- [88] J. L. Amphlett, G. Denuault, *J. Phys. Chem. B* **1998**, *102*, 9946.
- [89] R. D. Martin, P. R. Unwin, *J. Electroanal. Chem.* **1997**, *439*, 123.
- [90] A. J. Bard, M. V. Mirkin, P. R. Unwin, D. O. Wipf, *J. Phys. Chem.* **1992**, *96*, 1861.
- [91] A. J. Bard, G. Denuault, R. A. Friesner, B. C. Dornblaser, L. S. Tuckerman, *Anal. Chem.* **1991**, *63*, 1282.
- [92] P. R. Unwin, A. J. Bard, *J. Phys. Chem.* **1991**, *95*, 7814.
- [93] E. R. Scott, H. S. White, J. B. Phipps, *J. Membr. Sci.* **1991**, *58*, 71.
- [94] K. B. Holt, J. Hu, J. S. Foord, *Anal. Chem.* **2007**, *79*, 2556.
- [95] M. V. Mirkin, F.-R. F. Fan, A. J. Bard, *Science* **1992**, *257*, 364.



- [96] B. R. Horrocks, M. V. Mirkin, D. T. Pierce, A. J. Bard, G. Nagy, K. Toth, *Anal. Chem.* **1993**, *65*, 1213.
- [97] C. Wei, A. J. Bard, G. Nagy, K. Toth, *Anal. Chem.* **1995**, *67*, 1346.
- [98] J. Heinze, *Angew. Chem.* **1993**, *105*, 1327.
- [99] K. Aoki, *Electroanalysis* **1993**, *5*, 627.
- [100] R. M. Wightman, D. O. Wipf, *Electroanalytical Chemistry Vol. 15*, Marcel Dekker, New York, **1989**.
- [101] K. Stulik, C. Amatore, K. Holub, V. Marecek, W. Kutner, *Pure Appl. Chem.* **2000**, *72*, 1483.
- [102] M. Etienne, E. C. Anderson, S. R. Evans, W. Schuhmann, I. Fritsch, *Anal. Chem.* **2006**, *78*, 7317.
- [103] B. Ballesteros Katemann, A. Schulte, W. Schuhmann, *Electroanalysis* **2004**, *16*, 60.
- [104] B. Ballesteros Katemann, W. Schuhmann, *Electroanalysis* **2002**, *14*, 22.
- [105] C. Demaille, M. Brust, M. Tsionsky, A. J. Bard, *Anal. Chem.* **1997**, *69*, 2323.
- [106] M. V. Mirkin, F.-R. F. Fan, A. J. Bard, *J. Electroanal. Chem.* **1992**, *328*, 47.
- [107] C. G. Zoski, M. V. Mirkin, *Anal. Chem.* **2002**, *74*, 1986.
- [108] Y. Saito, *Rev. Polarogr.* **1968**, *15*, 177.
- [109] A. J. Bard, F.-R. F. Fan, D. T. Pierce, P. R. Unwin, D. O. Wipf, F. Zhou, *Science* **1991**, *254*, 68.
- [110] D. Mandler, A. J. Bard, *Langmuir* **1990**, *6*, 1489.
- [111] D. T. Pierce, P. R. Unwin, A. J. Bard, *Anal. Chem.* **1992**, *64*, 1795.
- [112] M. Arca, A. J. Bard, B. R. Horrocks, T. C. Richards, D. A. Treichel, *Analyst* **1994**, *119*, 719.
- [113] Y. Shao, M. V. Mirkin, *J. Phys. Chem. B* **1998**, *102*, 9915.
- [114] G. Denuault, personal communication.
- [115] R. Cornut, C. Lefrou, *J. Electroanal. Chem.* **2008**,  
doi:10.1016/j.jelechem.2007.09.021.
- [116] A. J. Bard, L. R. Faulkner, *Electrochemical Methods: Fundamentals and Applications*, John Wiley & Sons, **2004**.
- [117] R. M. Souto, Y. Gonzalez-Garcia, S. Gonzalez, *Corros. Sci.* **2005**, *47*, 3312.
- [118] E. Völker, C. G. Inchauspe, E. J. Calvo, *Electrochem. Commun.* **2006**, *8*, 179.
- [119] X. Zhang, X. Peng, W. Jin, *Anal. Chim. Acta* **2006**, *558*, 110.
- [120] C. Zhao, J. K. Sinha, C. A. Wijayawardhana, G. Wittstock, *J. Electroanal. Chem.* **2004**, *561*, 83.

- [121] C. Zhao, G. Wittstock, *Angew. Chem.* **2004**, *116*, 4264.
- [122] T. Wilhelm, G. Wittstock, *Angew. Chem. Int. Ed.* **2003**, *42*, 2247.
- [123] C. A. Wijayawardhana, N. J. Ronkainen-Matsuno, S. M. Farrel, G. Wittstock, H. B. Halsall, W. R. Heineman, *Anal. Sci.* **2001**, *17*, 535.
- [124] E. R. Scott, H. S. White, J. B. Phipps, *Anal. Chem.* **1993**, *65*, 1537.
- [125] E. R. Scott, A. I. Laplaza, H. S. White, J. B. Phipps, *Pharm. Res.* **1993**, *10*, 1699.
- [126] E. R. Scott, J. B. Phipps, H. S. White, *J. Invest. Dermatol.* **1995**, *104*, 142.
- [127] B. D. Bath, E. R. Scott, J. B. Phipps, H. S. White, *J. Pharm. Sci.* **2000**, *89*, 1537.
- [128] B. D. Bath, J. B. Phipps, E. R. Scott, O. D. Uitto, H. S. White, *Stud. Surf. Sci. Catal.* **2001**, *132*, 1015.
- [129] O. D. Uitto, H. S. White, *Anal. Chem.* **2001**, *73*, 533.
- [130] O. D. Uitto, H. S. White, *Pharm. Res.* **2003**, *20*, 646.
- [131] S. Nugues, G. Denuault, *J. Electroanal. Chem.* **1996**, *408*, 125.
- [132] J. V. Macpherson, M. A. Beeston, P. R. Unwin, *J. Chem. Soc. Faraday Trans. 1* **1995**, *91*, 899.
- [133] J. V. Macpherson, M. A. Beeston, P. R. Unwin, N. P. Hughes, D. Littlewood, *Langmuir* **1995**, *11*, 3959.
- [134] P. R. Unwin, J. V. Macpherson, M. A. Beeston, N. J. Evans, D. Littlewood, N. P. Hughes, *Adv. Dent. Res.* **1997**, *11*, 548.
- [135] C. Lee, J. Kwak, F. C. Anson, *Anal. Chem.* **1991**, *63*, 1501.
- [136] J. L. Fernandez, A. J. Bard, *Anal. Chem.* **2003**, *75*, 2967.
- [137] J. L. Fernandez, A. J. Bard, *Anal. Chem.* **2004**, *76*, 2281.
- [138] G. Lu, J. S. Cooper, P. J. McGinn, *Electrochim. Acta* **2007**, *52*, 5172.
- [139] J. L. Fernandez, N. Mano, A. Heller, A. J. Bard, *Angew. Chem. Int. Ed.* **2004**, *43*, 6355.
- [140] C. Zhao, G. Wittstock, *Anal. Chem.* **2004**, *76*, 3145.
- [141] C. A. Wijayawardhana, G. Wittstock, H. B. Halsall, W. R. Heineman, *Electroanalysis* **2000**, *12*, 640.
- [142] R. D. Martin, P. R. Unwin, *Anal. Chem.* **1998**, *70*, 276.
- [143] G. Denuault, M. H. T. Frank, L. M. Peter, *Faraday Discuss.* **1992**, *94*, 23.
- [144] P. Pohl, Y. N. Antonenko, E. Rosenfeld, *Biochim. Biophys. Acta* **1993**, *1152*, 155.
- [145] G. Nagy, L. Nagy, *Fresenius J. Anal. Chem.* **2000**, *366*, 735.
- [146] G. Denuault, G. Nagy, K. Toth, in *Scanning Electrochemical Microscopy* (Eds.: A. J. Bard, M. V. Mirkin), Marcel Dekker, New York, Basel, **2001**, p. 397.

- [147] B. R. Horrocks, G. Wittstock, in *Scanning Electrochemical Microscopy* (Eds.: A. J. Bard, M. V. Mirkin), Marcel Dekker, New York, Basel, **2001**, p. 445.
- [148] B. D. Bath, H. S. White, E. R. Scott, in *Scanning Electrochemical Microscopy* (Eds.: A. J. Bard, M. V. Mirkin), Marcel Dekker, New York, Basel, **2001**, p. 343.
- [149] G. Wittstock, C. Kranz, D. J. Strike, W. Schuhmann, H. L. Schmidt, *European Microscopy and Analysis* **1996**, 5.
- [150] D. H. Craston, C. W. Lin, A. J. Bard, *J. Electrochem. Soc.* **1988**, *135*, 785.
- [151] [http://www.ntb.ch/Pubs/sensordemo/wtm/m\\_op/LLHB\\_6\\_Keithley.pdf](http://www.ntb.ch/Pubs/sensordemo/wtm/m_op/LLHB_6_Keithley.pdf)
- [152] <http://zone.ni.com/devzone/cda/ph/p/id/287>
- [153] <http://www.solarbotics.net/library/pdflib/pdf/motorbas.pdf>
- [154] <http://www.shinano.com/xampp/docs/Stepper%20Motor%20Operation%20&%20Theory.pdf>
- [155] [http://www.clickautomation.com/PDF/categories/Step%20Motor%20Engineer%20\(2002%20Catlog\).pdf](http://www.clickautomation.com/PDF/categories/Step%20Motor%20Engineer%20(2002%20Catlog).pdf)
- [156] <http://www.allegromicro.com/en/Products/Design/compumot/a04a08.pdf>
- [157] <http://ww1.microchip.com/downloads/en/AppNotes/00907a.pdf>
- [158] [www.pi.ws](http://www.pi.ws)
- [159] B. Andersen, *Laser Focus World* **2002**, 38
- [160] <http://www.machinedesign.com/ASP/viewSelectedArticle.asp?strArticleId=59746&strSite=MDSite&catId=0>
- [161] G. Wittstock, H. Emons, T. H. Ridgway, E. A. Blubaugh, W. R. Heineman, *Anal. Chim. Acta* **1994**, *298*, 285.
- [162] [http://actuator.de/contents/pdf/programm/shorties/B7\\_0\\_spanner\\_s.pdf](http://actuator.de/contents/pdf/programm/shorties/B7_0_spanner_s.pdf)
- [163] K. Uchino, *Piezoelectric Actuators and Ultrasonic Motors*, Springer, **1996**.
- [164] D. Kang, G. Lee Moon, D. Gweon, *Rev. Sci. Instrum.* **2007**, *78*, 075112.
- [165] [http://www.mellesgriot.com/pdf/catalogx/x\\_26\\_5-7.pdf](http://www.mellesgriot.com/pdf/catalogx/x_26_5-7.pdf)
- [166] D. O. Wipf, *Scanning electrochemical microscopy*, Marcel Dekker Inc., New York, **2001**.
- [167] <http://www.microlink.co.uk/differential.html>
- [168] B. Ballesteros Katemann, A. Schulte, W. Schuhmann, *Chem. Eur. J.* **2003**, *9*, 2025.
- [169] J. Kwak, A. J. Bard, *Anal. Chem.* **1989**, *61*, 1794.

- [170] H. Yamada, M. Ogata, T. Koike, *Langmuir* **2006**, *22*, 7923.
- [171] M. F. Garay, J. Ufheil, K. Borgwarth, J. Heinze, *Phys. Chem. Chem. Phys.* **2004**, *6*, 4028.
- [172] P. James, L. F. Garfias-Mesias, P. J. Moyer, W. H. Smyrl, *J. Electrochem. Soc.* **1998**, *145*, 64.
- [173] Y. Lee, A. J. Bard, *Anal. Chem.* **2002**, *74*, 3626.
- [174] H. Yamada, H. Fukumoto, T. Yokoyama, T. Koike, *Anal. Chem.* **2005**, *77*, 1785.
- [175] M. Ludwig, C. Kranz, W. Schuhmann, H. E. Gaub, *Rev. Sci. Instrum.* **1995**, *66*, 2857.
- [176] M. Etienne, A. Schulte, S. Mann, G. Jordan, I. D. Dietzel, W. Schuhmann, *Anal. Chem.* **2004**, *76*, 3682.
- [177] M. Etienne, A. Schulte, W. Schuhmann, *Electrochem. Commun.* **2004**, *6*, 288.
- [178] L. P. Bauermann, W. Schuhmann, A. Schulte, *Phys. Chem. Chem. Phys.* **2004**, *6*, 4003.
- [179] J. V. Macpherson, P. R. Unwin, *Anal. Chem.* **2000**, *72*, 276.
- [180] J. V. Macpherson, P. R. Unwin, *Anal. Chem.* **2001**, *73*, 550.
- [181] C. Kranz, G. Friedbacher, B. Mizaikoff, A. Lugstein, J. Smolier, E. Bertagnolli, *Anal. Chem.* **2001**, *73*, 2491.
- [182] F.-R. F. Fan, D. E. Cliffel, A. J. Bard, *Anal. Chem.* **1998**, *70*, 2941.
- [183] T. H. Treutler, G. Wittstock, *Electrochim. Acta* **2003**, *48*, 2923.
- [184] D. E. Cliffel, A. J. Bard, *Anal. Chem.* **1998**, *70*, 1993.
- [185] D. A. Walsh, J. L. Fernandez, J. Mauzeroll, A. J. Bard, *Anal. Chem.* **2005**, *77*, 5182.
- [186] W. Nogala, M. Burchardt, M. Opallo, J. Rogalski, G. Wittstock, *Bioelectrochemistry* **2008**, *72*, 174.
- [187] K. Eckhard, C. Kranz, H. Shin, B. Mizaikoff, W. Schuhmann, *Anal. Chem.* **2007**, *79*, 5435.
- [188] J. Crummenauer, H. R. Stock, P. Mayr, *Mater. Manuf. Processes* **1995**, *10*, 1267.
- [189] L. A. Cyster, D. M. Grant, K. G. Parker, T. L. Parker, *Biomol. Eng.* **2002**, *19*, 171.
- [190] K. Holmberg, A. Matthews, in *Wear Materials, Mechanisms and Practice* (Ed.: G. W. Stachowiak), Wiley, **2004**.
- [191] L. E. Toth, *Transition Metal Carbides and Nitrides*, New York Academic Press, New York, **1971**.
- [192] N. J. Archer, *Thin Solid Films* **1981**, *80*, 221.
- [193] R. Roth, J. Schubert, M. Martin, E. Fromm, *Thin Solid Films* **1995**, *270*, 320.
- [194] J. E. Sundgren, *Thin Solid Films* **1985**, *128*, 21.

- [195] Z. Y. Chen, A. W. Castleman, Jr., *J. Chem. Phys.* **1993**, *98*, 231.
- [196] S. A. Catledge, M. Fries, Y. K. Vohra, *Nanostructured surface modifications for biomedical implants*, American Scientific Publishers, Stevenson Ranch, California, **2004**.
- [197] M. R. L. Glew, A. Vollmer, S. L. M. Schroeder, Z. H. Barber, *J. Phys. D: Appl. Phys.* **2002**, *35*, 2643.
- [198] M. Guemmaz, G. Moraitis, A. Mosser, M. A. Khan, J. C. Parlebas, *J. Phys.: Condens. Matter* **1997**, *9*, 8453.
- [199] H. Q. Lou, N. Axen, R. E. Somekh, I. M. Hutchings, *Surf. Coat. Technol.* **1997**, *90*, 123.
- [200] B. Rauschenbach, J. W. Gerlach, *Cryst. Res. Technol.* **2000**, *35*, 675.
- [201] F. Vaz, J. Ferreira, E. Ribeiro, L. Rebouta, S. Lanceros-Mendez, J. A. Mendes, E. Alves, P. Goudeau, J. P. Riviere, F. Ribeiro, I. Moutinho, K. Pischow, J. de Rijk, *Surf. Coat. Technol.* **2005**, *191*, 317.
- [202] K. Yokota, K. Nakamura, T. Kasuya, K. Mukai, M. Ohnishi, *J. Phys. D: Appl. Phys.* **2004**, *37*, 1095.
- [203] A. J. Dowling, M. K. Ghantasala, J. P. Hayes, E. C. Harvey, E. D. Doyle, *Smart Mater. Struct.* **2002**, *11*, 715.
- [204] M. Black, J. Cooper, P. McGinn, *Meas. Sci. Technol.* **2005**, *16*, 174.
- [205] L. A. Cyster, K. G. Parker, T. L. Parker, D. M. Grant, *J. Biomed. Mater. Res. Part A* **2003**, *67A*, 138.
- [206] L. A. Cyster, K. G. Parker, T. L. Parker, D. M. Grant, *Biomaterials* **2003**, *25*, 97.
- [207] L. A. Rocha, E. Ariza, J. Ferreira, F. Vaz, E. Ribeiro, L. Rebouta, E. Alves, A. R. Ramos, P. Goudeau, J. P. Riviere, *Surf. Coat. Technol.* **2004**, *180-181*, 158.
- [208] N. C. Saha, H. G. Tompkins, *J. Appl. Phys.* **1992**, *72*, 3072.
- [209] H. G. Tompkins, *J. Appl. Phys.* **1991**, *70*, 3876.
- [210] H. G. Tompkins, *J. Appl. Phys.* **1992**, *71*, 980.
- [211] Y. Wang, H. Yuan, X. Lu, Z. Zhou, D. Xiao, *Electroanalysis* **2006**, *18*, 1493.
- [212] T. Nakayama, H. Wake, K. Ozawa, H. Kodama, N. Nakamura, T. Matsunaga, *Environ. Sci. Technol.* **1998**, *32*, 798.
- [213] G. Sanchez, E. Dalchiele, A. Bologna Alles, *J. Mater. Sci.* **2006**, *41*, 3241.
- [214] K. Aoki, M. Morita, O. Niwa, H. Tabei, *J. Electroanal. Chem.* **1988**, *256*, 269.
- [215] M. Paeschke, U. Wollenberger, C. Köhler, T. Lisec, U. Schnakenberg, R. Hintsche, *Anal. Chim. Acta* **1995**, *305*, 126.

- [216] R. M. Ranade, S. S. Ang, W. D. Brown, *J. Electrochem. Soc.* **1993**, *140*, 3676.
- [217] F. T. Aldridge, *J. Electrochem. Soc.* **1995**, *142*, 1563.
- [218] A. Efremov, V. Svetsov, C.-I. Kim, *Proc. SPIE* **2003**, *5401*, 64.
- [219] L. Jiao, H. Gao, G. Zhang, G. Xie, X. Zhou, Y. Zhang, Y. Zhang, B. Gao, G. Luo, Z. Wu, T. Zhu, J. Zhang, Z. Liu, S. Mu, H. Yang, C. Gu, *Nanotechnology* **2005**, *16*, 2779.
- [220] S. A. Campbell, *The Science and Engineering of Microelectronic Fabrication*, Oxford University Press, New York, **2001**.
- [221] S. A. G. Evans, J. G. Terry, N. O. V. Plank, A. J. Walton, L. M. Keane, C. J. Campbell, P. Ghazal, J. S. Beattie, T.-J. Su, J. Crain, A. R. Mount, *Electrochem. Commun.* **2005**, *7*, 125.
- [222] J. R. Vig, *J. Vac. Sci. Technol. A* **1985**, *3*, 1027.
- [223] H. Höchst, R. D. Bringans, P. Steiner, T. Wolf, *Phys. Rev. B: Condens. Matter Mater. Phys.* **1982**, *25*, 7183.
- [224] J. Guillot, J.-M. Chappe, O. Heintz, N. Martin, L. Imhoff, J. Takadoum, *Acta Materialia* **2006**, *54*, 3067.
- [225] S. Badrinarayanan, S. Sinha, A. B. Mandale, *J. Electron Spectrosc. Relat. Phenom.* **1989**, *49*, 303.
- [226] I. Milosev, H. H. Strehblow, B. Navinsek, M. Metikos-Hukovic, *Surf. Interface Anal.* **1995**, *23*, 529.
- [227] R. S. Nicholson, *Anal. Chem.* **1965**, *37*, 1351.
- [228] J. Jiao, E. Nordlund, J. S. Lindsey, D. F. Bocian, *J. Phys. Chem. C* **2008**, *112*, 6173.
- [229] M. Tsionsky, O. Lev, *Anal. Chem.* **1995**, *97*, 2409.
- [230] O. Lev, Z. Wu, S. Bharathi, V. Glezer, A. Modestov, J. Gun, L. Rabinovich, S. Sampath, *Chem. Mater.* **1997**, *9*, 2354.
- [231] A. Walcarius, *Chem. Mater.* **2001**, *13*, 3351.
- [232] M. Tsionsky, G. Gun, V. Glezar, O. Lev, *Anal. Chem.* **1994**, *66*, 1747.
- [233] J. Wang, P. V. A. Pamidi, D. S. Park, *Anal. Chem.* **1996**, *68*, 2705.
- [234] M. Etienne, A. Walcarius, *Electrochem. Commun.* **2005**, *7*, 1449.
- [235] T. Yamane, N. Nagai, S.-i. Katayama, M. Todoki, *J. Appl. Phys.* **2002**, *91*, 9772.
- [236] N. Ariel, G. Ceder, D. R. Sadoway, E. A. Fitzgerald, *J. Appl. Phys.* **2005**, *98*, 023516.
- [237] D. K. Kambhampati, T. A. M. Jakob, J. W. Robertson, M. Cai, J. E. Pemberton, W. Knoll, *Langmuir* **2001**, *17*, 1169.
- [238] H. B. Liao, W. Wen, G. K. L. Wong, *J. Appl. Phys.* **2003**, *93*, 4485.

- [239] S. Bharathi, M. Nogami, O. Lev, *Langmuir* **2001**, *17*, 2602.
- [240] M. Opallo, J. Kukulka, *Electrochem. Commun.* **2000**, *2*, 394.
- [241] S. Sayen, A. Walcarius, *Electrochem. Commun.* **2003**, *5*, 341.
- [242] A. Walcarius, D. Mandler, J. A. Cox, M. Collinson, O. Lev, *J. Mater. Chem.* **2005**, *15*, 3663.
- [243] A. Graneli, J. Rydstrom, B. Kasemo, F. Hook, *Biosens. Bioelectron.* **2004**, *20*, 498.
- [244] K. Glasmastar, C. Larsson, F. Hook, B. Kasemo, *J. Colloid Interface Sci.* **2002**, *246*, 40.
- [245] C. Larsson, M. Rodahl, F. Hook, *Anal. Chem.* **2003**, *75*, 5080.
- [246] E. Reimhult, C. Larsson, B. Kasemo, F. Hoeoek, *Anal. Chem.* **2004**, *76*, 7211.
- [247] S. Szunerits, R. Boukherroub, *Langmuir* **2006**, *22*, 1660.
- [248] S. Szunerits, S. E. Pust, G. Wittstock, *Anal. Bioanal. Chem.* **2007**, *389*, 1103.
- [249] M. E. Williams, K. J. Stevenson, A. M. Massari, J. T. Hupp, *Anal. Chem.* **2000**, *72*, 3122.
- [250] T. Ito, A. A. Audi, G. P. Dible, *Anal. Chem.* **2006**, *78*, 7048.
- [251] A. K. Neufeld, A. P. O'Mullane, *J. Solid State Electrochem.* **2006**, *10*, 808.
- [252] S. Szunerits, R. Boukherroub, *Electrochem. Commun.* **2006**, *8*, 439.
- [253] S. Szunerits, Y. Coffinier, S. Janel, R. Boukherroub, *Langmuir* **2006**, *22*, 10716.
- [254] P. Schmuki, H. Boehni, J. A. Bardwell, *J. Electrochem. Soc.* **1995**, *142*, 1705.
- [255] O. Purrucker, H. Hillebrandt, K. Adlkofer, M. Tanaka, *Electrochim. Acta* **2001**, *47*, 791.
- [256] M. Chemla, V. Bertagna, R. Erre, F. Rouelle, S. Petitdidier, D. Levy, *Appl. Surf. Sci.* **2004**, *227*, 193.
- [257] I. H. Silman, E. Katchalski, *Annu. Rev. Biochem.* **1966**, *35*, 873.
- [258] R. S. Yalow, S. A. Berson, *Nature* **1959**, *184*, 1648.
- [259] D. S. Hage, *Anal. Chem.* **1995**, *67*, 455R.
- [260] R. F. Masseyeff, *Methods Immunol. Anal.* **1993**, *1*, 257.
- [261] R. F. Masseyeff, *Methods Immunol. Anal.* **1993**, *1*, 629.
- [262] J. Janata, M. Josowicz, D. M. DeVaney, *Anal. Chem.* **1994**, *66*, 207R.
- [263] D. L. Scott, S. Ramanathan, W. Shi, B. P. Rosen, S. Daunert, *Anal. Chem.* **1997**, *69*, 16.
- [264] Y. Yoshimoto, A. Shibukawa, H. Sasagawa, S. Nitta, T. Nakagawa, *J. Pharm. Biomed. Anal.* **1995**, *13*, 483.

- [265] J. G. Dorsey, W. T. Cooper, B. A. Siles, J. P. Foley, H. G. Barth, *Anal. Chem.* **1996**, *68*, 515.
- [266] S. R. Narayanan, *J. Chromatogr.* **1994**, *658*, 237.
- [267] M. B. Kerby, R. S. Legge, A. Tripathi, *Anal. Chem.* **2006**, *78*, 8273.
- [268] M. F. Chaplin, C. Bucke, Editors, *Enzyme Technology*, Cambridge University Press, Cambridge, **1990**.
- [269] J. M. Engasser, C. Horvath, *J. Theor. Biol.* **1973**, *42*, 137.
- [270] C. Horvath, J. M. Engasser, *Biotechnol. Bioeng.* **1974**, *16*, 909.
- [271] A. Kheirilomoom, F. Khorasheh, H. Fazelinia, *J. Biosci. Bioeng.* **2002**, *93*, 125.
- [272] I. Magario, X. Ma, A. Neumann, C. Syldatk, R. Hausmann, *J. Biotechnol.* **2008**, *134*, 72.
- [273] W. R. Berendsen, A. Lapin, M. Reuss, *Biotechnol. Prog.* **2006**, *22*, 1305.
- [274] T. M. Squires, R. J. Messinger, S. R. Manalis, *Nat. Biotechnol.* **2008**, *26*, 417.
- [275] M. S. Thomsen, P. Poelt, B. Nidetzky, *Chem. Commun.* **2007**, 2527.
- [276] Y. Okahata, T. Mori, H. Furusawa, T. Nihira, in *Piezoelectric Sensors, Vol. 5* (Eds.: C. Steinem, A. Janshoff), Springer, Berlin, Heidelberg, **2007**, p. 341.
- [277] S. Nayak, W.-S. Yeo, M. Mrksich, *Langmuir* **2007**, *23*, 5578.
- [278] A. Nag, T. Zhao, R. Dinner Aaron, *J. Chem. Phys.* **2007**, *126*, 035103.
- [279] C. Mateo, J. M. Palomo, G. Fernandez-Lorente, J. M. Guisan, R. Fernandez-Lafuente, *Enzyme Microb. Technol.* **2007**, *40*, 1451.
- [280] S. Braun, S. Rappoport, R. Zusman, D. Avnir, M. Ottolenghi, *Mater. Lett.* **2007**, *61*, 2843.
- [281] F. Ahmad, A. Christenson, M. Bainbridge, A. P. M. Yusof, S. Ab Ghani, *Biosens. Bioelectron.* **2007**, *22*, 1625.
- [282] F. Vianello, S. Ragusa, M. T. Cambria, A. Rigo, *Biosens. Bioelectron.* **2006**, *21*, 2155.
- [283] P. L. Urban, D. M. Goodall, N. C. Bruce, *Biotechnol. Adv.* **2006**, *24*, 42.
- [284] A. Nag, A. R. Dinner, *Biophys. J.* **2006**, *90*, 896.
- [285] B. Limoges, D. Marchal, F. Mavre, J.-M. Saveant, *J. Am. Chem. Soc.* **2006**, *128*, 2084.
- [286] J. Kobayashi, Y. Mori, S. Kobayashi, *Chem. Commun.* **2006**, 4227.
- [287] A. E. David, N. S. Wang, V. C. Yang, A. J. Yang, *J. Biotechnol.* **2006**, *125*, 395.
- [288] B. P. English, W. Min, A. M. van Oijen, K. T. Lee, G. Luo, H. Sun, B. J. Cherayil, S. C. Kou, X. S. Xie, *Nat. Chem. Biol.* **2006**, *2*, 87.
- [289] G. H. Seong, J. Heo, R. M. Crooks, *Anal. Chem.* **2003**, *75*, 3161.
- [290] U. T. Bornscheuer, *Angew. Chem. Int. Ed. Engl.* **2003**, *42*, 3336.



- [291] J. Zhang, J. Zeng, S. Zhang, Y. Wang, Y. Wang, *J. Bioact. Compat. Polym.* **2006**, *21*, 415.
- [292] J. Zhang, S. Zhang, J. Zeng, Y. Wang, Y. Wang, *Polym. Polym. Compos.* **2006**, *14*, 813.
- [293] B. Haupt, T. Neumann, A. Wittemann, M. Ballauff, *Biomacromolecules* **2005**, *6*, 948.
- [294] T. Neumann, B. Haupt, M. Ballauff, *Macromol. Biosci.* **2004**, *4*, 13.
- [295] Y. A. Yeung, K. D. Wittrup, *Biotechnol. Prog.* **2002**, *18*, 212.
- [296] C. A. Wijayawardhana, H. B. Halsall, W. R. Heineman, *Anal. Chim. Acta* **1999**, *399*, 3.
- [297] C. A. Wijayawardhana, S. Purushothama, M. A. Cousino, H. B. Halsall, W. R. Heineman, *J. Electroanal. Chem.* **1999**, *468*, 2.
- [298] J.-W. Choi, K. W. Oh, A. Han, N. Okulan, C. A. Wijayawardhana, C. Lannes, S. Bhansali, K. T. Schlueter, W. R. Heineman, H. B. Halsall, J. H. Nevin, A. J. Helmicki, H. T. Henderson, C. H. Ahn, *Biomed. Microdevices* **2001**, *3*, 191.
- [299] C. A. Wijayawardhana, G. Wittstock, H. B. Halsall, W. R. Heineman, *Anal. Chem.* **2000**, *72*, 333.
- [300] O. Sklyar, M. Träuble, C. Zhao, G. Wittstock, *J. Phys. Chem. B* **2006**, *110*, 15869.
- [301] N. M. Green, *Adv. Prot. Chem.* **1975**, *29*, 85.
- [302] L. De Backer, G. Baron, *Appl. Microbiol. Biotechnol.* **1993**, *39*, 281.
- [303] R. Krishnan, P. Atanasov, E. Wilkins, *Biosens. Bioelectron.* **1996**, *11*, 811.
- [304] D. Bozhinova, B. Galunsky, G. Yueping, M. Franzreb, R. Koester, V. Kasche, *Biotechnol. Lett* **2004**, *26*, 343.
- [305] Q. Fulian, A. C. Fisher, *J. Phys. Chem. B* **1998**, *102*, 9647.
- [306] Q. Fulian, A. C. Fisher, G. Denuault, *J. Phys. Chem. B* **1999**, *103*, 4387.
- [307] Q. Fulian, A. C. Fisher, G. Denuault, *J. Phys. Chem. B* **1999**, *103*, 4393.
- [308] O. Sklyar, G. Wittstock, *J. Phys. Chem. B* **2002**, *106*, 7499.
- [309] O. Sklyar, A. Kueng, C. Kranz, B. Mizaikoff, A. Lugstein, E. Bertagnolli, G. Wittstock, *Anal. Chem.* **2005**, *77*, 764.
- [310] O. Sklyar, J. Ufheil, J. Heinze, G. Wittstock, *Electrochim. Acta* **2003**, *49*, 117.
- [311] O. Sklyar, T. H. Treutler, N. Vlachopoulos, G. Wittstock, *Surf. Sci.* **2005**, *597*, 181.
- [312] H. T. Tang, C. E. Lunte, H. B. Halsall, W. R. Heineman, *Anal. Chim. Acta* **1988**, *214*, 187.
- [313] J. P. Richard, J. G. Westerfeld, S. Lin, J. Beards, *Biochemistry* **1995**, *34*, 117-13.
- [314] G. E. Briggs, J. B. S. Haldane, *Biochem. J.* **1925**, *19*, 338.

- [315] L. Michaelis, M. L. Menten, *Biochemische Zeitschrift* **1913**, *49*, 333.
- [316] R. Dayal, T. Godjevargova, *Enzyme Microb. Technol.* **2006**, *39*, 1313.
- [317] E. W. Thiele, *J. Ind. Eng. Chem.* **1939**, *31*, 916.
- [318] J. Sieler, E. Butter, P. Hallpap, G. Haucke, G. Kühn, A. Martin, E. Uhlig, *Struktur und Bindung-Aggregierte Systemse und Stoffsystematik*, Verlag Chemie, Weinheim, **1973**.
- [319] P. Franzen, *Rheol. Acta* **1979**, *18*, 518.
- [320] *Dynabeads® M-280 Streptavidin*, available from: <https://catalog.invitrogen.com>
- [321] M. V. Mirkin, A. J. Bard, *J. Electroanal. Chem.* **1992**, *323*, 29.
- [322] Q. Fulian, N. A. Williams, A. C. Fisher, *Electrochem. Commun.* **1999**, *1*, 124.
- [323] M. Träuble, O. Sklyar, G. Wittstock, in *International Conference on Boundary Element Techniques VI* (Eds.: A. P. Selvadurai, C. L. Tan, M. H. Aliabadi), EC ltd, Montreal, Canada, **2005**, pp. 161.
- [324] B. R. Horrocks, D. Schmidtke, A. Heller, A. J. Bard, *Anal. Chem.* **1993**, *65*, 3605.
- [325] M. Masson, Z. Liu, T. Haruyama, E. Kobatake, Y. Ikariyama, M. Aizawa, *Anal. Chim. Acta* **1995**, *304*, 353.
- [326] J. Zhang, S. Yao, L. Nie, W. Wei, *Anal. Sci.* **2000**, *16*, 87.
- [327] P. Guedon, T. Livache, F. Martin, F. Lesbre, A. Roget, G. Bidan, Y. Levy, *Anal. Chem.* **2000**, *72*, 6003.
- [328] M. L. Calvo-Munoz, A. Dupont-Filliard, M. Billon, S. Guillerez, G. Bidan, C. Marquette, L. Blum, *Bioelectrochemistry* **2005**, *66*, 139.
- [329] G. Bidan, M. Billon, M. L. Calvo-Munoz, A. Dupont-Fillard, *Mol. Cryst. Liq. Cryst.* **2004**, *418*, 255.
- [330] A. Dupont-Filliard, M. Billon, T. Livache, S. Guillerez, *Anal. Chim. Acta* **2004**, *515*, 271.
- [331] F. Garnier, H. Korri-Youssoufi, P. Srivastava, B. Mandrand, T. Delair, *Synth. Met.* **1999**, *100*, 89.
- [332] V. Dharuman, E. Nebling, T. Grunwald, J. Albers, L. Blohm, B. Elsholz, R. Woerl, R. Hintsche, *Biosens. Bioelectron.* **2006**, *22*, 744.
- [333] S. Reisberg, B. Piro, V. Noel, M. C. Pham, *Bioelectrochemistry* **2006**, *69*, 172.
- [334] Y. Chen, Elling, Y.-I. Lee, S.-c. Chong, *J. Phys.: Conf. Ser.* **2006**, *34*, 204.
- [335] M. H. Pournaghi-Azar, M. S. Hejazi, E. Alipour, *Anal. Chim. Acta* **2006**, *570*, 144.
- [336] Y. Roh, J. Sakong, *Proc. SPIE* **2006**, *6172*, 61720P/1.
- [337] T.-Y. Lee, Y.-B. Shim, *Anal. Chem.* **2001**, *73*, 5629.

- [338] F. Cattaruzza, A. Cricenti, A. Flamini, M. Girasole, G. Longo, T. Prospero, G. Andreano, L. Cellai, E. Chirivino, *Nucleic Acids Res.* **2006**, *34*, e32.
- [339] M. Schena, D. Shalon, R. W. Davis, P. O. Brown, *Science* **1995**, *270*, 467.
- [340] J. M. Brockmann, B. P. Nelson, R. M. Corn, *Annu. Rev. Phys. Chem.* **2000**, *51*, 41.
- [341] Y. Xia, G. M. Whitesides, *Angew. Chem. Int. Ed.* **1998**, *37*, 550.
- [342] E. Delamarche, D. Juncker, H. Schmid, *Adv. Mater.* **2005**, *17*, 2911.
- [343] S. P. Fodor, J. L. Read, M. C. Pirrung, L. Stryer, A. T. Lu, D. Solas, *Science* **1991**, *251*, 767.
- [344] S. P. Fodor, R. P. Rava, X. C. Huang, A. C. Pease, C. P. Holmes, C. L. Adams, *Nature* **1993**, *364*, 555.
- [345] E. Delamarche, A. Bernard, H. Schmid, A. Bietsch, H. Biebuyck, *J. Am. Chem. Soc.* **1998**, *120*, 500.
- [346] G. Wittstock, W. Schuhmann, *Anal. Chem.* **1997**, *69*, 5059.
- [347] I. Turyan, T. Matsue, D. Mandler, *Anal. Chem.* **2000**, *72*, 3431.
- [348] S. Szunerits, N. Knorr, R. Calemczuk, T. Livache, *Langmuir* **2004**, *20*, 9236.
- [349] S. Szunerits, L. Bouffier, R. Calemczuk, B. Corso, M. Demeunynck, E. Descamps, Y. Defontaine, J.-B. Fiche, E. Fortin, T. Livache, P. Mailley, A. Roget, E. Vieil, *Electroanalysis* **2005**, *17*, 2001.
- [350] E. Fortin, Y. Defontaine, P. Mailley, T. Livache, S. Szunerits, *Electroanalysis* **2005**, *17*, 495.
- [351] A. Roget, H. Bazin, R. Teoule, *Nucleic Acids Res.* **1989**, *17*, 7643.
- [352] T. Livache, A. Roget, E. Dejean, C. Barthet, G. Bidan, R. Teoule, *Synth. Met.* **1995**, *71*, 2143.
- [353] T. Livache, A. Roget, E. Dejean, C. Barthet, G. Bidan, R. Teoule, *Nucleic Acids Res.* **1994**, *22*, 2915.
- [354] T. Livache, P. Guedon, C. Brakha, A. Roget, Y. Levy, G. Bidan, *Synth. Met.* **2001**, *121*, 1443.
- [355] T. Livache, H. Bazin, P. Caillat, A. Roget, *Biosens. Bioelectron.* **1998**, *13*, 629.
- [356] X. Su, Y.-J. Wu, R. Robelek, W. Knoll, *Langmuir* **2005**, *21*, 348.
- [357] A. W. Peterson, R. J. Heaton, R. M. Georgiadis, *Nucleic Acids Res.* **2001**, *29*, 5163.
- [358] B. P. Nelson, T. E. Grimsrud, M. R. Liles, R. M. Goodman, R. M. Corn, *Anal. Chem.* **2001**, *73*, 1.
- [359] R.-Y. Zhang, D.-W. Pang, Z.-L. Zhang, J.-W. Yan, J.-L. Yao, Z.-Q. Tian, B.-W. Mao, S.-G. Sun, *J. Phys. Chem. B* **2002**, *106*, 11233.

- [360] L. M. Demers, C. A. Mirkin, R. C. Mucic, R. A. Reynolds, III, R. L. Letsinger, R. Elghanian, G. Viswanadham, *Anal. Chem.* **2000**, *72*, 5535.
- [361] K. Castelino, B. Kannan, A. Majumdar, *Langmuir* **2005**, *21*, 1956.
- [362] S. Asavapiriyant, G. K. Chandler, G. A. Gunawardena, D. Pletcher, *J. Electroanal. Chem. Interfacial Electrochem.* **1984**, *177*, 229.
- [363] A. F. Diaz, J. I. Castillo, J. A. Logan, W. Y. Lee, *J. Electroanal. Chem. Interfacial Electrochem.* **1981**, *129*, 115.
- [364] E. M. Genies, G. Bidan, A. F. Diaz, *J. Electroanal. Chem. Interfacial Electrochem.* **1983**, *149*, 101.
- [365] K. J. Kim, H. S. Song, J. D. Kim, J. K. Chon, *Bull. Korean Chem. Soc.* **1988**, *9*, 248.
- [366] Y. T. Kim, R. W. Collins, K. Vedam, D. L. Allara, *J. Electrochem. Soc.* **1991**, *138*, 3266.
- [367] Y. J. Qiu, J. R. Reynolds, *J. Polym. Sci., Part A: Polym. Chem.* **1992**, *30*, 1315.
- [368] C. A. Salzer, C. M. Elliott, S. M. Hendrickson, *Anal. Chem.* **1999**, *71*, 3677.
- [369] R. J. Waltman, J. Bargon, *Tetrahedron* **1984**, *40*, 3963.
- [370] R. J. Waltman, J. Bargon, *Can. J. Chem.* **1986**, *64*, 76.
- [371] G. Sabouraud, S. Sadki, N. Brodie, *Chem. Soc. Rev.* **2000**, *29*, 283.
- [372] B. D. Malhotra, N. Kumar, S. Chandra, *Prog. Polym. Sci.* **1986**, *12*, 179.
- [373] J. Rodriguez, H. J. Grande, T. F. Otero, *Handbook of Organic Conductive Molecules and Polymers*, John Wiley & Sons, New York, **1997**.
- [374] B. D. Bath, R. D. Lee, H. S. White, *Anal. Chem.* **1998**, *70*, 1047.
- [375] C. E. Jordan, R. M. Corn, *Anal. Chem.* **1997**, *69*, 1449.
- [376] J. Baumann, *Herstellung, Charakterisierung und Bewertung von leitfaehigen Diffusionsbarrieren auf Basis von Ta, Ti und W fuer die Kupfermetallisierung von Siliciumschaltkreisen*, Shaker Verlag, Herzogenrath, **2004**.
- [377] Sigma-Aldrich,  *$\beta$ -Galactosidase-biotin labeled from Escherichia coli, G5025*
- [378] R. Hesse, P. Streubel, R. Szargan, *Surf. Interface Anal.* **2005**, *37*, 589.

## LIST OF PUBLICATIONS

---

[A1] S. Szunerits; Gunther Wittstock; C. Nunes Kirchner; Rabah Boukherroub; Chantal Gondran

**Electrochemical investigation of the influence of thin SiO<sub>x</sub> films deposited on gold on charge transfer characteristics**

*Electrochimica Acta* **2008**, in press.

[A2] C. Nunes Kirchner; C. Zhao; G. Wittstock

**Analysis of the activity of b-galactosidase from Escherichia coli by scanning electrochemical microscopy (SECM)**

*Comprehensive Analytical Chemistry* **2007**, 49, e371-e379.

[A3] C. Nunes Kirchner; G. Wittstock

**Kinetic analysis of titanium nitride thin films by scanning electrochemical microscopy**

*Comprehensive Analytical Chemistry* **2007**, 49, e363-e370.

[A4] G. Wittstock; M. Burchardt; C. Nunes Kirchner

**Scanning electrochemical microscopy in biosensor research**

*Comprehensive Analytical Chemistry* **2007**, 49, 907-939.

[A5] M. Träuble; C. Nunes Kirchner; G. Wittstock

**Nonlinear boundary conditions in simulations of electrochemical experiments using the boundary element method**

*AIP Conf. Proc.* **2007**, 963, 500-503.

[A6] C. Nunes Kirchner; S. Szunerits; G. Wittstock

**Scanning electrochemical microscopy (SECM) based detection of oligonucleotide hybridization and simultaneous determination of the surface concentration of immobilized oligonucleotides on gold**

*Electroanalysis* **2007**, 19, 1258-1267.

[A7] C. Nunes Kirchner; K. H. Hallmeier; R. Szargan; T. Raschke; C. Radehaus; G. Wittstock

**Evaluation of Thin Film Titanium Nitride Electrodes for Electroanalytical Applications**  
*Electroanalysis* **2007**, *19*, 1023-1031.

[A8] S. E. Pust; D. Scharnweber; C. Nunes Kirchner; G. Wittstock

**Heterogeneous Distribution of Reactivity on Metallic Biomaterials: Scanning Probe Microscopy Studies of the Biphasic Ti Alloy Ti6Al4V**  
*Adv. Mater.* **2007**, *19*, 878-882.

[A9] P. Actis; M. Manesse; C. Nunes Kirchner; G. Wittstock; Y. Coffinier; R. Boukherroub; S. Szunerits

**Localized electropolymerization on oxidized boron-doped diamond electrodes modified with pyrrolyl units**  
*Phys. Chem. Chem. Phys.* **2006**, *8*, 4924-4931.

[A10] G. Wittstock; M. Burchardt; C. Nunes Kirchner

**Untersuchung dünner organischer Schichten**  
*LaborPraxis* **2005**, *9*, 20-22.

## CONFERENCES AND WORKSHOPS

---

03.2007 Oral presentation at the 5<sup>th</sup> Deutschen Biosensor Symposium in Bochum, Germany. Topic: **”Scanning electrochemical microscopy (SECM) based detection of hybridization of oligonucleotides and simultaneous determination of the surface coverage of immobilized oligonucleotides on gold”**

09.2006 Oral presentation at the 4<sup>th</sup> Workshop on Scanning Electrochemical Microscopy in Falcade, Italy. Topic: **”Mass transport investigation into microbeads with different saturations of  $\beta$ -galactosidase”**

- 11.2005                    Oral presentation at the 2<sup>nd</sup> International Workshop Surface Modification for Chemical and Biochemical Sensing in Kazimierz Dolny, Poland. Topic: **”Evaluation of titanium nitride thin film electrodes for electroanalytical purposes using scanning electrochemical microscopy”**
- 06.2004                    Poster presentation at the 3<sup>rd</sup> Workshop on Scanning Electrochemical Microscopy in Dublin, Ireland. Topic: **“Adapting scanning electrochemical microscopes for specific tasks”**
- 05.2004                    Poster presentation at the Bunsentagung in Dresden, Germany. Topic: **„Scanning electrochemical microscopy for characterization of galactosidase activity“**

## CURRICULUM VITAE

---

### PERSONAL DATA

---

Name: Carolina Nunes Kirchner  
Date of birth: 01.04.1979  
Place of birth: São Paulo, Brazil  
Marital status: married  
Citizenship: Brazilian

### GRADUATION

---

09/2004 - 07/2008 PhD student at the Physical Chemistry Department at the University of Oldenburg (Prof. Dr. G. Wittstock) - From 02/2005 - 07/2005 interruption due to traffic accident

08/1997 – 08/2002 Chemical Engineering University at the Centro Universitário UNIFEI (FEI), São Bernardo do Campo, Brazil

### EDUCATION

---

01/1994 – 12/1996 High school: Ministro Costa Manso, São Paulo, Brazil

### PROFESSIONAL EXPERIENCE

---

since 09/2003 Scientific co-worker at the Physical Chemistry Department at the University of Oldenburg (Prof. Dr. G. Wittstock)

04/2002 – 01/2003 Junior engineer at the White Martins Praxair Inc., Osasco, Brazil (Specialty Gases / Marketing division)

08/2000 – 03/2002 Intern at White Martins Praxair Inc., Osasco, Brazil (Specialty Gases / Marketing division)



## **ERKLÄRUNG**

---

Ich versichere hiermit, dass ich diese Arbeit selbständig verfasst und nur die angegebenen Quellen und Hilfsmittel benutzt habe. Aus der Dissertation sind die auf der folgenden Seite genannten Veröffentlichungen hervorgegangen. Die Dissertation hat weder zu Teilen noch in Gänze einer anderen wissenschaftlichen Hochschule zur Begutachtung in einem Promotionsverfahren vorgelegen.

Oldenburg, 28 Juli 2008

---

Carolina Nunes Kirchner